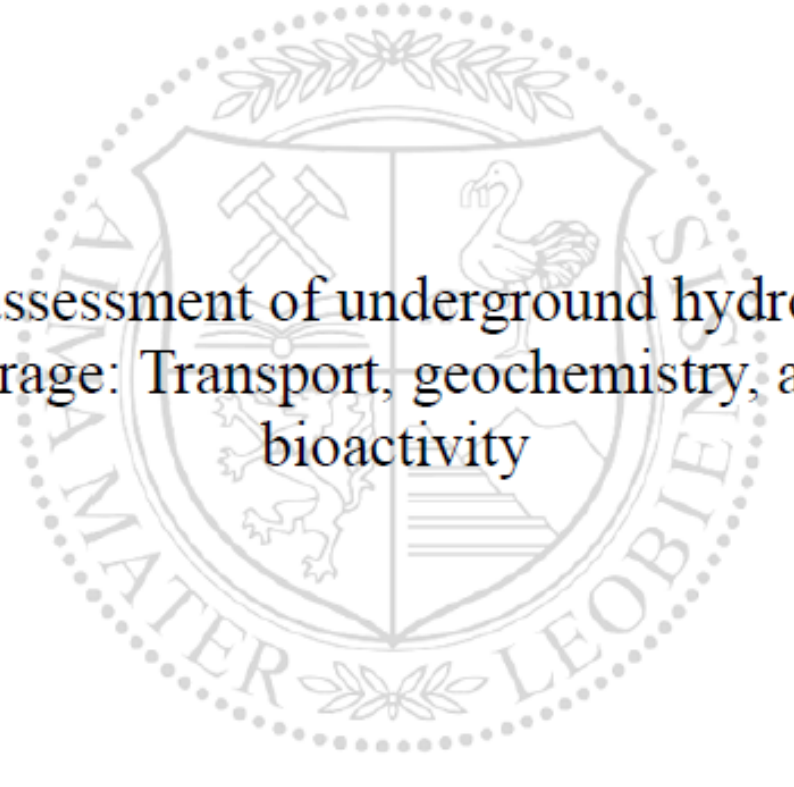




Chair of Reservoir Engineering

Doctoral Thesis



An assessment of underground hydrogen
storage: Transport, geochemistry, and
bioactivity

Neda Hassannayebi

November 2019

AFFIDAVIT

I declare on oath that I wrote this thesis independently, did not use other than the specified sources and aids, and did not otherwise use any unauthorized aids.

I declare that I have read, understood, and complied with the guidelines of the senate of the Montanuniversität Leoben for "Good Scientific Practice".

Furthermore, I declare that the electronic and printed version of the submitted thesis are identical, both, formally and with regard to content.

Date 22.11.2019

Signature Author
Neda, Hassannayebi

Neda Hassannayebi

To my parents

Acknowledgments

First of all, I would like to express my gratitude to my advisor Prof. Holger Ott for his constant support of my dissertation, for his brilliant ideas, and his trust in me. He provided me with the opportunity to be part of his team and grow personally and professionally.

I am very thankful to my former supervisor Dr. Siroos Azizmohammadi, for his guidance and support through my working time on the “Underground Sun Storage” project. I would also like to thank Prof. Stephan Mathai for giving me the chance to start my academic career at Montanuniversität Leoben.

I wish to thank Ms. Caroline Milliotte for her collaboration in constructing the geological model.

My sincere thanks also go to Dr. Marco De Lucia, who took a lot of his time for me and shared his immense knowledge in geochemistry and supported us greatly with the geochemical modeling. I would also like to thank Dr. Dmitrii A. Kulik for his guidance in the first year of the project for geochemical modeling.

I express my sincere thanks to Dr. Frieder Enzmann for welcoming me at the Johannes Gutenberg-Universität Mainz, for his inspiring advice and collaboration, and great support in carrying out numerical simulations. I would also like to thank Prof. Michael Kresten for his valuable comments and support in writing our manuscript.

I also would like to express thanks to Prof. Andreas Paul Loibner, DI Johanna Schritter, and Cathrine Zaknun, at Universität für Bodenkultur, Vienna for their collaboration in conducting bacterial studies and providing the bacterial strain for the experiments.

I am also thankful to Prof. Martin Fernø for his valuable suggestions and support during his visit to Leoben.

I would like to thank Mr. Michael Koopmans and Mr. Horst Resch for their continuous support and help in providing laboratory equipment. A special thanks to Ms. Bettina Matzer for all her support and kindness. I am also thankful to Ms. Janine Billiani at the Institute of “Chemie der Kunststoffe” at Montanuniversität Leoben for her support in the fluid viscosity measurement.

Also, my sincere thanks go to all my friends and colleagues at the petroleum engineering institute, at Montanuniversität Leoben, particularly to my lab friends Ahmad Kharrat and Mohannad Marouf.

I am also thankful to all my friends in Leoben and elsewhere, especially to Melahat (Sahin) Tayli, Aydan Cicek, and Khadija Andjar for their endless support during my research.

Finally, I express my greatest thanks and appreciation to my parents, and my brother and sister for their love, support, and constant encouragement. If it was not because of their immense help and sacrifice, this work could not have been accomplished.

Please note, an editor has not been used in the construction of this dissertation.

Abstract

In recent years, the demand for large-scale energy storage coming from renewable resources has been increased. Solar and wind plants contribute to generating gigawatts of electricity, which often have a considerable mismatch in grid power demand. Hydrogen gas is an effective and flexible energy carrier that can be generated by the conversion of renewable energy. There are conventional means of storing hydrogen, such as batteries; however, they provide limited capacity for storage. As an alternative, depleted natural gas reservoirs can serve as underground hydrogen storage (UHS) facilities with a huge storage capacity.

In this work, two major topics related to UHS in porous media were tackled and studied. The first topic investigates and addresses potential risks associated with hydrogen loss due to diffusion processes and reactions with minerals and brine. This part has been completed in the framework of an interdisciplinary project, “Underground Sun Storage” which aimed to store hydrogen in a depleted gas reservoir in Molasse Basin, Upper Austria. Based on field data, a geological and a transport model for this field were realized. An analytical diffusion model was employed to estimate the hydrogen loss into the caprock and the neighboring layers in a storage cycle based on hydrogen plume propagation. The diffusive loss depends on the diffusion coefficient and the exposed surface area to the hydrogen gas. Due to the scarcity of data and uncertainties of different nature, proper assumptions and simplifications were considered. Lastly, a geochemical modeling workflow was presented to study and quantify potential geochemical processes that can lead to hydrogen loss in the storage site. The geochemical reactions were assessed by equilibrium and kinetic batch models at the reservoir pressure and temperature to investigate the short- and long-term impacts of hydrogen on the formation-water and minerals.

The second major topic in this dissertation studies another aspect of such storage. It turns out *in-situ* bacteria in the reservoir, called Archaea, can metabolize hydrogen and CO₂ and produce natural gas. The fact that hydrogen is served as a substrate for these microorganisms results in the bacterial growth and induces hydrogen degradation. The question of how bacteria grow and transport in porous media is not known. In the same way, there is a concern about biofilm formation, which leads to injectivity issues. Finally, the conversion rate of hydrogen degradation to methane production is of much interest in energy conversion projects. The principal insights into bacterial growth and transport in pore space under saturated flow

conditions were achieved via experimental and numerical analysis; in addition, based on experimental outcomes, recommendations for future research were made. Finally, through the flow simulation on the experimental segmented images, the influence of the bacterial growth on the hydraulic properties of the porous medium is quantified, and changes in the flow field and the relationship between porosity and permeability modeling.

This dissertation attempts to contribute to knowledge by combining various aspects that are relevant for hydrogen storage and conversion assessment, both numerically and experimentally. The primary objective of this research was to create and introduce new insights and concepts that combine diverse disciplines that were related to hydrogen storage and conversion, deliver effective methodologies to identify the potentials and risks in such projects and provide the groundwork for future experimentations and numerical studies.

Zusammenfassung

In den letzten Jahren hat die Nachfrage nach großflächigen Speichern für Energie aus erneuerbaren Rohstoffen zugenommen. Solar- und Windkraftanlagen tragen zur Erzeugung von Gigawatt Strom bei, welcher jedoch häufig einen erheblichen Unterschied zum Bedarf des Stromnetzes aufweist. Wasserstoff ist ein effektiver und flexibler Energieträger, der durch die Umwandlung von erneuerbaren Energien erzeugt werden kann. Es gibt herkömmliche Mittel zum Speichern von Wasserstoff, wie beispielsweise Batterien; diese bieten jedoch nur eine begrenzte Speicherkapazität. Als Alternative können erschöpfte Erdgaslagerstätten als unterirdische Wasserstoffspeicher (UWS) mit einer enormen Speicherkapazität dienen.

In dieser Arbeit wurden zwei Hauptthemen im Zusammenhang mit UWS in porösen Medien behandelt und untersucht. Das erste Thema untersucht und adressiert potenzielle Risiken im Zusammenhang mit Wasserstoffverlust aufgrund von Diffusionsprozessen und Reaktionen mit Mineralien und Sole. Dieser Teil wurde im Rahmen eines interdisziplinären Projekts „Underground Sun Storage“ abgeschlossen, bei dem Wasserstoff in einer erschöpften Gaslagerstätte im oberösterreichischen Molasse-Becken gespeichert werden sollte. Basierend auf Felddarstellungen wurde ein geologisches und ein Transportmodell für dieses Feld erstellt. Ein analytisches Diffusionsmodell wurde verwendet, um den Wasserstoffverlust während eines Speicherzykluses basierend auf der Ausbreitung der Wasserstoffplumen in das impermeable Deckgestein und die benachbarten Schichten abzuschätzen. Der Diffusionsverlust hängt vom Diffusionskoeffizienten und der dem Wasserstoff ausgesetzten Oberfläche ab. Aufgrund der Datenknappheit und unterschiedlicher Unsicherheiten wurden angemessene Annahmen und Vereinfachungen berücksichtigt. Zuletzt wurde ein geochemischer Modellierungsworkflow vorgestellt, um potenzielle geochemische Prozesse zu untersuchen und zu quantifizieren, die zu einem Wasserstoffverlust am Speicherort führen können. Die geochemischen Reaktionen wurden mit Gleichgewichts- und kinetischen Chargenmodellen bei Speicherdruck und -temperatur untersucht, um die kurz- und langfristigen Auswirkungen von Wasserstoff auf das Formationswasser und Mineralien zu untersuchen.

Das zweite Hauptthema dieser Dissertation befasst sich mit einem weiteren Aspekt einer solchen Speicherung. Es stellt sich heraus, dass in-situ Bakterien, genannt Archea, im Reservoir Wasserstoff und CO₂ metabolisieren und Erdgas produzieren können. Die Tatsache, dass Wasserstoff als Substrat für diese Mikroorganismen dient, führt zum Bakterienwachstum und verursacht Wasserstoffabbau. Die Frage, wie Bakterien in porösen Medien wachsen und transportiert werden, ist nicht bekannt. In gleicher Weise gibt es Bedenken hinsichtlich der Bildung von Biofilmen, welche zu Injektionsproblemen führen. Letztendlich ist die

Umwandlungsrate des Wasserstoffabbaus zu Methan bei Energieumwandlungsprojekten von großem Interesse. Die wichtigsten Erkenntnisse zum Bakterienwachstum und -transport im Porenraum unter gesättigter Strömung wurden durch experimentelle und numerische Analyse erzielt. Darüber hinaus wurden basierend auf experimentellen Ergebnissen Empfehlungen für die zukünftige Forschung ausgegeben. Schließlich wird durch die Strömungssimulation auf den experimentell segmentierten Bildern der Einfluss des Bakterienwachstums auf die hydraulischen Eigenschaften des porösen Mediums sowie Änderungen im Strömungsfeld und die Beziehung zwischen Porosität und Permeabilitätsmodellierung quantifiziert.

In dieser Dissertation wird versucht ein Beitrag zu Erkenntnissen zu leisten, indem verschiedene Aspekte kombiniert werden, die sowohl numerisch als auch experimentell für die Bewertung der Speicherung und Umwandlung von Wasserstoff relevant sind. Das primäre Ziel dieser Forschung war es neue Erkenntnisse und Konzepte zu schaffen und einzuführen, die verschiedene Disziplinen kombinieren, effektive Methoden zur Identifizierung der Potenziale und Risiken in solchen Speicherprojekten liefern und die Grundlage für zukünftige Experimente und Studien bilden.

Table of Contents

Abstract	vii
Chapter 1 Introduction to the dissertation	1
Chapter 2 The Geological and transport modeling.....	11
2.1 Introduction.....	12
2.2 Geological modeling.....	16
2.3 Reservoir transport modeling.....	19
2.4 Estimation of hydrogen leakage through reservoir boundaries.....	24
Chapter 3 Geochemical modeling basics.....	29
3.1 Comprehensive View of Geochemical Models.....	30
3.2 Thermodynamic Equilibrium Modelling	32
3.3 Kinetic modeling.....	36
3.4 Hydrogen ecosystem.....	41
Chapter 4 Geochemical modeling of the target reservoir.....	43
4.1 Introduction.....	44
4.2 Geochemical modelling approach.....	47
4.3 Simulation results and discussion	53
4.3.1 Equilibrium batch models	55
4.3.2 Primary kinetic batch model	58
4.3.3 Final kinetic batch model.....	61
4.4 Summary and Conclusions.....	63
Chapter 5 A literature review to bacterial growth and transport	67
5.1 Introduction and literature review	68
5.2 Microbial growth, biofilm formation, and clogging	71
5.3 Microbial transport in porous media.....	79
5.4 Colloids transport in porous media	84
5.5 Limitations of the microbial transport formulations	88
Chapter 6 Bacterial growth and transport in porous media.....	91
6.1 Method development	92
6.2 Bacterial growth and transport under saturated condition	94
6.2.1 Experimental observations and elementary processes	96
6.3 Numerical modeling.....	110
6.3.1 Correlation between initial bacterial deposition and flow velocity.....	116
6.3.2 Microbial growth impact on hydraulic properties of pore-network.....	119
6.4 Particle tracing in an established medium of biomass	121
Chapter 7 Summary, conclusions, and recommendations	133
Chapter 8 Appendixes.....	149
Appendix A: Material balance analysis	149
Appendix B: Structure and Stratigraphy modeling steps.....	151
Appendix C: Bacterial growth curve and cell counting at the stationary phase	153
Appendix D: Image processing procedure.....	157
Appendix E: Clogging and unclogging of biomass	162
Appendix F: Biomass growth and pressure response during NF.....	163
Appendix G: Porosity-permeability relationship	164
Appendix H: Bacterial growth under the starvation condition	166
Appendix D: Bacterial growth and transport under unsaturated condition.....	168
Nomenclature	173
Abbreviations	174

Chapter 1 Introduction to the dissertation

The demand for large-scale energy storage solutions coming from renewable resources is becoming more critical where solar and wind plants are already generating gigawatts of electricity, which often have a substantial mismatch in grid power demand. Hydrogen gas is an effective and flexible energy carrier and is also regarded as one of the significant alternatives to fossil fuels, expressly in the transportation sector. Hydrogen generated from renewable resources may substantially reduce energy-related CO₂ emissions with its potential, and therefore, contributes to the reduction of greenhouse emissions.

Furthermore, compared to direct fossil fuel combustion, by using hydrogen, the local air pollutants and noise emissions can be lowered. Hydrogen as an energy carrier, allow for new links between energy supply and demand, which possibly improve the overall flexibility of the energy system. Low-carbon energy sources can be associated with end-use applications that involve challenges in decarbonization, comprising transport, industry, and buildings by connecting different networks of energy transmission and distribution (T&D). It is noteworthy to mention although hydrogen and fuel cells in end-use applications contribute to energy security, areas of hydrogen generation development, T&D, and retail infrastructure are challenging (OECD/IEA, 2015).

According to OECD/IEA (2015), to limit global warming to 2°C, the power sector must be intensely decarbonized. To accomplish this goal, the annual emissions on the global scale is required to decrease by 85% by 2050 compared to today's emission levels; this can be achieved when renewable power increases to nearly 63% of generated electricity by 2050. Therefore, power systems are required to adopt for deep structural changes to integrate this high level of renewable energy. Concerns such as flexibility (energy supply) and system integration are always in the center of low-carbon energy systems discussions. The fossil resources supply huge amounts of energy, and their high energy density allows them to be highly flexible and be efficiently transported over long distances. However, according to the demand for a low-carbon

energy system based on high shares of variable renewable energy, the temporal and spatial flexibility to modulate energy supply is limited (OECD/IEA, 2015).

The conversion of surplus electricity to other forms of energy (power) carriers and chemicals has received considerable attention through the advance of PtX processes; here P stands for the excessive renewable energy and X stands for the energy form or service to which this excess of the renewable energy is transformed to such as hydrogen, gas, chemicals or mobility (Lund, et al., 2015). PtX technologies include a variety of options. Figure 1-1 depicts different conversion routes. The selection of a specific PtX conversion route is based on the demand for a particular product (X), the characteristics of the technical process performance, cost, as well as the environmental impact compared to the alternative solutions (Eveloy & Gebreegziabher, 2018).

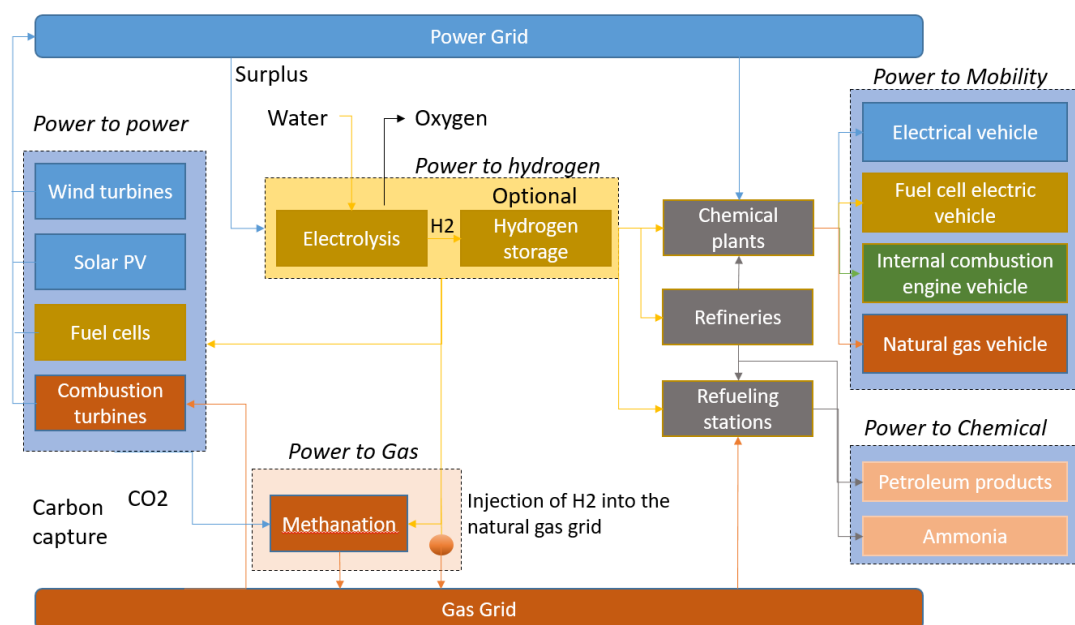


Figure 1-1 Schematic diagram of PtX conversion routes [adapted from (Thomas, et al., 2016)].

Hydrogen may integrate into renewable electricity in the energy system in many ways and partially compensate for the loss of flexibility that is caused by reduced use of fossil fuels. Hydrogen produced from electricity and water resources can be stored in large volumes over prolonged time durations. Then it can be converted to electricity (power-to-power); however, the efficiency cost of this process is more than 70% of the input electricity. Hydrogen can also be mixed into the natural gas grid, converted to synthetic methane (power-to-gas), or traded as fuel for fuel cell electric vehicles (FCEV) in the transport sector (power-to-mobility) (OECD/IEA, 2015).

Options for Hydrogen-based technologies include flywheels, batteries, compressed air, pumped hydroelectric storage, and geological hydrogen energy storage. Above all, in terms of storage capacity, power-to-gas (PtG) with the gas storage option holds significant potential. It allows for higher storage durations and has the seasonal capability; other remarkable features include conversion efficiency in terms of electricity to energy carrier, energy carrier portability, density, and cost (Eveloy & Gebreegziabher, 2018). Figure 1-2 presents different energy storage technologies with their power and discharge capacities.

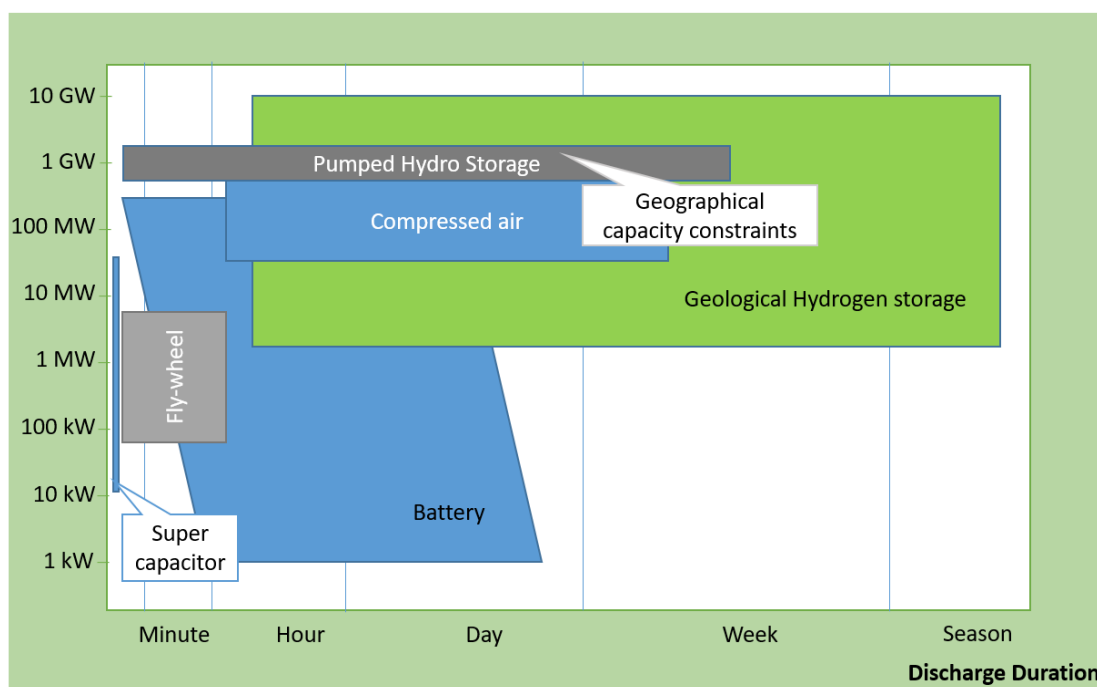


Figure 1-2 Power and discharge time of hydrogen-based electricity storage options [adapted and modified from (OECD/IEA, 2015)].

As this figure displays, geological hydrogen storage has the highest capacity in terms of power and discharge duration and, therefore, has received much attention in recent years for development. A variety of geological formations such as depleted gas reservoirs can serve as underground hydrogen storage (UHS) facilities to provide a massive capacity to store hydrogen gas. Gas reservoirs proved to be sealed; nevertheless, not much known about the economic and environmental risks of hydrogen storage because of the lack of field pilots. There are several open questions concerning the feasibility of UHS in depleted formations. Assessment of the integrity of the reservoir in terms of hydrogen leakage and loss, potential chemical interactions among injected gas, brine and reservoir rocks, and biological activity triggered by hydrogen are among the key questions.

The motivation of the Study

This study was primarily based on an integrated pilot project, “Underground Sun Storage” (www.underground-sun-storage.at), which aimed to store large quantities of hydrogen in an underground depleted gas field. In this project, the storage of hydrogen generated from a surplus of renewable resources in a depleted gas field in the Molasse Basin, Upper Austria, was tested. It turned out that some *in-situ* bacteria in the reservoir, Archaea, partially consume the injected H₂ and CO₂ that naturally exist in the reservoir, and produce CH₄. The outcomes motivated the follow-up project “Underground Sun Conversion” aiming for the production of natural gas by means of microbiological processes within a gas reservoir for storage in the same reservoir (<https://www.underground-sun-conversion.at>). This project goes hand in hand with the PtG concept, which in recent years is thought to be one of the practical solutions for the storage of large quantities of renewable energies.

This dissertation is composed of two main parts and addresses several aspects regarding the UHS. The initial part of this study has been completed in the framework of the “Underground Sun Storage” project. The envisioned proposal of the UHS assessment included the geochemical and reactive transport modeling to predict the evolution of the storage complex in the presence of H₂. The reactive-transport model contributes expressively to both fields of transport and geochemical modeling. Commonly, by coupling between fluid flow and geochemical interactions, the transport of the gas inside pore space, the minerals’ dissolution or precipitation, and the caprock alteration can be described. As the time scales of geochemical reactions were much longer than transport processes (injection and withdrawal-related flow processes and diffusion through caprock), the necessity of reactive transport modeling was excluded, and transport and reactions were treated separately.

In the first part of the dissertation, depletion history and gas injection and storage processes on a depleted gas reservoir are described. Followed by that, the results of an analytical model that estimated hydrogen loss through diffusion in the caprock and the reservoir boundaries in a typical storage cycle, are presented. Next, geochemical modeling of interaction among hydrogen, brine, and minerals in the reservoir are thoroughly discussed. A multi-step geochemical modeling approach is presented to study fluid-rock interactions, in which the long-term consequences of hydrogen storage were estimated by the equilibrium approach, whereas kinetic models were employed to explore the geochemical interactions on the time scales of typical storage cycles.

The second part of the study was inspired by the outcomes of investigations of the biological results in the aforementioned project (“Underground Sun storage”). The microbial

metabolism promoted by the injected hydrogen and carbon dioxide led to the production of methane. The microbiological activities in the reservoir encouraged the experimental study on bacterial growth and transport in the porous media. Questions such as hydrogen loss due to these activities, conversion rate of hydrogen into methane, the likelihood of bioclogging in the pore space, and whether injectivity encounters some problems due to pore plugging were among the motivations of this study. For this purpose, microfluidics experiments were performed to get primary insights into how microbes grow and transport in pore space under saturated conditions. Though the saturated flow condition is not the real case for hydrogen storage and conversion, it was the first step towards understanding the complex unsaturated system. Moreover, the effect of microorganisms' growth on hydraulic properties of the reservoir was predicted via numerical simulations. Figure 1-3 provides an overview of the scales and topics that have been tackled in this work.

Dissertation structure

The dissertation is structured as follows:

Chapter 1 introduces the dissertation.

Chapter 2 includes geological and transport modeling. This chapter describes the geological settings and historical production data of the studied field. Then, the steps that have taken for building the static and dynamic models are demonstrated. Finally, based on hydrogen plume propagation from the preceding models, the results of an analytical diffusion model that was employed to estimate hydrogen loss through caprock and the neighboring layers are discussed.

Chapter 3 covers the background and basic concepts of geochemistry and geochemical modeling. The main parameters for equilibrium and kinetic geochemical models are described, and the requirements of geochemical modeling in the context of H₂ storage are discussed.

Chapter 4 presents the numerical geochemical results that were obtained for the studied field. Here, steps towards building the geochemical models are discussed, including the mineral chemistry and thermodynamic data consistency of the sample, creation, and integrations of new solid solutions for clay minerals into the thermodynamic database, analysis on the formation-water sample, and application of the charge balance criterion. Moreover, a multi-step geochemical modeling approach that was used to study fluid-rock interactions by means of equilibrium and kinetic batch simulations, are discussed. Two approaches for modeling have been chosen: equilibrium and kinetic models. The equilibrium approach estimated the long-

term consequences of hydrogen storage, whereas kinetic models were used to explore the interactions between hydrogen and the formation of a typical hydrogen storage cycle.

Chapter 5 reviews literature and theoretical basics on bacterial evolution and transport in the porous media. It provides an overview of the relevant concepts of microbial and colloidal transport in porous media, which is valuable to comprehend the subsequent research chapter that includes experimental and numerical modeling of the growth and transport of microorganisms. Here, formulations of colloidal and microbial transport in porous media are discussed, and limitations of the models are listed. Different clogging processes are defined, and the effect of microbial growth on hydraulic properties of pore space is described. Some of the described concepts are of importance for future investigations that are recommended in the dissertation.

Chapter 6 describes the bacterial evolution and transport experiments. The pore-scale, microfluidic experiments using *Lactobacillus Casei* strain was employed to elucidate microbial growth and transport in porous media, discover the favorability of porous media for bacterial growth, and compare different flooding schemes. Experiments were completed in two flooding phases. In phase I, a bacterial suspension solution at the stationary growth phase was pumped into the pore network, and biomass formation and growth were monitored. Phase II was followed by the injection of nutrient (substrate) solution. This section discusses the qualitative and quantitative outcomes. Furthermore, findings of the flow simulations on the experimental segmented images in the pore space, including the impact of the bacterial growth on the hydraulic properties of the porous medium, and association of flow velocity and initial bacterial deposition are presented. Finally, findings on the closing part of the study that was devoted to the preliminary experimentations and modeling of particle tracing in a pore-network is discussed.

Chapter 7 summarizes the work, states the conclusions of this research, and suggests prospect directions to the current study.

Chapter 8 includes additional information structured in appendixes.

Some of the experimental data of this dissertation are provided in the supporting supplementary materials.

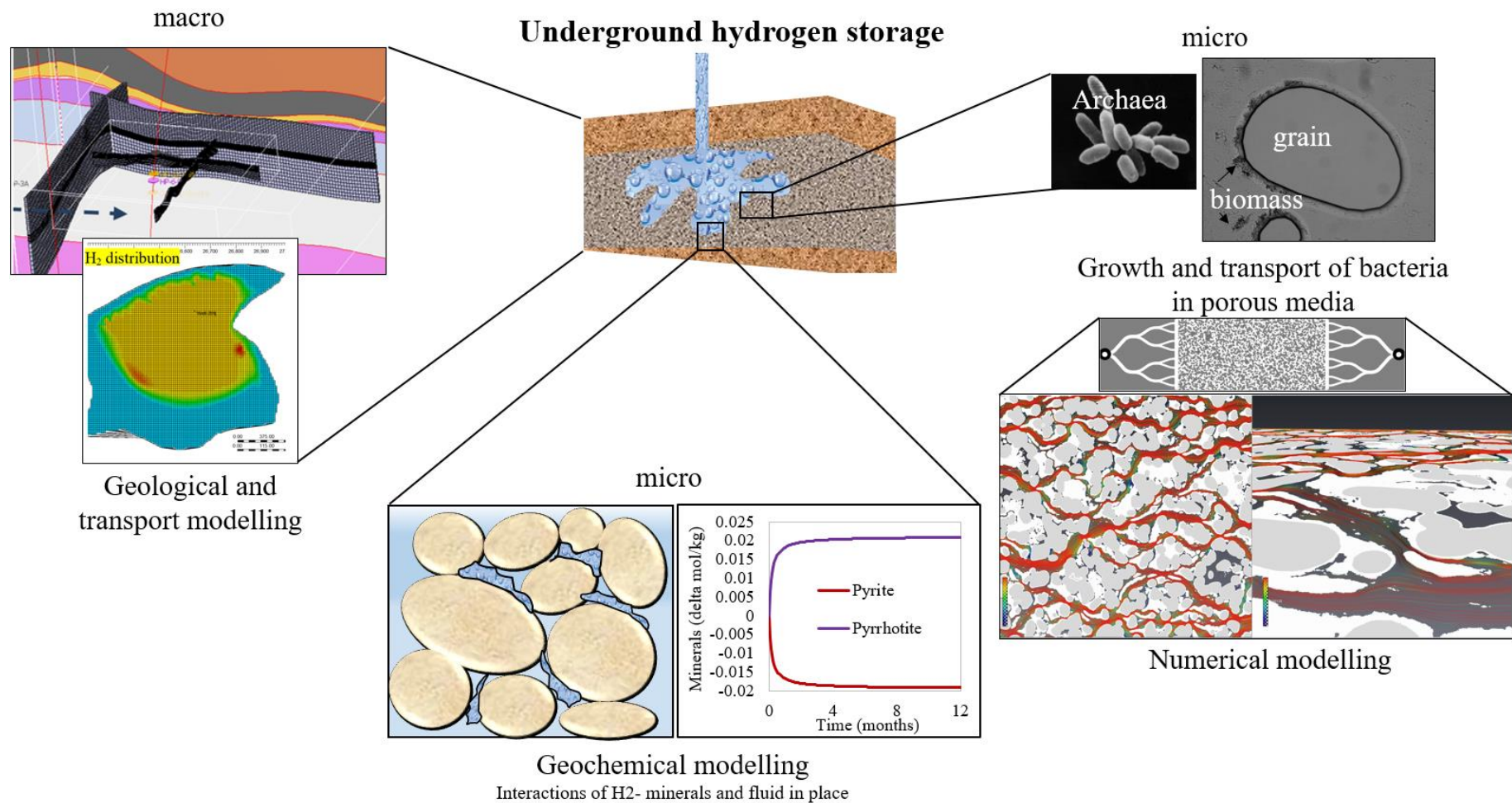


Figure 1-3 Schematic of the work structure in this dissertation at different levels and disciplines. Starting from the macro-scale view, geological and transport modeling of hydrogen in the field was accomplished, and diffusive hydrogen loss to the caprock was estimated. Next, geochemical modeling of hydrogen interaction with minerals and water in the reservoir was evaluated. Finally, experimental investigation of microbial growth and transport using microfluidics under saturated condition was performed, and via numerical simulations, microbial growth impact on hydraulic properties of the porous media was assessed.

Overview of Contributions

There is a long list of people who directly contributed to this work. The list begins with my advisor, Prof. Holger Ott, who envisioned our mission to combine different aspects of UHS, especially by commencing the idea of the use of microfluidics as a tool to directly observe the microbiological processes in porous media. He provided me with continuous support and opportunities in all aspects of the research that were the key drivers of this dissertation.

Dr. Siroos Azizmohammadi collaborated throughout the “Underground Sun Storage” project; his comments and contributions are reflected in chapters 2 and 4.

The geological modeling described in chapter 2 was performed with the support of Ms. Caroline Milliotte.

The content volume of chapter 4 is a result of collaboration with Dr. Marco De Lucia at the Department of Fluid Systems Modelling at GFZ German Research Centre for Geosciences, Potsdam, Germany.

Ms. Johanna Schritter and Prof. Andreas Paul Loibner from Universität für Bodenkultur, Vienna, collaborated in the preparation of microbial strain and suspensions. Also, Ms. Cathrine Zaknun supported the bacterial growth curve experiment.

The viscosity measurements presented in chapter 6 were carried out at the Institute of “Chemie der Kunststoffe” at Montanuniversität Leoben with the support of Ms. Janine Billiani.

Dr. Frieder Enzmann at Institut für Geowissenschaften at Johannes Gutenberg-Universität Mainz supported conducting the numerical simulations to estimate the microbial growth on hydraulic properties of porous media, as well as numerical modeling of particle tracing.

One master thesis was performed and co-supervised in association with the second part of the dissertation. Results of this thesis were partially used and cited within this doctoral thesis: Mohannad Marouf (2018): *“Particle Tracing in Saturated Micromodel Combined with the application of defining colloidal preferential flow pathways in porous media.”*

Publications and conferences

The outcomes of this work are written and presented through the publications and presentations listed below.

Publications

1. “Hassannayebi, N., Azizmohammadi, S., *Does Injected H₂ Induce Interactions among Brine and Minerals in Reservoir? An Equilibrium Geochemical Modelling Approach*, (2015), DOI: 10.3997/2214-4609.201414275
2. Hassannayebi, N., Azizmohammadi, S., De Lucia, M. Ott, H., *Underground hydrogen storage: application of geochemical modelling in a case study in the Molasse Basin, Upper Austria*, *Environ Earth Sci* (2019) 78: 177. <https://doi.org/10.1007/s12665-019-8184-5>
3. Hassannayebi, N., Enzmann, F., Schritter, J., Ferno, M., Loibner, A., Ott, H., *Influence of Microbial Growth on Hydraulic Properties in a Saturated Porous Media*, 2019, in the submission process
4. Marouf, M., Hassannayebi, N., Enzmann, F., Ott, H., *Particle Tracing in a Saturated Porous Media – A Statistical Comparison of Experimental and Simulation Data*, 2019, in the submission process

Presentations

1. Oral presentation: Azizmohammadi S., Hassannayebi N., *Geochemical modelling of hydrogen interaction with minerals and aqueous species*, International Conference of Energy, Science and Technology (EST), Karlsruhe, Germany 2015
2. Poster presentation: Hassannayebi N., Azizmohammadi S., *Does Injected H₂ Induce Interactions among Brine and Minerals in Reservoir? An Equilibrium Geochemical Modelling Approach*, Third Sustainable Earth and Sciences (SES) conference in Celle, Germany 2015
3. Oral presentation: Hassannayebi N., Azizmohammadi S., *Modelling the Geochemical Impact of hydrogen interaction with minerals and aqueous species using GEM-Selektor geochemical modelling package*, Goldschmidt 2015 conference, Prague, Czech Republic 2015
4. Poster presentation: Hassannayebi N., Azizmohammadi S., *Kinetic Geochemical Modelling of Brine-Water Chemistry as Consequences of Hydrogen Injection*, Goldschmidt 2016 conference, Yokohama, Japan
5. Oral presentation: Hassannayebi N., Schritter J., Ferno M., Enzmann F., Loibner A., Ott H., *Microbial Growth and its Influence on Hydraulic Properties in Saturated Porous Media – a Microfluidic Study*, Interpore 2019 conference, Valencia, Spain
6. Poster presentation: Ott H., Hassannayebi N., Schritter J., Ferno M., Enzmann F., Loibner A., *The Impact of Microbial Growth on Hydraulic Properties in Saturated Porous Media*, SCA 2019 conference, Pau, France ”

Chapter 2 The Geological and transport modeling

Large scale UHS is considered as a suitable candidate to store large quantities of renewable energy over several months to compensate mismatches of energy demand and production. One option for such storage is the use of the depleted underground porous reservoirs. To predict and evaluate the behavior of a subsurface gas storage reservoir, an understanding and quantification of the underlying transport processes are required.

This chapter was completed based on the “Underground Sun Storage” project. A small depleted gas field located in the Molasse Basin in Upper Austria has been designated as a storage site for this project. Based on the geological and historical production data, a geological model was built, and a transport model was subsequently generated according to the geological model. Afterward, the lateral propagation of the injected hydrogen was simulated and predicted. Finally, by estimating the gas plume migration extension, the diffusive hydrogen loss into the caprock and the reservoir boundaries was evaluated by an analytical model for a typical storage cycle.

2.1 Introduction

Underground formations for gas storage include depleted oil or gas reservoirs, aquifers, rock caverns, and salt caverns. The practice of underground natural gas storage history goes back to 1916, using a depleted natural gas reservoir. Much of the experience still applies to the geological hydrogen storage (Taylor, et al., 1986).

Depleted natural gas reservoirs as one of the UHS options deliver massive storage capacity and are proved to be sealed. However, due to the lack of field pilots, there is not much known about the economic and environmental risks of hydrogen storage. Carden and Paterson (1979), described a number of associated risks, for instance, operational losses, corrosion, leakage through the casing, diffusive gas loss the caprock, hydrogen loss due to solubility in the brine, and chemical and biochemical reactions (Hassannayebi, et al., 2019).

The storage operation may be a cyclic process with the alternating periods of injection, withdrawal, and shut-in. Demand in energy production determines the duration of each period. A common scheme is a seasonal operation, while gas is injected during the summer and is withdrawn during the winter. In case of a need for balancing the electrical energy production, more frequent changes in the operation schedule may be foreseen.

The gas storage requires high production rates, often one or two orders of magnitude higher than the depletion of a classical gas reservoir. For this reason, the main driving force of the storage operation is the compression and expansion of the gas phase (Hagemann, 2018). The usable amount of gas volume is known as the working gas. As well, there is always a certain amount of gas, which remains in the reservoir as cushion gas, which is needed for an effective underground gas storage operation. It provides the necessary levels of pressure and gas column height for the desired deliverability of working gas, as well, it prevents the wells drowning by water. The cushion gas can make up to half of the total amount of the stored gas and may contain both recoverable and unrecoverable gas; therefore, it is one of the largest upfront investments in a storage project (Dussaud, 1989).

Geological setting

The Molasse Basin located between Linz and Salzburg (Figure 2-1) is one of the main gas-producing areas in Austria, where up to now, more than 40 gas fields have been discovered. Many of these gas fields are found in “deep-water sandstone sediments, the conglomerate of the Oligocene–Miocene Puchkirchen, and Hall formations” (De Ruig & Hubbard, 2006). Map

of the Molasse Basin in Upper Austria is shown in Figure 2-2; the studied field is located between Linz and Salzburg, and the location of the only producer well is marked.

The studied field includes a single production well (Lehen-2). The gas supply for this well comes from the Hall formation, which is bounded to a sandstone layer formed at the top of the Hall base layers. The reservoir thickness is around 1.2 m that lies in the gas-producing zone in the interval between 1147.8-1149.3 m (TVD) (Smuk, 2007).

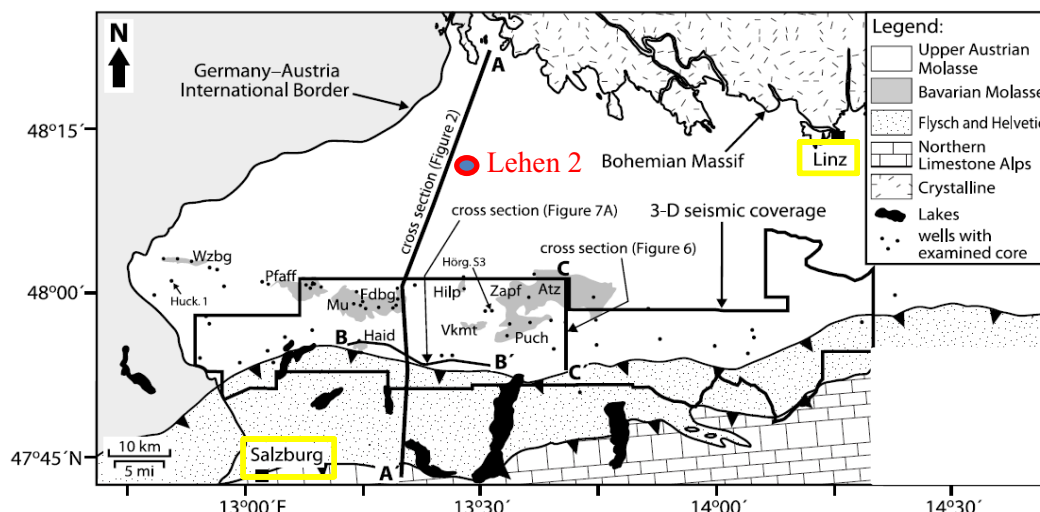


Figure 2-1 Map of the Molasse Basin in Upper Austria; the studied field is located between Linz and Salzburg, and the location of the only producer well “Lehen 2” is marked [source: (De Ruig & Hubbard, 2006)].

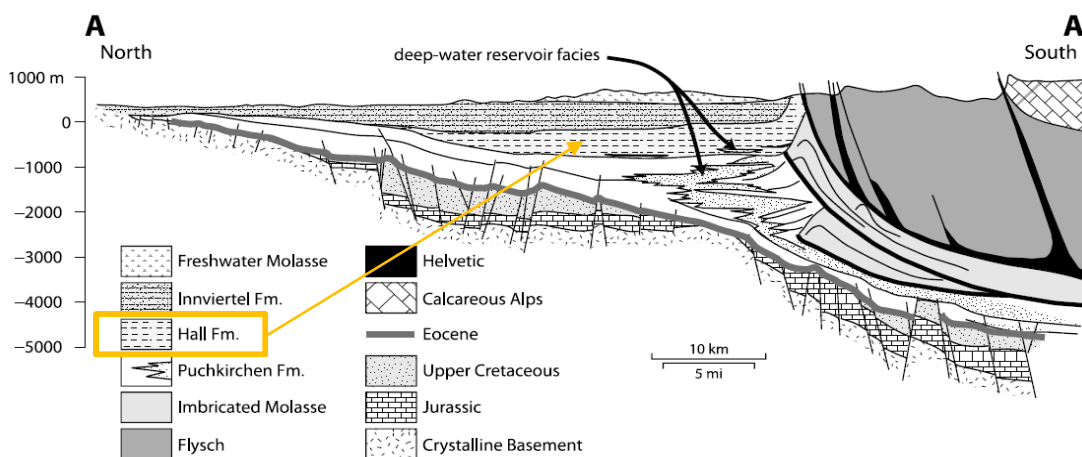


Figure 2-2 The regional geological cross-section through the Upper Austrian Molasse Basin; the studied reservoir is located within the Hall formation [Source: (De Ruig & Hubbard, 2006), modified from Wagner, (1996)].

For this study, three structural maps were provided by the operating company RAG (Rohöl-Aufsuchungs Aktiengesellschaft) (see Figure 2-3). A structural map is a subsurface map whose contour lines display the elevation of a specific formation or a reservoir with the geologic structures such as folds, faults, synclines, and anticlines. The top structural map corresponds to the reservoir layer, and the other two maps correspond to the upper and lower Puchk formations

(UPF and LPF). There is an unconformity layer below the reservoir layer and the other two maps. To construct the 3D geological model, all the structural maps were utilized since the information for the reservoir layer was not available until the very end of the project. A fault network can be seen at the top of UPF and LPF maps. The reservoir is confined to the water-bearing layers from the left and right edges and the shaley layers from the top and bottom.

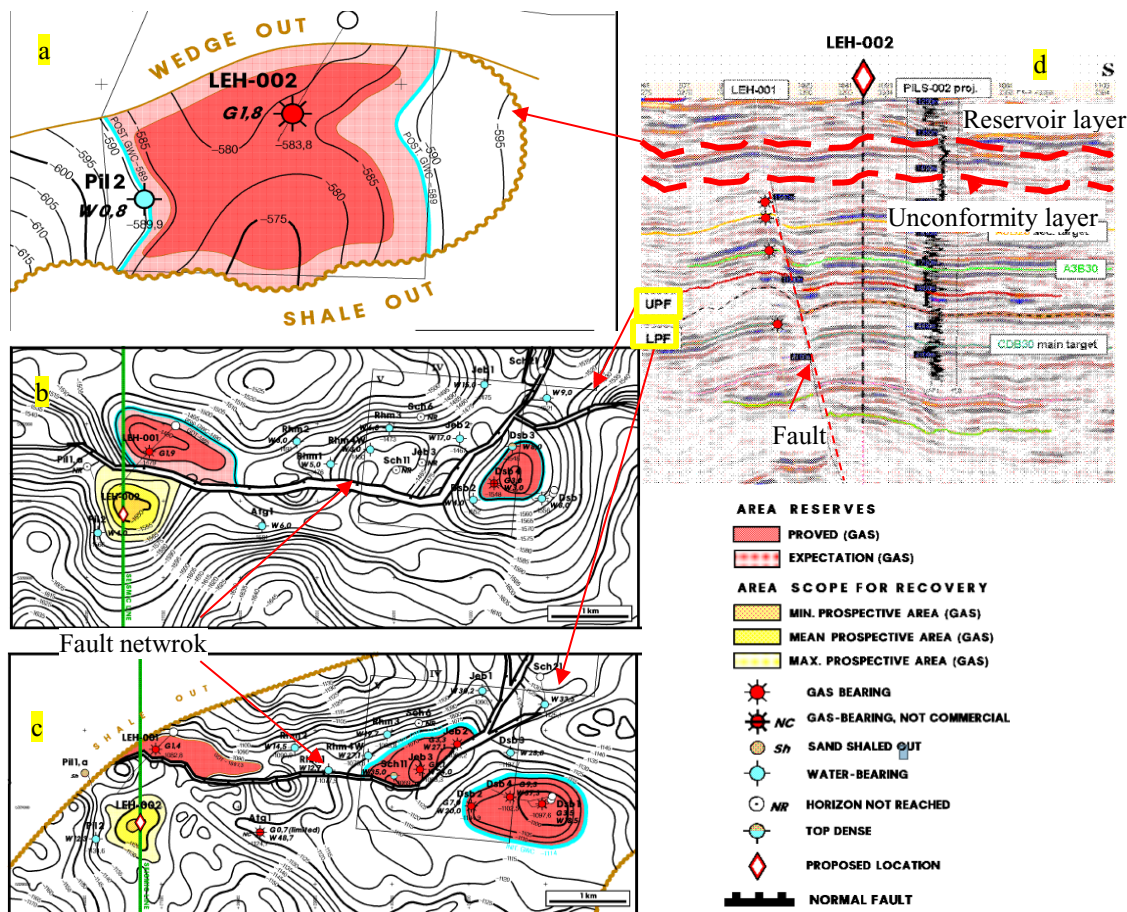


Figure 2-3 Structural maps used for the realization of the 3D geological model. (a): Reservoir layer; (b): the upper Puchk formation; (c): the lower Puchk formation; (d): seismic data showing the corresponding layers to the structural maps, unconformity layer, fault position, and the well location.

Reservoir data

Figure 2-4 shows the sequence of events concerning the production and injection operations. Initial gas production started from June 2007 to the end of June 2010. Later the well was shut-in until October 2015. A hydrogen-methane mixture was injected into the formation in three intervals. Due to the shortage of hydrogen supply during the first two injection intervals, only a small amount of H₂ was injected into the reservoir. In the last attempt, the gas injection was sustained for three months.

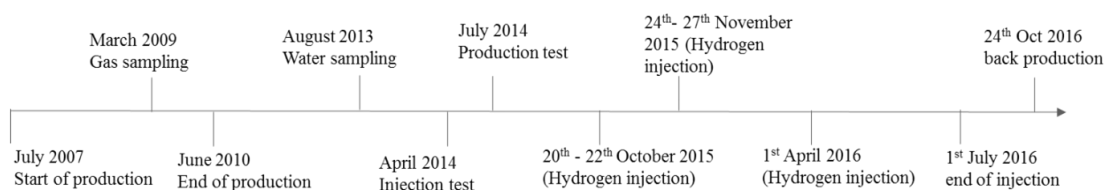


Figure 2-4 Sequence of production-injection events in Lehen-2 [source: (Hassannayebi, et al., 2019)].

Field observation displayed pressure support during the well shut-in period; an increase in the bottom hole pressure (BHP) data from 20 to 35 bars. Recorded pressure values versus time for the producer well may be interpreted by the existence of two compartments in the reservoir (see Figure 2-5); the main one contributes to the storage of initial gas, and the second one is supporting pressure at a later production stage. This cumulative produced water production values indicate the lack of an active aquifer in the vicinity of the reservoir. A material balance analysis was performed and confirmed this fact (see Appendix A: Material balance analysis). Another mechanism that may lead to the observed pressure increase may be associated with the shale-out area adjacent to the reservoir, as shown in the reservoir's structural map (see Figure 2-3, a).

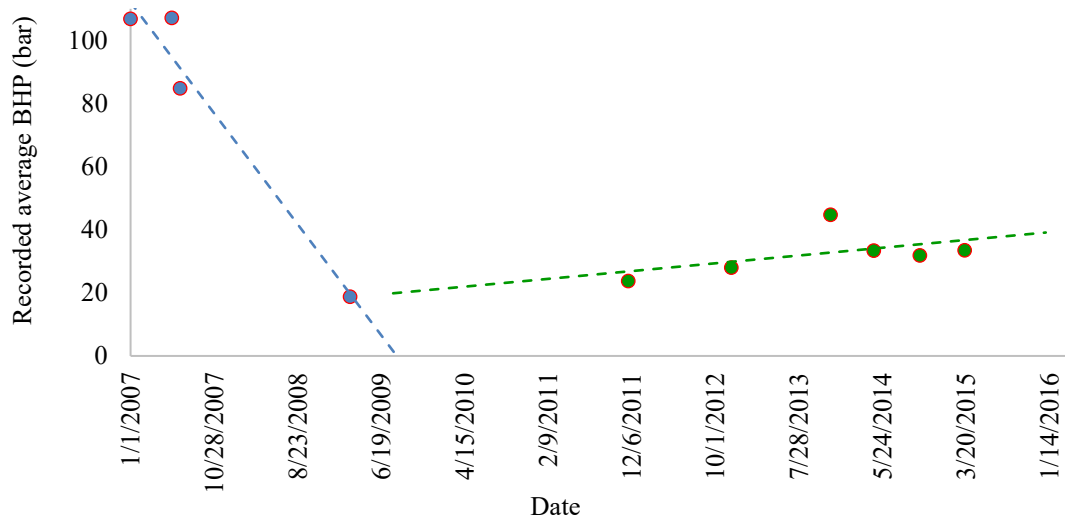
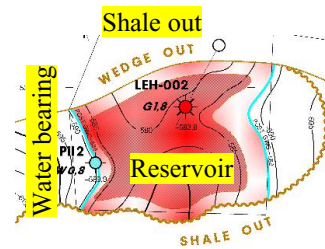


Figure 2-5 Recorded BHP pressure values versus time for the production well; the trend of pressure data indicates the existence of two active compartments in the reservoir. The main compartment is the primary gas storage, and the second one is supporting pressure as the reservoir pressure declines.

As there was limited information about the reservoir heterogeneity and due to small thickness of it, we constructed a simple model, still in agreement with the available geological data, and considered uniform rock properties in the model (see Table 2-1).

Table 2-1 Reservoir properties.

Reservoir property	Value
Reservoir Porosity Φ / permeability k	0.2/ 700 mD
Shale out zone Porosity/ permeability	0.05/ 0.1 mD
Water bearing zone Porosity/ permeability	0.10/ 100 mD
Initial and final reservoir pressure	[107-34] bars
Initial water saturation	0.35
Reservoir temperature	40 °C



2.2 Geological modeling

The reservoir structural properties influence the plume migration. These include the reservoir structural shape, reservoir thickness, and the distribution of the physical parameters in the porous rock. Hydrogen plume migration in the subsurface formation was estimated by a static (geological) and a dynamic (transport) model. The uncertainties in geological models are inevitable as they arise from the measurement uncertainty, natural variability in the geological system and interpretation imprecision. The modeler decides the acceptable level of inaccuracy based on the relevant resolution for the specific model. Here, such uncertainties were handled by choosing a proper tool and taking the appropriate assumptions.

The data source of this reservoir was relatively scarce, similarly typical for a relatively small gas reservoir. Datasets that were used for modeling consist of structural maps, well markers of the production well and a few nearby wells, and part of a seismic data in the time domain. The geological model was constructed in Paradigm-SKUA (<https://www.pdgm.com>) by completing the following steps:

- Interpretation and digitization of the structural maps
- Extraction of the well markers from the production logs
- Interpretation of the seismic data including conversion of data in the depth domain and correlating a well marker to a seismic event to interpret seismic data
- Upscaling the grids for numerical simulation

Data interpretation

The structural maps were imported into the geomodelling tool and were digitized, and then integrated into a geological model. For this purpose, maps were imported as 2D voxel objects and scaled up to the actual size. Next, the isolines and fault network were interpreted as polylines and open lines. The digitized lines are representative of the reservoir geometry and the fault network (see Figure 2-6 and Figure 2-7).

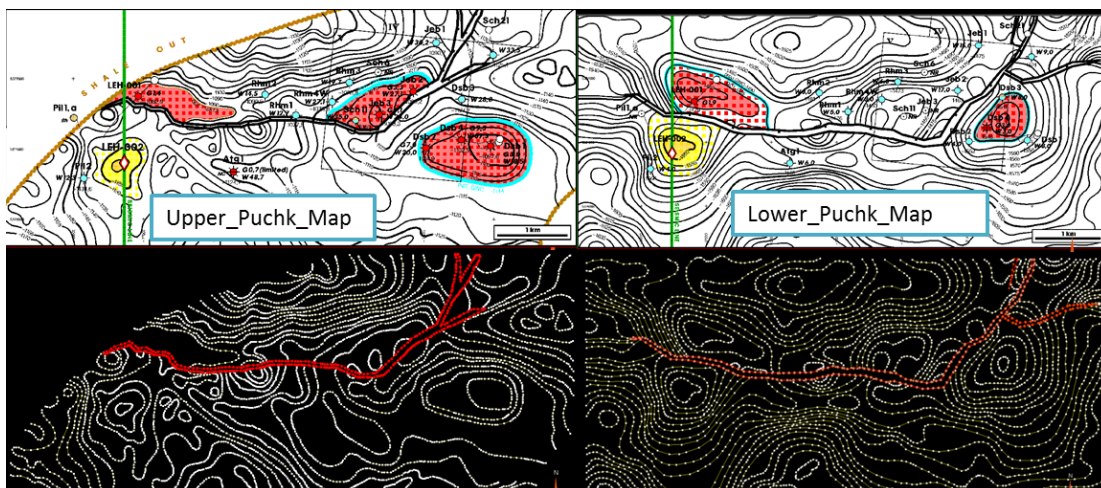


Figure 2-6 The structural maps were imported into the geomodelling tool and were digitized. The fault network is presented in the upper and lower Puchk formations.

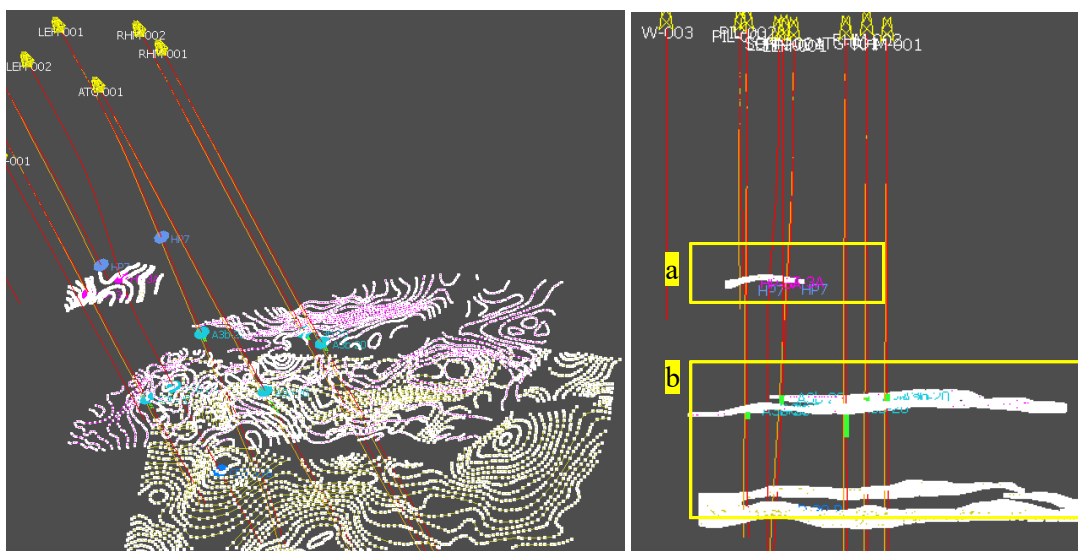


Figure 2-7 Digitized contour lines of the structural maps; a: digitized lines corresponding to reservoir layer; b: digitized lines corresponding to upper and lower Puchk layers.

The next input data, the well markers for the only production well in the reservoir, and the nearby wells in the field were extracted from completion logs and then imported into the model (Figure 2-8). The well markers were attentively correlated to identify the key stratigraphic layers. Other applications of well correlation are estimating the spatial continuity of geological formations and characterizing the properties of reservoir units.

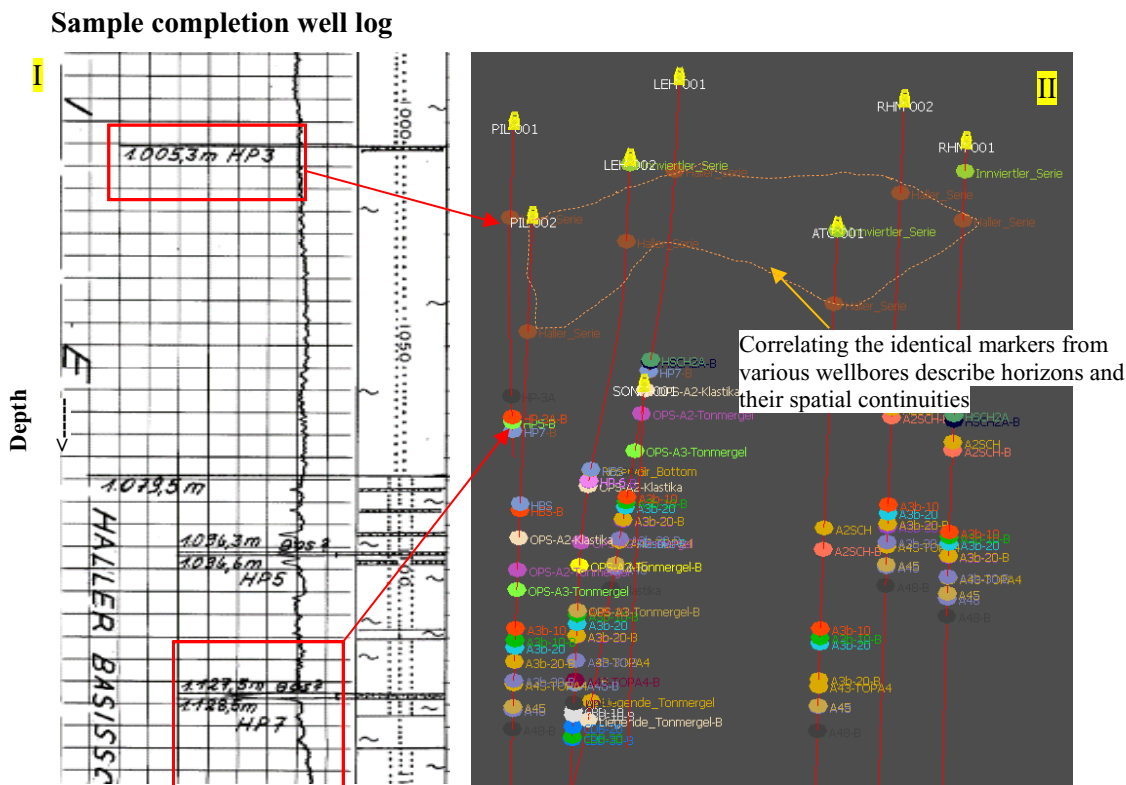


Figure 2-8 Well markers' depth was read and extracted from completion logs and then entered in the model. In (I), an example of a completion well log is shown; markers' depths correspond to the top of a horizon. These values were entered into the geological model (II). Markers' correlation supports identifying the horizons and their spatial continuity in a geological formation.

Another data source, the local seismic data in the time domain, was imported into the model. The display of seismic and well data results in a stronger interpretation of both data. Seismic data is a measure of the sound wave travel time, which provides an image of the subsurface in time; however, the objects in real space must be manipulated in the depth domain. The velocity model from seismic velocity and well data (check-shot and velocity log) was created, and the depth to time conversion was performed.

The seismic data were interpreted based on the seismic reflectors (seismic events). A well marker associated with a seismic reflector was used for the interpretation of a horizon above the unconformity layer in the reservoir. The reflector was interpreted manually by picking polylines within various crossline and inline sections through the seismic cube (Figure 2-9).

Lastly, using a velocity log, the digitized lines corresponding to the horizon was converted to the depth domain to be employed in the geological model.

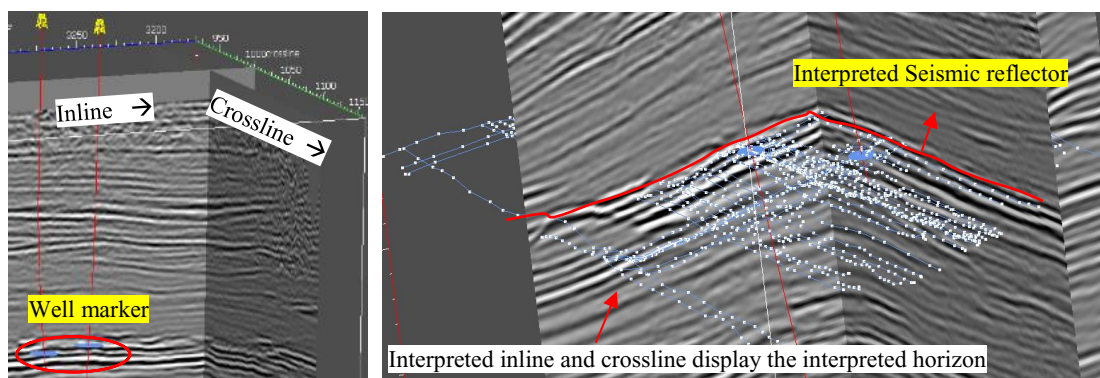


Figure 2-9 Interpreted horizon based on a seismic reflector. The reflector was interpreted manually by picking polylines within various crossline and inline sections within the seismic cube.

The structural and stratigraphic workflow in the software includes advanced functionality. This workflow is an organized process that simplifies the construction task of the structure and stratigraphy of a geologic model, as well as building a geological grid for reservoir property modeling and volume calculation. This workflow includes the following units: the selection of horizon data, and fault data, defining the volume of interest, building the fault network, modeling horizons, honoring the well data, checking and editing the SKUA model, and finally building the geologic grid. All steps were carried out successfully, and the final geological grid was created. The detailed steps that were applied in this module are documented in Appendix B: Structure and Stratigraphy modeling steps.

2.3 Reservoir transport modeling

A typical reservoir contains different fluids (i.e., gas, oil, and water). Fluid flow in a reservoir is governed by the conservation of mass, momentum, and energy. Mass balance equations can be employed for the assessment of the fluids in the reservoir at a given time and location. Darcy's Law is used to express the momentum conservation equation in porous media. In Darcy's equation, the relative permeability of any fluid is a function of saturation; and is defined as the ratio of the effective permeability at any saturation to the permeability at 100% saturation. Additionally, the capillary pressure is a function of saturation. The capillary pressure data is derived from two-phase data (Corapciog & Panday, 1989).

Numerical fluid flow techniques require discretization of the reservoir space into elementary volumes. For each gridblock, the average characteristics, including parameters such as depth, thickness, porosity, permeability, relative permeability, and capillary pressure are assigned. With the today's advanced development of the digital interpolation techniques, it is possible to calculate the numerical values that have to be attributed to the gridblock cells, from a limited number of pinpoint data (Fasanino & Meunier, 1989). In the following relevant equations for a two-phase (water and gas) system is described.

Two-phase flow equations for a gas reservoir

In a water-gas system, we consider water as the wetting phase, and gas as the non-wetting phase. Several parameters have been introduced in flow equations, namely saturation, capillary pressure, and relative permeability. In the pore space, the summation of fluid saturation is one. Since there are two fluids to fill the void space, we have:

$$S_g = 1 - S_w$$

Capillary pressure, p_c is a function of saturation, and is defined as the pressure difference between the pressure of the non-wetting phase (p_n) and the wetting phase (p_w):

$$p_c = p_n - p_w$$

Permeability is the intrinsic property of formation rock, and it refers to the connectivity of pore spaces to one another. In a multi-fluid system, relative permeability is used and defined as the ratio of the effective permeability of any fluid phase to the absolute permeability of the rock. Darcy's law describes the fluid flow in the pore space and has the following equations for the wetting and non-wetting phases:

$$\vec{v}_w = -\frac{K K_{rw}}{\mu_w} (\nabla p_w - \rho_w g \nabla h),$$

$$\vec{v}_n = -\frac{K K_{rn}}{\mu_n} (\nabla p_n - \rho_n g \nabla h).$$

Here \vec{v}_w and \vec{v}_n are the flow velocities for the wetting and non-wetting phases, respectively; and ρ_w, ρ_n, μ_w and μ_n are the respective viscosities, and densities for wetting and non-wetting phases. K is the medium's permeability and K_{rw} and K_{rn} are the relative permeabilities for wetting and non-wetting phases. In the above equation, the gravity effect is considered. Here, $g = 9.81 \text{ m/s}^2$, and $h(x, y, z)$ is the reservoir height, where typically $h = z$ when the z axis points upwards.

The mass conservation equation for two-phase flow is written as:

$$-\nabla \cdot (\rho_w \vec{u}_w) + q_w = \phi \frac{\partial (\rho_w S_w)}{\partial t},$$

$$-\nabla \cdot (\rho_n \vec{u}_n) + q_n = \phi \frac{\partial (\rho_n S_n)}{\partial t}.$$

Here q_w and q_n are the mass rate of injection per unit volume of the reservoir. By substituting the flow velocities in the conservation equation, the following equations are obtained:

$$\nabla \cdot \left(\frac{\rho_w K K_{rw}}{\mu_w} (\nabla p_w - \rho_w g \nabla h) \right) + q_w = \frac{\partial(\phi \rho_w S_w)}{\partial t}$$

$$\nabla \cdot \left(\frac{\rho_n K K_{rn}}{\mu_n} (\nabla p_n - \rho_n g \nabla h) \right) + q_n = \frac{\partial(\phi \rho_n S_n)}{\partial t}$$

The compositional model

In a compositional model, a mass balance equation must be specified for each component. In this section, a very general case is considered where there are N chemical species, or components, which may exist in the water or gas phase.

We designate the mass fraction of the i^{th} component in the gas phase by C_{ig} , and the mass fraction of the i^{th} component in the water phase by, C_{iw} . In a compositional model, due to the possibility of the transfer of various components between the phases, the mass of each phase is no longer conserved. Instead, the total mass of each component is conserved. According to the mass flux densities for each phase ($\rho_g \vec{v}_g$ and $\rho_w \vec{v}_w$), the flux density on the i^{th} component can be written as:

$$C_{ig} \rho_g \vec{v}_g + C_{iw} \rho_w \vec{v}_w$$

The mass of component i per unit bulk volume of the porous medium can be written as:

$$\phi (C_{ig} \rho_g S_g + C_{iw} \rho_w S_w)$$

Symbolizing the injection rate for each component as q_i , the conservation equation for each component may be written as :

$$-\nabla \cdot (C_{ig} \rho_g \vec{v}_g + C_{iw} \rho_w \vec{v}_w) + q_i = \phi \frac{\partial}{\partial t} (C_{ig} \rho_g S_g + C_{iw} \rho_w S_w)$$

Darcy's law, in this case, is written as:

$$\nabla \cdot \left(\frac{C_{ig} \rho_g K K_{rg}}{\mu_g} (\nabla p_g - \rho_g g \nabla h) + \frac{C_{iw} \rho_w K K_{rw}}{\mu_w} (\nabla p_w - \rho_w g \nabla h) \right) + q_i$$

$$= \phi \frac{\partial}{\partial t} (C_{ig} \rho_g S_g + C_{iw} \rho_w S_w)$$

Reservoir model

We have employed a compositional transport model (CMG-GEM reservoir simulator) (<https://www.cmgl.ca/gem>) to model the gas plume migration. The reservoir model is an upscaled grid obtained from the geological model. Reservoir properties are shown in Table 2-1.

As previously discussed, due to limited information about the reservoir heterogeneity and due to small thickness of it, we considered uniform rock properties in the model within each region in the reservoir formation (Figure 2-10).

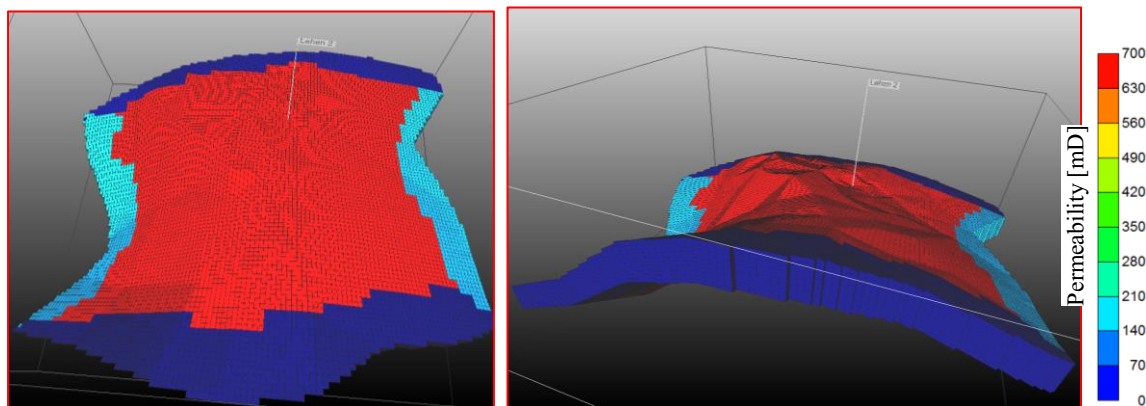


Figure 2-10 3D view of the permeability distribution based on the structural map of the reservoir. The porosity is distributed in the same way in different regions.

Prediction of fluid phase behavior is a fundamental step to generate phase behavior data for both primary fluid in place and the injected gas. Characterization of the initial and injected fluid was performed in WinProp (an Equation-of-State-based fluid behavior and PVT modeling package). Table 2-2 shows the initial and injected gas components. The gas phase is modeled using the Peng-Robinson (1978) Equation of State. A mixture of gas (10% H₂+ 90% CH₄) was injected into the reservoir with an injection rate of 100 Nm³/h for hydrogen for three months to simulate the real operational scheme.

Table 2-2 Composition of injected and reservoir fluid.

Component	Reservoir fluid	Injected fluid
CO ₂	0.0334	0.02
H ₂	0.0015	-
CH ₄	99.4955	0.98
C ₂ H ₆	0.3566	-
C ₃ H ₈	0.113	-

Due to the lack of the core sample, the value of relative permeability was taken from the literature for a typical gas field. Pressures were determined from the hydrostatic equation. The reference pressure and depth were assigned, and the initial gas composition was allocated in the gas zone. A linear solver was used for solving the equations. The well location and perforation through the reservoir were allocated, and production and injection data were applied.

The extension of gas plume migration was simulated and is shown as a temporal evolution of hydrogen concentration in Figure 2-11 and Figure 2-12. In early times, most of the injected gas is located around the injection well, by the time the injected gas migrates by buoyancy towards the anticline crest and the boundaries. As the injection period only lasts for three

months, the difference of gas migration after the 3rd and the 12th month is not too much. As can be seen, the gas plume migrates toward the boundaries in the direction of the low elevated layers.

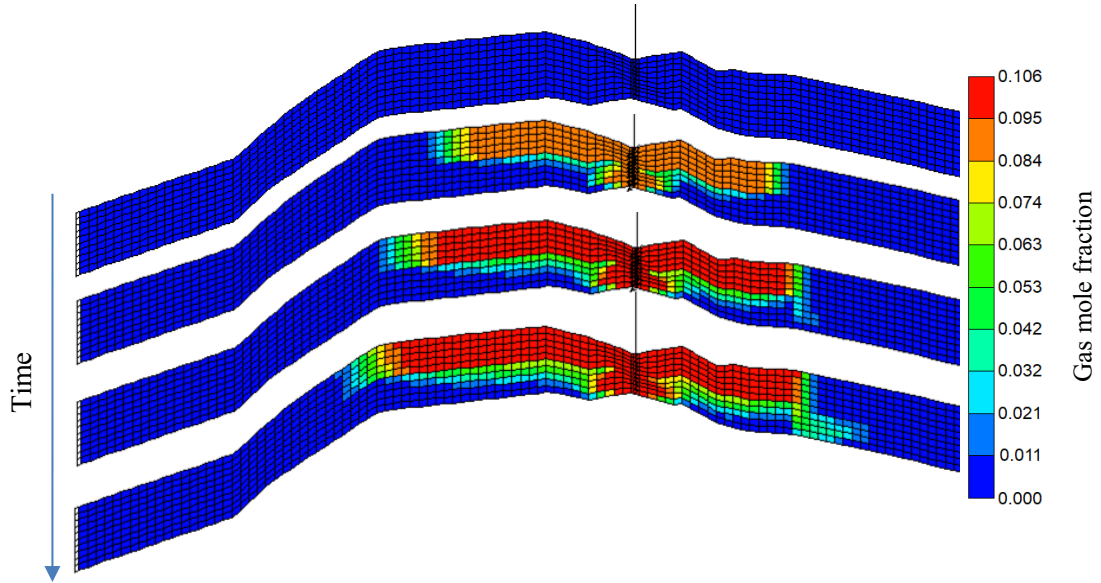


Figure 2-11 Side-view of the evolution of the hydrogen gas mole fraction, initially and after 1, 3 months of injection, and gas propagation after 12 months.

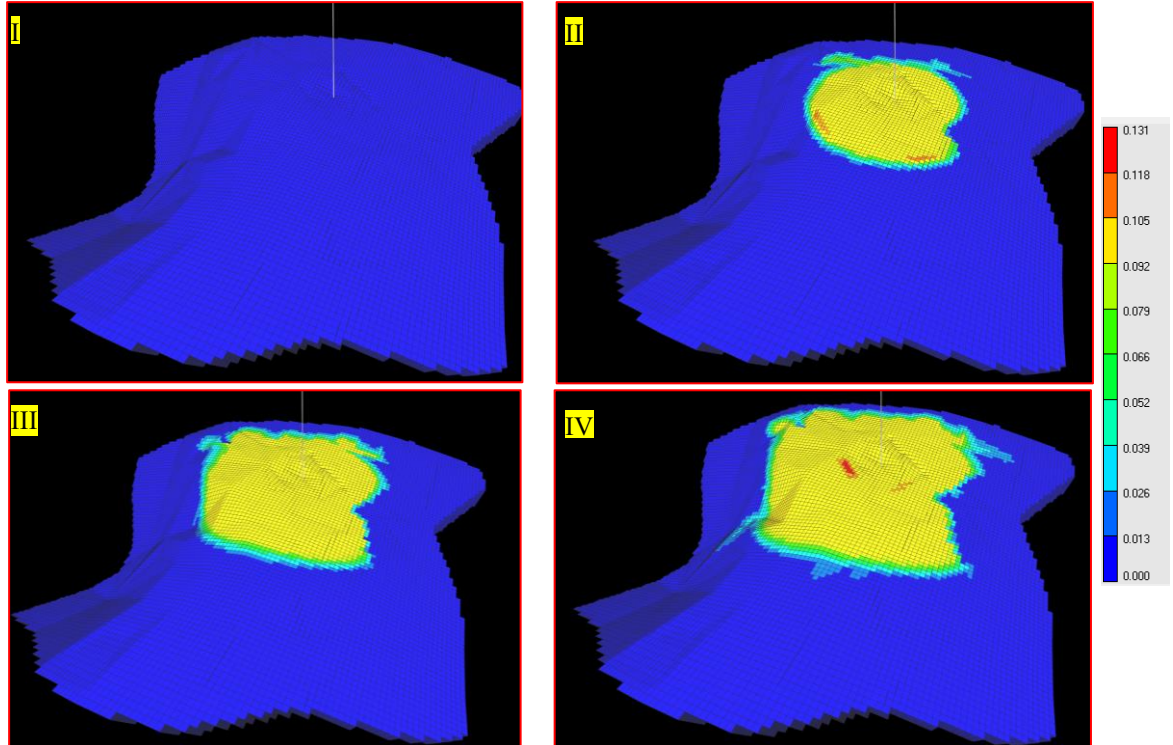


Figure 2-12 Hydrogen gas plume distribution inside the reservoir (I) initially, (II) after one, and (III) three months of injection, and (IV) migration of plume after one year in the reservoir formation.

Figure 2-13 shows a comparison of hydrogen and methane distribution in the model. As can be seen, the injected mixture of hydrogen and methane is accumulated at the top of the

reservoir. The estimated areas contacted by hydrogen from this model are used in the analytical diffusion model to compute hydrogen diffusive losses to the reservoir caprock and boundaries, as discussed in the following.

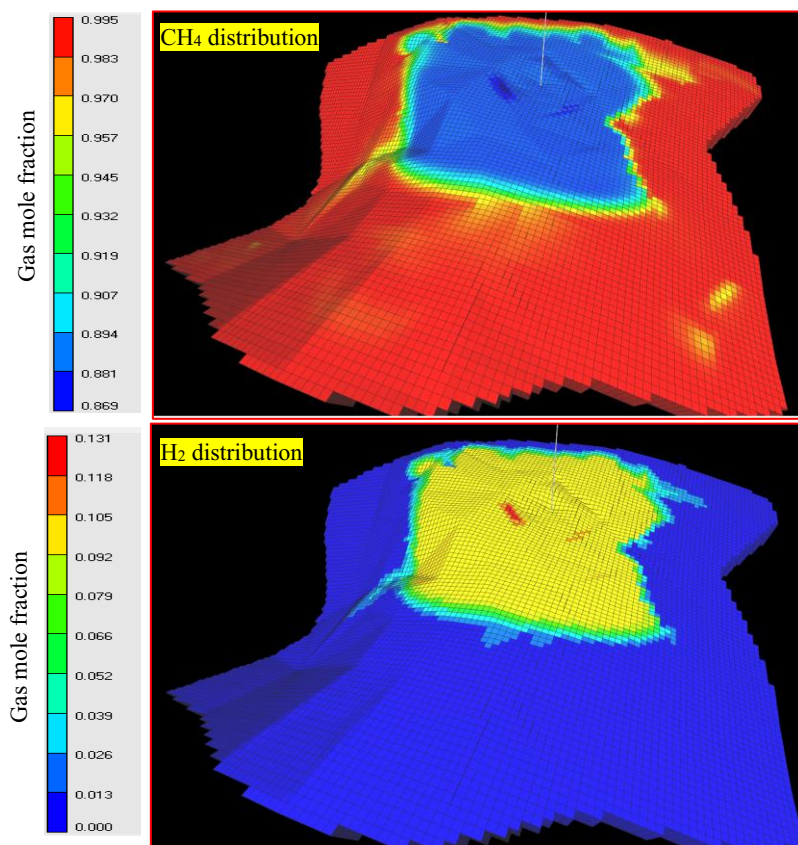


Figure 2-13 Comparison of spatial distributions for CH_4 and H_2 gas mole fraction in the reservoir (after 12 months).

2.4 Estimation of hydrogen leakage through reservoir boundaries

Hydrogen diffusive loss through reservoir boundaries is part of the routine assessment of gas storage (Wang & Peng, 2014). The leakage mechanisms are associated with various reasons; diffusive loss of dissolved gas through the caprock, potential leakage through faults or fractures, and well leakage. As there is no fault in the studied field, and no information was available for the well integrity, we expected gas diffusion through the caprock and the adjacent layers to be the dominant mechanism for gas loss. The trapped gas may dissolve in the interstitial clay water and then be transported by the diffusion process. To estimate the diffusive gas loss, a conceptual model was employed, and the hydrogen diffusion coefficient in the water was considered; the calculated gas loss in the first storage cycle was maximum, and later, and then it was reduced as the water ultimately saturated with gas.

Caprocks are sealing layers that are typically water-saturated tight formations having a sufficient capillary entry pressure to avoid migration of reservoir fluid. However, gas migration

can happen due to the diffusion process. Gas diffusion in caprocks has been widely studied both experimentally and numerically for storage projects, exclusively for CO₂ sequestration and repository projects (Wang, et al., 2015; Li, et al., 2006; Hoch & James, 2012; Song & Zhang, 2013; Jacobs, et al., 2013; Fleury, et al., 2008; Hou, et al., 2012; Amann-Hildenbrand, et al., 2013; Jones, et al., 2003; Karimaie & Lindeberg, 2017).

The balance between opposing forces of gravity (buoyancy) and capillarity determines the sealing capability of caprocks (Ingram, et al., 1997). Caprocks' failure mechanism is classified into the membrane (capillary leakage) and hydraulic seals (Watts, 1987). The sealing capability of the membrane seals is controlled by capillary entry pressure and fail due to capillary leakage. The largest throat radius of the interconnected pore acts as the weakest point of a membrane seal, and it controls the minimum gas entry pressure. Moreover, the primary trapping mechanism of membrane seals is related to the caprock capillary properties (e.g., pore size distribution, wettability, and gas-water interfacial tension). Hydrocarbon is trapped in a seal caprock while the net buoyancy pressure, which is associated with the difference between the hydrocarbon and water densities, is less than the seals' capillary displacement pressure (Watts, 1987).

In hydraulic seals, the capillary entry pressure is extremely high, that only fracturing results to failure in the seal. Some caprocks such as evaporates and extremely tight shales have such an excessive entry pressure that capillary failure is improbable; therefore, leakage can only occur by fracturing or vertical migration along faults (Watts, 1987). Figure 2-14 exemplifies the failure shown in pressure profile versus depth for capillary and hydraulic seals.

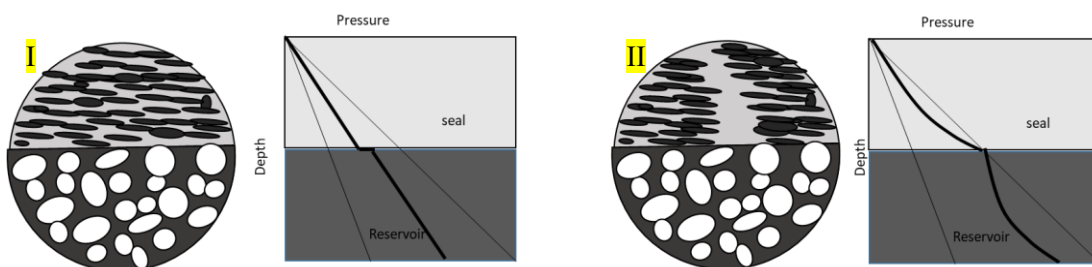


Figure 2-14 (I): Membrane (capillary) seal and (II): hydraulic seal. Failure in capillary seals is due to capillary leakage, and in hydraulic seals is due to hydro-fracturing [adapted from (Ingram, et al., 1997)]

Diffusion model

Gas diffusion is a thermal movement of gas molecules with a net motion of a matter from a high to a low-concentration zone; the diffusive flow rate is proportional to the concentration gradient (Liu, et al., 2016). The characteristic porous structure of the caprock influence the effective gas diffusion coefficient (D_{eff}) (Song & Zhang, 2013). The increase in tortuosity and fewer and narrower pore network results in the reduction of the gas molecules' mobility in the

water-saturated pore space; thus, the effective diffusion coefficients decrease. On the contrary, an increase in porosity leads to a rise in the diffusion rate (Krooss et al., 1998). An increase in effective stress also will decrease the effective diffusion coefficient (Krooss & Leythaeuser, 1988). Besides, the fluid properties in the porous media influence the diffusion coefficient. Experimental studies of (Krooss & Leythaeuser, 1988) show an increase in the pore water salinity causes a reduction in diffusion coefficients. The dependency of D_{eff} on the pore structures is described by the following expression (Song & Zhang, 2013):

$$D_{eff} = D_{aqu} / \tau$$

where D_{aqu} is the diffusion coefficient in the formation water, and τ is the tortuosity.

Researchers have a different understanding of the diffusive processes of natural gas in reservoir formation. This is due to the different rock composition and the complexity of the gas diffusion in rocks (Guangdi, et al., 2012). In some research, the amount of free gas per unit volume of rock is used as a diffusive concentration. In other studies, diffusive concentration is defined as the quantity of dissolved gas per unit volume of pore water as it was believed that the gas diffusion mainly occurs in the pore water in the rocks (Guangdi, et al., 2012).

Here, a one-dimensional analytical model was constructed to describe the diffusive losses of the stored gas in the reservoir. The concentration of H_2 in the caprock versus invaded H_2 has been calculated from the analytical solution. Two diffusion coefficients considered for hydrogen in brine (4.5×10^{-9} (Cussler, 1984) and 4.5×10^{-10} [m^2/s]), the latter value accounts for the heterogeneity of the reservoir and tortuosity. The numerical model aims to predict gas losses through caprock, and reservoir boundaries over a typical storage cycle time (1 year).

General one-dimensional diffusion equation has the following form:

$$\frac{\partial C}{\partial t} = D \frac{\partial^2 C}{\partial x^2}$$

where $C(x, t)$ is the molar concentration of a component in the fluid, “ x ” is the distance, “ t ” is time, and “ D ” is the diffusion coefficient. The boundary conditions in a 1D case are displayed in Figure 2-15. Initially, below and above the boundary of the caprock and reservoir layer, fluid is at its maximum and minimum concentration with regards to hydrogen. The gas concentration above the caprock rises by time due to diffusion.

The problem has characterized the concentration, C , as a function of x and t (Ogata & Banks, 1961). The analytical solution to the 1D diffusion equation is written as follows:

$$C(x, t) = C_i \operatorname{erfc}(\alpha); \quad \alpha = \frac{x}{2\sqrt{Dt}}.$$

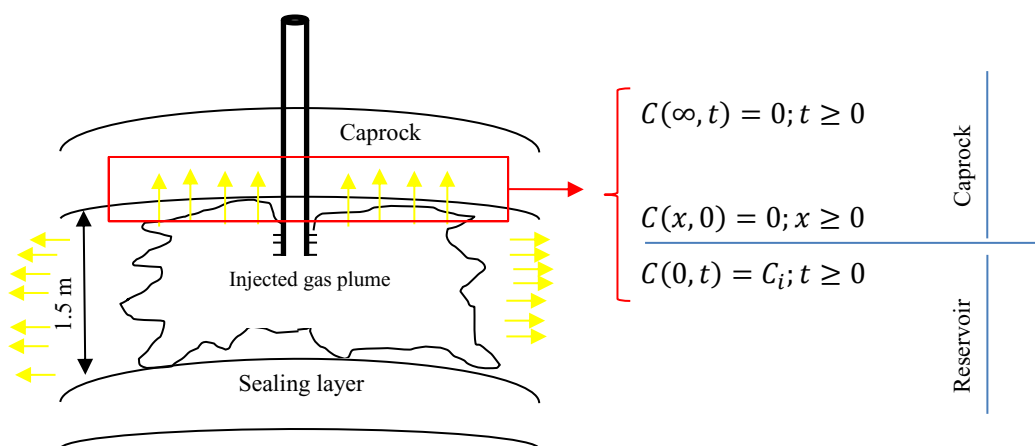


Figure 2-15 Distribution of injected gas plume and the boundary conditions for a 1D case study; the possibility of diffusive loss increases as the injected gas covers higher areal surfaces and reach the boundaries.

Diffusive loss of the stored gas is calculated based on the gas injection-storage scheme for three months injection followed by one year of storage. The injection values and gas properties are similar to those that were used in operation (Table 2-3). The hydrogen accounts for a total of 10 percent of the total injected gas, with a partial pressure of 7.5 bars. The following formulation was utilized to estimate the hydrogen diffusive loss in caprock relative to the amount of the injected gas in the reservoir:

$$\text{Diffusive loss} = \frac{\text{amount of } H_2 \text{ lost during shut – in period}}{\text{amount of injected } H_2 \text{ in 3 months}}$$

Initial concentration C_0 , is estimated as follows:

$$C_i = \frac{p}{ZRT} = \frac{7.5 \text{ bar}}{(1.05)(8.314 \times 10^{-5})(313)} = 274 \text{ mol/m}^3$$

Total moles of injected $H_2 = C \times \text{volume of injected } H_2$.

Table 2-3 Injection data and reservoir data used for diffusive loss calculations

H_2 injection rate	100 Nm ³ /h
Gas FVF (at 75 bars)	0.0153 m ³ /sm ³
H_2 injection rate	6535 m ³ /h
The injected volume of hydrogen	14117647 m ³
Reservoir pressure injection	75bar
Reservoir temperature	40°C
Gas Z-factor	1.05
Injected moles of hydrogen	3.88×10^9 moles

The profile of H_2 concentration versus invaded H_2 in the caprock was calculated from the analytical solution. Figure 2-16 depicts how a diffusion front will advance with time.

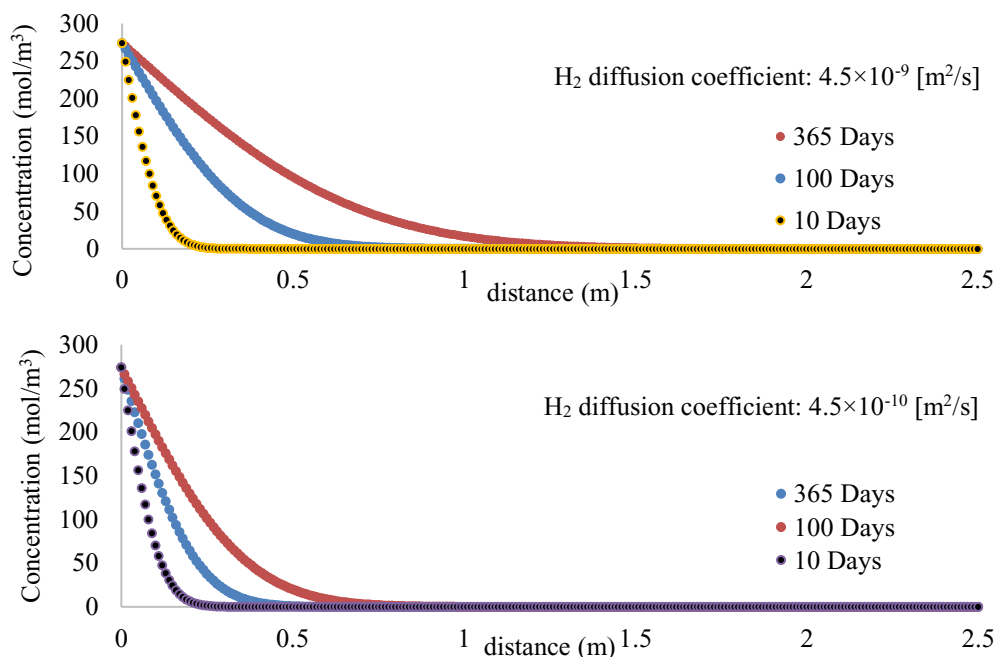


Figure 2-16 The advance of the diffusion front in the caprock with time for two diffusion coefficients.

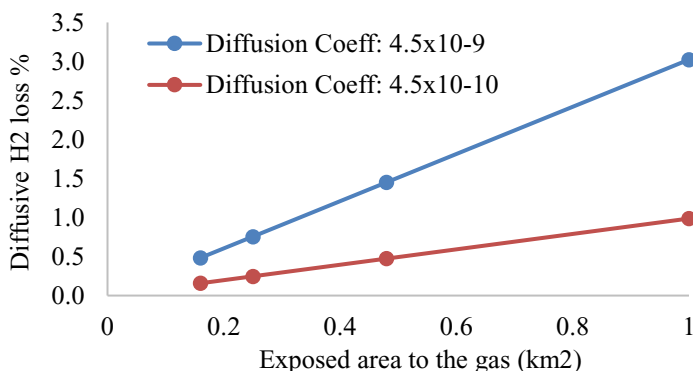


Figure 2-17 Diffusive loss through caprock during a one-year storage cycle for assumed diffusion coefficient and the exposed area to the gas.

Using the dynamic model, we estimated the areal plume propagation. The diffusive loss in the caprock has been calculated as a function of the caprock exposed area to the injected gas for two diffusion coefficients and plotted in Figure 2-17. The minimum estimated diffusive loss is around 0.16%, and maximum diffusive loss is 3%. The diffusive loss has a linear relationship with the exposed area to the injected gas. Moreover, the diffusive loss is only significant at first storage cycles as the injected gas has limited solubility in water. In case hydrogen gas reaches reservoir boundaries (shale out and water-bearing), the possibility of diffusive loss into the neighboring layers increases. For lateral boundaries, a higher diffusion coefficient was considered, whereas the exposed surface area to hydrogen was smaller compared to the caprock diffusion. Diffusive loss, in this case, was minor compared to the caprock; the maximum amount of calculated diffusive loss could reach to 0.603%.

Chapter 3 Geochemical modeling basics

Geochemical models are an abstract representation of the natural processes of a system, which are identified by a set of principal variables and expressed by mathematical equations (Gonçalves, 2005). The initial step in developing a geochemical model is to conceptualize the system or process of interest. The system means the portion of the universe that is relevant for modeling. It is a grouping of atoms, minerals, rocks, gases and waters under consideration within a single volume of space. Boundaries of a system can be defined as it is convenient; it is closed, meaning composition of it, is fixed, or open in which mass can enter and leave. The modeler decides a system with its extent, by setting the quantities of the fluids, and minerals they considered in the calculation (Langmuir, 1997; Bethke, 2008). In order to conceptualize a geochemical model three key matters should be regarded (1) the nature of attained equilibrium, (2) the initial state of the equilibrium system (composition, pressure and temperature), and (3) the potential mass transfer or temperature variation that can occur over the course of the planned reaction process (Bethke, 2008).

The basis of geochemical models may be divided into three main processes: thermodynamic equilibrium model, reaction kinetics model, and flow and transport processes. Batch models do not consider the flow and transport processes and can be conceptualized as a tank reactor. Reactive transport models, on the other hand, couple geochemical reactions, flow and transport processes. An equilibrium model assumes the attainment of some forms of chemical equilibrium; this model gives no information regarding the pathways or time it takes to attain equilibrium. A kinetic model, instead, describes kinetic reactions pathways toward equilibrium and reaction position and times along those pathways (Bethke, 2008).

This chapter presents an overview of the thermodynamic equilibrium and kinetics modeling methods within the context of batch modeling. The thermodynamic background of this chapter is mainly taken from (Bethke, 1996; Langmuir, 1997; Zhu & Anderson, 2002; Bethke, 2008).

3.1 Comprehensive View of Geochemical Models

Natural geochemical systems are complex. There are numerous processes related to the movement and distribution of chemical species, which are coupled to each other. These processes include chemical reactions, transport, biological processes, fluid flow, and heat transfer (Zhu & Anderson, 2002). The processes that are intrigued by chemical reactions control partitioning of the species among different phases, as well as the aqueous phase for a given amount of mass at a fixed point and time. Through transport, chemicals are transported either by advection (water carries the dissolved solids with it) or hydrodynamic dispersion (the spreading and mixing made due to molecular diffusion and microscopic velocity variation within individual pores (Zhu & Anderson, 2002)). Biological processes refer to microbial activities, which can catalyze chemical reactions. Fluid flow may account for precipitation and dissolution reactions that potentially alter porosity and permeability in the reservoir and may change the flow velocity. Consequently, this can disturb the advective-dispersive transport of the contaminants, as mentioned above (Zhu & Anderson, 2002).

Geochemical modeling is a combination of the use of thermodynamics, reaction kinetics, or both to explore the chemical reactions of a geological system. Geochemical modeling is commonly done employing numerical simulation in the context of the processes that are expected in a reservoir. Geochemical models can be divided according to their complexity level to zero-dimensional (batch) models, reaction-path models, and reactive transport models (Zhu & Anderson, 2002). Figure 3-1 demonstrates the complexity levels of geochemical models. Understanding the underlying science of any case study allows for an accurate geochemical model prediction. For this, we need to comprehend the geochemical properties of the system of interest (e.g., minerals, brine and gas composition, temperature, and pressure, etc.), gather the thermodynamic and kinetic properties of the system, and understand the interaction between chemical, physical, and biological processes. As an example, a speciation–solubility model contains no spatial or temporal information and is considered as a zero-dimensional model.

A reaction path model can be employed to simulate the successive reaction steps of a system in response to a process (e.g., the mass or energy flux). This model includes some temporal information regarding reaction progress, ζ , with no spatial information. A reactive transport model contains both temporal and spatial information about chemical reactions; this model often is used for the examination of coupled physical, chemical, and biological processes in the natural systems. This model is the most complex and expensive one. Almost for more than three decades, reactive transport models have been utilized in many applications to

understand chemical and biogeochemical systems (Steeffel & Lasaga, 1994; Saaltink, et al., 1998; Zheng & Spycher, 2017; Wolterbeek & Raouf, 2018; Meile & Scheibe, 2019).

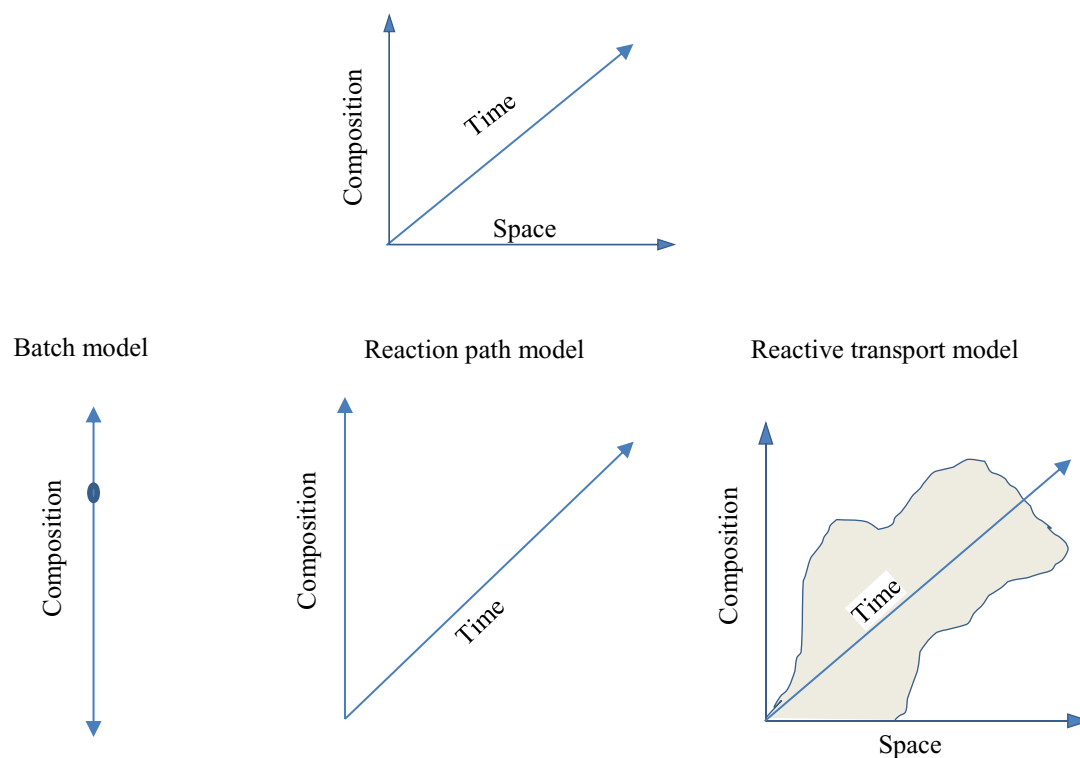


Figure 3-1 Various complexity levels of geochemical models. A batch model is a zero-dimensional model; in a reaction path model, some temporal information regarding reaction progress is included; and a reactive transport model contains both temporal and spatial information [adapted from (Zhu & Anderson, 2002)].

There are several deficiencies in the current geochemical models due to the lack of system comprehension, which limits the applications of these models. These deficiencies are (Zhu & Anderson, 2002):

- Many of the geochemical models can only perform batch simulations. These models suffer from a lack of time and spatial information to address some site-specific problems. Still, these models are broadly used and can be employed in assessing laboratory experiments.
- The lack of thermodynamics and kinetic data for many of the critical environmental and geochemical processes, as well as the uncertainty in many of the data taken from the laboratory and extending them to field situations, limit the accuracy of predictions.
- In natural aquatic systems, the lack of equilibrium among redox couples is well known; however, a proper way to model the redox couples in geochemical models is challenging and unclear.

- Chemical heterogeneity in the solid matrix of aquifers is often not well characterized. Nevertheless, chemical heterogeneity has a significant role in the model uncertainty assessment.

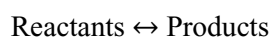
Due to the current state of knowledge, many geochemical models are geochemical equilibrium (thermodynamics) models. Geochemical models of natural and engineered systems approximate the real situation. For many of the geochemical processes, geochemical equilibrium models are the best that modelers can do. These models deal with the equilibrium state; they can be utilized and indicate, for example, that a specific mineral should be dissolved or precipitate in or from a particular solution. Nonetheless, equilibrium models do not give any information about how fast a reaction will happen. In natural systems, many processes are rate limited or in some cases do not occur at all. This indeed is a serious limitation of an equilibrium model. Kinetics, on the contrary, deal with the mechanisms and rates of chemical reactions. Commonly, understanding the equilibrium of the system is a decent starting point for understanding kinetics. Moreover, it is preferred that the kinetic models be incorporated into geochemical models, along with thermodynamic equilibrium models.

3.2 Thermodynamic Equilibrium Modelling

A geochemical system is an assemblage of one or more phases of a certain bulk composition (Bethke, 1996). A phase is a region of space that has distinct physical properties and is mechanically separable. Moreover, it is homogeneous in its composition and properties. In a geochemical system, species are represented as the molecular units, which can be distinguished by their molecular formula (e.g., the gases such as N₂ and O₂ in a gas, or the electrolytes Ca⁺ and Cl⁻ in an aqueous solution that exist within a phase) (Bethke, 1996).

Gibbs energy

A geochemical system determines the significant chemical reactions, as well as the direction of them; either they proceed to the right or the left, or they retain equilibrium. To find out whether a particular mineral is dissolving or precipitating in a reaction, one must look at the direction of the equation. If this reaction proceeds to the right, the mineral is dissolving. If it proceeds to the left, it is precipitating (Bethke, 1996).



Through the energy per mole calculation of each product and reactant of interest, the reaction direction under the chosen conditions can be determined. When the products have

higher Gibbs potential than the reactants, the reaction goes to the left, and vice versa. The appropriate energy for the calculation is the Gibbs energy, G . Gibbs free energy cannot be measured for any substance; only variances in G (written as ΔG°) are measurable. For a typical reaction, the standard Gibbs energy of a reaction is written as follows:

$$\Delta_r G^\circ = \Delta_f G^\circ_{\text{reactants}} - \Delta_f G^\circ_{\text{products}}.$$

Here $\Delta_r G^\circ$ is the standard Gibbs free energy change per mole of reaction for unmixed reactants and products, and $\Delta_f G^\circ$ is the standard Gibbs free energy of formation of a compound. When the quantity of $\Delta_r G^\circ$ is negative, the reaction proceeds towards precipitation. If it is positive, reactions proceed towards dissolution. Most of the time, products and reactants are not in their standard states. Hence, another term is used to describe G° of products and reactants in their standard state, and G of each in the real state:

$$G_i - G_i^\circ = RT \ln G_i.$$

Here G_i and G_i° are Gibbs energy per mole of i component in the real and standard state, and R is the gas constant ($8.3143 \text{ J K}^{-1} \text{ mol}^{-1}$).

Activity, Fugacity, and Chemical Potential

The activity of a species, a_i , is calculated as a product of an activity coefficient γ_i and a molal concentration m_i and it is used to account for non-ideal effects that occur at high ionic strength, temperature, and pressure. The following equation describes the relationship between chemical activity and the activity coefficient:

$$a_i = \gamma_i m_i.$$

The activity coefficient in a very dilute solution is 1.0; in this case, the activity equals the concentration. Activity coefficients are a function of ionic strength, I , and calculated as follows:

$$I = \frac{1}{2} \sum m_i z_i^2$$

where m_i is the molal concentration and z_i is the charge of ionic species i . The ionic strength of a solution determines the concentration of ions in a solution and refers to the degree of mineralization of a solution. At moderate concentrations, while ionic strength increases, activity coefficients decrease. Usually, activity coefficients are calculated using three equations depending on ionic strength; the Debye-Hückel equation for ($I < 0.1$), the Davies equation for ($I < 0.5$), and the Pitzer ion interaction model for higher ionic strengths (Langmuir, 1997).

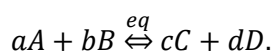
When enough time is given to a system, chemical substances in contact with each other, tend to reach chemical equilibrium. Equilibrium is the basis for thermodynamic modeling. Thermodynamics controls the direction, and the scope of reactions that occur as the chemical

system attains equilibrium. Chemical equilibrium is determined as the time-invariant, most stable state of a closed system; also, the state of minimum Gibbs free energy (Langmuir, 1997). The equilibrium point of a chemical reaction defined regarding the chemical potential. In real systems, equilibrium implies a state in which the characteristics of a system undergo no alteration throughout an indefinite time. The chemical potential of a species that makes up a phase is defined as follows:

$$\mu_B = \frac{\partial G_B}{\partial n_B}.$$

Where the chemical potential of a species B , μ_B , is the derivative of the species 'free energy G_B with respect to its mole number n_B . The chemical potential value depends on temperature, pressure, and the mole numbers of each species in the phase (Bethke, 1996).

The reaction's equilibrium point can be determined by having the chemical potential function for each species in a reaction. An example of a typical reaction among species A , B , C , and D is written as:



Where a , b , c , and d are the reaction coefficients. The equilibrium point is defined at a point where free energy is at a minimum (Figure 3-2). The point at which G is minimum should satisfy the following equation using the chemical potential equation:

$$d\mu_D + c\mu_C - b\mu_B - a\mu_A = 0.$$

In this reaction, d moles of D and c moles of C are produced while b moles of B and a moles of A are consumed.

The chemical potential of a species can be calculated from the potential of the species in its pure form (ideal) at any temperature and pressure of interest; also known as the theory of ideal solutions (Pitzer & Brewer, 1961; Bethke, 1996). The chemical potential of a species is related to its standard potential by the following equation:

$$\mu_B = \mu_B^\circ + RT_K \ln X_B.$$

Where, μ_B° is the standard potential of component B , R is the gas constant, T_K is the absolute temperature, and X_B is the mole fraction of component B in a solution phase. It is clear by knowing the standard potential values μ° , the equilibrium point can be determined. However, in real studies, geochemical phases are not ideal and don't occur in a pure form. Accordingly, the standard state needs to be defined in another form. Even though the same equation is retained, the chemical potentials of species in solution are expressed less directly. As a result,

the mole fraction of X in the previous equation is swapped with a new variable called the species' activity, as follows:

$$\mu_i = \mu_i^\circ + RT_K \ln a_i.$$

In the above equation, the standard potentials μ_i° are arranged at a new standard state, which is a hypothetical one-molal species solution, wherein activity, and molality are equal, besides the properties of species have been extrapolated to infinite dilution.

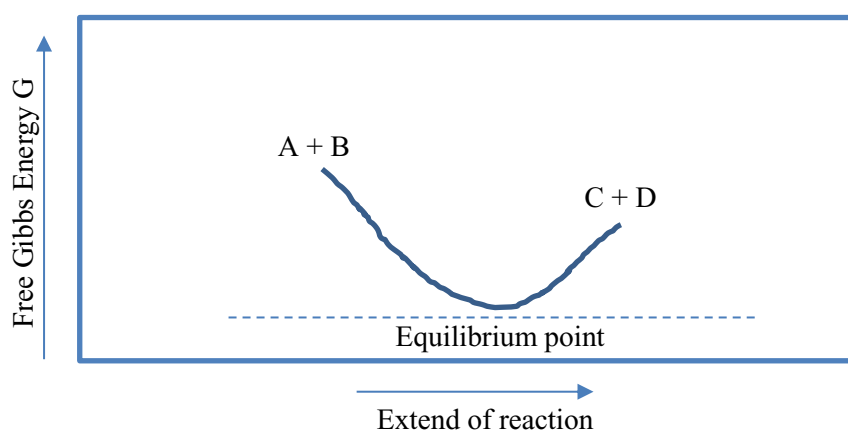


Figure 3-2 The free Gibbs energy G versus reaction progress for a typical reaction of ($aA + bB \leftrightarrow cC + dD$). The equilibrium is at the point where the Gibbs energy is minimized [adapted from (Bethke, 1996)].

For gas species, the chemical potential is described in terms of the standard potential of the pure gas at 1 atm, the temperature of interest and the gas fugacity, which is shown by f_i :

$$\mu_i = \mu_i^\circ + RT_K \ln f_i.$$

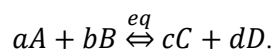
Fugacity itself is related to the partial pressure (p_i) by the fugacity coefficient (x_i):

$$f_i = x_i p_i.$$

At low temperatures and pressure, the ideal gas law ($x_i \rightarrow 1$ & $f_i \rightarrow p_i$) can be assumed.

Equilibrium Constant, K

The equilibrium constant, K , is the ratio of product activities to reactant activities when the reaction has reached equilibrium. K value is independent of the reactant and product species concentrations in a mixture but depends on the temperature and ionic strength. The chemical reaction of reactants A and B , which are in equilibrium with the products C and D are written in the following manner:



In the previous equation, lowercase letters represent the stoichiometric coefficients, and uppercase letters represent the chemical species. The following expression writes the equilibrium constant, K :

$$K = \frac{(a_C)^c (a_D)^d}{(a_A)^a (a_B)^b}$$

Where a_i represents the chemical activity of species i . Activity a_i is the “thermodynamic concentration” or the fraction of total concentration that contributes to the geochemical reactions.

For many reactions, equilibrium constants have been determined experimentally, and the values reported in the literature. Various geochemical software generally embed equilibrium constants as a function of temperature in their thermodynamic database. A prerequisite step of modeling is then, checking the consistency of the thermodynamic database of the chosen software (Kroupa, 2013; Giffaut, et al., 2014; Voigt, et al., 2018).

3.3 Kinetic modeling

In geochemical kinetics models, the rates at which reactions proceed must be stated. When concentrations of reactants and products in a given chemical reaction are defined, a mathematical expression can be used to describe the reaction progress in time.

Depending on a system condition (e.g., the composition of fluid, species and minerals, etc.) there may be various reaction mechanisms. This is due to the species in a solution that can assist catalyzing or inhibiting the reaction mechanism. There may be several valid rate laws that describe the reaction of a single mineral. In the literature (e.g., Palandri & Kharaka, 2004 (Marty, et al., 2015), rate constants are given for different pH conditions, i.e., acidic, neutral, and alkaline condition.

Geochemists distinguished the overall dissolution and precipitation reactions to proceed in five generalized steps (Bethke, 2008):

- 1) reactants diffusion to the mineral surface,
- 2) adsorption of the reactants onto reactive sites,
- 3) chemical reactions that include breaking and creation of new bonds,
- 4) reaction products desorption, and
- 5) products diffusion from the mineral surface to the bulk fluid.

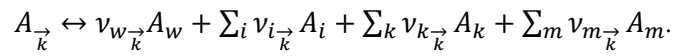
Steps 2 and 4, the adsorption of reactants and desorption of products onto/from reactive sites, occur quickly. This means other steps can be rate-limiting processes. They are categorized

into transport controlled and surface-controlled reactions or processes. When the reaction rate is dependent on the speed of the reactants and products to reach to or move away from the mineral surface by aqueous diffusion (steps 1 and 5), the reaction called “transport controlled.” In contrast, when the speed of the surface reaction controls the rate (step3), the reaction is called “surface controlled.” Sometimes it can be observed a reaction is transport controlled if its rate varies with stirring speed (Bethke, 2008).

Transition state theory (TST) is the basis of many rate laws for surface-controlled reactions (Bethke, 2008). TST states that the rate of an elementary reaction is associated with the “activated complex concentration or the maximum free energy for the reactants to be transformed into products” (Schott & Oelkers, 1995). Based on this theory the dissolution rate is independent of the mineral’s saturation state. On the contrary, the rate of precipitation is dependent on the saturation and only can go above the dissolution rate when the mineral is supersaturated. When a reaction attains an equilibrium, the dissolution rate equals the rate of precipitation; this means the total rate of reaction is zero (Bethke, 2008).

Kinetic reactions formulation

In the following paragraphs, the way a kinetic reaction is formulated is summarized (Bethke, 2008). Here we consider one or more minerals $A_{\vec{k}}$ that kinetic rate laws control their dissolution and precipitation rates. Having the assumption that the minerals $A_{\vec{k}}$ are not in equilibrium with the system (they do not appear in the basis), a reaction for $A_{\vec{k}}$ can be written for the system composed of basis (A_w, A_i, A_k and A_m) as follows to calculate reaction’s equilibrium constant, $K_{\vec{k}}$:



A rate law for a given dissolution rate $r_{\vec{k}}$ (negative change of the minerals’ mole number over time) of mineral $A_{\vec{k}}$ can be written in the following form:

$$r_{\vec{k}} = -\frac{dn_{\vec{k}}}{dt} = (A_S K_+)_{\vec{k}} \prod (m_{\vec{j}})^{P_{\vec{j}\vec{k}}} \left(1 - \frac{Q_{\vec{k}}}{K_{\vec{k}}}\right).$$

The dissolution rate is a function of A_S , the minerals surface area (cm^2) and K_+ , the intrinsic rate constant for the reaction, ($mol/cm^2 sec$). The concentrations of certain species $A_{\vec{j}}$, that contain the rate laws promoting and inhibiting species, are represented by $m_{\vec{j}}$, and

$P_{j \rightarrow k}$ that are those species' exponents (values are derived empirically). The activity product is shown by $Q_{\rightarrow k}$.

In the previous equation, three functional parts can be distinguished. The first grouping is $A_S K_+$. The rate constant is determined experimentally. The second grouping, \prod grouping signifies the role of the species in solution. The species are generally aqueous species but might also be mineral, gas, or surface species, and they can promote the reaction or inhibit its progress. If the $P_{j \rightarrow k}$ is positive, the reaction is promoted by a species (e.g., catalyzing the formation of the activated complex). The negative sign of $P_{j \rightarrow k}$, on the other hand, show the reaction is inhibited. The last grouping accounts for the thermodynamic drive of the reaction. In case $Q_{\rightarrow k} > K_{\rightarrow k}$, the mineral $A_{\rightarrow k}$ is supersaturated and the mineral precipitates. In contrary when the mineral is undersaturated, it dissolves ($Q_{\rightarrow k} < K_{\rightarrow k}$).

The rate constant is linked to temperature by the Arrhenius equation:

$$K_+ = A e^{-E_A/RT_K}$$

Here A is the pre-exponential factor ($mol\ cm^{-2}\ s^{-1}$), E_A is the activation energy ($J\ mol^{-1}$), R is the gas constant, and T_K is absolute temperature (K). The activation energy is derived experimentally for a mineral phase.

Estimation of mineral specific surface areas

Knowledge of the mineral surface area is essential for the quantification of mineral-water reaction rates. There are various methods to measure the interfacial area among phases. The surface area can be measured either by a nitrogen adsorption technique, known as the BET (Brunauer–Emmett–Teller) method (Brunauer, et al., 1938) or estimated from geometric aspects.

According to the BET method, the molecules will deposit on the surface in the form of a thin, multilayer film when the gas pressure and temperature approach the pressure and temperature of the liquid and vapor at equilibrium. The method uses a powdered sample that is in an evacuated chamber, which is immersed in boiling liquid nitrogen to set a specific temperature. By increasing the injected nitrogen gas into the chamber, the pressure varies, and the adsorbed gas is measured at several points. These data points are then fit to the BET isotherm, and the amount of gas on the solid surface is calculated from the slope and intercept of the isotherm. By assuming a sorption cross-section for an adsorbed N_2 molecule, the surface area is calculated. Surface areas which are derived from BET method (also named as total

surface area), A_{BET} , are commonly greater than those estimated from the geometric surface area (Rimstidt, 2014). Practically, large surface area, (i.e., 1–1,000 m^2/g) can be best measured by the BET method. Smaller surface areas are challenging to measure with sufficient precision. Using Krypton as the adsorbate gas, measurements of the specific surface area as low as 0.1 m^2/g would be possible (Lüttge & Arvidson, 2008).

The geometric surface area is a useful method to develop idealized reference models to calculate reacting surfaces (Rimstidt, 2014). Even though idealized surface area models ignore some important surface features, they provide a handy and straightforward estimate of the relationship between surface geometry and reaction rates. As the geometric surface area is based on crystal dimensions, it requires a simplified model of the mineral grain, e.g., a sphere, cube, or rhombohedron. As a first approximation, the surface areas of solid particles can be modelled as if the grains are smooth spheres with an effective diameter equal to the real grain's smallest dimension. Particle size is determined by various methods that find a range of grain sizes, such as sieving, sedimentation rates, light scattering, and optical measurements. For the small range of particle sizes, a weighted average of the maximum diameter (D_{max}, m) and minimum diameter (D_{min}, m) is used to determine an effective diameter (D_e, m):

$$D_e = \frac{D_{max} - D_{min}}{\ln\left(\frac{D_{max}}{D_{min}}\right)}$$

A simpler model to calculate the specific geometric surface area ($A_{geo}, m^2/g$) is to relate the specific surface area of grains to their diameter, assuming spherical grains. In the following equation, the geometric surface area is related to the molar volume of a substance ($V_m, m^3/mol$), the grains diameter (D, m), and the molecular weight of the substance ($W_m, g/mol$).

$$A_{geo} = \frac{6 V_m}{DW_m} \left(\frac{m^2}{g}\right)$$

By substituting density ($\rho, g/cm^3$) in the above equation, the succeeding equation is obtained:

$$A_{geo} = \frac{6 * 10^{-6}}{DW_m} \left(\frac{m^2}{g}\right)$$

By assuming a perfectly smooth surface excluding any internal porosity, values of surface area for geometric and BET measurements would be similar. Nonetheless, as the BET method measures the surface areas on an atomic scale, surface etching, and pitting shaped by weathering are included in the measurements. Surface roughness λ is the ratio of the geometric

surface area to the surface area derived from the BET method (Helgeson, 1971; Helgeson, et al., 1984; White & Peterson, 1990; White, 2008).

$$\lambda = \frac{A_{geo}}{A_{BET}}$$

According to (White & Peterson, 1990) synthesis of data displays that BET surface area values of fresh surfaces exceed geometric estimates by the roughness factor of 7 over an extensive range in particle sizes. For naturally weathered silicates, the roughness factors can approach 200; the roughness values are strongly dependent on mineral composition.

Kinetics of redox reactions

Reduction-oxidation (redox) reactions in the aqueous phase play an essential role in controlling chemical composition, solubility, reactivity, along with dissolution and precipitation of mineral phases in the reservoir (Bethke, 2008; Kohen & Nyska, 2002). These reactions are principal in groundwater chemistry and can control the abundance of elements such as oxygen, nitrate, and sulfate as well as other redox-sensitive elements. Oxidation and reduction reactions occur together; in other words, they are related continuously to another. That is why the overall reaction is referred to as a redox reaction. Oxidation reaction includes electron(s) loss of an element, whereas reduction reaction involves electron(s) gain for an element (Bethke, 2008).

Table 3-1 A couple of examples of the redox couples in the LLNL database (Bethke, 2008).

CH ₃ COO ⁻ — HCO ₃ ⁻	CH ₃ COO ⁻ + 2 O ₂ (aq) ⇌ 2 HCO ₃ ⁻ + H ⁺
CH ₄ (aq) — HCO ₃ ⁻	CH ₄ (aq) + 2 O ₂ (aq) ⇌ H ₂ O + HCO ₃ ⁻ + H ⁺
Fe ³⁺ — Fe ²⁺	Fe ²⁺ + H ⁺ + ¼ O ₂ (aq) ⇌ Fe ³⁺ + ½ H ₂ O
H ₂ (aq) — O ₂ (aq)	H ₂ (aq) + ½ O ₂ (aq) ⇌ H ₂ O
HS ⁻ — SO ₄ ²⁻	HS ⁻ + 2 O ₂ (aq) ⇌ SO ₄ ²⁻ + H ⁺
N ₂ (aq) — NO ₃ ⁻	N ₂ (aq) + H ₂ O + 5/2 O ₂ (aq) ⇌ 2 H ⁺ + 2 NO ₃ ⁻
NH ₄ ⁺ — NO ₃ ⁻	NH ₄ ⁺ + 2 O ₂ (aq) ⇌ NO ₃ ⁻ + 2 H ⁺ + H ₂ O
NO ₂ ⁻ — NO ₃ ⁻	NO ₂ ⁻ + ½ O ₂ (aq) ⇌ NO ₃ ⁻

Numerous elements in natural systems can have more than one oxidation state (e.g., iron as either Fe²⁺ or Fe³⁺, or sulfur in valence states from S⁻² to S⁺⁶ and many more) (Bethke, 2008). To set up a geochemical model, the redox state should be specified. Elements in a model should have a definite state of whether the valance states have independent concentrations, or they attain equilibrium. For this, the activities of each pair states (e.g., $a_{Fe^{3+}}/a_{Fe^{2+}}$) in addition to the total amount of the element must be specified. In geochemistry, redox potential (E_h) measurements are used to characterize the oxidation-reduction status of surface environments (Bethke, 2008). A couple of examples of the redox couples in the Lawrence Livermore National Laboratory (LLNL) database is shown in Table 3-1.

In geochemical modeling tools, the user can control the redox state, either by defining it or by “decoupling” those redox pairs that may have not attained equilibrium (Bethke, 2008). At low temperatures, many redox reactions are unlikely to achieve equilibrium (Bethke, 2008). Many studies demonstrated the relation of microbial metabolism that couples the inorganic redox chemistry of groundwater to the oxidation of organic carbon (Lovley & Phillips, 1988; Murphy, et al., 1992; Kohen & Nyska, 2002; Kuypers, et al., 2018)

3.4 Hydrogen ecosystem

Hydrogen is one of the most active substrates in subsurface ecosystems and can link the subsurface geological system with the biological system. Hydrogen contributes in both anabolic and catabolic metabolisms. Anabolic metabolism happens via carbon and nitrogen fixation (reduction with hydrogen); while catabolic metabolism occurs via electron transfer of hydrogen in the form of redox-active components as well as carbon oxidation (Libert, et al., 2011; Nealson, et al., 2005; Konn, et al., 2015).

Figure 3-3 illustrates the role of hydrogen in the geological and biological systems. Both abiotic and biotic processes can produce hydrogen. Via abiotic processes, hydrogen can be formed by various chemical reactions. Hydrogen-rich fluids or minerals can be generated through a well-known process called Serpentinization. This process consists of the hydrolysis and transformation of minerals containing iron and magnesium as major components (e.g., olivine ((Mg,Fe)₂SiO₄), pyroxenes ((Mg, Fe)SiO₃)) to generate hydrogen-rich fluids as well as a range of secondary minerals over wide-ranging environmental conditions (Holm, et al., 2015). The serpentinization process and consequently, hydrogen formation results in pH increase (typically > 9) in the associated fluids of the system (Holm, et al., 2015). Additional biotic processes that result in hydrogen production include active volcanic events or seismic activities in the lower crust (e.g., deep faults), which produce compounds such as H₂, CO₂, and H₂S (Libert, et al., 2011). The last proposed hydrogen production source due to biotic processes is the outgassing of magma-hosted systems.

Figure 3-4 describes two different sights that we can look at the hydrogen-driven ecosystems. This image displays the way that hydrogen can move between cells to ease substrates metabolism that may thermodynamically be difficult in the absence of hydrogen. The first one is utilizing oxygen or an oxygen-derived oxidant, such as nitrate or sulfate, to metabolize the hydrogen, and the second one is using geologically supplied oxidants, such as carbon dioxide (Nealson, et al., 2005).

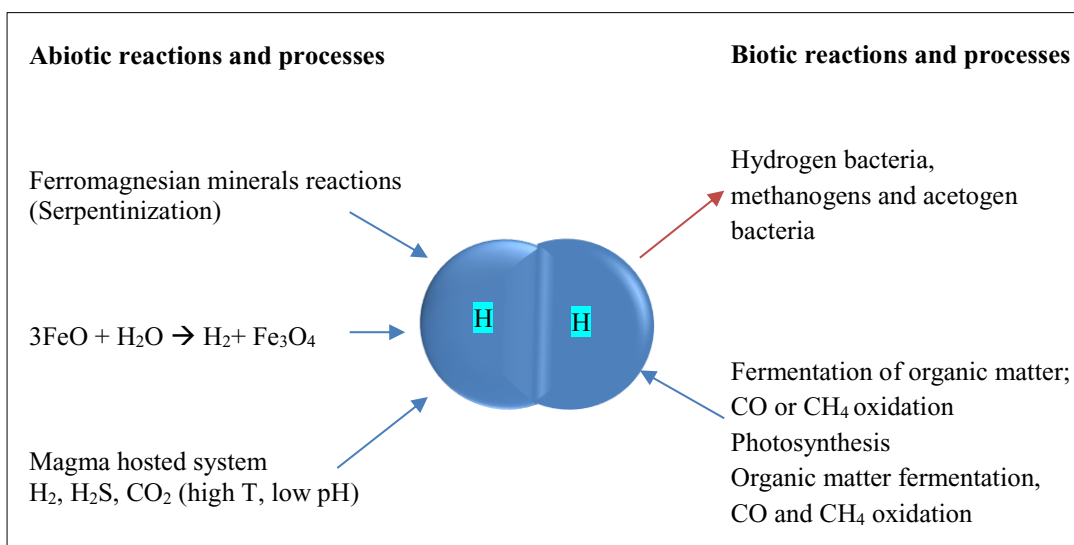


Figure 3-3 Biotic and abiotic related processes to hydrogen and the role of hydrogen in linking the geological and the biological world [adapted from (Libert, et al., 2011; Nealson, et al., 2005)].

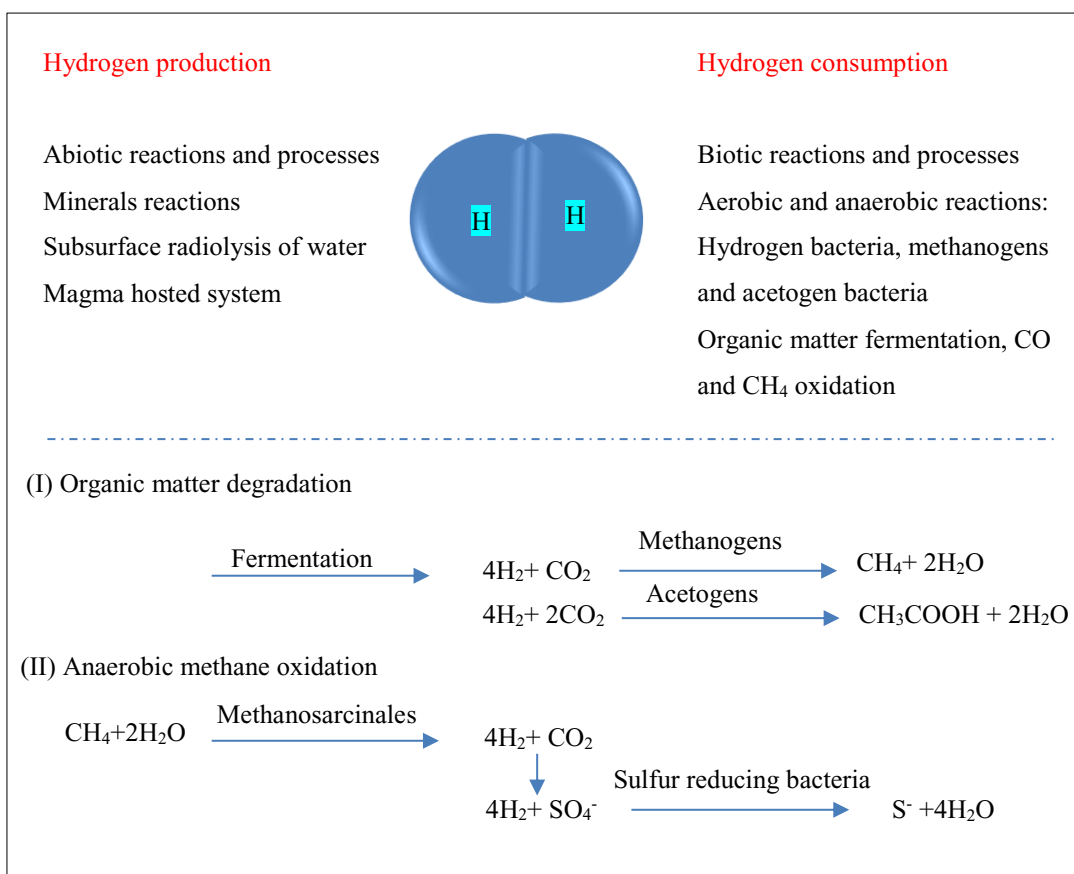


Figure 3-4 Hydrogen ecosystems: interspecies hydrogen transfer. This figure illustrates the way that hydrogen can move between cells to ease substrates' metabolism that may be thermodynamically hard in the absence of hydrogen [adapted from (Libert, et al., 2011; Nealson, et al., 2005)].

Chapter 4 Geochemical modeling of the target reservoir¹

“Hydrogen storage in depleted gas fields is a promising option for the large-scale storage of excess renewable energy. In the framework of the hydrogen storage assessment for the “Underground Sun Storage” project, we conduct a multi-step geochemical modeling approach to study fluid-rock interactions by means of equilibrium and kinetic batch simulations. With the equilibrium approach, we estimate the long-term consequences of hydrogen storage, whereas kinetic models are used to investigate the interactions between hydrogen and the formation on the time scales of typical storage cycles.”

“The kinetic approach suggests that reactions of hydrogen with minerals become only relevant over timescales much longer than the considered storage cycles. The final kinetic model considers both mineral reactions and hydrogen dissolution to be kinetically controlled. Interactions among hydrogen and aqueous-phase components seem to be dominant within the storage-relevant time span. Additionally, sensitivity analyses of hydrogen dissolution kinetics, which we consider to be the controlling parameter of the overall reaction system, were performed. Reliable data on the kinetic rates of mineral dissolution and precipitation reactions, specifically in the presence of hydrogen, are scarce and often not representative of the studied conditions. These uncertainties in the kinetic rates for minerals such as pyrite and pyrrhotite were investigated and are discussed in the present work”.

¹ The content of this chapter is published in Environmental Earth Sciences as : Neda Hassannayebi, Siroos Azizmohammadi, Marco De Lucia, and Holger Ott, *Underground Hydrogen Storage: Application of geochemical modelling in a case study in the Molasse Basin, Upper Austria*, Environ Earth Sci (2019) 78: 177. <https://doi.org/10.1007/s12665-019-8184-5>

“The proposed geochemical workflow provides valuable insight into controlling mechanisms and risk evaluation of hydrogen storage projects and may serve as a guideline for future investigations”.

Keywords: Underground hydrogen storage, depleted gas reservoir, geochemical modelling, rock-fluid interactions

4.1 Introduction

“Hydrogen is an effective energy carrier that can be generated from excess renewable energy, which is a technique called peak shaving. Hydrogen is considered as an alternative to fossil fuels in the transport sector. However, peak shaving requires large-scale storage options, orders of magnitude larger than typically discussed in relation to mobility and transportation and other applications. Taylor *et al.* (1986) evaluated the technical and economic aspects of hydrogen storage in large quantities using five site-specific scenarios: (1) pressure vessel storage, (2) liquid hydrogen for aircrafts, (3) salt cavern storage, (4) mined cavern storage and (5) underground porous media storage. According to their study, underground hydrogen storage (UHS) is the most economical means of storing large quantities of gaseous hydrogen. Foh *et al.* (1979) presented a few examples of UHS projects, including the successful hydrogen storage in solution-mined salt caverns at Teeside in England by Imperial Chemical Industries and hydrogen storage in an aquifer reservoir site near Beynes, France, which was operated by Gaz de France to store hydrogen-rich gas (50% to 60%) from 1950 to 1972. Apart from these case studies and a few more projects, there has never been a pilot test on using depleted gas reservoirs as hydrogen storage sites”.

“Depleted natural gas reservoirs provide massive storage capacity and are therefore suitable for large-scale UHS facilities. Gas reservoirs have proven to be sealed; however, because of the lack of field pilots, there is not much knowledge about hydrogen-induced fluid-rock interactions for such reservoirs, and an assessment of economic and environmental risks is needed for commercial implementation of UHS projects. Possible risks associated with UHS include operational losses, corrosion, leakage through the casing, diffusion of gas into the caprock, the solubility of hydrogen into the brine formation, and chemical and biochemical reactions (Carden and Paterson, 1979)”.

“A small depleted gas field located in the Molasse Basin in Upper Austria has been selected as a suitable storage site and as a target for the integrated pilot project “Underground Sun Storage”, which for the first time tests the storage of hydrogen generated from a surplus of

renewable resources in a depleted gas reservoir. The Molasse Basin, situated between Linz and Salzburg, is one of the main gas-producing regions in Austria. To date, more than 40 gas fields have been discovered in this basin. Many of these gas fields are found in deep-water sandstone, conglomerates of the Oligocene–Miocene Puchkirchen and Hall formations (De Ruig and Hubbard, 2006). This field exhibits unique characteristics as it is homogenous, optimally sealed by shale layers and without connections to aquifers, which makes it a promising site for a pilot project. The reservoir layer is characterized by a thickness of 1.5 meters, 22% porosity, 22% irreducible water saturation and a temperature of 40 °C”.

“In this work, we developed a workflow to evaluate gas-brine-mineral interactions. The proposed workflow starts with investigating the geochemical system through equilibrium batch modeling, where reactions are considered to be instantaneous. Even though outcomes of the equilibrium model are not apt for a typical hydrogen storage cycle, they are still valuable as indicator of long-term risk assessment for hydrogen storage projects. As the second step, we include the kinetics for mineral reactions, while hydrogen solubility and thus availability for reactants is assumed to be at equilibrium with the gas phase. This step quantifies the alteration of the mineral phase during a typical hydrogen storage cycle, which is assumed to be on the order of 3 to 6 months. Lastly, to have a more realistic geochemical model, we consider both the mineral and hydrogen availability in reactions to be kinetically controlled. Owing to the lack of knowledge/scarcity of data concerning reaction rates among hydrogen and reservoir brines, we instead investigated the sensitivity of the results to the reaction rate parameters as a result of hydrogen injection.

Field data

The availability of data from small gas fields is typically limited. Water and gas samples were available for this formation; however, no core sample was extracted. Data on a core sample from a well of a nearby reservoir were used as analogue for the mineralogy, as we assume similar mineralogy to the field studied here. The equilibrium between the initial brine and mineral phases is assumed and is considered in this study by an initial equilibration step in the numerical simulations.

Production-injection scheme

Gas production of this field started in June 2007, and the well was ceased at the end of June 2010. The well was shut in until October 2015. Thereafter, a hydrogen-methane mixture was injected in three subsequent periods. Two of these periods lasted for only a few days

because of a shortage of hydrogen at the site. In the third attempt, hydrogen was injected into the formation for three months. Figure 4-1 illustrates the sequence of events for this reservoir.

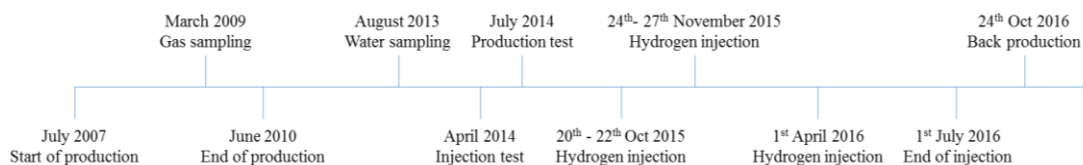


Figure 4-1 Sequence of events in Lehen-2.

Rock and fluid compositions

X-ray diffraction (XRD) data were used to characterize the volumetric mineral compositions of the formation rock. The analyzed core sample was taken from a nearby well and is assumed to have a similar composition as the reservoir under investigation. The mineral composition is as follows: quartz (20 vol%), muscovite and clay minerals (47 vol%), subordinate plagioclase (4 vol%), K-feldspar (2 vol%), calcite (20 vol%), dolomite (9 vol%), ankerite (4 vol%), siderite (2 vol%), and pyrite (1 vol%). In this study, clay minerals were assumed to make up approximately 40 vol% of the total reservoir volume. The volumetric percentage of clay particles is given as follows: illite (59 vol %), smectite (29 vol %), chlorite (15 vol%) and kaolinite (3vol%) (analysis performed by OMV Exploration & Production GmbH Laboratory, 2007).

The volumetric percentage of minerals was converted to mole values for each mineral to be used in the geochemical models. Using Eq. (1), the amount of each mineral was calculated as:

$$n_{\text{mineral}} = \frac{m_w}{\rho_w} \left(\frac{1-\phi}{\phi} \right) \frac{\rho_{\text{mineral}}}{M_{\text{mineral}}} \cdot SVF, \quad (1)$$

where ρ_w is water density, m_w is water mass (basis=1 kg), ϕ is porosity, ρ_{mineral} is the mineral density, SVF is the solid volume fraction of minerals, M_{mineral} is mineral molar weight, and n_{mineral} is the number of moles of each mineral.

The formation water was sampled from the well under investigation and is mainly dominated by K^+ , Cl^- , HCO_3^- , and Na^+ , with considerable amounts of SO_4^{2-} , Mg^{2+} , NO_3^- , NH_4^+ , Ca^{2+} and some dissolved Fe^{2+} and Mn^{2+} (see Table 4-1).

The initial gas composition of the studied reservoir (sampled by RAG (Rohöl-Aufsuchungs Aktiengesellschaft)) consists of CH_4 (98.33 mol%), C_2H_6 (0.49 mol%), CO_2 (0.08 mol%) and N_2 (0.84 mol%). The maximum sulfide content (H_2S) is reported to be 5 mg/m³. The initial reservoir pressure is around 100 bars. The amount of CO_2 in the gas phase is

incorporated in the geochemical models to account for the degassing effect during water sampling.

Table 4-1 Chemical composition of the brine sample from the well under investigation (analysis performed by Dr Begert Umweltconsulting GmbH, 2013).

Aqueous Species	Measured value (mg/l)	Measured value (molal)
NH ₄ ⁺	13.5	7.53E-04
NO ₂ ⁻	<0.010	2.19E-07
Cl ⁻	5900	1.95E-01
NO ₃ ⁻	12.4	2.01E-04
Mg ²⁺	12.3	5.09E-04
SO ₄ ²⁻	16.9	1.77E-04
Ca ²⁺	7.23	1.81E-04
Fe ²⁺	0.31	5.58E-06
Mn ²⁺	0.088	1.61E-06
Na ⁺	181	7.92E-03
K ⁺	7820	2.01E-01
HCO ₃ ⁻	943	1.55E-02

4.2 Geochemical modelling approach

Modelling tool and thermodynamic database

“Geochemist’s workbench (GWB) (Bethke *et al.*, 2016) was used as a geochemical modelling tool for this study. The software has numerous capabilities, such as the implementation of kinetic rate laws for mineral dissolution and precipitation reactions, complex association and dissociation, redox transformation, gas transfer, 1-D and 2-D reactive transport, and bio-reactive and colloidal transport (<http://www.gwb.com/>)”.

The internal LLNL thermodynamic database (Lawrence Livermore National Laboratory) was used throughout the study. Consistent and comprehensive thermodynamic data are key to the accurate evaluation of the quality and accuracy of the geochemical model. Database consistency and completeness with respect to the mineralogy of the reservoir were checked. Aside from subordinate plagioclase, potassium feldspar, ankerite, illite, smectite and chlorite, data for the rest of the primary minerals present in this database. Our strategy for modelling was to look up the thermodynamic properties of the absent minerals and integrate them into the LLNL database. Proxy minerals were chosen for minerals for which thermodynamic properties could not be found. The thermodynamic properties of ankerite (Holland and Powell, 1998) were integrated directly into the database. Montmorillonite was chosen to represent the smectite group. Albite and anorthite were chosen as proxy minerals for plagioclase. Microcline was selected as an alternative mineral for potassium feldspar. Finally, clinocllore and daphnite were

chosen as the two end members of chlorite. Table 4-2 illustrates the final set of minerals used in the geochemical study.

Table 4-2 The final minerals assemblage used in the geochemical models.

	Primary minerals	Alternative/ substituted minerals	Final mineral assemblage used in models	Calculated minerals (moles)	Chemical formula
Rock Minerals	Quartz		Quartz	25.91	SiO ₂
	Muscovite		Muscovite	1.47	KAl ₂ (AlSi ₃ O ₁₀)(OH) ₂
	Calcite		Calcite	9.57	CaCO ₃
	Dolomite		Dolomite	4.12	CaMg(CO ₃) ₂
	Ankerite		Ankerite	1.76	Ca(Fe ²⁺ ,Mg,Mn)(CO ₃) ₂
	Subordinate Plagioclase	Albite	Albite	0.59	NaAlSi ₃ O ₈
		Anorthite	Anorthite	0.57	Ca[Al ₂ Si ₂ O ₈]
	Potassium feldspar	Microcline	Microcline	0.55	KAlSi ₃ O ₈
	Siderite		Siderite	2.03	Fe ²⁺ (CO ₃)
Pyrite		Pyrite	1.24	FeS ₂	
Clay fraction	Illite		Illite (FeII)	1.63	K _{0.85} Fe _{0.25} Al _{2.35} Si _{3.4} O ₁₀ (OH) ₂
	Smectite	K- Montmorillonite	K- Montmorillonite	0.45	KS _{10.473} Al _{4.132} Mg _{0.737} Fe ^{III} _{0.237} Fe ^{II} _{0.211} O _{44.316} H _{30.737}
	Chlorite	Clinochlore	Clinochlore	1.04	Mg ₆ Si ₄ O ₁₀ (OH) ₈
		Daphnite	Daphnite	1.07	Fe ₅ Al ₂ Si ₃ O ₁₀ (OH) ₈
	Kaolinite		Kaolinite	2.39	Al ₂ Si ₂ O ₅ (OH) ₄

Modelling methodology

As part of the UHS feasibility assessment, metabolize is proposed (Figure 4-2) to characterize the behaviour of the geochemical system in the presence of hydrogen. As at the time of the study, there was no data available to be benchmarked with the simulation results, several scenarios applying different assumptions were simulated. In the course of modelling relative adjustments and assumptions are incorporated into the models to have results that are more representative of what might happen in the field during a storage cycle. Even though we believe the final kinetic batch model has the highest relevance for the specific study, other scenarios as well as the long-term storage consequences under elevated conditions (longer time scales or elevated temperatures) should not be overlooked.

In this approach, we suggest different modelling steps to study the short- and long-term impacts of hydrogen on the reservoir; proper assumptions were considered for all stages of modelling. The modelling steps are: (1) the equilibrium batch model, which assumes instantaneous reactions (equilibrium) for both hydrogen and minerals; (2) the primary kinetic batch model, which considers mineral reactions to be kinetically controlled, while hydrogen reactions are assumed to occur at local thermodynamic equilibrium; this stage is composed of two modelling steps. In the first model, all the mineral reactions are taken from literature data, and in the second, reactions of pyrite and pyrrhotite are assumed to take place at equilibrium. The reason for doing this relates to experimental evidence indicating that these reactions are relatively fast in the presence of hydrogen, while the literature data do not consider this fact. Further discussions are given in the results section. The last step (3) is the final kinetic batch model, in which both minerals and hydrogen reactions are assumed to be kinetically controlled. A sensitivity analysis on the hydrogen reaction rate (low/moderate/high) and the assumption of having equilibrium/disequilibrium for redox pairs are made to investigate their significance on the results.

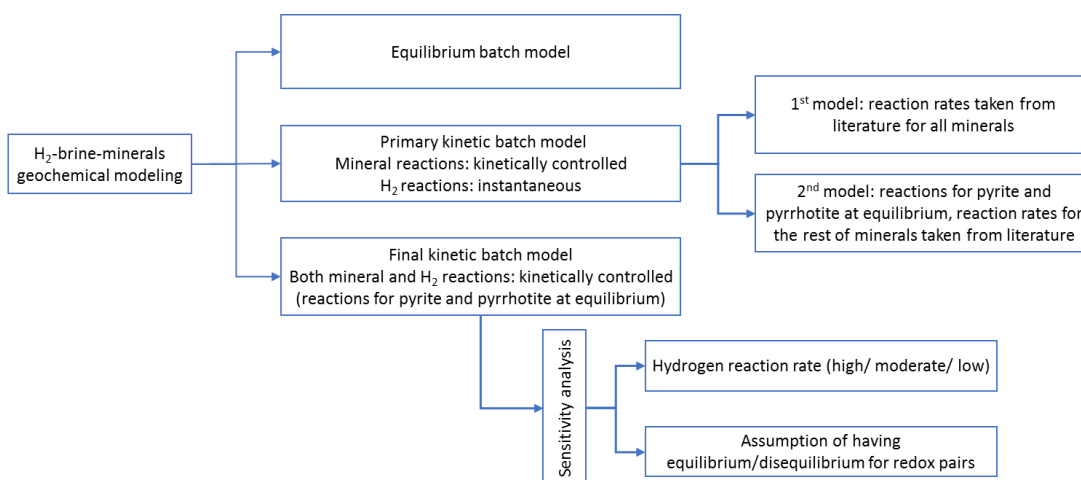


Figure 4-2 The geochemical modelling workflow as proposed and applied in this work.

The results obtained from the equilibrium batch model assist in estimating the long-term consequences of hydrogen injection in the reservoir. However, the model has its limitations to predict sensible results for the cyclic hydrogen storage, therefore, it should only be looked at as part of risk assessment study. From the primary kinetic batch model, we conclude that H_2 interactions with minerals require time scales much larger than a typical hydrogen storage cycle. Consequently, the interactions among hydrogen and brine components are recognised to be more relevant within the storage cycle of hydrogen. Because of the general lack of knowledge concerning the rates of hydrogen dissolution in brine, a sensitivity analysis on H_2 reaction-controlling parameters was performed in the final kinetic batch model. With the kinetic

approach, a case was studied in which reactions of pyrite and pyrrhotite are considered at equilibrium. This imitates the reduction of pyrite to pyrrhotite, which can be significant at low-temperature conditions in the presence of hydrogen.

Charge balance analysis

One of the main steps in geochemical modelling is the charge balance calculation to determine the accuracy of the brine analysis. A routine criterion to evaluate this is the charge balance error (CBE) of the reported cation and anion concentrations, as follows (Freeze and Cherry, 1979):

$$CBE = \frac{\sum cations - |\sum anions|}{|\sum cations| + |\sum anions|} \quad (2)$$

Table 4-3 Calculated milliequivalents per liter value for the aqueous species.

Component	Measured (mg/L)	Charge	(meq/L)
NH ₄ ⁺	13.5	1	0.74844
NO ₂ ⁻	<0.010(+)	-1	-0.00022
Cl ⁻	5900	-1	-166.439
NO ₃ ⁻	12.4	-1	-0.20001
Mg ²⁺	12.3	2	1.012167
SO ₄ ²⁻	16.9	-2	-0.35186
Ca ⁺	7.23	2	0.360777
Fe ²⁺	0.31	2	0.013877
Mn ²⁺	0.088	2	0.0364
Na ⁺	181	1	7.8735
K ⁺	7820	1	247.0338
HCO ₃ ⁻	943	-1	-15.4558
charge balance error		17%	

The concentration unit in Equation (2) is milliequivalents per litre. The conversion factor from milligram per litre to milliequivalents per litre is taken from (Zhu and Anderson, 2002) and has been used for the charge balance calculation. According to Freeze and Cherry (1979), a charge balance error of less than 5% is acceptable for most laboratories. The result of the analysis is shown in Table 4-3. The calculated CBE is 17% for the water sample, which indicates that the initial water composition needs to be reassessed. In the course of modelling, the charge balance was compensated by varying the Cl⁻ concentration.

Initial equilibrium state

As the charge imbalance error was higher than acceptable, the measured initial water composition needs to be reevaluated and corrected. Generally, prior to geochemical simulations, a proper chemical equilibrium state between brine and primary mineral assemblage states must be established in order to have a consistent and reliable initial system (Cantucci *et al.*, 2009;

De Lucia *et al.*, 2012). Incorporating all detected minerals in the equilibration step leads to numerical issues and does not represent the water sample taken from the well. Thus, we calculated various scenarios to establish the initial state of the system. These scenarios enable us to consider different starting states for our models to account for incompatibilities in the mineralogy and brine sample (note that the rock sample is from a nearby reservoir). The purpose of establishing an “initial equilibrium state” is to identify mineral phases that control the concentrations of aqueous species, to make hypotheses about the equilibrium between brine and rock mineralogy and to estimate the concentrations of missing species (such as Al^{3+} and Si). Various representations of the mineral composition were equilibrated with the aqueous phase to determine the initial brine compositions. For each case, the calculated brine concentrations were compared to the measured values. Based on the reported natural gas phase in the reservoir, CO_2 with the fugacity of 0.08, was included in the models. With this step, the loss of dissolved CO_2 during the water sampling was taken into account. We further excluded NH_4^+ , NO_2^- and NO_3^- from the calculations as there is no indication of minerals containing nitrogen. Another reason for eliminating these species is due to not expecting the nitrate reduction by H_2 in the absence of bacteria, or any other specific catalysts (Fanning, 2000; Truche *et al.*, 2013). It is worth noticing the co-existence of these redox species will require further discussions and investigations as it has a strong association in term of oxygen fugacity in the system, likewise on the redox disequilibrium. Investigation of the latter is beyond the scope of this work. Small initial amounts of Al^{3+} and SiO_2 (aq) were added into the calculations to represent minerals containing these components (e.g., clay minerals). Table 4-4 presents four scenarios representing different mineral compositions from high to low complexity.

Imposing equilibrium conditions in all scenarios results in inconsistencies with regard to the Cl^- and HCO_3^- concentrations. In the first scenario, the assumed equilibrium state of both dolomite and calcite resulted in an overestimation of Ca^{2+} and HCO_3^- ion concentrations. Similarly, SiO_2 (aq) was overestimated because of the assumption of equilibrium for muscovite and microcline. In the second scenario, calcite was excluded from the equilibrium model, which led to a better match for Ca^{2+} and HCO_3^- . In the third case study, microcline was eliminated from the equilibrium model, which improved the SiO_2 (aq) concentration. Scenario 4, which assumes equilibrium among the fewest minerals and the analytical brine (incorporated minerals represent entirely analytical brine components), gives the best match, and the Fe^{2+} and Ca^{2+} concentrations improved. Further studies considering hydrogen injection in the equilibrium batch models performed based on the initial states derived from scenarios 3 and 4.

Table 4-4 Simulated and measured brine compositions. The different case studies and scenarios result in equilibrium assumptions for different sets of minerals in aqueous solution. Case studies 3 and 4 will be used in the following as initial brine compositions.

Aqueous concentration/ Minerals included	Case study 1	Case study 2	Case study 3	Case study 4	Measured value (mg/l)
Al ³⁺	9.0E-01	9.0E-01	1.2E-01	0.6E-01	not determined
Ca ²⁺	67.22	7.46	7.46	7.34	7.23
Cl ⁻	6820.37	6820.53	6820.54	6820.54	5900
Fe ²⁺	0.48	0.48	0.48	0.31	0.31
HCO ₃ ⁻	1109	1022	1021	1021	943
K ⁺	7820.55	7820.73	7819.62	7819.59	7820
Mg ²⁺	12.40	12.40	12.40	11.03	12.3
Mn ²⁺	0.09	0.09	0.09	0.087	0.088
Na ⁺	180.99	180.99	180.99	180.98	181
SO ₄ ²⁻	17.14	17.14	17.14	16.89	16.9
SiO ₂ (aq)	5.46	5.46	2.6E-01	1.3E-01	not determined
Dolomite	X	X	X	X	
Muscovite	X	X	X	X	
Pyrite	X	X	X	X	
Ankerite	X	X	X		
Microcline	X	X			
Calcite	X				
pH	7.59	7.6	7.6	7.6	8.7
Pe	-4.22	-4.13	-4.13	-3.95	not determined

Kinetics of precipitation and dissolution

The dissolution rate constants at standard conditions, activation energies and specific surface areas for minerals of interest were taken from literature (Table 4-5); most of the data were obtained from Palandri and Kharaka (2004). Mineral reactions often depend on pH, requiring different kinetic rates for acidic, neutral and basic reaction mechanisms. Normally, all three mechanisms are not incorporated in geochemical modelling applications, e.g., in applications of CO₂ storage; often, only neutral or acidic mechanisms are employed (Gaus *et al.*, 2008). In the present case, the reservoir conditions are of high pH, as indicated by the initial brine composition and by the results of the equilibrium approach, which shows an increasing tendency of pH with the injection of H₂. For this reason, only the basic reaction mechanisms for minerals has been used in this study. For minerals for which no basic reaction data are published, data for neutral mechanisms have been used. Due to the scarcity of experimental precipitation rates in the literature, the precipitation rates for secondary minerals were set equal to dissolution rates. It is noteworthy to mention that the precipitation rates for some minerals can be slower than the respective dissolution rates. GWB implements the Lasaga type of reaction rate law:

$$r_k^{\rightarrow} = A_s k_+ \left(1 - \frac{Q}{K}\right) \quad (3)$$

where r_k^{\rightarrow} is the reaction rate (mol/s), A_s is the mineral's surface area (cm²), k_+ is the rate constant (mol/(cm²s)), and Q and K represent the activity product and equilibrium constant for the dissolution reaction, respectively. The surface area is calculated from the specific surface area (cm²/g). The temperature dependence of the reaction rate constant is described by the law of Arrhenius:

$$k_+ = A e^{-E_A/RT_K} \quad (4)$$

Here, A is the pre-exponential Arrhenius factor, E_A is the activation energy, R is the gas constant and T_K is the absolute temperature in Kelvin. Since we have no information on the effective reactive surface area, we use typical values of 10 cm²/g for non-clay minerals and 100 cm²/g for clay minerals.

Generally, kinetic parameters are obtained in the absence of hydrogen, which makes their precision and applicability in hydrogen storage questionable. The rate constant of pyrite reduction by hydrogen is obtained from the experimental work of (Truche et al., 2010). This particular study offers the most relevant and practical values for pyrite dissolution and pyrrhotite precipitation in the presence of hydrogen. The experimental kinetic rate constant for pyrite reduction to pyrrhotite by H₂ was reported in the unit of [mol/m²/h^{0.5}]. This unit needed to be converted to [mol/m²/s]. Truche, 2009 reproduced the dependency of the square root of time virtually by increasing the simulated reaction times. In our study, we reproduced this dependency by testing models with pyrite kinetic rate coefficient up to 2 orders of magnitude higher than the base model. Likewise, we made two case studies for pyrrhotite; in one the rate constant is set to be the same as pyrite and in the other one pyrrhotite reactions assumed to be at equilibrium. No significant difference was observed in these case studies. In the last part, for pyrite and pyrrhotite, which are the minerals that may most likely react with hydrogen, an extra case study is considered and discussed in the simulation results section.

4.3 Simulation results and discussion

Batch geochemical modelling addresses the complex, thermodynamically controlled reactions between water, injected hydrogen gas and rock-forming minerals. The requirements for running simulations are the initial formation water chemistry, minerals mass (specified in grams) in equilibrium with the formation water and the kinetic parameters for the primary and secondary phases. In this chapter, the results from the equilibrium and kinetic batch models are shown and discussed.

Table 4-5 pH-dependent kinetic reaction rate constants at 25 °C (mainly from Palandri and Kharaka (2004)). All rate constants are listed for dissolution.

Mineral	A ^a (cm ² /g)	Kinetic rate parameters								
		Acid Mechanism			Neutral Mechanism		Base Mechanism			
		K ^b ₂₅ (mol/m ² s)	Ea ^c (KJ/mol)	n ^d (H ⁺)	K ₂₅ (mol/m ² s)	Ea (KJ/mol)	K ₂₅ (mol/m ² s)	Ea (KJ/mol)	n (H ⁺)	
Calcite	10	5.01E-01	14.4	1	1.55E-06	23.5	3.31E-04	35.4	1	
Dolomite	10	6.46E-04	36.1	0.5	2.95E-08	52.2	7.76E-06	34.8	0.5	
Illite	100	1.05E-11	23.6	0.34	1.66E-13	35	3.02E-17	58.9	-0.4	
K-feldspar	10	8.71E-11	51.7	0.5	3.89E-13	38	6.31E-22	94.1	-0.82	
Albite	10	6.92E-11	65	0.457	2.75E-13	69.8	2.51E-16	71	-0.57	
Kaolinite	100	4.90E-12	65.9	0.777	6.92E-14	22.2	8.91E-18	17.9	-0.47	
Anorthite	10	3.16E-04	16.6	1.411	7.59E-10	17.8				
Muscovite	100	1.00E-11	23.6	0.34	1.66E-13	35	3.02E-17	58.9	-0.4	
Siderite	10	6.46E-04	36.1	0.5	1.26E-09	62.76		34.8	0.5	
Ankerite	10	6.46E-04	36.1	0.5	1.26E-09	62.76				
Quartz	10				1.00E-14	87.7				
Pyrite*	10				1.94E-12	53				
Pyrrhotite		Set to Pyrite/ set to equilibrium								
K-Montmorillonite	100	2E-13	48	0.22	3.89E-15	48	3.89E-15	48	-0.13	
Chlorite	10	7.76E-12	88	0.5	3.02E-13	88				
Laumontite**	10	5E-13		0						
Daphnite		Set to Kaolinite								
Clinochlore		Set to Kaolinite								
Microcline		Set to K-feldspar								

^a reactive surface area ^brate constant ^c activation energy ^d pH dependency power term * rate constant is obtained from the Arrhenius plot of the inverse of reaction temperature (at 25°C) versus rate constant under 8 bars of hydrogen partial pressure (Truche et al., 2010); ** (Arthur et al., 2000)

4.3.1 Equilibrium batch models

The prediction of the geochemical reactivity of hydrogen via equilibrium batch modelling is crucial to assess the potential long-term impacts on UHS on one hand, and on the other it allows to test different hypotheses concerning uncertain parametrization with simpler calculations. In these calculations, equilibrium of the aqueous phase with the injected H_2 is maintained; likewise, mineral reactions with the formation water are considered at equilibrium. Two starting points – i.e., initial conditions – were considered corresponding to case studies 3 and 4 from Table 4-4. The initial state is equilibrated with injected hydrogen with a partial pressure up to 7.5 bars, corresponding to the operational H_2 partial pressure during the injection operation. The reactions are monitored as a function of hydrogen fugacity. The formation of CH_4 (aq) has been suppressed as its formation is not realistic and would lead to misinterpretations. As a further assumption, all other redox couple reactions are treated at equilibrium. As a consequence of hydrogen injection, primary minerals dissolve partially into the formation water, modifying the formation water composition, which leads to the precipitation of other mineral phases. Here, we present outcomes of a model, in which the calcite formation is excluded as it gave more sensible results. The behavior of pH shows first a sharp peak, followed by a smooth increase, as shown in Figure 4-3. In case study 3, a slightly higher increase in pH value has been observed. The mineral reactions in the system explain this observation.

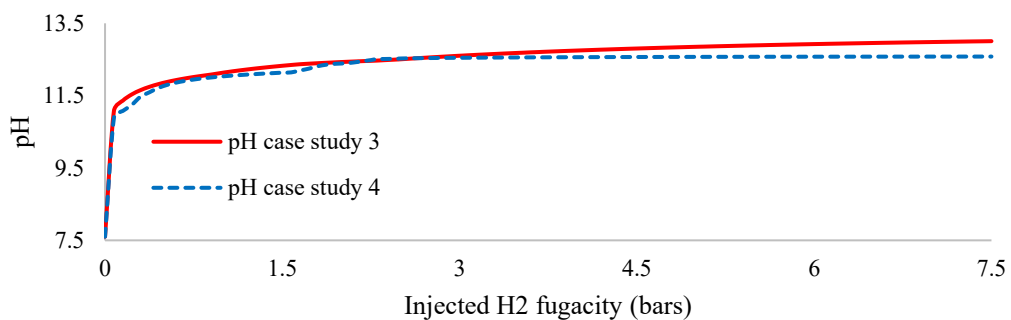


Figure 4-3 Evolution of pH obtained from equilibrium batch models as a function of injected hydrogen fugacity

A detailed view on the mineral phase, mineral dissolutions and mineral precipitations alongside the variation in pH is provided in Figure 4-4. The mineral reactions included in each case study are enumerated in Table 4-6.

Table 4-6 Main chemical reactions extracted from equilibrium batch models marked by “*”. Primary and secondary minerals are indicated by “P” and “S”

Mineral reaction	Precipitation/dissolution	case study			
		3		4	
Muscovite	$\text{Muscovite} + 5\text{H}^+ + 5\text{H}^+ \leftrightarrow \text{K}^+ + 3\text{Al}^{+3} + 3\text{SiO}_2(\text{aq}) + 6\text{H}_2\text{O}$	*	P	*	P
Dolomite	$\text{Dolomite} \leftrightarrow \text{Ca}^{+2} + \text{Mg}^{+2} + 2\text{CO}_3^{2-}$	*	P	*	P
Pyrite	$\text{Pyrite} + \text{H}_2(\text{aq}) \leftrightarrow \text{Fe}^{+2} + 2\text{HS}^-$	*	P	*	P
Ankerite	$\text{Ankerite} + 2\text{H}^+ \leftrightarrow \text{Fe}^{+2} + \text{Ca}^{+2} + 2\text{HCO}_3^-$	*	P		
Clinochlore	$\text{Clinochlore} + 10\text{H}^+ \leftrightarrow 2\text{AlO}(\text{OH}) + 5\text{Mg}^{2+} + 3\text{SiO}_2(\text{aq}) + 8\text{H}_2\text{O}$	*	S	*	S
Pyrrhotite	$\text{FeS}_2 + (1-x)\text{H}_2 \leftrightarrow \text{FeS}_{1+x} + (1-x)\text{H}_2\text{S}$	*	S	*	S
Daphnite	$\text{Daphnite} + 10\text{H}^+ \leftrightarrow 2\text{AlO}(\text{OH}) + \text{Fe}^{2+} + 3\text{SiO}_2(\text{aq}) + 8\text{H}_2\text{O}$			*	S

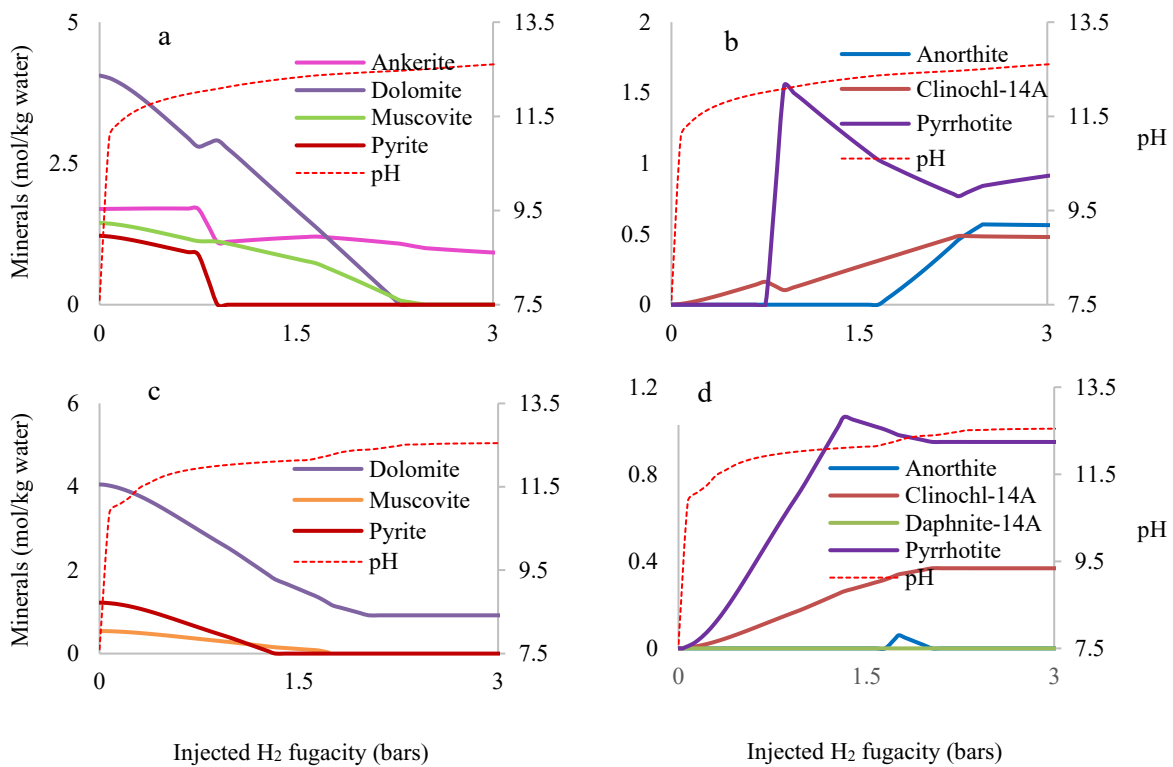


Figure 4-4 Distribution of mineral phases (precipitation and dissolution, plotted on the primary y-axes) and pH variance (plotted on the secondary y-axes) obtained from equilibrium batch models as a function of injected hydrogen fugacity. Most changes occur at the beginning of injection; therefore, these plots are only shown for injection of H₂ up to 3 bar fugacity (dissolution of primary minerals and precipitation of secondary minerals for case study 3 and 4 are shown in panels a / b and c / d respectively).

The injection of hydrogen, and consequently the change in pH value, results in the formation of pyrrhotite from pyrite in reservoir conditions (Figure 4-5). This reaction is understood to occur in the presence of hydrogen (Truche *et al.*, 2013; Betelu *et al.*, 2012). The relationship between pyrite and pyrrhotite can be expressed by the general redox equation (Hall 1986): $2\text{FeS} \leftrightarrow \text{FeS}_2 + \text{Fe}^{2+} + 2\text{e}^-$.

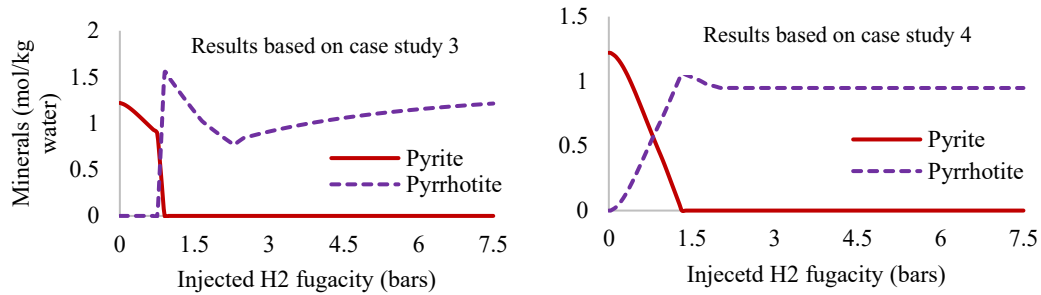


Figure 4-5 Dissolution of pyrite and formation of pyrrhotite as a consequence of hydrogen injection obtained from equilibrium batch model based on initial state of case study 3 and 4.

Changes in aqueous species are expected and could be correlated with mineral dissolution and precipitation reactions. Figure 4-6 shows the changes hydrogen sulfide, calcium, potassium, acetate and bicarbonate components as a function of the injected H_2 fugacity. There is a noticeable decrease in a few aqueous species (HCO_3^-) with increasing H_2 fugacity because of mineral precipitation. The dissolution of muscovite can explain the increase in K^+ in the system. The increase in sulfide and calcium concentrations are in agreement with the observed experimental trend in both species in the presence of hydrogen (Truche, et al., 2010). The more pronounced production of H_2S at the beginning of the reaction was similarly in agreement with the experimental results (Truche, et al., 2010).

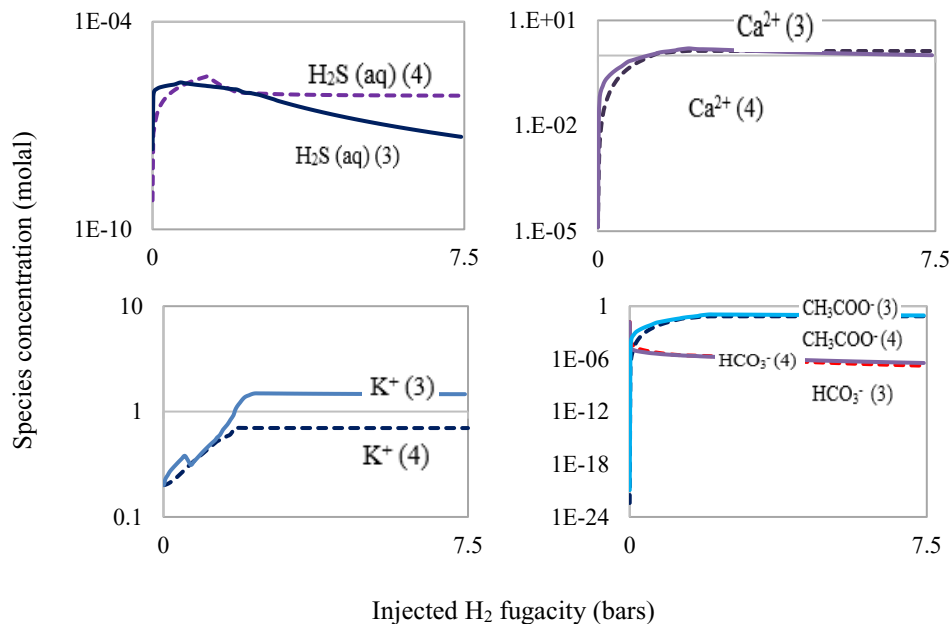


Figure 4-6 Major changes in aqueous chemical composition as function of injected gas fugacity (results based on initial system from case study 3 and 4 are depicted as solid lines (3) and dashed lines (4), respectively)

The findings from the equilibrium batch models indicate that potential redox couples can play a big role in the consumption of hydrogen and increases in pH. However, the likelihood of their occurrence within hydrogen storage time cycles needs further investigation. Defining

the rates of redox reactions in the presence of hydrogen requires laboratory data which are not yet widely existing within the various range of temperatures and hydrogen partial pressures. However, there are valuable experimental data for higher ranges of temperatures in presence of hydrogen (e.g. aqueous sulfate reduction by H₂ at 250-300°C under 4-16 bars H₂ partial pressure (Truche et al., 2009), nitrate reduction in the presence of H₂ and specific catalyst (stainless steel 316L and Hastelloy C276) at 90-150°C under 0-10 bars H₂ partial pressure (Truche et al., 2013), pyrite reduction into pyrrhotite at temperatures higher than 90°C and under pressures higher than 10 bars H₂ partial pressure pressures (Truche et al., 2010), and carbonates reduction (Berndt et al., 1996; McCollom and Seewald, 2001). Many redox couples are unlikely to reach equilibrium. Nordstrom (2000) states that redox disequilibrium is the rule and that many redox species in water will not attain an equilibrium state freely. The main redox couples contributing to the consumption of hydrogen are identified as CH₄-HCO₃⁻, HS⁻-SO₄²⁻, and CH₄-CH₃COO⁻. The CH₄-CH₃COO⁻ redox couple seems irrelevant in the model as a very high formation of acetate is unreasonable (Seewald et al., 2006; Truche et al., 2010). In the presented equilibrium model, this redox pair was decoupled. There are some data available indicating that H₂-induced redox reactions (pyrite reduction and the precipitation of pyrrhotite) can be substantial at low temperatures (Hall, 1986; Betelu *et al.*, 2012; Truche *et al.*, 2013). As the kinetic rates for the reactions of acetate/bicarbonate and methane/bicarbonate redox pairs are not reported in the literature, in the kinetic batch models, these redox pairs are decoupled. Assuming an equilibrium for the HS⁻/SO₄²⁻ redox pair may be more relevant for the reaction of pyrite-pyrrhotite, however, previous studies show at the low temperature of the studied system this reaction must be decoupled as well (Kiyosu and Krouse 1993; Cross, et al. 2004; Truche et al., 2009). As decoupling of the HS⁻/SO₄²⁻ redox pair requires additional constraints, we have made disequilibrium assumption by adjusting the kinetic redox reaction with a negligible rate constant to this redox pair reaction to allow the pyrite-pyrrhotite reaction. The decoupling reaction among these redox pairs lessens the disturbance of the pH state; likewise, a higher amount of H₂ stayed in the gas phase.

4.3.2 Primary kinetic batch model

Quantification of the chemical interactions related to a storage cycle requires a kinetic approach. Compared to equilibrium models, accurate kinetic data are scarce and are difficult to acquire, especially for complex systems as in the present case. A hydrogen storage cycle is typically limited to seasons – less than one year. Many of the mineral reactions occurring in equilibrium batch models would not occur on those relatively short timescales. Therefore, to understand what is more likely to occur within a hydrogen storage cycle, the integration of mineral reaction rates (listed in Table 4-5) was essential. Kinetic modelling indicates how fast

the system reacts to a perturbation of its geochemical equilibrium state. In this section, we only show the results of the kinetic models based on the initial system of case study 3, which we consider to be the most relevant. In the batch kinetic simulation, a typical cycle of hydrogen injection (we assume 12 months) with hydrogen partial pressure of 7.5 bar was considered. In the primary kinetic batch model, the mineral kinetic reaction rates were integrated in the model, while hydrogen dissolution in brine was assumed to be instantaneous.

Variations in pH and changes of mineral quantities in contact with hydrogen are displayed in Figure 4-7. A minor pH increase is observed; likewise, changes in mineral quantities, which proceed extremely slowly, are only notable for primary minerals; none of the secondary minerals were formed in this case. As it was discussed earlier two models were tested for pyrrhotite reaction rate; in one the rate constant is set to be the same as pyrite reaction rate and in the other reactions of pyrrhotite assumed to be at equilibrium. The results did not show any significant difference.

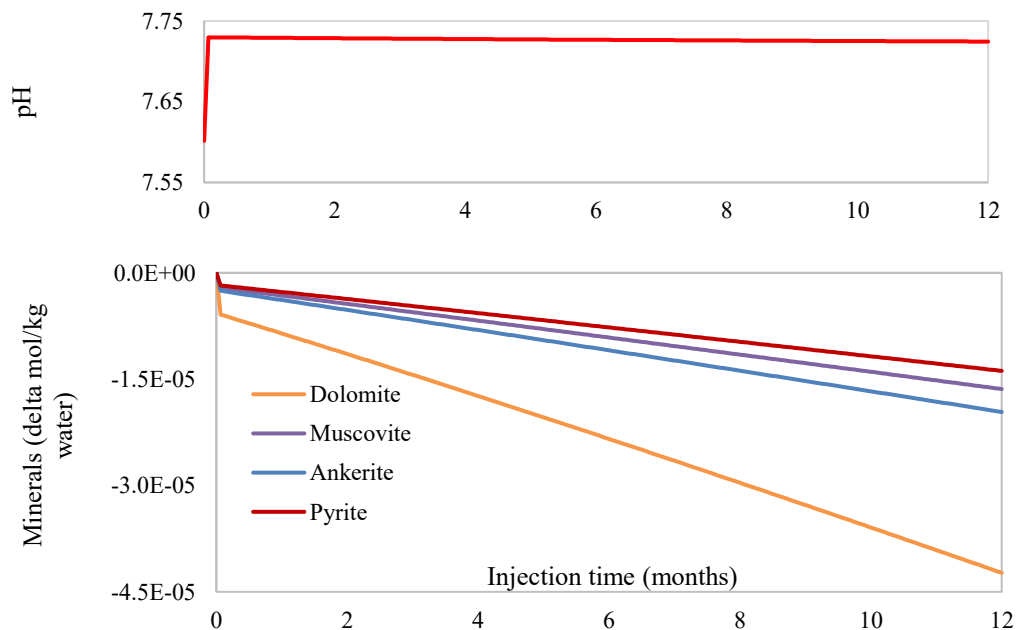


Figure 4-7 Variation in pH (top panel) and mineral abundance change (bottom panel) within one year of injection at an H_2 partial pressure of 7.5 bar (primary batch kinetic model based on initial system in case study 3).

In the next model calcite was excluded from the secondary minerals and a kinetic rate was assigned to the redox pair of HS^-/SO_4^{2-} . For this model, we implemented a zeroth order equation with rate constants ranging from $5E^{-9}$ mol/s (Berta, et al., 2018) to $5E^{-20}$ mol/s (considering slower rate constant for abiotic reactions). Only for rate constants lower than $1E^{-12}$ did our kinetic simulations converge and produce meaningful results. The kinetic rate of $1E^{-12}$ leads to the same results as what is already depicted in Figure 4-7. Moreover, for the rate constant of $1E^{-20}$ and decoupling, no pH increase observed, still the minerals change shows the same change

illustrated in Figure 4-7. As it has been discussed in the previous chapter, the major uncertainties in the kinetic model results are the assigned reaction rates, which are taken from laboratory experiments. These experiments are generally performed in the absence of a hydrogen partial pressure. Truche *et al.* (2013) state that abiotic hydrogen redox reactivity is kinetically restricted and that many of the potentially hydrogen-induced redox reactions (e.g., sulfate and carbonate reduction) stay insignificant at low temperatures. However, there could be exceptions: a reduction of pyrite into pyrrhotite is one such possible exception. pH controls the extent of the reaction through alkaline conditions, which may promote pyrrhotite precipitation at lower temperatures and low hydrogen partial pressures. For these reasons, we ran another case study in which reactions of pyrite and pyrrhotite were considered at equilibrium. In this model, primary minerals and pyrrhotite alter the most during one year of hydrogen injection (Figure 4-8).

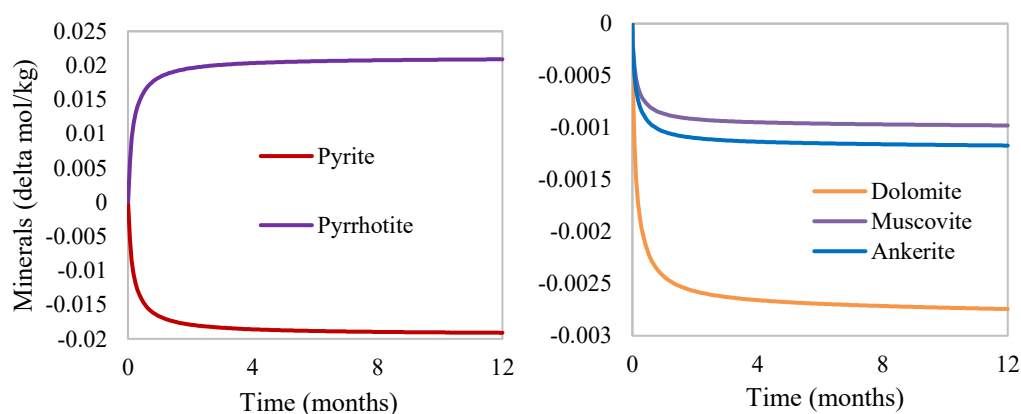


Figure 4-8 Mineral abundance change within one year of injection at an H_2 partial pressure of 7.5 bar (primary batch kinetic model based on initial system of case study 3 and assuming reactions of pyrite and pyrrhotite are at equilibrium).

Mineral reactions proceed faster than in the previous case, and although the changes are still minor, the pH increase is high and can be problematic (Figure 4-9).

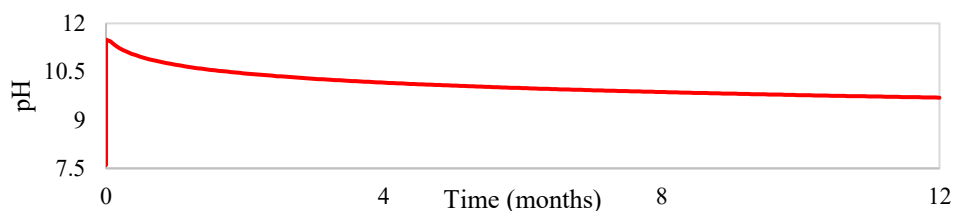


Figure 4-9 Variation in pH (primary batch kinetic model based on initial system of case study 3 and assuming reactions of pyrite and pyrrhotite are at equilibrium).

Despite the uncertainty in the equilibrium assumption for reactions of pyrite and pyrrhotite, this case study represents more realistic and reliable outcomes as these reactions are likely to

occur in the presence of hydrogen. However, experimental data on reaction kinetics in the presence of hydrogen would be desirable and would reduce the uncertainties.

4.3.3 Final kinetic batch model

The equilibrium assumption for hydrogen reactions in brine in the primary kinetic batch model results in a large pH increase that seems implausible in short timescales. In the final model, we consider the most realistic scenario, and we used the implemented gas transfer option to account for the hydrogen kinetic reaction rate. The equilibrium assumption for pyrite and pyrrhotite reactions is valid in this model. Literature data on hydrogen gas dissolution kinetics are not available, and we, therefore, defined three categories for kinetic parameters to account for slow, moderate, and fast reactions. Here, the presented terminologies as slow, moderate and high rates (shown in Table 4-7) serve as rough estimates for the speed of reactions in the presence of hydrogen in a typical storage cycle (12 months) with the operational hydrogen partial pressure of 7.5 bars. These values are determined based on numerous simulations performed to determine the impact of kinetic rate on the pH rise for this particular model. It should be noted that these values are approximations based on simulations in our specific case study and may not be generalised. Varying the kinetic rate-controlling parameters classifies scenarios that can possibly occur in our reservoir. The gas transfer is a rate expression option that describes the dissolution of gases from an external reservoir. The rate r_k^{\rightarrow} (mol/s) at which a kinetic gas dissolves into the fluid is calculated via the built-in equation:

$$r_k^{\rightarrow} = n_w A_{sp} k_+ (f_{ext} - f_{k^{\rightarrow}}) \quad (5)$$

n_w accounts for the solvent mass (kg), k_+ is the rate constant (mol/cm² sec), A_{sp} is the specific contact area (cm²/kg water) between the reservoir and fluid, and f_{ext} and $f_{k^{\rightarrow}}$ are the external and in-fluid gas fugacity. For convenience, we defined a new variable α (mol/kg water sec), which is the product of A_{sp} and k_+ .

The results of the selected case study (α [mol/(kg(water)s)]: 1e-7; injected H₂ fugacity: 7.5 bar; time span: 1 year) are shown below. This case study accounts for quite a high reaction rate of hydrogen. Compared to the primary kinetic model, assigning a kinetic rate for hydrogen solubility controls the increase of pH in the system (Figure 4-10).

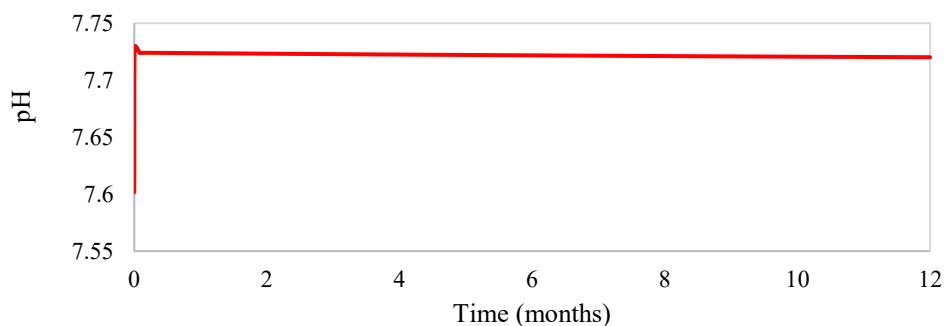


Figure 4-10 The evolution of pH as a consequence of hydrogen injection within 1 year (obtained from the final kinetic model; A_{sp} specific contact area ($\text{cm}^2/\text{kg water}$):1; Rate constant ($\text{mol}/(\text{cm}^2\text{s})$): $1\text{e-}7$; injected H_2 fugacity: 7.5 bar).

Minerals abundance change is negligible and at a lower amount compared to the previous case (Figure 4-11).

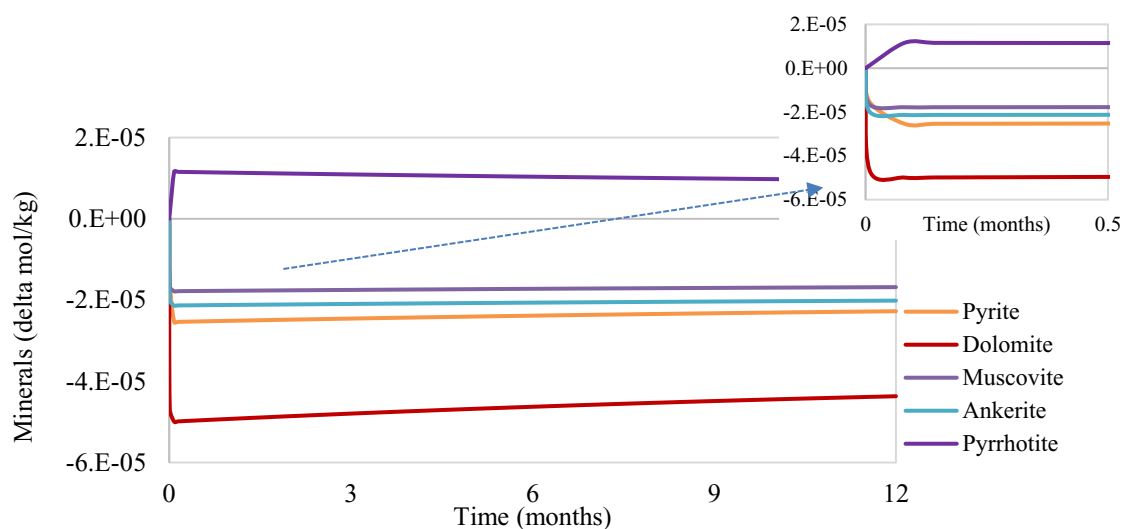


Figure 4-11 Mineral abundance changes (obtained from final kinetic model; A_{sp} specific contact area ($\text{cm}^2/\text{kg water}$):1; Rate constant ($\text{mol}/(\text{cm}^2\text{s})$): $1\text{e-}7$; injected H_2 fugacity: 7.5 bar)

The effect of the H_2 dissolution rate on the pH increase is tested within one year of hydrogen injection. Furthermore, the influence of redox pair equilibrium is investigated for the different models (Table 4-7).

Table 4-7 Sensitivity analysis of kinetic rate-controlling parameters for hydrogen reactions; three rate constants (high, moderate and slow) are tested with variations of specific contact area and external H_2 fugacity (after 12 months with fugacity of 7.5 bars).

Case	α (mol/(kg water s))	pH increase	
		Disabling redox pairs and formation of CH_4	Assuming equilibrium for redox couples
High H_2 kinetic rate	1E-07	0.1148	3.67
Moderate H_2 kinetic rate	1E-10	0.1148	2.88
Low H_2 kinetic rate	1E-13	0.0191	0.0039

In the case of assuming disequilibrium for redox pairs, when the hydrogen reaction rate remains relatively low, the pH increase is minor, and hydrogen gas acts like an inert gas in the system. This is valid for the case where the equilibrium assumption is considered for redox pairs. In the cases of the moderate and high hydrogen rate constants, a higher increase in pH is observed; however, this amount remains insignificant. It is worth noting that the changes in mineral abundances in all cases are negligible. The equilibrium assumption for redox pairs in these cases triggers hydrogen consumption and results in the considerable pH increase.

4.4 Summary and Conclusions

In this paper, a geochemical modelling workflow is presented to study and quantify potential geochemical processes that can lead to hydrogen loss in a hydrogen storage site in the Molasse Basin, Upper Austria. The processes were investigated by equilibrium and kinetic batch models at constant pressure and temperature. The modelling methodology considers site-specific mineralogy, mineral reaction rates obtained from the literature and coupling to fast equilibrium processes, such as aqueous speciation reactions. To investigate the short- and long-term impacts of hydrogen on the reservoir, various batch geochemical scenarios were modelled.

In the first stage, all possible reactions within phases were identified by imposing an equilibrium assumption for hydrogen-brine-mineral reactions. The model outcomes indicate that hydrogen can considerably influence the integrity of the reservoir. Giving enough time for all reactions to occur (e.g., carbonate dissolution/precipitation, redox reactions and aqueous speciation) results in a substantial pH increase. The CH_4 - HCO_3^- , HS^- - SO_4^{2-} , and CH_4 - CH_3COO^- redox couples are the main sinks for hydrogen consumption in the system. Furthermore, the presence of H_2 in this system affects the thermodynamic stability of pyrite and the redox reaction in which pyrite is reduced to pyrrhotite.

In the following stage, the kinetic rates parameters for the primary and secondary minerals were included in the primary kinetic model. The $\text{CH}_4\text{-HCO}_3^-$ and $\text{CH}_4\text{-CH}_3\text{COO}^-$ redox couples are decoupled to approach realistic conditions. The results indicate that geochemical reactions of H_2 with minerals are generally slow kinetic rates obtained from literature. Apart from few studies (Betelu, et al., 2012; Truche, et al., 2010), the kinetic parameters are generally derived in absence of a hydrogen gas phase or at very high temperatures which it is not applicable to this study; thus, uncertainty with regards to these rates are considered. A case study in which reactions of pyrite-pyrrhotite are considered at equilibrium estimated which of the revealed hydrogen reactions with these minerals are fast enough to effectively increase pH in the system. The latter model is most relevant to the application of underground hydrogen storage.

Finally, hydrogen dissolution kinetics were added to the model. The dissolution kinetic rate is based on a typical storage cycle (12 months) and operational hydrogen partial pressure of 7.5 bars which is derived from many simulation for this specific case study. Owing to a lack of data for kinetic hydrogen dissolution reactions in the literature, we defined several scenarios to understand under which conditions the likelihood of hydrogen loss is considerable. We further compared the same models to cases in which the reactions of redox couples remained at equilibrium. When applying assumptions of both disequilibrium and equilibrium for reactions of redox couples, when the hydrogen reaction rate remains low, the pH increase is minor, and hydrogen behaves like an inert gas. In the case of moderate to high hydrogen rate constants, a higher increase in pH is observed; however, this amount remains insignificant when assuming disequilibrium for redox couple reactions and is substantial in the case of the equilibrium assumption for these reactions.

From the modelling results, we conclude that the main reason for an increase in pH and consequently hydrogen loss is the equilibrium assumption among redox pairs and the pyrite reduction to pyrrhotite. The question of whether local equilibrium for redox pairs is a reasonable assumption must be addressed using the appropriate data, which requires further experimental investigation. The abiotic hydrogen redox reactivity is kinetically restricted, and many of the potential hydrogen-induced redox reactions tend to stay negligible at low temperatures. The exception for H_2 -induced redox reactions is pyrite reduction into pyrrhotite, which can be significant at low-temperature conditions. Alkaline pH conditions may further promote pyrrhotite precipitation. Quantifying how much hydrogen will be lost due to geochemical reactions is out of the scope of this work.

Considering the full range of uncertainty mainly caused by the lack of reliable kinetic data, the risk of hydrogen loss and the disturbance of reservoir integrity associated with geochemical interactions with hydrogen cannot generally be ruled out. The potential risk of hydrogen loss

increases when redox couple reactions are assumed to be at equilibrium. The reaction rates incorporated in this work that were obtained from literature data are mainly derived from laboratory experiments. It is important to note that field-scale reaction rates are often orders of magnitude lower than laboratory values. Consequently, we expect more moderate results in terms of disturbance in field applications than those observed in the simulations – this study is a conservative risk assessment. It should also be noted that the present simulation results are site-specific; therefore, particular consideration should be paid when extrapolating the outcomes and conclusions to other storage sites”.

Acknowledgement

We would like to express our gratitude to the sponsoring agencies, the Austrian Research Promotion Agency (FFG) and “Klima- und Energiefonds”. We would like to thank RAG (Rohöl-Aufsuchungs Aktiengesellschaft) for providing the field data used in this study. Furthermore, we would like to thank the GWB support team for their helpful comments and feedback to our questions. We would like to thank the two reviewers, Dr Laurent Truche and the second anonymous reviewer for their insightful comments that remarkably improved the manuscript.”

Chapter 5 A literature review to bacterial growth and transport

Understanding the extent of microbial growth, transport, distribution, and activity in subsurface environments is vital for a variety of biotechnological applications. This part of the study was inspired by the outcomes of the “Underground Sun Storage” project and the ongoing “Underground Sun Conversion” project. One of the main findings of the first project was the microbial activities that resulted in the partial consumption of hydrogen. It turned out the microbial activities have a more significant impact on the storage formation in terms of hydrogen consumption and conversion than geochemical and transport (diffusion) processes. The microbial metabolism promoted by the injected hydrogen and carbon dioxide can turn to be a positive consequence as the product of such metabolism is methane, which is also aligned with the concept of PtG technology.

This chapter discusses some fundamental concepts in microbiology. In addition, microbial enhanced oil recovery, clogging types, factors affecting the growth and transport of bacteria, and bacterial and colloid transport formulations and their limitations are discussed. The majority of the content in this chapter assists in better understating the study presented in the following chapter, where the experimental and numerical analysis of bacterial transport and growth are described, and preliminary results to tracing experiments are discussed.

Lastly, some of the discussed concepts in this chapter are rather future-oriented and are partially relevant to the experimental and numerical study in chapter 6. Specifically, the addressed content on the bacterial and colloidal formulations and limitations are relevant where processes such as attachment, detachment, filtration, and microbial inactivation or death are intended to be modelled numerically.

5.1 Introduction and literature review

Even though the primary focus of this work was on the *in-situ* microbial activities in the context of hydrogen storage and conversion, the extensive literature on other microbial related processes is given, which applies to the mentioned matter.

In the subsurface, there are vast regions that may be inhabited by microorganisms. The majority of the terrestrial subsurface environments are inaccessible and remote. Due to this fact, many severe environmental problems (such as toxic waste dumps and urban landfills) have occurred, which ultimately cost billions of dollars to rectify (Ghiorse & Wilson, 1988; Christensen, et al., 1994). Understanding the biological activities in the subsurface environment is essential to control the associated issues to groundwater pollution; in addition, subsurface biological activities elevated the hope for cleaning up polluted aquifers (McNabb & Dunlap, 1975; Freeze & Cherry, 1979; Lovley, 2003).

Aquifers and subsurface water resources are vital components in human life and many industrial processes. For decades, groundwater has been the most significant source of drinking water. Since the 1980s, awareness of groundwater microbiology has raised (Kolbel-Boelke, et al., 1988). Due to the high specific surface area of aquifer porous media, most bacteria are attached to the soil solids and potentially make biofilm. The bacteria and biofilm formation in many applications such as contaminates biodegradation, water waste disposal, and the bioclogging of porous media have received particular attention, primarily when water injection stimulates microbial activities (Raleigh & Flock, 1965; Oberdorfer & Peterson, 1985; Rittmann, 1993; Sugai, et al., 2013).

Subsurface microbial activities have similarly received attention in energy storage and oil and gas-related practices. Researchers have investigated oil and gas reservoirs' microbial ecology for various applications such as reservoir specific treatment that intend to use the microbial populations for beneficial purposes such as microbial oil recovery (MEOR), whereas inhibiting those known to be unfavorable (Jang, et al., 1984; Bryant & Douglas, 1988; Bryant, et al., 1990; Paulsen, et al., 1999; Emadi, et al., 2011; Afrapoli, et al., 2012; Kryachko, 2018; Halim, et al., 2015; Halim, et al., 2017; Sivasankar & Suresh Kumar, 2019). Additionally, in recent years, power-to-gas (PtG) technology is thought to be one of the practical solutions for the storage of large quantities of renewable energies. PtG aims to transform renewable electric energy via electrolysis and methanation of H₂/CO₂ mixtures by microorganisms (Archaea) in the underground (Götz, et al., 2016).

Solute transport, water flow, and microbial interactions may be coupled in porous media and can result in a change in the physical, chemical, and microbial properties of porous media

over time (Vandevivere & Baveye, 1992). These activities may cause gas production as by-products of reactions, or biomass production and resulting bioclogging. Bioclogging refers to the capacity of microorganisms to decrease the hydraulic conductivity of a saturated porous media (Baveye, et al., 1998). Bioclogging has both beneficial and unfavorable aspects. It could be favorable in situations in which thief zones, high permeable regions, are blocked to avoid the bypass of hydrocarbon in low permeable zones. This matter is particularly crucial in water flooding of petroleum reservoirs (Updegraff, 1983; Knapp, et al., 1993). Negative sides of Bioclogging have been observed in applications such as difficulties reported in the disposal of wastes of various components due to hydraulic conductivity reduction (Allison, 1947; Rajinder & Swartzendruber, 1962; Seki, et al., 1996; Baveye, et al., 1998). Bioclogging around the wellbore areas may also affect the injectivity of wells. This can negatively impact operations such as MEOR and underground energy storage.

Understanding the mechanisms associated with biomass growth, propagation, and bioclogging plug development is required for any technology and application related to microorganisms' activities in the pore space. The microfluidic experiments allow for the direct observation and imaging of microbial growth under the desired conditions with a high spatial and temporal resolution by means of optical microscopy. Numerous researchers have been studied the transport and growth of microorganisms through saturated and unsaturated pore networks for various applications using microfluidics (Wan, et al., 1994; Stewart & Fogler, 2001; Sirivithayapakorn & Keller, 2003; Nambi, et al., 2003; Crescente, et al., 2006; Zhu, et al., 2015; Armstrong & Wildenschild, 2012).

Microbial Enhanced Oil Recovery (MEOR)

Water injection to increase oil recovery has been applied for decades. As bacteria are naturally present in the water, they can adhere to available surfaces and produce biofilms (Cusack, et al., 1987). MEOR is one of the tertiary recovery mechanisms that refers to the use of microorganisms in oil-bearing formation to produce *in-situ* metabolic products or nutrients that stimulate indigenous microbes (Rudyk & Sogaard, 2011). Though the technology is not entirely new (Bryant & Douglas, 1988; Bryant, et al., 1990; Updegraff & Wren, 1954; Zobell, 1946; Raiders, et al., 1989), not much is known about the actual microbial processes in pore space. The use of microorganisms to promote oil recovery from underground formations initially proposed in 1926 by Beckman. Though, the first practical aspect of MEOR was revealed in the 1940s by the work of Zobell (Jack, 1993; Brown, 2010).

While general purposes of MEOR include an increase in oil production, a decrease in the water cut, and extend the productive life of the oilfield, microorganisms can enhance the oil recovery in other ways (Rudyk & Sogaard, 2011; Patel, et al., 2015). They can reduce the

paraffin build-up in producing wells; they can create bio-solvents or bio-polymers for pumping into the oil-bearing formations as it is done in other EOR processes, as well they can reduce sulfur corrosion in sour fields (Brown, 2010; Rudyk & Sogaard, 2011). Another aspect of MEOR is bacterial selective plugging that is suggested to modify the microscopic and volumetric efficiencies of the reservoir. Bacterial at the exponential phase of their growth life can considerably plug the high permeable zones and increase the oil recovery in other zones (Patel, et al., 2015). A summary of microorganisms' types and their beneficial activities and products related to MEOR application are listed in Table 5-1.

Table 5-1 Microbial activities, products and action mechanism beneficial regarding MEOR application [adapted from (Youssef, et al., 2009)].

Microbial products	Type of microorganisms	Action mechanisms
Hydrocarbon metabolism activity	Aerobic hydrocarbon degraders	Remove paraffin deposits; Metabolites mobilize oil
Gases (CO₂, CH₄)	Fermentative and methanogens bacteria	Reduction in oil viscosity & improve flow characteristics
Acids	Fermentative bacteria	Minerals and deposits dissolution Significant improvement of permeability and porosity
Solvents	Fermentative bacteria	Dissolve and remove heavy and long-chain hydrocarbons from pore throat; Alteration of wettability
Emulsifiers	Acinetobacter sp., Candida, Pseudomonas sp., Bacillus sp.	Emulsify oil to form o/w emulsions (or less commonly w/o emulsions)
Biosurfactants	Bacillus sp., Pseudomonads, Rhodococcus sp.	Lower interfacial Tension
Biomass	Many kinds	Plug high permeability zones and decrease permeability in water-swept regions by biomass formation
Biopolymer	Many kinds	Improve water viscosity in water flooding Plug high permeability zones or water-invaded zones (improve water flooding recovery)

MEOR technique can apply to a flooding operation or single-well treatments; the method is called huff-and-puff. A single-well treatment, alternatively, is a more effective practice and refers to conditions, in which the bacteria and nutrients are injected in the single well. The well

is then shut-in for a while to permit the bacteria to disperse deeply into the reservoir and, consequently, for better interaction between metabolic products and oil. A higher shut-in period leads to higher colonization and deeper infiltration of bacteria into the distant parts of the oil layer (Rudyk & Søgaaard, 2011).

Although MEOR processes have been practiced to enhance oil recovery, many operations encountered challenges. Many of the MEOR processes, in particular, those that involved an injection of the microorganisms into the reservoir faced well-plugging, or they were challenged by corrosion problems due to hydrogen sulfide production (Brown, 2010; Bachmann, et al., 2014). Bioplugging is not only happened due to the injected bacteria themselves but also due to the by-products of their metabolism, such as ferric hydroxide (Brown, 2010). The pore size distribution is a vital parameter when it comes to plugging. To avoid serious plugging issues, the pore entry diameter must be at least two times larger than the diameter of the microbial cells (Davis & Updegraff, 1954).

5.2 Microbial growth, biofilm formation, and clogging

Influence of Environmental Factors on Microbial Growth

The chemical and physical nature of the contiguous environment of the microorganisms affects the growth of them. The main physical factors that influence microbial growth are temperature, pressure, oxygen level, pH, and solutes, and water activity (Prescott, et al., 2002).

Temperature

Environmental temperature has a profound influence on the lifetime of bacteria to remain viable in soil and water. The most substantial element underlining the effect of temperature on the growth of the microorganisms is the enzyme-catalyzed reactions' temperature sensitivity (Prescott, et al., 2002). Microorganisms have distinct cardinal temperatures, the minimum and maximum temperatures that define growth and development limits of an organism, and an optimum temperature at which growth happens at the highest speed. The cardinal temperatures differ significantly for numerous microorganisms. The optimum temperature may range from 0°C to 75°C, while microbial growth lies from temperatures as low as -20°C to over 100°C (Prescott, et al., 2002). Table 5-2 displays the five classes of microorganisms based on their temperature ranges.

Table 5-2 Classification of microorganisms according to the temperature ranges for microbial growth (Prescott, et al., 2002).

Psychrophiles	“Can grow well at 0°C, the optimum growth temperature of 15°C or lower; the maximum is around 20°C”
Psychrotrophs	“Grow at 0 –7°C; optimum growth between 20 and 30°C and a maximum of about 35°C”
Mesophiles	“Have a temperature minimum of 15 to 20°C. Their maximum is around 45°C or lower. Have growth optimum around 20–45°C”
Thermophiles	“Can grow at 55°C or higher; optimum growth often between 55 and 65°C and their growth minimum is usually around 45°C”
Hyperthermophiles	“Can grow at 90°C or above; some even have maxima above 100°C. Have an optimum between 80 and about 113°C”

Pressure

The majority of microorganisms live on land or the surface of the water, therefore exposed to the atmospheric pressure (1atm); hence, they are never affected considerably by pressure (Prescott, et al., 2002). Yet, in the deep sea, the hydrostatic pressure can reach up to 1,100 atm, while the temperature is around 2 to 3°C. Despite the extreme conditions, bacteria survive and adapt. Microorganisms are divided in their behavior towards pressure to barotolerant and barophilic. Barotolerant types of microorganisms affected adversely by a pressure increase. Barophilic microorganisms, on the other hand, grow more rapidly at high pressures (Prescott, et al., 2002).

Oxygen Concentration

Organisms are categorized depending on their growth ability in the presence of oxygen. Aerobe microorganisms can grow in the presence of atmospheric O₂, whereas anaerobe microorganisms can grow in its absence. Obligate aerobes referred to all multicellular organisms that are entirely dependent on atmospheric oxygen for growth. Facultative anaerobes correspond to the organisms that do not need oxygen to grow but do grow better when O₂ presents. Aerotolerant anaerobes ignore the presence of oxygen and can grow similarly well whether oxygen is present or not. On the contrary, strict or obligate anaerobes cannot tolerate oxygen at all and die in the presence of it. Microaerophiles require O₂ levels less the range of 2 to 10% for their growth (Prescott, et al., 2002).

pH

Environmental pH strongly affects microbial growth. Different microbial groups have a definite pH growth range, as well as, pH growth optimum. For *Acidophiles* the growth optimum lies between pH 0 and 5.5; *neutrophiles* have the optimum growth at pH from 5.5 and 8.0, and *alkalophiles* favor the pH range of 8.5 to 11.5. Finally, the extreme alkalophiles have growth optimum at pH 10 or higher (Prescott, et al., 2002).

Water Activity and Solutes

Microorganisms are influenced by the osmotic concentration variation in their environment. This is due to the selectively permeable plasma membrane that splits microorganisms from their surroundings. Microorganisms in a hypotonic solution (a solution with a lower osmotic concentration) are vulnerable to adsorb water in their cell and burst, except when other causes prevent the influx (Prescott, et al., 2002).

Most bacteria have rigid cell walls that preserve the shape and integrity of the cell. The plasmolysis process refers to a condition in which the microorganisms with rigid cell walls exposed to a hypertonic environment, and water leaves their cells, and the plasma membrane shrinks. This process leads to cell dehydration and plasma membrane damage, which subsequently results in metabolically inactive cells (Prescott, et al., 2002).

The interaction of microorganisms with solute molecules (the osmotic effect) or the adsorption of them to the surfaces of solids (the matric effect) reduce the water availability to the microorganisms. Water availability expressed as water activity (a_w), is a terminology defined commonly by microbiologists. The water activity is described as the ratio of the solution's vapor pressure (P_{solution}) to the pure water vapor pressure (P_{water}) (Prescott, et al., 2002):

$$a_w = \frac{P_{\text{solution}}}{P_{\text{water}}}$$

To measure the water activity of a solution or solid, the sample is sealed in a chamber, and the relative humidity after the system attains the equilibrium is measured. Different microorganisms have a wide range of tolerance to adapt to environments with low water activity. When the habitat of the microorganisms has a low a_w value, the microorganisms require extra effort to grow, as they must preserve a high internal solute concentration to keep water. Osmotolerant microorganisms can grow over wide ranges of water activity or osmotic concentration. Microorganisms that are truly osmotolerant are limited, and most of them can only grow well at water activities around 0.98 or higher. Food protection from microbial spoilage by drying or salt or sugar usage is also due to this fact (Prescott, et al., 2002).

Biofilm development

The microbial settings are complex and prone to change continuously. Microorganisms in different locations are exposed to overlapping nutritional gradients as well as other environmental factors. Microorganisms continue growing until nutritional or ecological factors limit their growth. **Liebig's law of the minimum** states in environments where multiple nutrients are in relatively low concentrations, only one nutrient (most growth-limiting nutrient) affects the organism's growth. This means that most growth-limiting nutrient dictates the

evolutionary population growth (Warsi & Dykhuizen, 2017). If a particular nutrient is a limiting one, other nutrients' change, will not affect the biomass growth.

Moreover, there are limits to the environmental factors that are out of a specific range; microorganisms cannot survive and grow, irrespective of the nutrient supply. This is the principle of **Shelford's law of tolerance** (Shelford, 1931). For instance, any microorganism has a particular temperature range that it can grow, above or below this range microorganism cannot grow. Other parameters, such as pH, oxygen level, and hydrostatic pressure in the marine environment obey the same rule. In general, microorganism's growth depends on both the nutrient supply and their tolerance of the environmental conditions (Prescott, et al., 2002).

Bacteria are frequently studied planktonically (free-living organisms that float or drift in liquid) in the laboratory as pure cultures. Commonly, in natural settings, bacteria do not grow as single cultures but interact with other bacteria and produce some complex physical assemblages, typically termed as biofilms (Prescott, et al., 2002). Bacterial biofilms form microcolonies on the surfaces (e.g., liquid, gas, or solid surfaces); within these microcolonies, bacteria develop communities with functional heterogeneity (Costerton, et al., 1999; Watnick & Kolter, 2000). Biofilms are principally composed of microbial cells and extracellular polymeric substances (EPS). EPS is composed mainly of polysaccharides and may differ in chemical and physical properties. EPS is highly hydrated as it includes significant amounts of water into its structure by hydrogen bonding. EPS could be hydrophobic, though most sorts of EPS are both hydrophilic and hydrophobic (Donlan, 2002).

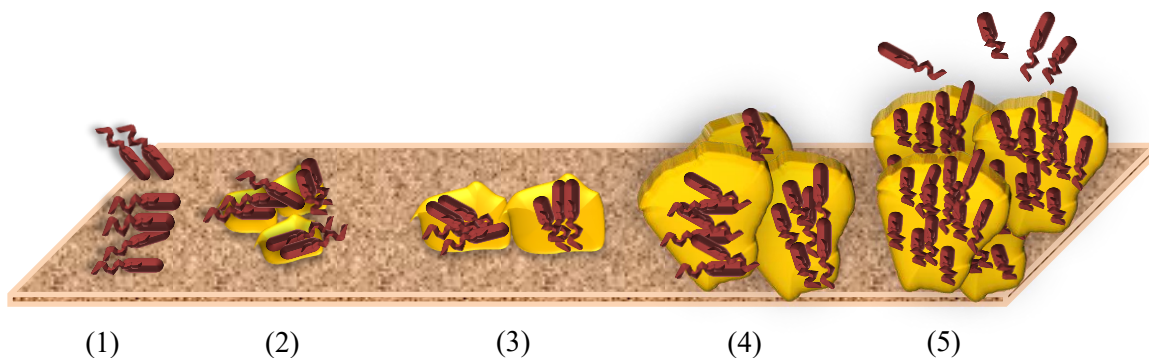


Figure 5-1 The five steps of biofilm development. (1): The initial (reversible) attachment phase of biofilm, in which the Planktonic bacteria adhere to the solid surface. (2): Irreversible attachment of bacteria to the surface, (3): maturation phase I, where the biofilm is formed and matured. (4): Maturation phase II, in which maturation of the biofilm is continued, and it protects the host defense mechanism. (5): Dispersal phase due to the shedding of daughter cells from actively growing cells or removal of biofilm aggregates because of flow effects, in which biofilm reaches a critical mass and diffuses planktonic bacteria that are ready to colonize other surfaces [adapted from (Kostakioti, et al., 2013)].

The formation of biofilm on the surface is a complex phenomenon and consists of multiple events that often occur concurrently. The evolution of bacterial aggregations and subsequent biofilms consist of reversible and irreversible stages. These stages are an initial attachment to a solid surface, irreversible attachment, maturation I, maturation II, and dispersal (see Figure 5-1). The first step is the initial attachment of bacteria to a surface, a process that influenced by substratum, hydrodynamic forces, and characteristics of the medium (Donlan, 2002; Kostakioti, et al., 2013).

The solid surface characteristics play an essential role in the attachment process. As the surface roughness increases, the microbial colonization level increases. Theoretically, the flow velocity adjacent to the substratum/liquid interface is negligible (Donlan, 2002). This region is called the hydrodynamic boundary layer. An increase in the velocity results to decrease in the thickness of the boundary layer. In a liquid medium, microorganisms (cells) act as particles. The settling rate is a function of the fluid velocity characteristics. Higher linear velocities employ substantial shear forces on the attached cells, consequently resulting in detachment of these cells. Additional aqueous medium characteristics (e.g., pH, liquid ionic strength, nutrient richness, temperature, etc.) influence the rate of microbial attachment to a substratum (Donlan, 2002).

The initial attachment phase of biofilm is a dynamic and reversible process, during which bacteria can detach and re-join the planktonic population in case of hydrodynamic forces perturbation. Bacteria that can endure the shear forces and maintain a firm hold on the surface make irreversible attachment (Kostakioti, et al., 2013).

During the maturation phase I, the biofilm is formed. The biofilm matures, and cells produce the multi-layered clusters. During the maturation phase II, further maturation of the biofilm is continued, which protects host defense mechanisms and antibiotics. At the dispersal phase, biofilm reaches a critical mass and diffuses planktonic bacteria that are ready to colonize other surfaces. Biofilm cells and aggregates removal and dispersal occur due to the detachment of daughter cells from growing cells, change in nutrient levels, and fluid flow (Donlan, 2002).

Porous media provide bacteria with an attractive habitat. The dynamics of microbial interactions, populations, and transport in porous media offer significant opportunities for improving the industrial and environmental processes. Porous media composed of the tortuous pore-structure that possesses a high specific area. The complex porous systems can provide bacteria with versatile ecological locations of large gradients of many properties, such as nutrient concentrations, ionic strength, pressure, and pH. The individual processes contributing to biofilm accumulation and detachment in porous media are schematically shown in Figure 5-2.

Bioclogging is a significant process in underground porous media and may exert a considerable impact on the hydraulic properties of porous media. The decrease in hydraulic conductivity (K) in porous media is commonly known as Clogging. Clogging or reduction of porosity and permeability of porous media due to biofilm formation in the pore-spaces is one of the severe physical consequences of bacterial activity in such a complex medium. Clogging that result in change in hydraulic conductivity may be due to the biomass growth and polysaccharide production, accumulation of particles, release of gas bubbles, minerals dissolution or formation enhanced by microbial activities, or an increase in the pore channel friction factor (Rinck-Pfeiffer, et al., 2000; Ehrlich, 1996; Vandevivere & Baveye, 1992; Jeong, et al., 2018).

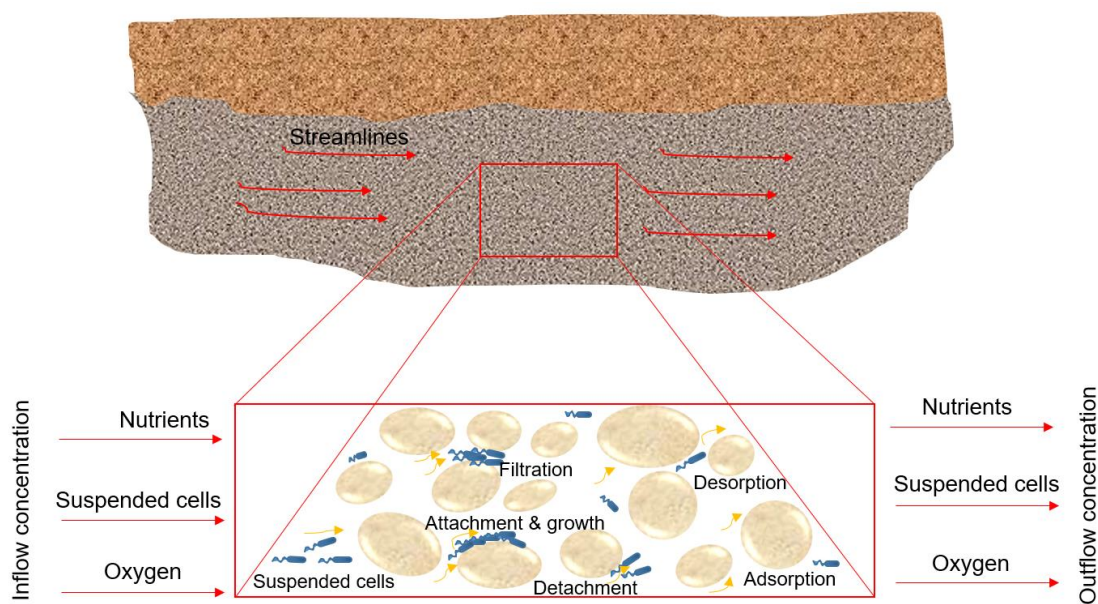


Figure 5-2 The processes contributing to biofilm accumulation and detachment in porous media. Microbial cells in porous media may exist in suspension or may adsorb to solid surfaces. The adsorbed cells grow in favorable environmental conditions. When the adsorption and growth rates of bacterial cells beat the desorption rate, a net accumulation of biomass occurs on the surfaces. The high nutrient loading conditions lead to an increase in the average biofilm thickness, consequently, a decrease in pore space. At the same time, the increase in biofilm thickness results in the average pore velocity. On the other hand, due to biofilm growth, nutrients may be depleted within the biofilm structure. This may also escalate the detachment rate of biofilm. Finally, as the evolution of biofilm thickness reaches a quasi-steady-state, the average biofilm growth rate must be balanced with the net detachment rate. The suspended particles in the fluid may be removed by the attached biomass through filtration processes (e.g., diffusion, interception, and sedimentation) [adapted from (Cunningham, et al., 1997)].

Clogging mechanisms

Clogging processes are essential in many areas. Clogging can impair the injectivity in water flooding projects. It may also reduce the water volume that can infiltrate the aquifer. In wells where the injection rate is constant, clogging may increase the wellhead pressure that can lead to failure of the reservoir formation (Martin, 2013). Underground clogging is classified into the following groups: physical, biological, mechanical, and chemical (Rinck-Pfeiffer, et al., 2000; Martin, 2013). In a survey ran by (Dillon, et al., 1994) for 40 aquifer injection wells, clogging problems occurred in the majority of them (around 80%). This study indicates suspended solids and gas bubbles (physical clogging) caused 70% of clogging, followed by 15% by microbial clogging, 10% by chemical clogging, and 5% by other reasons.

Physical clogging may result from the accumulation of suspended solids in the fluid, migration of fines such as illite or smectite, clay swelling, or invasion of drilling fluid in porous media (Martin, 2013). The second category of clogging induced by biological activities. Subsurface and injected fluids, irrespective of their source, contain some microorganisms. Clogging by microbial growth affects a wide range of systems including the water injection into or out of wells, production and recharge of groundwater, injection of the engineered microorganisms, bioremediation, microbial enhanced oil recovery, also in bioengineering processes such as water purification or bio-metabolite production (Vandevivere, 1995). Bacterial clogging related to injection operation occurs with the bacterial growth in the surface equipment, pumps, tubing, downhole equipment, and in the porous media. Biological growth is related to the amount of carbon and nutrients (Martin, 2013). Entrained air/gas binding causes mechanical clogging. Chemical clogging includes precipitation of elements such as iron or aluminum by geochemical reactions, aquifer matrix dissolution, and temperature (Martin, 2013).

Methanogenesis

Methanogens or methane-producing archaeobacteria metabolize a limited range of substrates, the most important ones being acetate, H₂, and CO₂ (Balch, et al., 1979). In biological methanation, Archaea use CO₂ and H₂ and/or acetate, formate, and methylamine and convert it to methane (Enzmann, et al., 2018). While the archaea bacteria confined to strictly anaerobic environments, they are widely found in nature. Biological methanation occurs naturally in aquatic sediments (such as swamps, lakes, and oceans), digestive systems of animals, landfills, the heartwood of living trees, mid-ocean ridges, oil wells, and other environments (Garcia, et al., 2000; Mand & Metcalf, 2019).

Various groups of microorganisms contribute to the anaerobic degradation of dead organic matter. The degradation proceeds in three steps. Firstly, fermenting bacteria produce some enzymes that hydrolyze organic polymers such as polysaccharides. The subsequent monomers are catabolized to alcohols, fatty acids, and H_2 . Next, the syntrophic bacteria degrade the alcohols and fatty acids to components such as acetate, H_2 , or formate and CO_2 . Finally, methanogens occur by acetate, H_2 , and CO_2 . Homoacetogenic bacteria may catabolize many of the monomers to acetate that later serves as a substrate for acetotrophic methanogens converting it to CH_4 and CO_2 (Conrad, 1999). This process is shown in Figure 5-3.

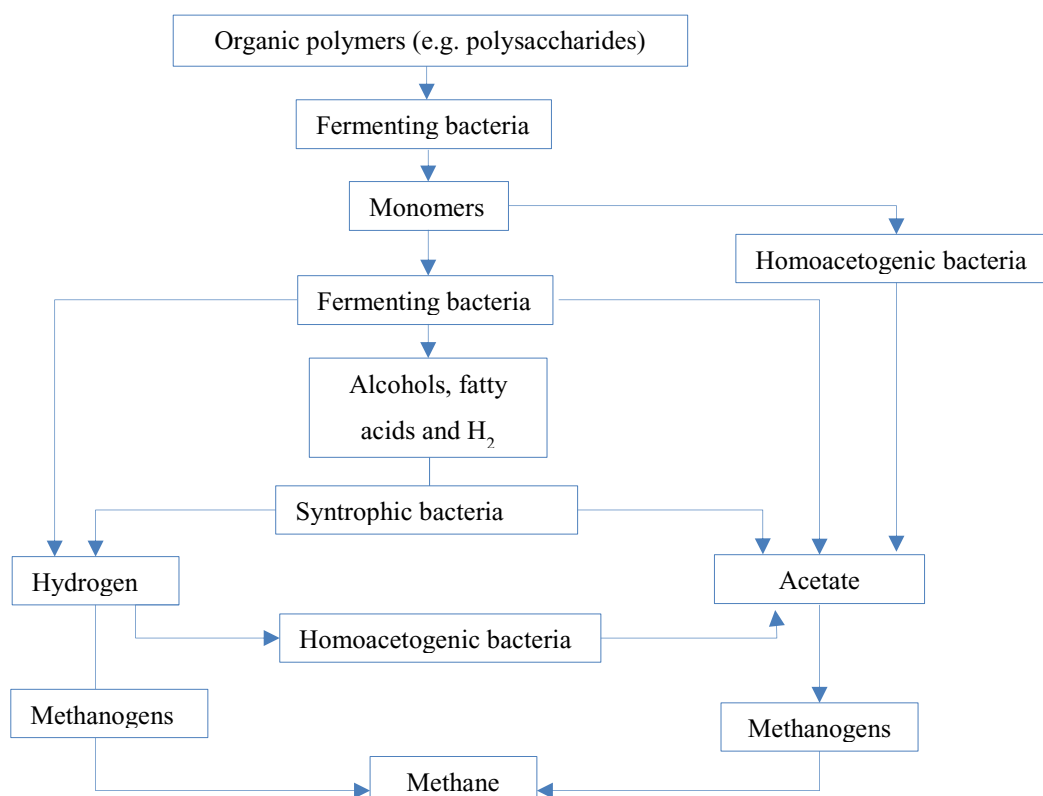


Figure 5-3 Anaerobic degradation workflow of organic matter to methane [adapted from (Conrad, 1999)].

Table 5-3 Some reactions and the standard free energies changes for methanogenesis [adapted from (Garcia, et al., 2000)]. The standard energy change for methanogenesis explains the classification of the methanogens into three nutritional. The most favorable reaction is the oxidation of H_2 and the reduction of CO_2 into methane, and the least favorable is the acetoclastic reaction.

Reaction	ΔG° (KJ/mol CH_4)
$H_2 + CO_2 \Leftrightarrow CH_4 + 2H_2O$	-135.6
Formate $\Leftrightarrow CH_4 + 3CO_2 + 2H_2O$	-130.1
Ethanol + $CO_2 \Leftrightarrow CH_4 + 2$ Acetate	-116.3
Methanol + $H_2 \Leftrightarrow CH_4 + H_2O$	-112.5
Methanol $\Leftrightarrow 3CH_4 + CO_2 + 2H_2O$	-104.9
Methylamine + $2H_2O \Leftrightarrow 3CH_4 + CO_2 + 4NH_4$	-75
Trimethylamine + $6H_2O \Leftrightarrow 9CH_4 + 3CO_2 + 4NH_4$	-74.3
Dimethylsulfide + $2H_2O \Leftrightarrow 3CH_4 + CO_2 + H_2S$	-73.8
Dimethylamine + $2H_2O \Leftrightarrow 3CH_4 + CO_2 + 2NH_4$	-73.2
Propanol + $CO_2 \Leftrightarrow CH_4 + 4$ Acetone + $2H_2O$	-36.5
Acetate $\Leftrightarrow CH_4 + CO_2$	-31

According to (Garcia, et al., 2000) up to now, 83 species of methanogens are recognized that can be subdivided into three main nutritional categories. The first category includes species of hydrogenotrophs that oxidize H_2 and reduce CO_2 to CH_4 and species of formatotrophs that oxidize formate to CH_4 . The second category contains species of methylotrophs that use methyl compounds and species are obligate methylotrophs. The last category includes species of acetoclastic methanogens that use acetate to produce CH_4 , with two species in this group being obligate acetotrophs (Garcia, et al., 2000). The classification of the methanogens into three nutritional groups can be explained by the standard changes in free energies for methanogenesis.

Methanogenesis is a beneficial process in the oil industry. It is the key terminal process of subsurface anaerobic organic-matter degradation. The CO_2 -reducing and acetoclastic methanogenesis are recognized as the two major subsurface methanogenic pathways resulting in the primary and secondary biogenic gas generation (Strapoć, et al., 2011). In Table 5-3, some reactions and the standard free energies changes for methanogenesis are summarized.

5.3 Microbial transport in porous media

There are wide-ranging abiotic and biotic parameters that control microbial transport through porous media. Microorganisms' sorption and straining in soils, vadose zone materials and sediments can be influenced by the physical and chemical factors including pore space characteristics (i.e. sediment type, pore size distribution, clay and organic matter content, and mineralogy), fluid flow rates, solution chemistry (i.e. solute composition, pH, ionic strength and the presence of surfactants). Likewise, biological parameters including the cell physiological state (i.e., cell viability, cell size and shape, and medium's nutritional status), cell surface properties (i.e., charge, hydrophilicity, and exopolymer composition), cell motility, and cell growth phase and decay can influence bacterial transport (Blackburn, et al., 1994; Camesano & Logan, 1998; Hendry, et al., 1997; Johnson, et al., 1996; Lappin-Scott, et al., 1988; Schafer, et al., 1998; Rijnaarts, et al., 1996; Zhong, et al., 2017; Ren, et al., 2018).

Gannon and his co-workers (1991) suggested microorganisms transport through the soil with flowing water is related to more than one characteristic of bacterial cells (i.e., cell size, cell hydrophobicity, cells net surface electrostatic charges, and the presence of capsular polysaccharides) (Gannon, et al., 1991). In an experimental study using sand columns by (Fontes, et al., 1991) effect of parameters such as grain size, bacteria cell size, and ionic strength were tested on bacterial transport. According to their study, the grain size was the most critical factor controlling the transport of bacteria over a range of values tested for other tested factors. Next was cell size and ionic strength that were equally positioned.

Later in 1998, the impact of fluid velocity and cell concentration on the transport of motile and nonmotile bacteria in porous media studied by Camesano & Logan. They suggested for the cells to disperse into distance locations, a combination of motile cells, low velocities, and low ionic strength solutions should be used (Camesano & Logan, 1998). A variety of means to enhance bacterial transport in the subsurface were tested by (Johnson, et al., 1996), including decreases in ionic strength solution, the addition of surfactant, various cell-surface modifiers, and natural organic matter. According to this study, the highest reductions in bacterial attachment were achieved by lowering the ionic strength of the solution and the addition of surfactant. Often bacterial transport in aquifers involves the passage through the vadose zone. The presence of air adds an air-water interface besides the water-solid interface. Many studies showed that bacteria tend to accumulate at the air-water interface, which suggests the impact of soil air on bacterial transport (Marshall & Cruickshank, 1973; Powelson & Mills, 1996; Schafer, et al., 1998).

Filtration and physical straining

Colloidal filtration theory (CFT) has been broadly used for transport modeling of bacteria in porous media. Physical straining or filtration of microorganisms by pore throats is one of the main mechanisms, which limits their transport through porous space. Physical straining is dependent on bacterial size and shape (Fontes, et al., 1991; Gannon, et al., 1991).

Despite a number of uncertainties in applying filtration theory to describe bacterial transport in groundwater, filtration theory can describe bacterial adsorption or attachment, which is a significant control parameter for the extent of bacterial movement in the pore space (Harvey & Garabedian, 1991). In a study by (Martin, et al., 1992) filtration theory used to describe the bacterial cell deposition in porous media. The agreement among results of observation and predictions from models proposes that mechanistic particle transport models can be effectively applied to bacteria transport.

The microbial transport equations in saturated medium

The temporal and spatial microbial concentration variation in a homogeneous, saturated porous medium is described by the advection-dispersion equation (Tufenkji, 2007):

$$\frac{\partial C}{\partial t} = D \frac{\partial^2 C}{\partial x^2} - v \frac{\partial C}{\partial x}$$

here C is the concentration of the microbe, x and t are travel distance and time for the microbe in a saturated medium, D is the dispersion coefficient, and v is the interstitial velocity of the microbe.

Transport of the microorganisms into porous media involves the physicochemical filtration (removal from pore fluid and attachment to the grain surfaces). The previous equation, however, accounts for the physical advection and hydrodynamic dispersion transport processes. The physicochemical filtration includes either the irreversible or the reversible process. When the filtration processes are considered in the modeling, the following equation for microbial transport is derived:

$$\frac{\partial C}{\partial t} + \frac{\rho_b}{\phi} \frac{\partial S}{\partial t} = D \frac{\partial^2 C}{\partial x^2} - v \frac{\partial C}{\partial x} .$$

Where S is the microbial concentration on the solid phase, ρ_b is the sediment bulk density, and ϕ is the porosity.

The microbial equilibrium adsorption to the solid surfaces is described by Langmuir and Freundlich isotherms (Tufenkji, 2007). Considering a linear adsorption isotherm, as an example $S = K_{eq}C$, the previous equation is written as:

$$\left(1 + \frac{\rho_b K_{eq}}{\phi}\right) \frac{\partial C}{\partial t} = D \frac{\partial^2 C}{\partial x^2} - v \frac{\partial C}{\partial x} .$$

Here the term $\left(1 + \frac{\rho_b K_{eq}}{\phi}\right)$ is generally referred to as the retardation factor (R). A kinetic process models microbial attachment and detachment, which control the microorganisms' removal from the aqueous phase, as first-order reactions (Zhang, et al., 2001; Tufenkji, 2007):

$$R_A = K_{att}C \quad R_A = \frac{\rho_b}{\phi} K_{det}S.$$

Here K_{att} and K_{det} are the rate coefficients of attachment and detachment processes. These equations, however, neglect processes such as the microbial growth effect or the interactions among microbes (Tufenkji, 2007).

As discussed, the filtration theory has been widely used to describe the microbial transport behavior both in the laboratory and field-scale studies (Harvey & Garabedian, 1991; Martin, et al., 1992). A one-dimensional equation that describes the bacterial transport based on the colloid filtration model accounting for the storage, reversible and irreversible adsorption, dispersion, and advection phenomena, is written as (Harvey & Garabedian, 1991):

$$\phi \frac{\partial C}{\partial t} + \rho_b \frac{\partial S}{\partial t} = D \frac{\partial^2 C}{\partial x^2} - v \left(\frac{\partial C}{\partial x} + K_{att}C \right).$$

Colloid filtration theory describes the mass transport process by a single-collector efficiency, η ; likewise, it represents the surface attachment step by the collision (attachment) efficiency factor, α (Tufenkji, 2007). The single-collector efficiency, η , refers to the ratio of the particle's rate, which hits a single grain to the particle's rate, which moves toward the grain

and implies the physical factors defining particle collision (Harvey & Garabedian, 1991). The single-collector efficiency, η includes the colloid collector collision caused by Brownian motion, interception, and the settling (Harvey & Garabedian, 1991).

Irreversible attachment formulation

For many practical applications in which the system is at steady-state, free of microorganisms at the beginning, and the hydrodynamic dispersion impact can be neglected, (i.e., the dispersion influence is much smaller compared to the advection influence), the classical colloid filtration theory model can be used. Following solutions for a continuous particle injection at a concentration C_0 (at $x = 0$) and time period t_0 to the previous equation are derived (Tufenkji, 2007):

$$C(x) = C_0 \exp\left(-\frac{K_{att}}{v} x\right),$$

$$S(x) = \frac{t_0 \phi K_{att} C_0}{\rho_b} \exp\left(-\frac{K_{att}}{v} x\right).$$

The rate coefficient of the microbe attachment to the surface may be described by the filtration theory using single-collector efficiency and the collision efficiency factor, to explain the colloid material removal during filtration in packed-bed systems (Hendry, et al., 1997):

$$K_{att} = \frac{3(1-\phi)v}{2d} \eta \alpha,$$

here d is the diameter of the porous media grains.

Microbial inactivation or death

The inactivation (also named as death) is one of the main mechanisms, which contributes to the removal of microbes during transport in porous media. Various parameters can influence the microbial inactivation, such as solution composition, pH, temperature, and attachment to sediment surfaces (Tufenkji, 2007). Both adsorption and simultaneous inactivation of microorganisms can be studied at different scales: in batch, column, and field experiments. In batch experiments, nearly always, only equilibrium adsorption is studied (Schijven & Hassanizadeh, 2000).

Effect of biofilm on the hydrodynamics of pore-space

The relationship between biofilm growth and hydrodynamics of porous media is two-folded. Biomass growth can change the hydrodynamics of pore-space; at the same time, the hydrodynamic conditions may influence characteristics of the biofilm growth (Gerlach & Cunningham, 2011).

Effect of biofilm formation and distribution on hydraulic properties of pore space have been studied by numerous researchers (Stoodley, et al., 1999b; Alami, et al., 2000; Cunningham, et al., 1991; Aufrecht, et al., 2019). The porosity and permeability of the porous media belong to the category of the properties that measure the flow field alteration. Through the permeability concept, one can avoid the necessity of a detailed description of the fluid-solid interface. Additionally, to integrate the pore structure and morphology changes, typically the permeability is related to another scale parameter, the porosity (Hommel, et al., 2018).

Affected porosity by biomass growth in pore space can be described in different ways; first, the overall (bulk) porous space porosity; second, the effective pore space porosity; and third, the internal biomass porosity (Gerlach & Cunningham, 2011). Nevertheless, most of the experimental and numerical studies only consider the overall and effective porosity (Gerlach & Cunningham, 2011). Often porosity alterations have been evaluated via direct microscopic observation associated with image analysis techniques or using tracer breakthrough curves (Gerlach & Cunningham, 2011).

The effect of the altered porosity led by biofilm growth on the permeability of the pore space depends on the location of the deposited biofilms. If bacterial cells start to grow on the inside of large pores or fractures and form biofilms in these areas, even a substantial change in porosity due to these biofilms can have a negligible effect on permeability. On the contrary, if biofilms deposit in the pore throats or fracture entrances, even a minor change in porosity can have a substantial impact on permeability (Gerlach & Cunningham, 2011).

Permeability is the most common parameter that is used to describe the influence of biofilm formation on pore space properties. Generally, in the literature, reduction of permeability up to three orders of magnitude or less are reported; in some cases, more significant reductions have been reported (Gerlach & Cunningham, 2011). It is similarly reported that the permeability reduction in fine-grain materials is more pronounced than coarse-grain ones (Vandevivere, 1995). In a few studies, the importance of the internal penetrability for biofilms has been investigated. These studies revealed that adapting this assumption of internal permeability for biofilms, has a considerable influence on the predicted hydraulic properties of pore space (Pintelon, et al., 2012; Thullner & Baveye, 2008).

5.4 Colloids transport in porous media

The study of the colloidal particles' behavior and transport in porous media has quite an old history. Colloids are defined as particles with diameters of less than 10 μm (McCarthy & Zachara, 1989). There are a variety of underground colloid particles both organic and inorganic materials (Figure 5-4); subsurface colloid particles include macromolecular constituents of dissolved organic carbon (DOC), biocolloids, non-aqueous liquids microemulsions, weathering products, and fragments of rock and minerals (McCarthy & Zachara, 1989). Colloid particles such as viruses, bacteria, and clay minerals can noticeably move in porous media. Estimates from fields show microorganisms migrate significant distances due to porous preferential flow paths, wormholes, cracks, and fractures (Abu-Ashour, et al., 1994; Morales, et al., 2010). Chemical and hydraulic properties of porous media are then affected and altered by variations that particle release and capture induce in aqueous chemistry (Molnar, et al., 2015). The release and capture of colloid particles into soil solution and underground water occurs via a range of hydrologic, geochemical, and microbiological processes (Bradford, et al., 2002).

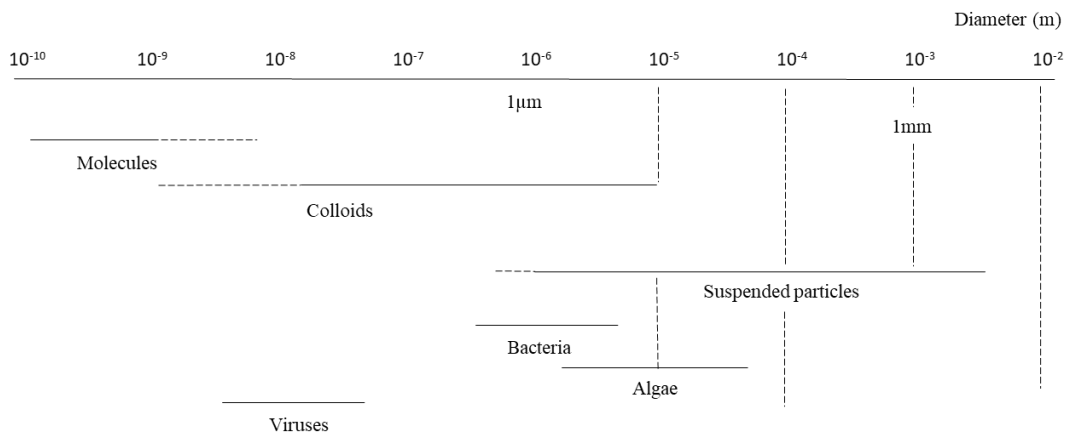


Figure 5-4 Various particle sizes underground [adapted from (McCarthy & Zachara, 1989)].

To manage and engineer many environmental contaminants and related issues, the processes that control colloid transport and fate should be well understood. For example, a comprehensive description of microbial transport is needed: (a) to evaluate contamination potential and to protect drinking water from pathogenic bacteria (Hunt & Johnson, 2017); (b) to develop and apply in-situ bioremediation and bioremediation strategies (Wilson, et al., 1986; Lefevre, et al., 2016); (c) in removal of microbial and fines plugging in injection wells (Cusack, et al., 1987); (d) and in application of microbial enhanced oil recovery (Jack, 1993).

Many of the similar physical and chemical processes that affect solute transport in the porous media influence colloid transport (e.g., advection, diffusion, dispersion, and sorption). Sorption processes in colloid transport are often referred to as attachment, deposition, or filtration. Colloid attachment is assumed as the fundamental mechanism controlling colloid

transport in pore space (Bradford, et al., 2002). The colloid attachment is sensitive to the solution chemistry (electrolyte concentration). Moreover, it depends on factors such as chemical-colloidal interactions that act among particles and surfaces at short distances, electrical double layer and van der Waals interactions, hydrodynamic, hydration, and interactions among macromolecular adsorbed layer (Elimelech & O'Melia, 1990).

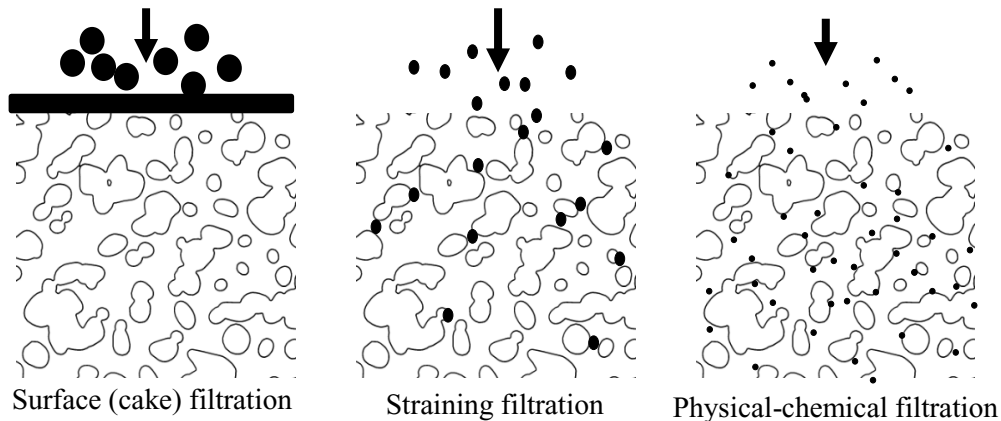


Figure 5-5 Particle filtration mechanisms in porous media, including the particle size dependence and a difference in deposit morphology [adapted from (McDowell-Boyer, et al., 1986)].

Colloid and particle migration in porous media can be limited by three mechanisms (Figure 5-5). Colloid particles and particle aggregates having a similar or larger size than the porous media grain sizes will not penetrate the media. They rather form a filter cake or surface mat above the media. The collection of particles and aggregates above porous media is referred to as surface filtration. Consequently, particle accumulation leads to a decrease in permeability. Smaller particles can penetrate the porous media and can be mechanically removed by straining in smaller pores. Straining is referred to as colloid particles trapping in pore throats, which are too small to allow particle passage. As the particle straining has a lower particle accumulation capacity, a smaller decrease in permeability is likely to occur. Particles much smaller than the media size are retained in solution by physical-chemical forces among particles and the media (physical-chemical filtration). Electrostatic and London-van der Waals forces determine whether particle-media and particle associations are favorable. Due to low media capacity to gather oppositely charged particles (i.e., particles cannot attach to already deposited particles), the permeability reduction, in this case, is smaller (McDowell-Boyer, et al., 1986).

Yao and his co-workers presented three main transport mechanisms (Figure 5-6) of a suspended particle in porous media (Yao, et al., 1971). In Figure 5-6, fluid flows with the velocity of V in the gravity direction. Here a single spherical particle of the filter media (considered as a collector), which is not influenced by its neighbors, is considered.

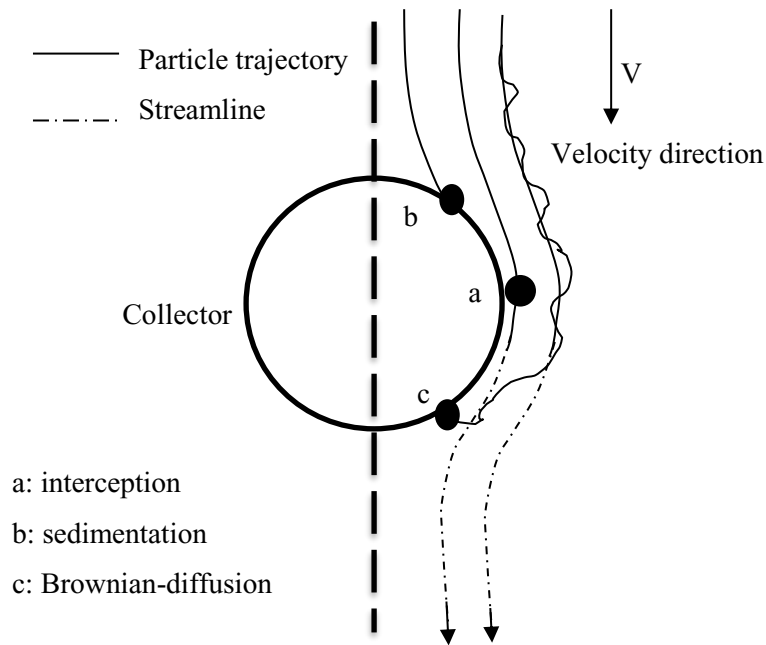


Figure 5-6 Basics of the transport mechanism of a colloid particle to a collector surface [adapted from (Yao, et al., 1971)].

The first transport mechanism referred to interception (case “a” in Figure 5-6) includes a suspended particle following a flow streamline that comes in contact with the collector (friction with fluid). A function of an interception parameter for spherical particles and media is written as:

$$\left(d_p/d_m\right)^2,$$

here d_p/d_m is the ratio of the particle diameter to the media diameter (McDowell-Boyer, et al., 1986). In case the suspended particle has a different density than suspending fluid, a different trajectory is expected for the particle to follow (case “b” in Figure 5-6). This transport mechanism is referred to as gravitational sedimentation. Sedimentation can result in particles deviation from fluid streamlines and collision with the collector surface, also known as an electric attraction. In this case, the buoyant weight of the particle and the fluid drag on the particle influence the path that a particle takes. The Stokes settling velocity of the spherical particle controls the gravitational sedimentation (McDowell-Boyer, et al., 1986):

$$v_s = \frac{g}{18\mu}(\rho_p - \rho_f)d_p^2,$$

where g is the gravitational acceleration, μ is fluid dynamic viscosity, ρ_p and ρ_f are particle and fluid densities, correspondingly. Microscopic particles in the suspension are subject to random bombardment by the molecules in the suspension medium. This leads to the

Brownian motion of the particle (case “c” in Figure 5-6). The particles transport is characterized by a particle diffusivity, D_p (McDowell-Boyer, et al., 1986):

$$D_p = KT/3\pi\mu d_p,$$

Here, K is the Boltzmann constant, T absolute temperature, and μ is fluid dynamic viscosity.

Four mechanisms associated with physical-chemical filtration are: (I) particle-media collision, (II) particle-media attachment, (III) kinetics of removal for clean media, and (IV) kinetics of removal during clogging (McDowell-Boyer, et al., 1986).

Colloidal interactions and DLVO theory

The DLVO (Derjaguin-Landau-Verwey-Overbeek) theory describes the attractive and repulsive forces among colloid and grain surfaces in the interface potential energy profiles. The DLVO theory looks at the two main forces (electrostatic repulsion and van der Waals attractive force) that are acting on the charged colloidal particles in a solution (Park & Seo, 2011). Summing the double layer, London-van der Waals, and short-range repulsive potential energies over the separation distance between the colloids and grains build the potential energy profile (Ryan & Elimelech, 1996).

DLVO theory efficiently describes the electrostatic stabilization of particles in a suspension. The interaction among two particles in a suspension is caused by “the van der Waals attraction potential and the electrostatic repulsion potential” (Jucker, et al., 1998). The DLVO is commonly utilized to describe the attractive and repulsive forces which are acting at the bacterial/colloidal-substratum interface. Examples for DLVO theory include a description of the bacterial adhesion to solids as a crucial step in the initiation of biofilms (Jucker, et al., 1998).

DLVO theory has some main assumptions (Park & Seo, 2011):

- “Infinite flat solid surface”
- “The electric charge density is uniformly distributed over the solid surface”
- “Constant surface electric potential (no re-distribution of the surface charges)”
- “Unchanged electric potential (concentration profile of the counter-ions and the surface charge determining ions remains constant)”
- “No chemical reactions between the particles and solvent”

Assumptions such as infinite flat particles or unchanged surface charge density are quite far from the reality of the suspended particles in a solution. DLVO theory states that the potential energy of the particles (Φ_T) comes from the superposition of potential energy of the

repulsive electrostatic interaction (ϕ_R) and attractive interaction due to van der Waals force (ϕ_A):

$$\phi_T = \phi_A + \phi_R$$

Figure 5-7 illustrates the DLVO potential energy as a function of the separation distance from a spherical particle surface. As can be seen, at a distance that is far from the solid surface, the van der Waals attraction potential and the electrostatic repulsion potential approach to zero. A deep minimum (primary minimum) in the potential energy created by the van der Waals attraction near the surface. A little farther from the surface, another minimum (secondary minimum) is located as the electric repulsion potential take over the van der Waals attraction potential. Moreover, the maximum is known as the repulsive barrier (Park & Seo, 2011).

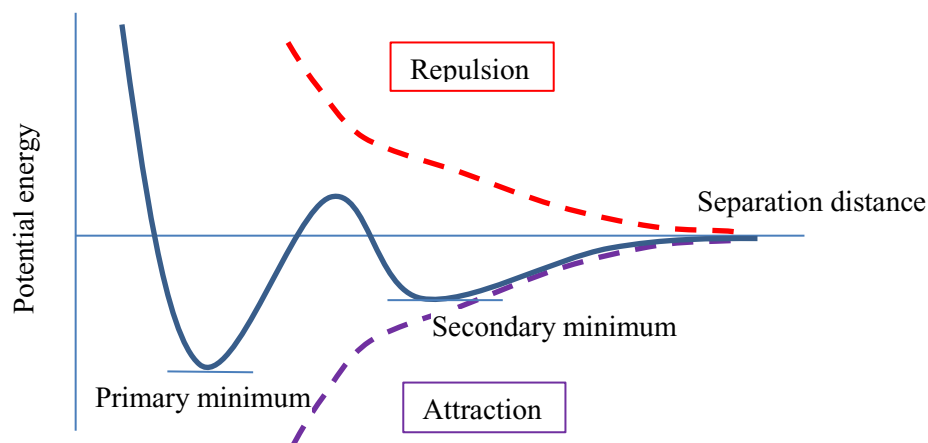


Figure 5-7 Schematic of DLVO potential energy as a function of separation distance [adapted from (Park & Seo, 2011)].

5.5 Limitations of the microbial transport formulations

The discussed mathematical formulations to model microbial transport in saturated porous media have weaknesses or inconsistencies. These limitations include: (a) inadequacy of equilibrium adsorption mechanism; (b) inaccuracy of the colloid filtration theory under unfavorable (repulsive) conditions; (c) complexity involved in determination of the attachment efficiency (particle deposition rates); (d) inadequacy in understanding of the impact of cell surface biomolecules; (e) higher importance of physical straining for larger microorganisms; (f) difficulty in prediction of microbial growth and inactivation; and (g) ignoring the detachment (release) of microorganisms (Tufenkji, 2007).

The first limitation for the microbial transport formulation is the inadequacy of the equilibrium adsorption mechanism. The microorganism's attachment (also known as equilibrium adsorption mechanism) has been considered in both laboratory and field-scale

research (Tufenkji, 2007). However, the equilibrium adsorption does not account for the removal of microorganisms from the pore space (Schijven & Hassanizadeh, 2000). Therefore, to formulate the microbial attachment, the microbial removal may be regarded only by counting an inactivation term alongside with an additional sink term for attachment (Tufenkji, 2007).

The next limitation in microbial transport formulation is the inaccuracy of the colloid filtration theory under unfavorable conditions. Some studies advise that the filtration of microorganisms may not always be consistent with colloid filtration theory (Tufenkji & Elimelech, 2005; Redman, et al., 2001; Martin, et al., 1996; Bolster, et al., 1999). A method to assess the reliability of the CFT is a comparison of the spatial distribution of retained microorganisms from the measurement to the predicted values based on the measured breakthrough curve (Tufenkji, 2007).

Determining the attachment efficiency involves high complexity and contributes as another limitation to the microbial transport formulations. The trajectory analysis for non-Brownian particles and numerical solutions of the convective–diffusion equation are the theoretical approaches that are used to define the rate of particle deposition in the presence of repulsive energy barriers (Tufenkji, 2007). Numerical solution of the convective–diffusion equation is an estimated analytical solution, and it incorporates the DLVO theory that has been traditionally unsuccessful in predicting the observed particle deposition rates under unfavorable settings. The particle deposition rates that are calculated by these models are generally many orders of magnitude smaller than experimentally measured values (Tufenkji, 2007).

The next limiting factor is the insufficiency in understanding the impact of cell surface biomolecules. The complexity and heterogeneity in the surface cell of various microbial strains make the generalization of the findings regarding the mechanisms of microbial adhesion difficult and complex (Tufenkji, 2007).

The fact that the physical straining for larger microorganisms may be more critical in pore space is another limiting factor (Tufenkji, 2007). In an experimental study done by Sakthivadivel in 1969, it was shown that the most critical factor determining straining within porous media was the ratio of the media diameter to the particle diameter ($\frac{d_m}{d_p}$). Particle straining potential predictions based on the system geometry suggest that when the particle diameter ratio to the median grain diameter ($\frac{d_p}{d_c}$) is greater than 0.05, the physical straining becomes very significant (Tufenkji, 2007). Other experimental studies suggest that straining could be substantial when the ratio ($\frac{d_p}{d_c}$) is less than 0.05, and even when it is as low as 0.002 (Tufenkji, 2007).

The difficulty in the prediction of microbial growth and inactivation is another matter. The processes of microbial growth and inactivation or decay are often represented using the first-order rate expressions (Corapeioglu & Haridas, 1985; Schijven & Hassanizadeh, 2000). Bacterial growth is dependent on the substrate. The bacterial growth can be described using the Monod relationship. This equation defines a link between the concentration of a limiting nutrient and the growth rate of microorganisms (Corapeioglu & Haridas, 1985). The difficulty with using the Monod equation is defining the parameters' values, the maximum growth rate, and the affinity constant as these parameters are specific to the strain and, similarly, are sensitive to the environmental settings and nutritional conditions (Tufenkji, 2007). The biological nature of bacterial growth and decay presents a challenge for transport modeling, as the biological mechanisms are frequently dependent on one another. Therefore, the prediction of the microbial growth and inactivation processes in different conditions should be treated on a case-by-case basis.

The last remark affecting the microbial transport formulation is overlooking the detachment (release) of microorganisms. The detachment of bacteria from surfaces is of importance in many systems. An example is the detachment of pathogenic microbes from media, which may pose a substantial risk to the safety of drinking water (Kumara, et al., 2017). During the *in-situ* bioremediation processes in which a critical microbial mass at a specific location should be attained, detachment of bacteria considered an undesirable event. The spontaneous and sudden release of microorganisms has been observed both in the laboratory and field-scale experiments (Tufenkji, 2007). Various factors are affecting the rate and the extent of microbial detachment from sediment grain surfaces. Many studies have reported that the detachment process of the microorganisms may be linked to local nutrient availability, survival mechanisms, and growth (Ginn, et al., 2002). Even though the detachment process of microorganisms has been observed in many experiments, the microbial transport formulations have often overlooked this behavior. An example is the classical colloid theory that is the most general approach for predicting microbial migration and fate in saturated porous media, which fails to consider the detachment process (Tufenkji, 2007).

Chapter 6 Bacterial growth and transport in porous media

This chapter describes the experimental and numerical study of microbial deposition and transport in a saturated pore-network under different flow conditions. The main objectives in this part of the study have been: (1) to assess the microorganisms' growth as a function of time under different growth modes, (2) to evaluate the impact of bacterial growth on the hydraulic properties of the media, and (3) to qualitatively visualize the pore space and flow pattern change.

Experiments were performed using microfluidics, i.e., 2D porous media etched in the glass. Microfluidic devices are an emerging technology that combines the advantage of high throughput with high spatial and temporal resolution imaging.

The microbial transport and growth were visualized in two phases using *Lactobacillus Casei* as a model organism. In phase I, a bacterial suspension solution in a stationary growth phase was flooded through microfluidic chips, which led to the initial accumulation of microbes in the pore space. In phase II, a nutrient (substrate) solution was injected; the supply of nutrients changed the bacterial growth to the exponential mode. In this phase, biomass accumulated with a higher rate not only in the pore space but also in the flow lines and valves, which at later times was released and resulted in a partial filtration of the pore space.

By means of the numerical modeling on the segmented images, the impact of bacterial colonization and filtration on the hydraulic properties of the medium was quantified. Similarly through solving the Navier–Stokes equations on the pore scale, the porosity-permeability relationship was attained.

The closing part of the study was devoted to the preliminary examination of particle tracing in a pore-network with the established biomass in it. The first insights into particle tracing modeling were achieved by simulating tracing experiments.

Finally, due to the complexity of the experiments, different adaptations and tests have been left for the future. Future work particularly concerns unsaturated flow experimentations, which has much relevance to the hydrogen storage and conversion problem, a more in-depth analysis of particular mechanisms, and combining the tracing experiments with the present study.

6.1 Method development

Bacteria, bacterial growth medium and growth curve

Lactobacillus Casei strain (provided from BOKU, Universität für Bodenkultur Wien) was used in the experiments. This bacterium is a Gram-positive, non-motile rod-shaped, non-sporing bacteria, and facultatively anaerobic (i.e., can grow in both aerobic and anaerobic conditions; while it grows faster in the presence of oxygen). The bacteria's cell size is around $0.7\text{--}1.1 \times 2.0\text{--}4.0 \mu\text{m}$, and they often have square ends and tend to form chains. This bacterium can survive in harsh environments (i.e., acid-tolerant bacteria), and stand in a wide range of temperatures and pH (optimum temperature of 30 to 40 °C and an optimum pH of 5.5-6.2). This bacterium gets most of its energy from converting glucose to lactic acid (Ludwig, et al., 2009).

The media in which bacteria grow can significantly affect the growth speed of the microorganisms. Two types of media may be provided for bacterial growth. Differential media, which are referred to a media that discriminate among different microbial groups. Most kinds of organisms can grow in differential media, but they display different growth behaviors. Selective media allow and favor the growth of particular microorganisms; for example, gram-negative bacteria (Prescott, et al., 2002).

Agar is the most commonly used medium. Agar is a gel-type substance that is usually placed in a petri dish. Microbial culture can be transferred to the edge of the agar plate using an inoculating loop or swab and streaked out over the surface. This process is called plating. Follow-on, bacteria grow and can be observed as visible colonies growing on the surface of the agar. The number of microorganisms that form colonies is called a colony-forming unit (CFU); also an indication of the number of viable microorganisms in a sample (Prescott, et al., 2002).

Lactobacillus MRS Broth and agar were used for cultivating bacterial culture. For this purpose, 26.1 g MRS broth was suspended in 500 ml of water, autoclaved for 15 min at 121°C, while pH of the solution was kept at the range of 5.7 ± 0.2 at 25 °C. MRS agar was made by suspending 34.1 gram MRS agar in 500 ml water, followed by an autoclaving procedure as for MRS broth. Bacterial culture was made by mixing freeze-dried powder of *Lactobacillus Casei* with MRS broth. The contents were transferred aseptically into a bottle. Several drops of the culture were used to inoculate the MRS broth and MRS agar plates, overnight at 37°C. *Lactobacillus* Colonies on agar media are typically small (around 2–5 mm), rounded, shining, smooth, and mostly dense without pigment (Ludwig, et al., 2009) (see Figure 6-1).

Microorganisms' cultivation is done in a liquid medium, commonly in batch culture or in a closed system. Through the incubation in a closed system, there is no fresh medium supply; therefore, nutrient concentration declines, and waste concentration increases.

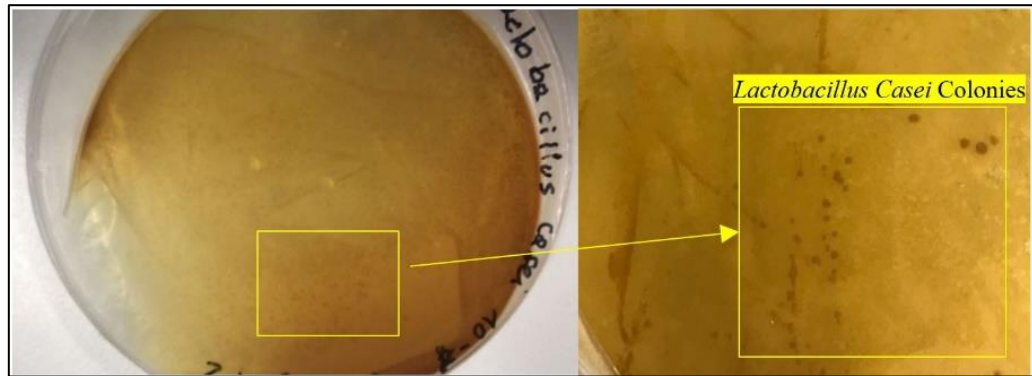


Figure 6-1 *Lactobacillus Casei* colonies on an agar petri dish (prepared at the University of Natural Resources and Life Sciences, Vienna).

A Spectrophotometer was utilized for the cell mass growth measurement. The primary purpose of this measurement was to identify the starting point of the stationary phase, which was employed in the experiments. The beginning of the stationary phase was estimated at around 22 hours after incubation. The total number of cells in the stationary phase was calculated by a direct cell counting method at about 95680000 cells in 1 ml of the bacterial solution. General literature on the bacterial growth curve and the measurement are documented in Appendix C: Bacterial growth curve and cell counting at the stationary phase.

Viscosity measurement

The viscosity of autoclaved water, nutrient solution, and bacterial suspension fluid (at stationary phase and higher concentrated solutions) were measured using a Modular Compact Rheometer – MCR 102 (Anton Paar® Germany GmbH, Ostfildern, Germany). All tests were conducted under isothermal conditions at 37°C and a shear rate of 300 s⁻¹. The testing procedure starts by adding 1mL of a sample over the surface of the plate reading. Readings were taken with permanent control of gap measurement with supported TruGap™ in 0.062 mm, using Rheoplus V3.62 software. The measurements and the average values of the viscosities were calculated (see Figure 6-2). Despite apparent visual variance among fluids, the difference in viscosity values was negligible.

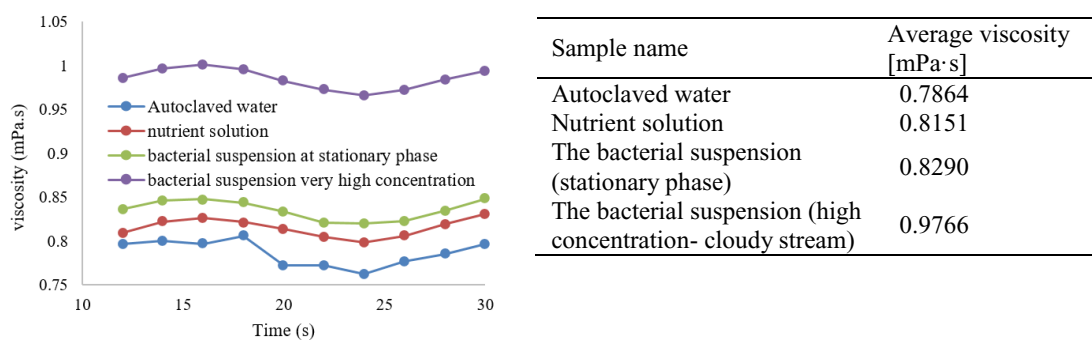


Figure 6-2 Viscosity measurement for different solutions and their average values in [mPa·s].

6.2 Bacterial growth and transport under saturated condition

Micromodels are 2D porous media, which are etched in a glass to simulate fluid flow in porous rock (Balch, et al., 1979). Information on the micromodel production procedure can be found in the literature (Chatenever & Calhoun Jr., 1952; McKellar & Wardlaw, 1982; Zarikos, et al., 2018; Yun, et al., 2017).

Experiments were conducted using micromodel chips made from borosilicate glass, representing a 2D porous media (see Figure 6-3). The pore network depth, porosity, permeability, and pore volume are reported as $20\ \mu\text{m}$, 0.57, 2.5 D, and $4\ \text{mm}^3$, respectively. Channels and structures were made by wet etching (hydrofluoric acid). The side view shows a curved structure in the depth profile as a result of the etching technique (www.micronit.com).

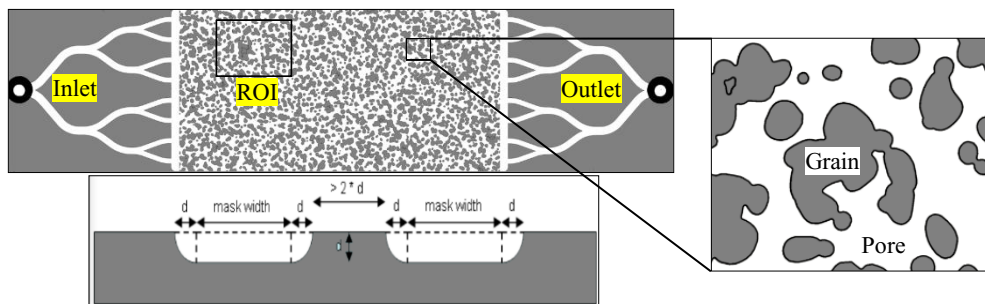


Figure 6-3 2D pore structure of the microfluidic chip. The total porous domain is $1\ \text{cm} \times 2\ \text{cm}$ with channel systems at the inlet and outlet for proper fluid distribution; the side profile and the region of interest (ROI) are shown.

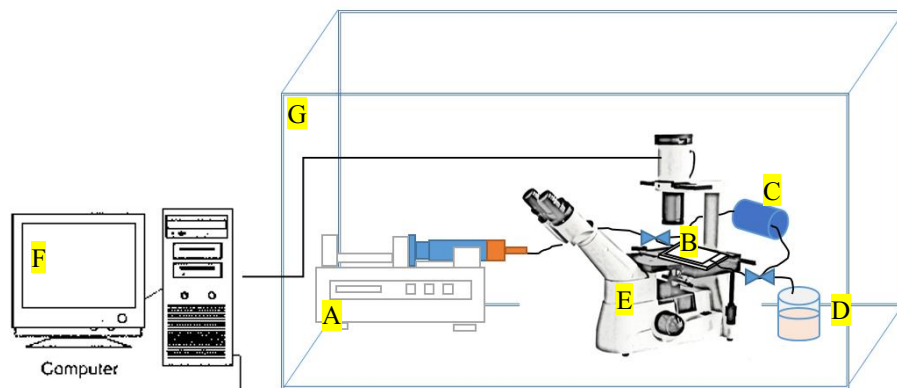


Figure 6-4 Schematic of the experimental apparatus. Fluid flow was established at $2\ \text{ml}\ \text{h}^{-1}$ by (A) a syringe pump. The flow passed through (B) the micromodel, and the pressure was recorded by (C) a pressure transmitter. The effluent was collected in (D) a Becher. The observation was done using (E) an inverted microscope connected to (F) a processor unit. The whole system was kept in (G) a built-in chamber with heating lines (called microscope incubator) at a constant temperature of 37°C during the entire experiments.

The accumulation of bacteria was captured using time-lapse imaging, allowing quantification of biomass growth over time. The micromodel was connected to a syringe pump for fluid injection at a constant flow rate of $0.2\ \text{ml/hr}$. A differential pressure transducer was

used to record the pressure drop across the micromodel. The experiments were carried out with two inverted microscopes. The first microscope (“Motic’s AE2000” with a digital camera) provided a partial image of the micromodel; while the second one (“Leica DMi 8 high-end microscope” with a Leica DMC2900 camera) was equipped with the stitching tool, which enabled having a complete view of the micromodel with high resolution throughout the experiments. A microscope incubator was built, which kept the entire experimental components at a constant temperature of 37(±1) °C during the tests (see Figure 6-4).

General experimental workflow

The present study focuses on saturated flow, which is a prerequisite for understanding the two-phase condition. The experimental workflow is shown in Figure 6-5.

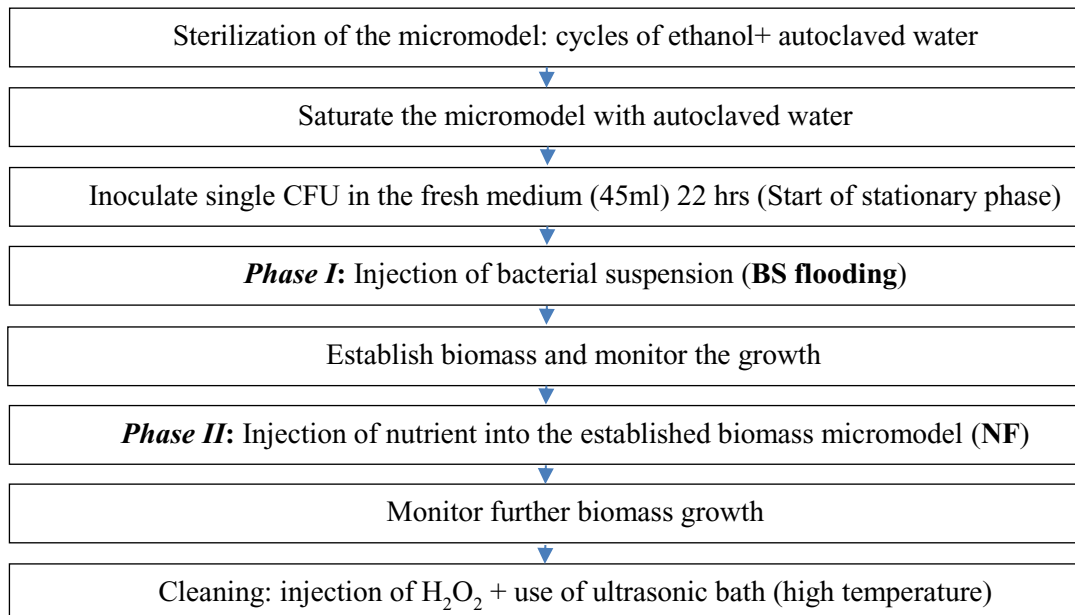


Figure 6-5 Schematic drawing of experimental sequences.

Five flooding experiments- four on the region of interest (ROI) and one on the total domain (TD) of the micromodel- were conducted to explore the microbial growth and transport mechanism in the pore space. Table 6-1 presents a summary of the experimental setting. Experiments have different duration times due to challenges in keeping an equal amount of fluid in the syringes and changing the flow lines after each test.

Table 6-1 Summary of the experimental conditions and settings.

Exp. No	Bacterial suspension duration (hrs.)	Nutrient flooding duration (hrs.)	Pressure data	Local biomass increase data	Total domain information
1 (ROI)	31	46	-	X	-
2 (ROI)	36	50	X	X	-
3 (ROI)	28	35.5	X	X	X
4 (ROI)	27.5	35.5	X	X	-
5 (TD)	27	29	X	X	X

6.2.1 Experimental observations and elementary processes

In the first phase of the experiment (BS flooding), the suspended microbial cells were transported with the stream of liquid into the pore space; they hit the surfaces, and some cells adhered and attached to them; in contrast, some cells attached and then detached and left the surface (Figure 6-6, I). At the end of the BS flooding, some biomass has accumulated in the porous network. The formation of biofilm on the surface is a complex phenomenon and consists of multiple events, in which the solid surface characteristics play an essential role in the attachment process (see more details in section 5.2).

In the second phase, the nutrient was supplied and boosted the bacterial activities; aggregated biomass was formed with higher intensities, which consisted of microcolonies that were separated by interstitial channels (Figure 6-6, II). The spatial distribution of biomass across the pore-space at this step appeared to evolve predominantly from the locations, in which bacteria initially attached. Finally, at the end of this phase, significant parts in the micromodel were occupied by biomass, and preferential paths could be observed (Figure 6-6, III, IV). The massive biomass growth was not merely due to the nutrient supply, but it was strongly affected by filtration events. This occurred due to the sudden release of the accumulated biomass in the flowlines and valves, which entered the pore space as a cloudy stream. This phenomenon is elucidated in greater detail in the upcoming sections.

There are major factors that influence the biofilm structure (Stoodley, et al., 1997; Donlan, 2002; Stoodley, et al., 1999a; Thullner, 2010). These include surface or interface characteristics, characteristics of microorganisms' consortia, hydrodynamic conditions, and nutrient and inhibitors availability and existence. Similarly, biofilm heterogeneity is multifold (Picioreanu, et al., 2000; Milferstedt & Morgenroth, 2009; Wimpenny, et al., 2000; Stewart & Franklin, 2008; Farhat, et al., 2016). The geometrical heterogeneity includes biofilm thickness, surface roughness, porosity, and the biofilm surface coverage. The chemical heterogeneity involves variations in nutrients, metabolic products and inhibitors, pH, and diversity of reactions. The biological heterogeneity includes microbial strain diversity, cells, and EPS activities. The physical heterogeneity consists of the biofilm density, strength, permeability, viscoelasticity, viscosity, EPS properties, solute concentration and diffusivity, and the presence of abiotic solids. Even though it was not possible to identify the impact of the mentioned factors on the experimental results, we believe some of these aspects must have contributed and influenced the biomass structure and its heterogeneity over the micromodel model throughout the tests. Time-lapse videos available in supplementary materials illustrate different phenomena such as attachment and detachment of bacterial cells and aggregates, and biomass growth and filtration (also see an example in Appendix E: Clogging and unclogging of biomass).

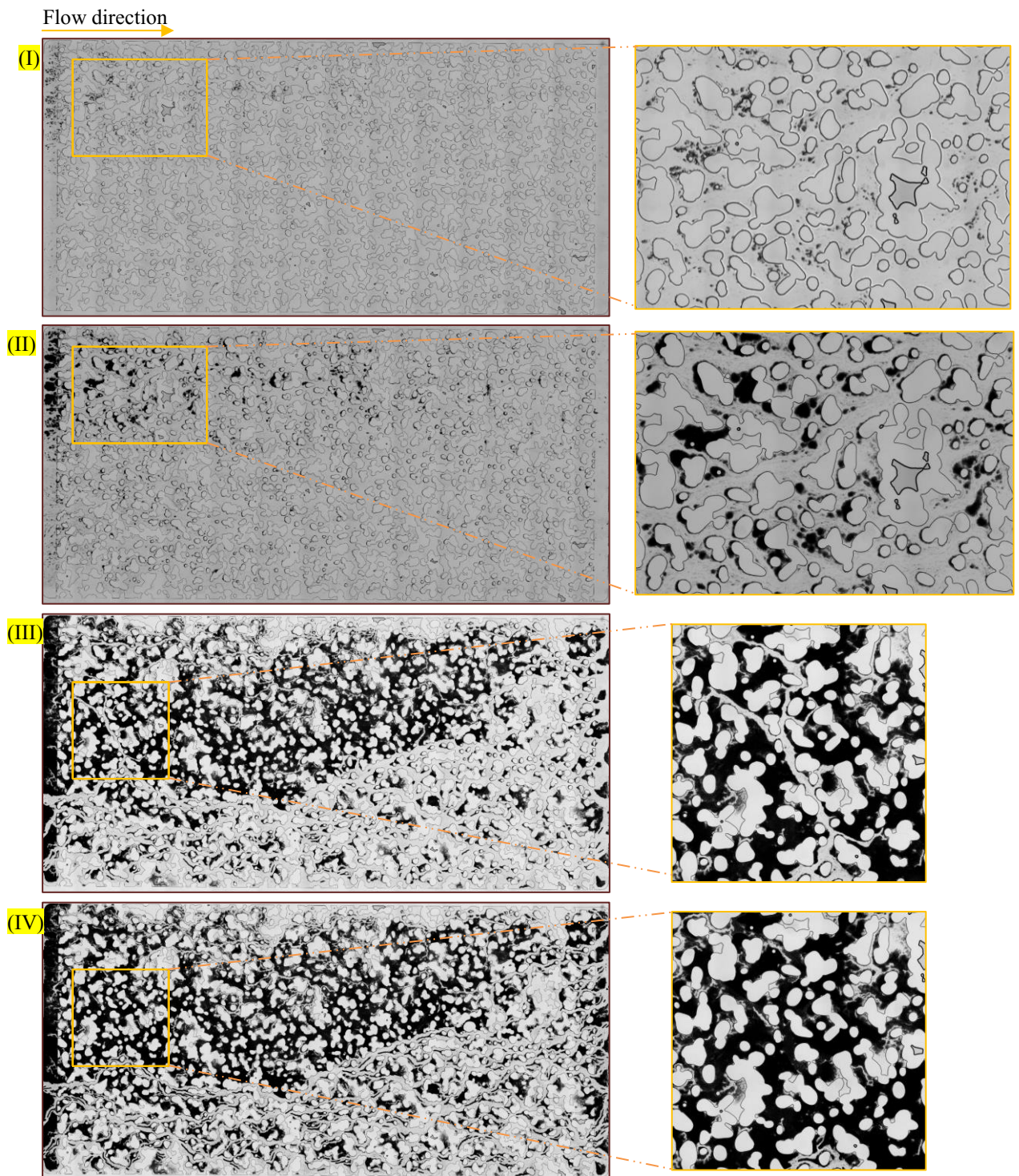


Figure 6-6 Bacterial growth and clogging during flooding phases. (I): At the end of BS flooding (27 hrs); biomass with a higher intensity close to the inlet area was formed. This may be due to the large grain obstacle (zoomed-in image) that created a low-velocity region for bacterial cells and aggregates to adhere to the surfaces. (II): After 16 hrs NF, before a massive biomass filtration happened, here the growth was merely due to nutrient supply; the spatial distribution of biomass across the pore-space at this step appeared to evolve mainly from the locations, in which bacteria initially attached. (III) & (IV): After 23 and 29 hrs of NF, where the cloudy stream invaded the pore space and led to massive biomass filtration; channel formation and channel closings are seen in the zoomed-in images.

Figure 6-7 displays the microscopic images of the bacterial evolution in the micromodel. As discussed, at first, bacterial suspension solution (I) was flooded, then bacterial and aggregated cells accumulated on surfaces over time and began to grow and divide, which led

to the formation of microcolonies (II). Most areas of the micromodel were covered by scarce microbial cells. The growth of bacteria during NF was elevated, and at some point, the accumulated mass in the flowlines and valves got released, which came as a cloudy stream into the system (III) leading to filtration, biomass accumulation, and channel formation. Elongated-streamer shape masses appeared after this event (Figure 6-7, IV). Additionally, flow channels in the inlet and the central areas of the micromodel are shown in (V& VI). Some studies reported the formation of biofilm as streamers under turbulent conditions (Stoodley, et al., 1999b; Stoodley, et al., 1999a). However, the experiments were performed under laminar flow.

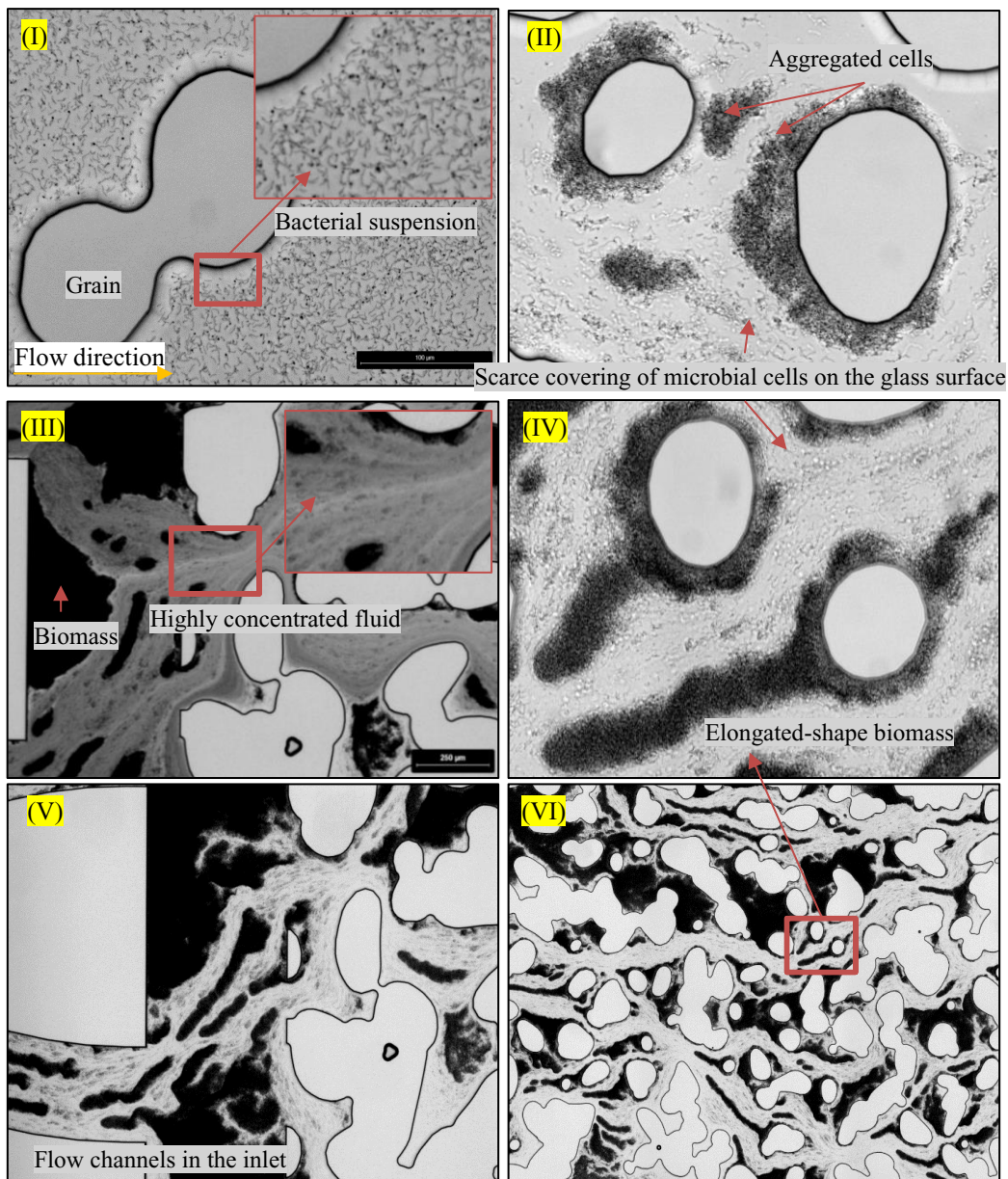


Figure 6-7 High-quality microscopic images of the bacterial evolution during BS flooding and NF. (I): BS solution; (II): the suspended microbial cells are transported along with the stream of liquid into the porous network, and some cells adhere and attach to them, and start to grow; (III): invasion of the highly concentrated fluid, during NF; (IV): characteristic elongated shape biofilm which is left after invasion of the cloudy stream; (V& VI): formation of channels in the inlet and in the center of the micromodel at the end of NF.

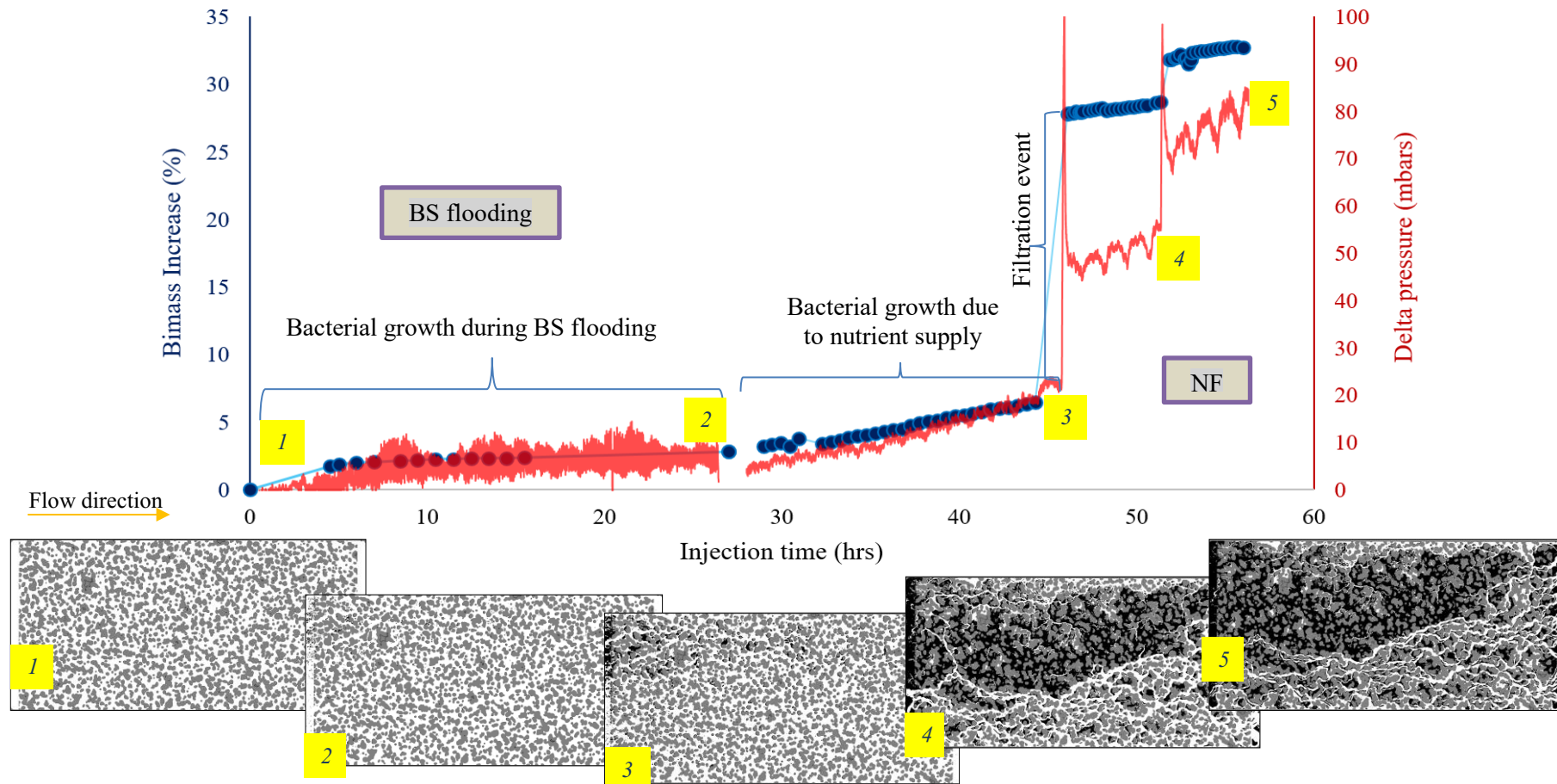


Figure 6-8 The correlation between biomass growth and pressure drop across micromodel over the flooding time. (1): The initial state. (2): End state of BS flooding: the microbial cells and aggregates accumulated on surfaces over time and began to grow and divide, leading to biomass formation; here, the bacterial growth and pressure drop occur at a minor rate. (3): Additional growth and accumulation of biomass (especially in the initial precipitation locations) by NF, leading to a moderate increase rate for both biomass growth and pressure drop graphs. (4 & 5): Massive filtration through two steps formed by the invasion of a cloudy stream (due to discharge of biomass accumulated in flowlines and valves), leading to a stepwise trend in both plots. The oscillation in the pressure data is due to the artifacts of the injection pump.

Pressure drop data across the micromodel was recorded, and the montaged images of micromodels were segmented and processed to quantitatively evaluate the growth behavior over time (see Figure 6-8). The detailed processing procedure is described in Appendix D: Image processing procedure. By segmenting the optical images, the occupied biomass was calculated (i.e., the number of black pixels subtracted from grain and the open pore space). As images are two dimensional, the biomass below the threshold value was assumed to occupy the entire micromodel channel depth. This assumption is not valid at all times as the density of biomass varies by location and time at different depths; therefore, it results in an approximate indicator of the amount of biomass.

During the BS flooding, initial attachment of cells and aggregates happened, both the pressure drop and biomass accumulation occurred at a minor rate, which are reflected in Figure 6-8, steps 1 to 2. The growth of these masses amplified during the NF phase with a stepwise trend (from steps 2 to 5). From steps 2 to 3, the pressure drop and the bacterial growth occurred at a higher rate, merely due to bacterial colonization due to the nutrient supply. Points 3 and 4 correspond to the spikes, which denote the times, in which the cloudy stream entered the pore space. Massive filtration through these two steps led to a stepwise trend in both plots (changes from steps 3 to 4, and steps 4 to 5). The oscillation in the pressure data was due to the artifacts of the injection pump. This observation has been repeated in all the replicate tests (see Appendix F: Biomass growth and pressure response during NF).

The images of micromodel initially, at the end of BS and NF for four ROI replicate experiments, are presented in Figure 6-9. As can be seen, during the BS phase, bacterial attachment sites and colonization intensity are not alike. ROI-test 1 shows the highest growth, while ROI- test 3 has the lowest biomass formation. The variance in the bacterial attachment and colonization in each test may have been influenced by the bacterial suspension solution. Even though special care was devoted to the solution preparation, the initial BS solution may have deviated from the stationary phase of the bacterial growth. At the end of NF, significant parts of the pore space were occupied by biomass, and preferential flow paths were detected.

Biomass increase as a function of time for all experiments is plotted in Figure 6-10. As discussed previously, the biomass growth for ROI- Test 1 during the BS phase seems to be off-trend. The overall behavior of growth in the two phases was very similar, and the effect of filtration events was detected as spikes in all tests. Additional results recorded as time-lapse videos from ROI replicate experiments that display the bacterial evolution during the flooding phases are available in the supplementary materials.

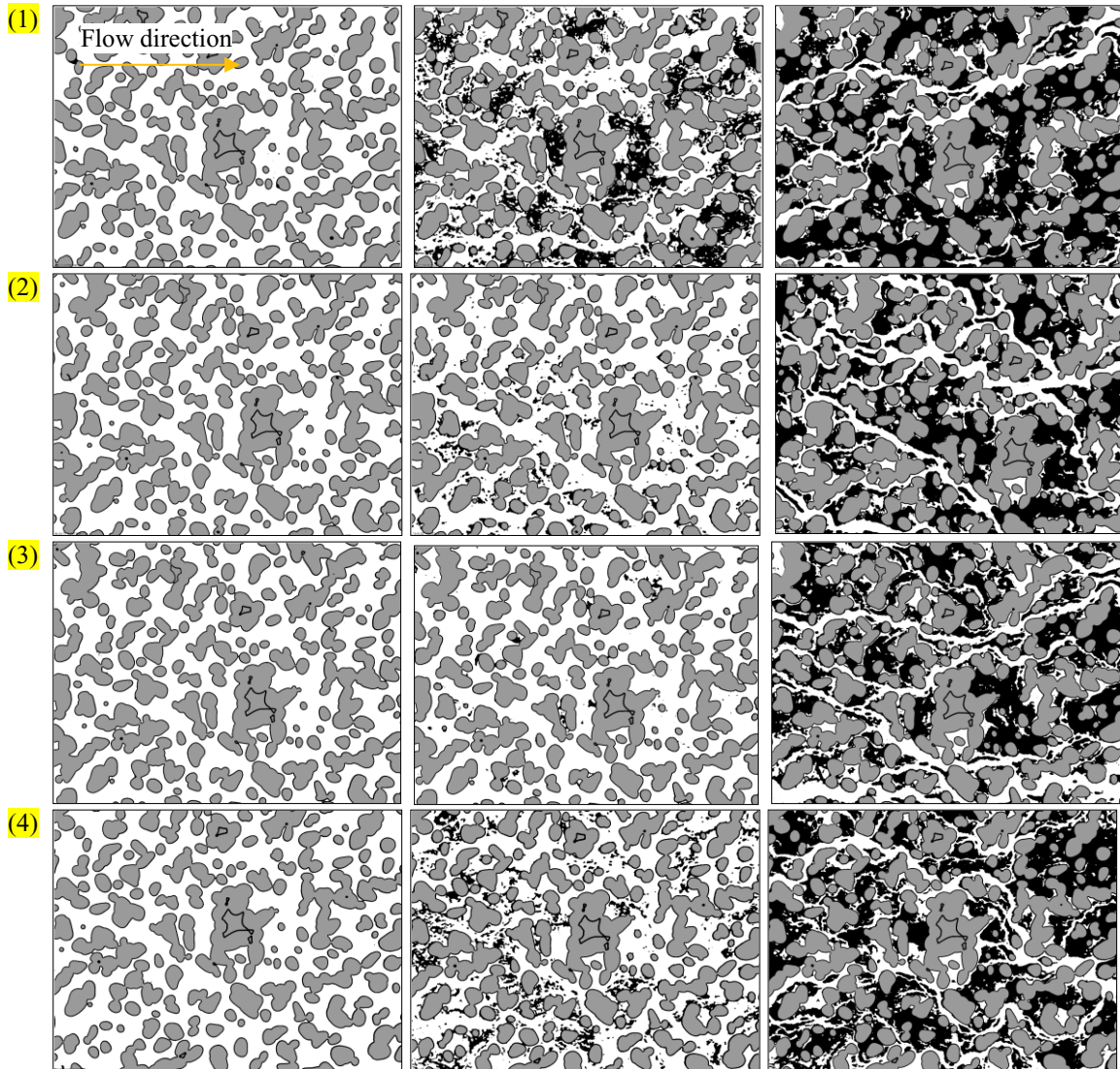


Figure 6-9 bacterial colonization and filtration in ROI tests. Images from the left side show the initial water-saturated micromodel and the final state of BS & NF. Initial biomass accumulation occurs in different sites with different intensity. The preferential flow paths at the end of NF are seen, which are affected by filtration.

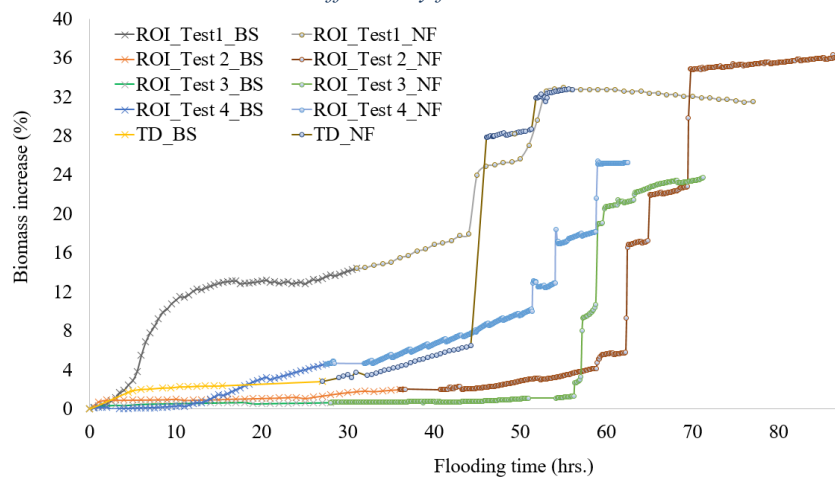


Figure 6-10 Comparison of the biomass increase in the ROI and TD test during Phase I & II. The biomass growth during BS remains minor except for ROI-Test1, which seems to be off-trend. Through NF, the growth slope increases gradually before the filtration events, which cause sudden jumps in graphs.

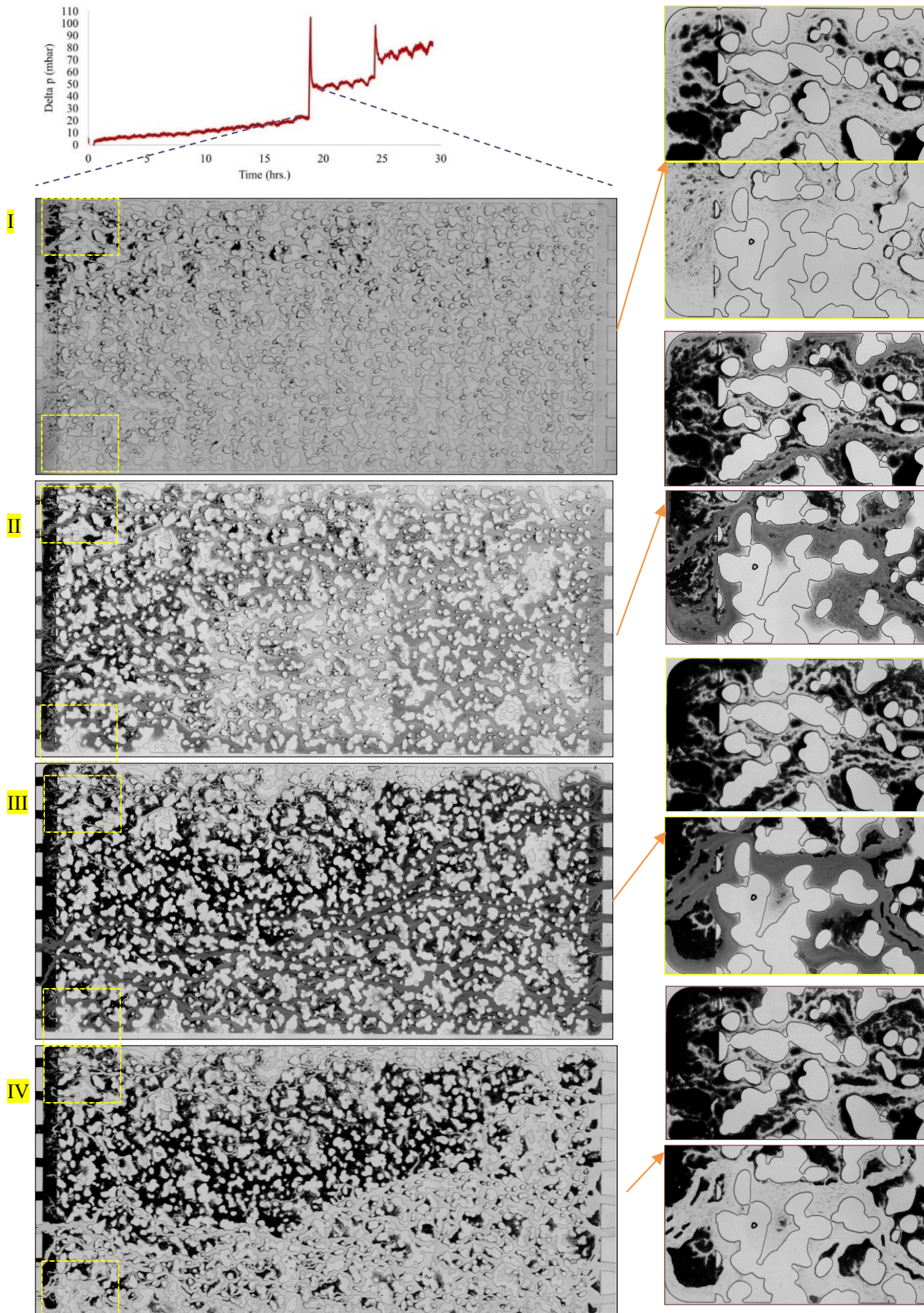


Figure 6-11 The invasion of the cloudy stream in the micromodel correlated with the 1st pressure spike. (I): before the flow of the cloudy fluid; (II & III) passage of the highly concentrated fluid; (IV): massive filtration which was remained at the end.

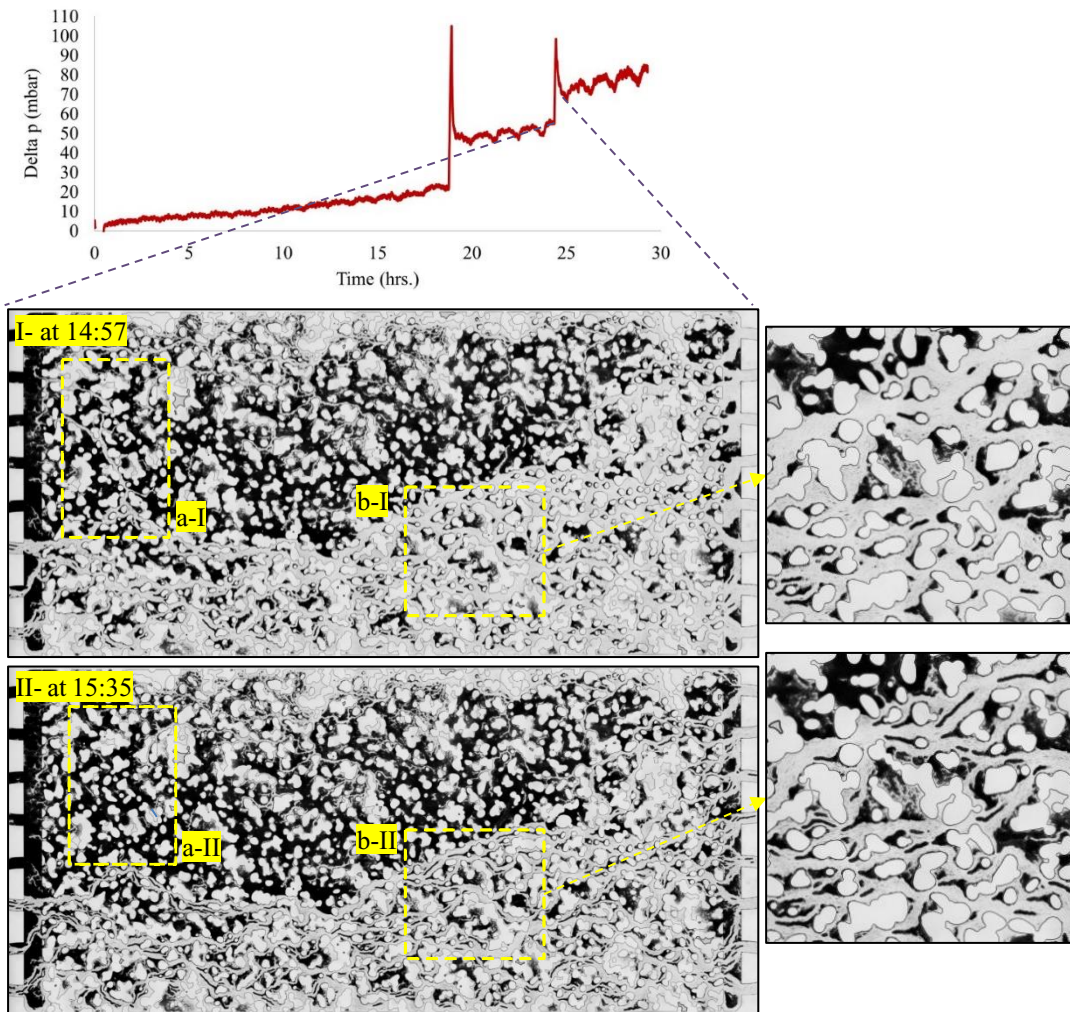


Figure 6-12 The invasion of the cloudy stream in the micromodel correlated with the 2nd pressure spike. More paths are filled (a-I to a-II). Also, the elongated shaped biomasses, which are typical characteristics of biomass caused by the cloudy solution, appear in the pore-network (b-I to b-II);

Further investigations on the delta pressure data and microscopic images revealed a perfect agreement for the times when two pressure spikes appeared and times when the cloudy stream has been detected (Figure 6-11 and Figure 6-12). As can be seen, massive plugging remains after the 1st pressure spike after exposure to the highly concentrated fluid. The second pressure spike leaves a trace of elongated shape biomass (also see Figure 6-7, IV). This feature is observed in all tests and can be considered as a characteristic of the biomass after the exposure to a cloudy stream.

Biomass internal porosity and permeability

An extra test (ink -injection) was carried out at the end of NF (ROI- Test1), which proved that the biomass acts as a porous material that allowed the flow of ink within its structure (see Figure 6-13). After around 90 minutes of ink injection, all the investigated regions, including high dense areas, were filled by ink. This process happened at a much shorter time than the estimated time for diffusion within this distance, and the biomass seemed to be much more permeable than expected. Moreover, the depth profile mapped in Figure 6-14 confirms the porous nature of biomass. Additional depth profiles are presented as time-lapse videos in the supplementary materials.

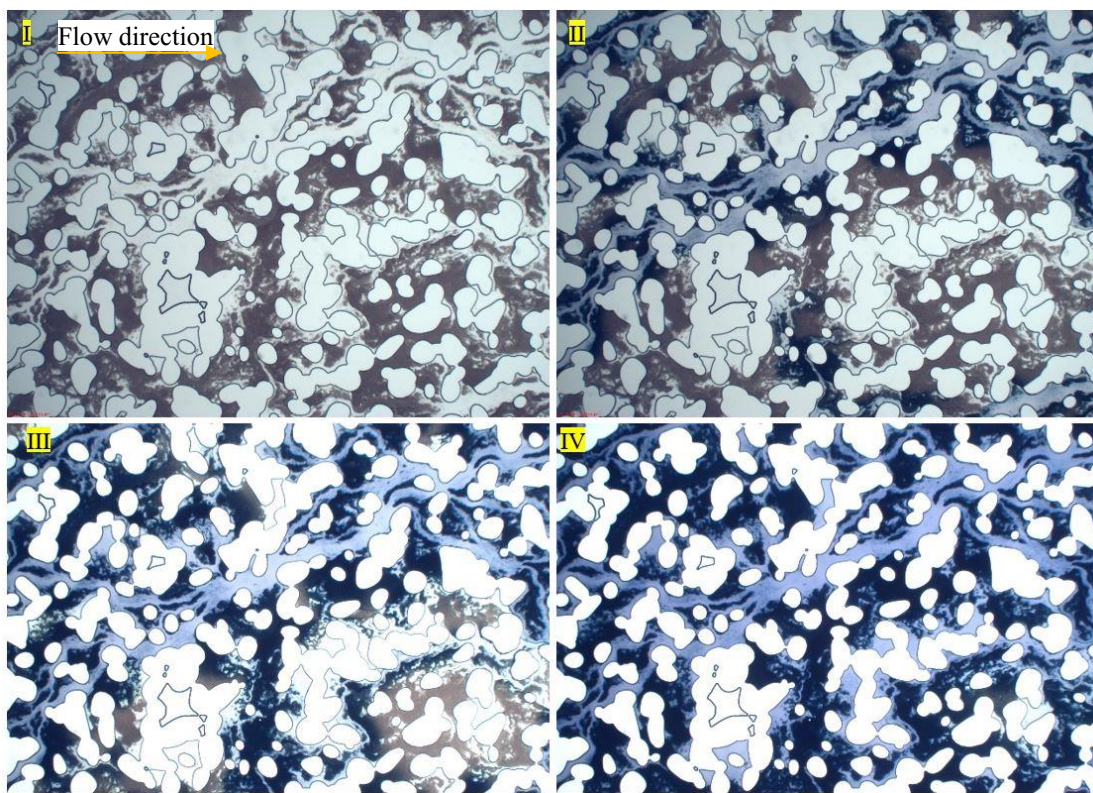


Figure 6-13 Invasion of ink in the micromodel showing the porous nature of biomass even in high dense areas. (I) Start of ink flooding; (II) invasion of ink after 50 minutes, the main pore throats were filled by ink while some areas still not affected; (III) after 60 minutes, more regions were occupied by ink; (IV) after 90 minutes, all the pore spaces were filled by ink.

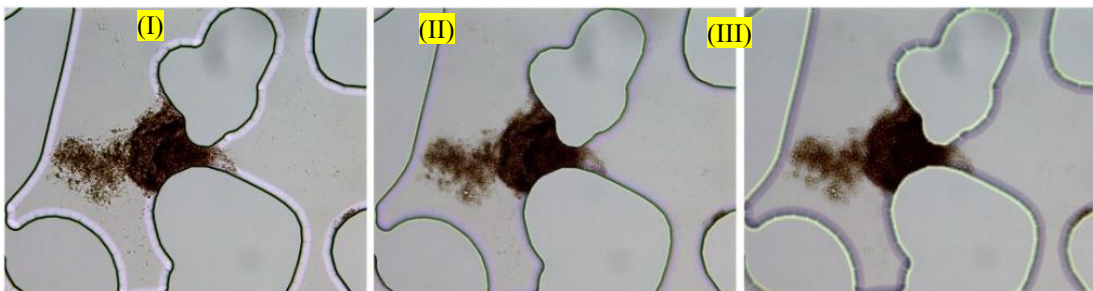


Figure 6-14 Depth profile showing the cell density at different sections of the micromodel at (I) top, (II) middle, and (III) bottom of the micromodel.

The representative elementary volume concerning biomass growth

The representative elementary volume (REV) is defined as the smallest volume at which property does not change by incremental changes in dimensions (Bear, 1988). REV is commonly used to characterize spatial scale dependencies (Hommel, et al., 2018). The size of the REV depends on a property, and it often may not be identical throughout the same pore space. Also, depending on the porous medium, or the overall dimensions of the studied problem, the REV size will vary (Hommel, et al., 2018).

The question of whether the changes in the pore space resulted from the biomass growth has occurred in an REV were studied by comparing the pore network end state at the of the BS and NF for two experiments (ROI-test 3 & TD-test). For the ROI test, the stitching of images was performed manually. As can be seen in Figure 6-15, at the end of BS flooding, the biomass has filled some of the pore spaces and flow channels; the bacterial colonization has formed more homogenously in the ROI test (I-1), while many regions are relatively free of biomass in TD test (II-1).

In phase II, biomass distribution has been massively amplified due to nutrient supply and filtration. In ROI test (I-2), a more homogenous distribution of biomass can be seen, while the TD test (II-2) displays a highly heterogeneous pattern of deposited biomass. The overall pictures of micromodel in these experiments do not quite match. Created preferential flow paths after the NF are dissimilar. This is expressly affected by filtration effect, likewise an indication that the total domain of the micromodel may not represent an REV regarding biomass evolutions in the experiments. On the other hand, different sub-domains, in which biomass is distributed more homogenously, may be considered as an REV. This matter is addressed once more in section 6.3.2.

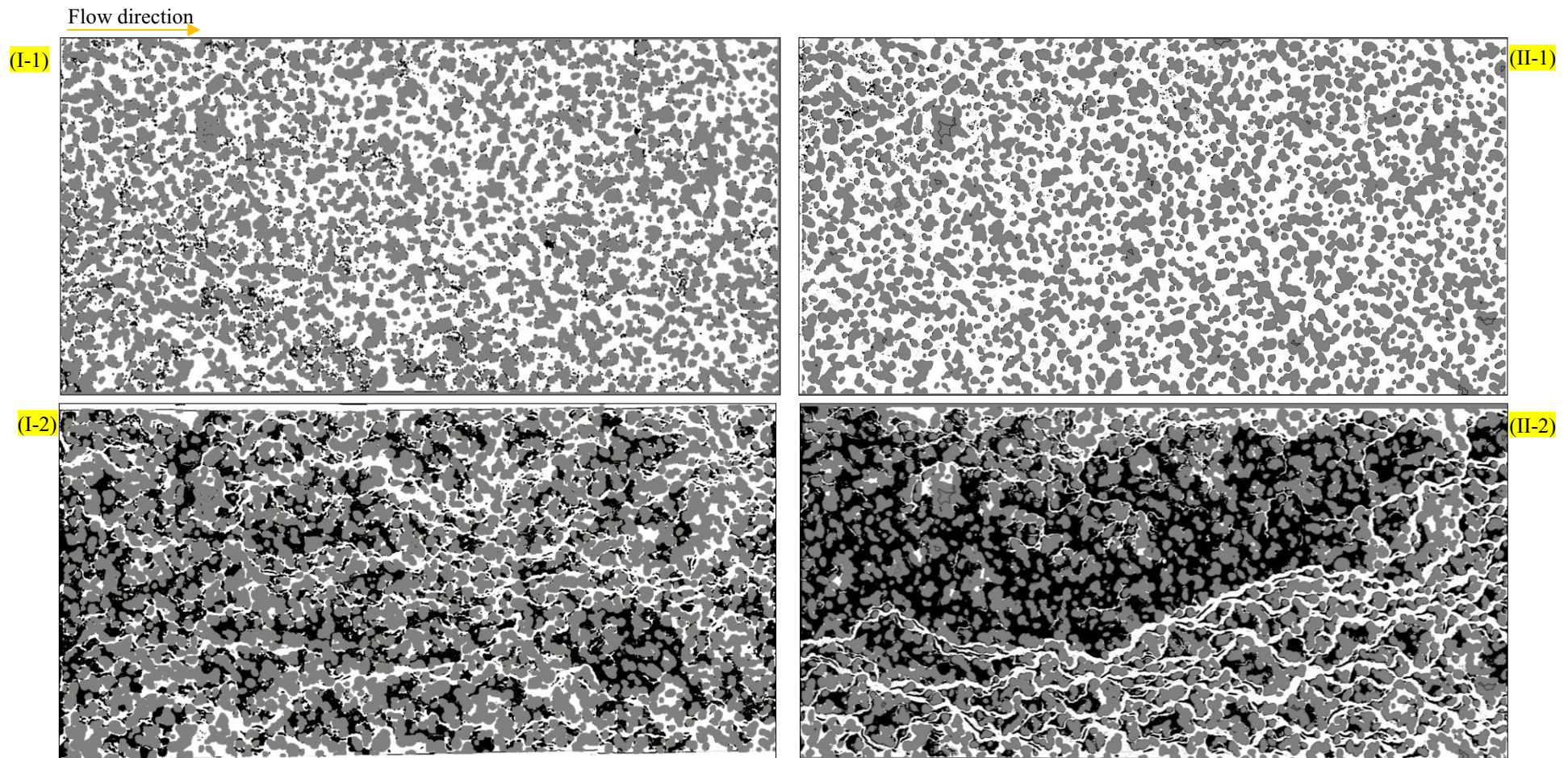


Figure 6-15 Final profile after BS and NF; on the left side: ROI-Test 3, and on the right side: TD test. (I-1): Biomass distribution at the end of BS flooding (after 27.5 hrs), (I-2): biomass distribution at the end of NF (after 40 hrs); (II-1): biomass distribution at the end of BS flooding (after 27 hrs), (II-2): biomass distribution at the end of NF (after 29 hrs). The overall pictures of micromodel in these experiments are different. Created preferential flow paths after the NF are dissimilar. This is expressly affected by filtration effect, also an indication that the TD of the micromodel may not represent an REV concerning the bacterial growth. On the other hand, different sub-domains, in which biomass is distributed more homogeneously, may be considered as an REV

Flow velocity variation in the pore-network

In a liquid medium, microorganisms (cells) act like particles, and their settling rate is a function of the fluid velocity characteristics (Donlan, 2002). Due to the distribution of various features (e.g., pore channels, apertures, and curvatures) in the pore space, various velocity regions exist (Malkovsky & Pek, 2009). Through experimentations, different velocity regions in the pore space have been detected (see Figure 6-16). This image displays the passage of bacterial cells in one frame in the pore space. In region 1, bacterial cells, which are seen as black dots, are located at a slower velocity zone compared to bacterial cells in region 2, where they are seen as strips due to their higher speed at a high-velocity zone. The time-lapse movies taken during experiments display the movement of planktonic and conglomeratic bacteria in the diverse velocity regions (see supplementary material).

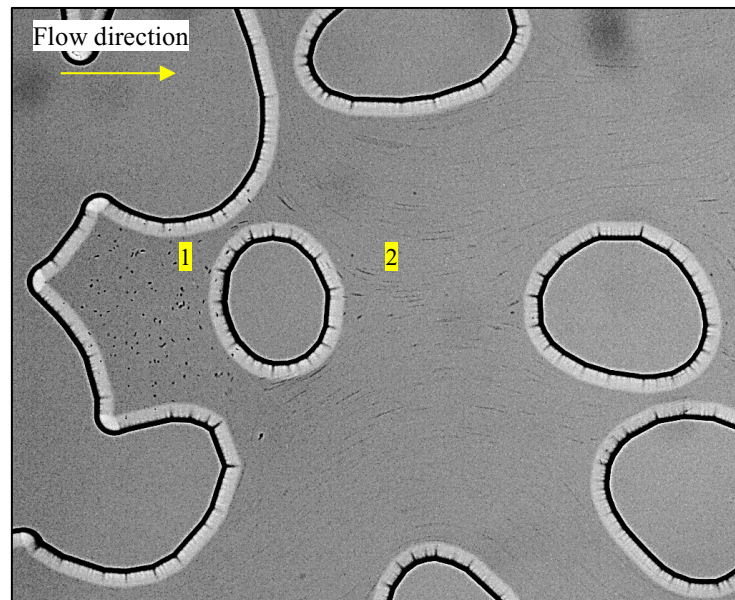


Figure 6-16 Different areas of micromodel showing varied flow velocity fields; the (1) slow and the (2) high-velocity regions.

Another finding through the experimentation was the detection of a hydrodynamic layer. A typical velocity profile in a region near a solid surface is shown in Figure 6-17. The local velocity in the stream direction (x) is denoted as u , and the distance normal to the surface as y . The velocity at the surface is zero which is often called a no-slip condition. The velocity away from the surface will have some value depending on the free-stream velocity, U_e . Between the values of 0 and U_e , the velocity profile smoothly changes asymptotically. The region, in which fluid makes a change from stream velocity to a velocity of zero at the surface is called the hydrodynamic or velocity boundary condition. For the sake of simplicity, the velocity boundary layer thickness, δ , is identified as the distance from the surface to where 99% of U_e is reached.

(Schetz & Bowersox, 2011). In literature, the biofilm is similarly treated as a solid surface where the hydrodynamic boundary condition can be seen and identified (Bishop, et al., 1997). In addition, as the velocity increase, the thickness of the boundary layer decreases (Donlan, 2002).

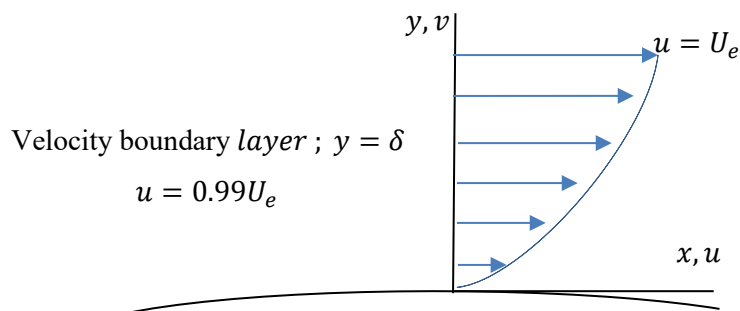


Figure 6-17 Typical velocity boundary condition [adapted from (Schetz & Bowersox, 2011)].

A sample image presenting the hydrodynamic boundary layer is displayed in Figure 6-18. As previously discussed, the discharge of the accumulated biomass in the flowlines and valves produces a cloudy stream; due to its sudden release, the concentrated fluid has a higher velocity during its discharge. This fact led to visible white traces of fluid flow that may represent the hydrodynamic boundary layer, in which the velocity in the vicinity of the surface (biomass)/liquid is negligible.

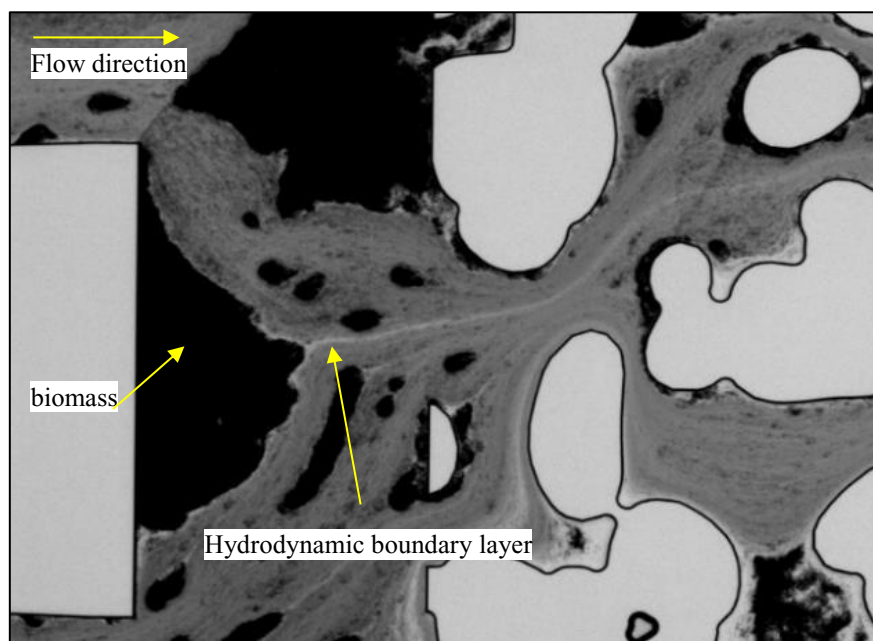


Figure 6-18 Hydrodynamic boundary layer; negligible velocity in the vicinity of the surface (biomass)/liquid, which is demonstrated as a white trace.

Future-oriented experiments

Apart from experiments in saturated medium, nutrient-limited system, and unsaturated system were tested as outlook to future investigations. Experimental details are discussed in Appendix H: Bacterial growth under the starvation condition and Appendix D: Bacterial growth and transport under unsaturated condition.

The preliminary study on bacterial growth under the limited nutrient condition (starvation condition) can represent settings in the reservoir during well shut-in, in which no extra nutrient can reach microorganisms. The results of the tests showed limited growth and no trace of biofilm formation. For future experiments, it can be suggested to expose the micromodel with some established biomass to the nutrient-limited condition. In this way, possible processes such as decreases in the growth, detachment, and biofilm sloughing can be studied.

The unsaturated test outcomes revealed the attachment and growth of bacterial cells and aggregates during the BS and NF phases; however, the entrance of gas bubbles extremely redistributed the biomass and affected the pressure response. *Lactobacillus Casei* is a facultatively anaerobic strain (i.e., can grow in both aerobic and anaerobic conditions; while it grows faster in the presence of oxygen), which is a suitable strain for testing the passive unsaturated state.

By the passive state, we refer to a two-phase condition, in which inactive gas present as an irreducible (residual) phase. The residual saturation is the fraction of the pore space, which is occupied by an immobile trapped phase. The inactive gas phase, such as N₂, allows the observations of how bacterial cells behave in the gas-water interface and in what ways biomass develops. The injection rate should also be carefully adjusted not to change the initial gas distribution in the pore-network.

The active two-phase system has the highest complexity and involves the injection of the active gas phase. The active gas phase, in the case of hydrogen storage and conversion, is a mixture of H₂ and CO₂, which is the nutrient for Archaea. The product of microbial activities, in this case, is biomass and CH₄. In this circumstance, we intend to find influencing controlling parameters that are involved in hydrogen consumption, biomass growth, and plugging in porous media.

6.3 Numerical modeling

The changes in the flow field and permeability with the biomass growth were investigated in the virtual pore space derived from image binarization. Using GeoDict[®] software (<https://www.math2market.com>), and via the FlowDict module, numerical models were constructed. The LIR solver was selected for solving slow creeping flows governed by the Navier-Stokes equation from fluid flow equations, and advection-diffusion for solving the transport (Linden, et al., 2019).

Different mathematical equations can be selected to solve the flow field; this depends on the model structure. By choosing Stokes equations, the flow when the particles' size is one or several voxels is characterized. In case the particles are much smaller than the scale of the structure, the Brinkman equations (e.g., Stokes-Brinkman and Navier-Stokes-Brinkman) can be selected (Wiegmann, et al., 2014). The velocity fields in FlowDict, are computed via setting up the pressure drop in the three directions and choosing the computation directions (flow direction) in the solver (Linden, et al., 2019). Flow permeability, as the structures' intrinsic property, is strongly dependent on its geometry (Linden, et al., 2019).

Navier-Stokes equations are used for the standard description of the fluid flow. In this case, purely viscous, incompressible, and stationary flows (no time dependency) are considered (Wiegmann, et al., 2018). Mass and momentum conservation can be described in terms of pressure-velocity formulations:

$$-\mu\Delta\vec{u} + (\rho\vec{u} \cdot \nabla)\vec{u} + \nabla P = \vec{f} \text{ (Conservation of momentum)}$$

$$\nabla \cdot \vec{u} = 0 \text{ (Conservation of mass).}$$

In the above equations, μ is the fluid viscosity, ρ is the fluid density, \vec{u} is the fluid velocity, P is the pressure, and \vec{f} is the force density. In case of a very slow flow, the inertia term $(\rho\vec{u} \cdot \nabla)\vec{u}$ from the Navier-Stokes can be omitted to reach the Stokes equations; as the velocity and the gradient of the velocity are small values, the product of these terms is also much lower (Wiegmann, et al., 2018). Stokes equation is written as follows:

$$-\mu\Delta\vec{u} + \nabla P = \vec{f} \text{ (Conservation of momentum)}$$

$$\nabla \cdot \vec{u} = 0 \text{ (Conservation of mass).}$$

As mentioned, the Navier-Stokes-Brinkman equations are used when the particle sizes are much smaller than the filter media. In these equations, an additional term is added to account for particles of sub-grid size. These equations link the free flow in the pore network, which is often described by the Darcy equation (Wiegmann, et al., 2018).

$$-\mu\Delta\vec{u} + (\rho\vec{u}\cdot\nabla)\vec{u} + \mu K^{-1}\vec{u} + \nabla P = \vec{f} \text{ (Conservation of momentum)}$$

$$\nabla\cdot\vec{u} = 0 \text{ (Conservation of mass).}$$

Here K^{-1} is the flow resistivity. In empty cells, K^{-1} vanishes from the equation, and we have the Navier-Stokes equation once more. In the porous cells, flow resistivity becomes so large, consequently \vec{u} becomes very small. The velocity terms in this regime may be neglected, resulting in Darcy's law (Wiegmann, et al., 2018):

$$\vec{u} = -\frac{K}{\mu}(\nabla P - \vec{f}) \text{ (Darcy Law).}$$

Model setup

The computational model was employed for two sets of experiments (one on the total domain of the micromodel and one on the sub-domain). After the image acquisition and processing step, images were imported in GeoDict[®]. Then properties were assigned, boundary conditions were adopted, and finally, simulations were carried out via FlowDict module. Avizo[™] software (Thermo Scientific[™]) was used for visualization of the results. For this purpose, the output files from Geodict were converted into readable files for Avizo[™] using an in-house code written in Matlab (courtesy of Dr. Enzmann).

Even though visual information from micromodel experiments are in 2D, models were simulated as 3D structures, assuming a sharp etching in the channel depth and the biomass as a non-porous material. As the side view of micromodel shows (see Figure 6-3, II), the wet-etching technique results in curvature in the depth profile, and therefore, the accessible volume of micromodel is less than the sharpened etched profile. To compensate for this circumstance, we have optimized the micromodel depth by checking the estimated permeability value of a water-saturated micromodel against the experimental value. Once this step was fulfilled, simulations on the selected images were performed, and the permeability values at each step were calculated.

Figure 6-19 displays an example of the model description on ROI and TD models, in which boundaries are indicated. Boundary conditions in all directions, apart from the flow direction, were the same for both models (see Table 6-2). "No-slip" boundary condition was assigned in the z -direction and the top and bottom of micromodel (y -direction); this boundary condition represents the condition of the solid/fluid interface. For the ROI model, the symmetric boundary condition was set, which defines a mirror face/surface. The selection of this boundary condition decreased the computational domain size and enabled the modeling of a sub-domain. In the TD model, the periodic boundary condition was employed. Periodic boundary condition in the flow direction was due to the assumption of homogeneity of the micromodel in the x -direction.

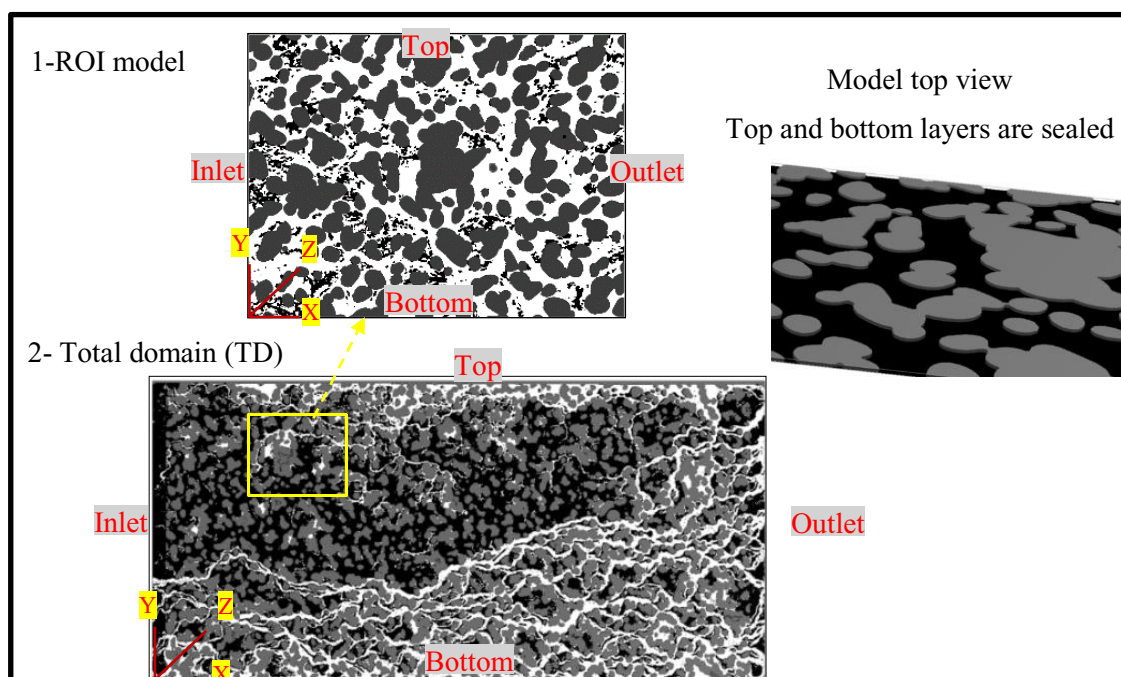


Figure 6-19 Model description for simulations. The top view of the models are sealed to account for a “no-slip” boundary condition.

Table 6-2 Description of models’ boundary conditions

Model	BCs (flow, x -direction)	BCs (y -direction)	BCs (z -direction)	Voxel size (μm)
ROI	Symmetric	No-slip	No-slip	1.83
Total domain (TD)	Periodic	No-slip	No-slip	1.83

In the numerical models, a viscous, incompressible fluid flowing stationary was assumed to avoid the time dependency in the simulations. The viscosity of the bacterial suspension and nutrient were assigned to the viscosity of autoclaved water (measured in the lab at 37°C). This assumption was justified as the viscosity values for these solutions did not deviate much from the autoclaved water (also see Figure 6-2). The Error bound threshold of 0.01 was assigned for the flow permeability as the simulation termination criterion.

Simulations on the TD model were performed based on the pressure difference across the micromodel to account for the pressure variations due to bacterial growth and filtration at different flooding times. However, the ROI model was always run based on a single pressure drop, since the pressure drop, in this case, didn't correspond to the changes in the sub-domain.

Figure 6-20 displays a visualized sample output of overlaid velocity and streamlines from the ROI simulation, in which water was flooded at a rate of 0.2 ml/hr. The zoomed-in image shows the higher velocity values at the narrower pore throats; the streamlines show the direction of flow.

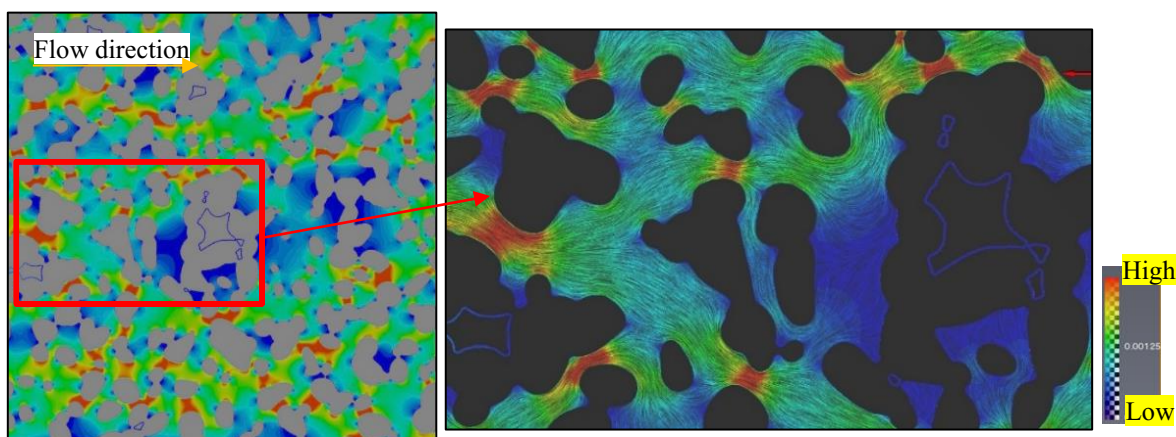
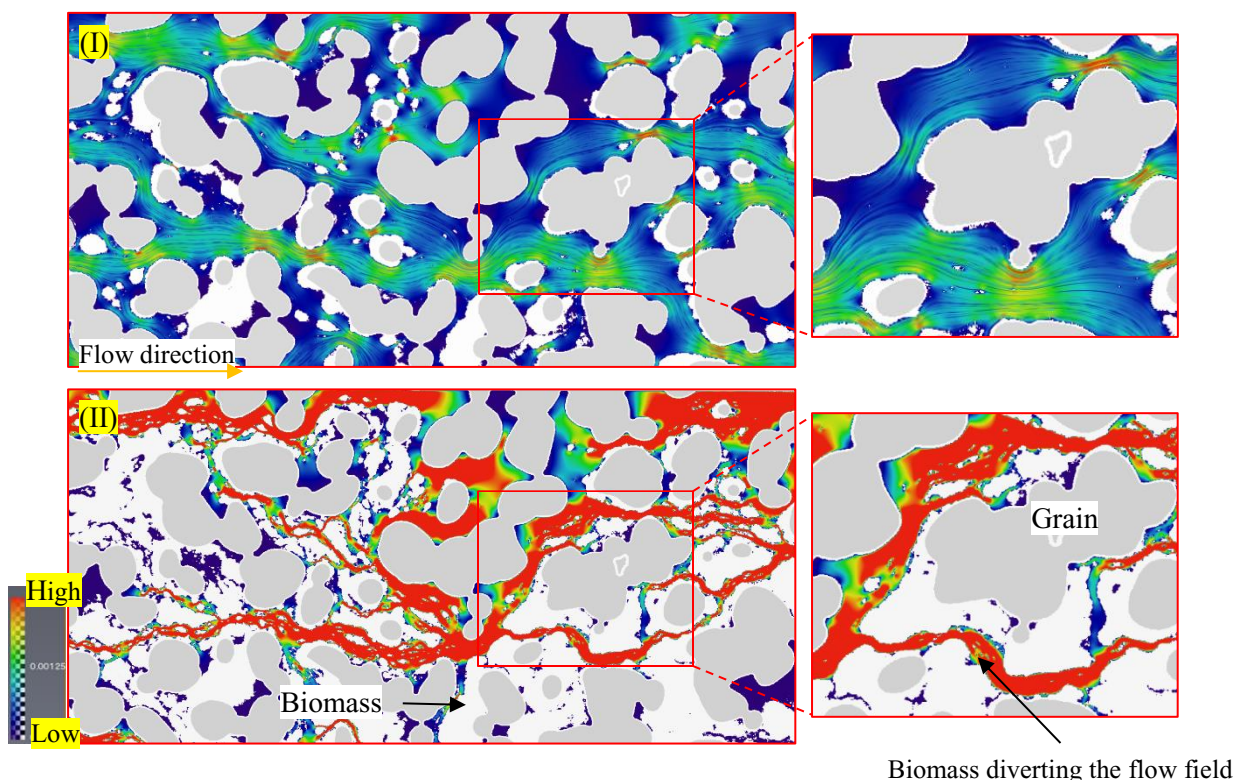


Figure 6-20 Visualized simulated results of overlaid velocity and streamline in a water-saturated micromodel. As expected, velocity magnitude values are higher in narrower pore throats.

Another output from a model with existing biomass is presented in Figure 6-21. In this figure, two steps during the NF is displayed, and the impact of biomass growth on the velocity field is seen. The white masses represent the biomass. The growing biomass patches tend to reduce their access to flow while increasing the flow velocity and diverting flow directions. In the zoomed-in images, moving from step I to II, growth of the biomass has led to increase in velocity values, as well, the velocity field is diverted.



Biomass diverting the flow field

Figure 6-21 Velocity field is shown for two steps during the NF. From I to II, the bacterial activities are enhanced. The growing biomass patches tend to reduce their access to flow while increasing the flow velocity and diverting flow directions.

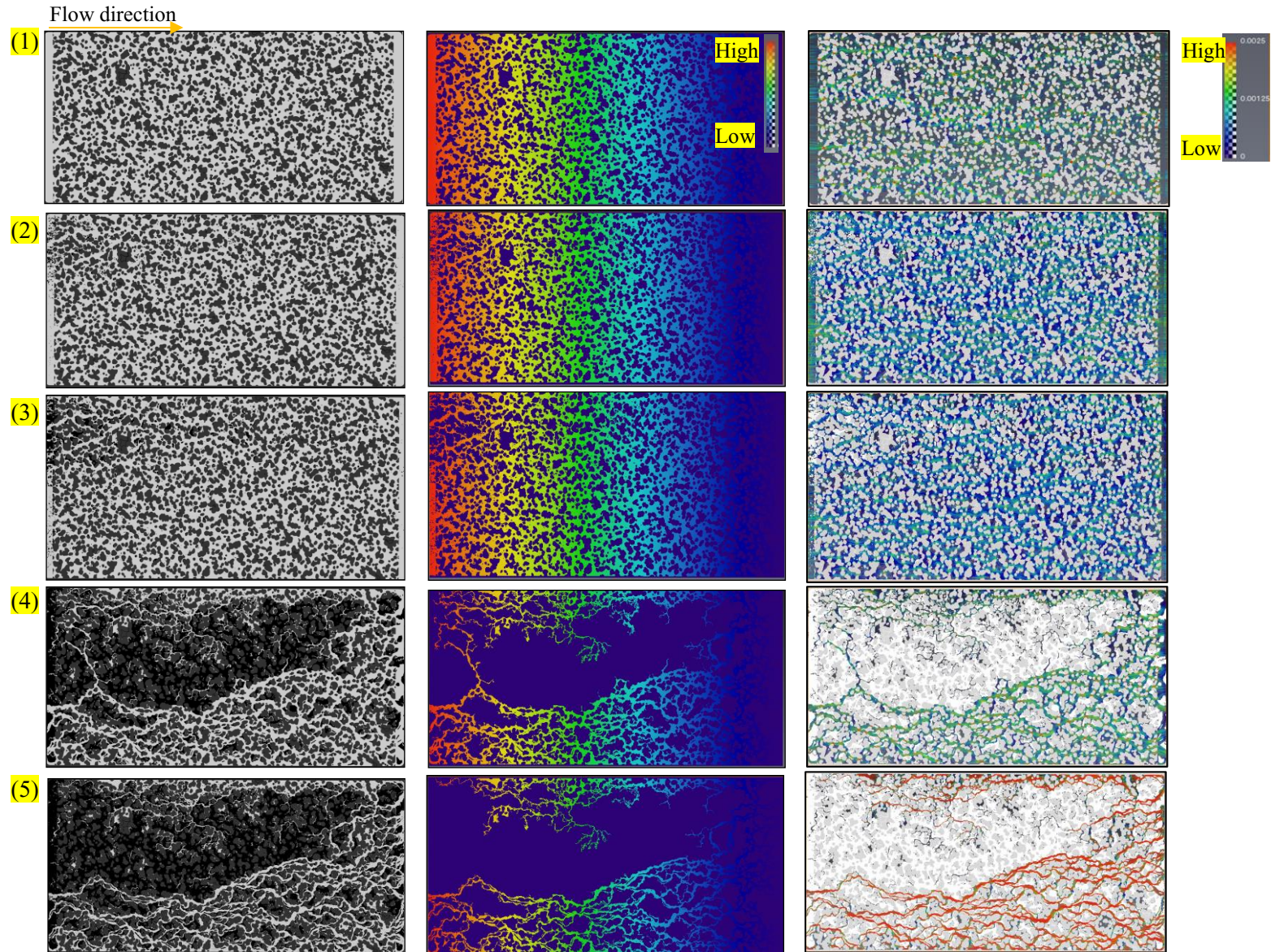


Figure 6-22 Biomass growth, pressure profile, and streamlines at different steps during BS and NF. (1): start of BS flooding; (2) end of BS flooding (27hrs); (3) after 3.5 hrs of NF; (4) after 20 hrs of NF; and (5) at the end of NF (29hrs). As the biomass is assumed as a nonporous material, pressure values in these areas are zero.

Figure 6-22 shows the bacterial evolution, and simulated pressure and streamlines field at different flooding times. Image 1 and to 2 correspond to the initial and the end state of BS flooding after 27 hrs of flooding. Image 3, 4, and 5 correspond to three steps during NF after 3.5, 20, and 29 hrs of flooding. Upon the microbial activity enhancement, more biomass is deposited in the pore network, and the pore space is deformed, reduced, and the pathways become narrower; consequently, the velocity magnitude values rise in narrowing pore spaces.

Velocity histogram counts for the mentioned steps are plotted in Figure 6-23. The same findings are seen. Velocity magnitude values increase by bacterial growth, except for NF after 3.5 hours of flooding. This exception is due to the assigned delta pressure value for this simulation point, which was smaller than the delta pressure for the initial state and BS simulations. As the biomass features were assumed as nonporous material, zero values increase by injection time (see the zoomed-in image), i.e., the microbial growth.

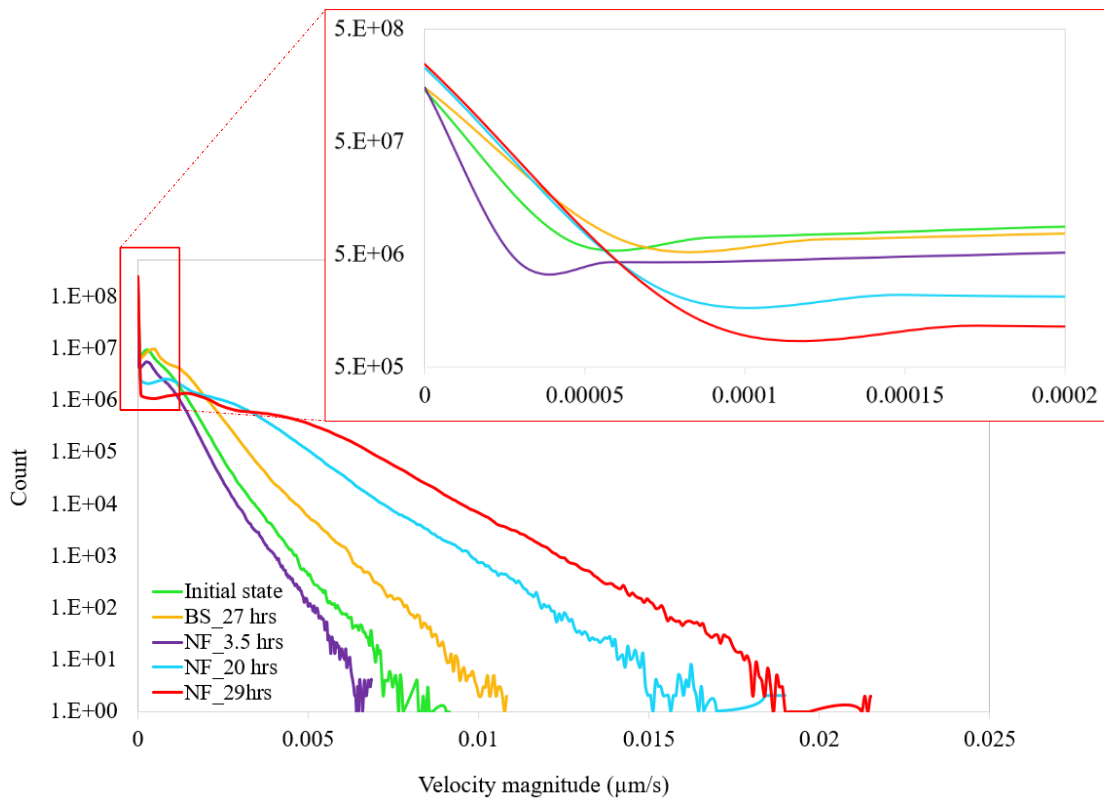


Figure 6-23 Comparison of velocity histogram counts at different times during the BS and NF phases.

Upon microbial activity, more biomass is deposited in the pore network, and the pathways become narrower; consequently, the velocity magnitude values increase in narrowing pore spaces. Likewise, as the biomasses were presumed as nonporous material, zero values increase by injection time (zoomed-in image).

6.3.1 Correlation between initial bacterial deposition and flow velocity

The relationship between biomass growth and hydrodynamics of porous media is two-folded. Biomass growth can change the hydrodynamics of pore-space; at the same time, the hydrodynamic conditions influence the characteristics of biomass growth (Gerlach & Cunningham, 2011). The coupling of the flow hydrodynamics and bacterial deposition and biofilm formation in porous media has been of interest to researchers in recent years. A study by (Carrel, et al., 2018) showed that the wall shear stresses control the spatial biofilm development in a 3D pore network. Similarly, (Aufrecht, et al., 2019) suggested a correlation of clogging probability with shear rate regimes.

Comparisons between the simulated velocity field and the experimental data suggest a link between the spatial distribution of the bacterial cells and aggregates (deprived of filtration impact) and the flow hydrodynamics across the pore space (Figure 6-24). Image (I) presents the microscopic image of bacterial growth during the NF and before filtration occurred. Image (II) displays the simulated velocity field in a water-saturated medium, and Image (III) shows the overlaid images. As can be seen, microbial attachment and biomass growth have occurred in low-velocity areas, while high-velocity channels contributed to nutrient transportation to the outer channels.

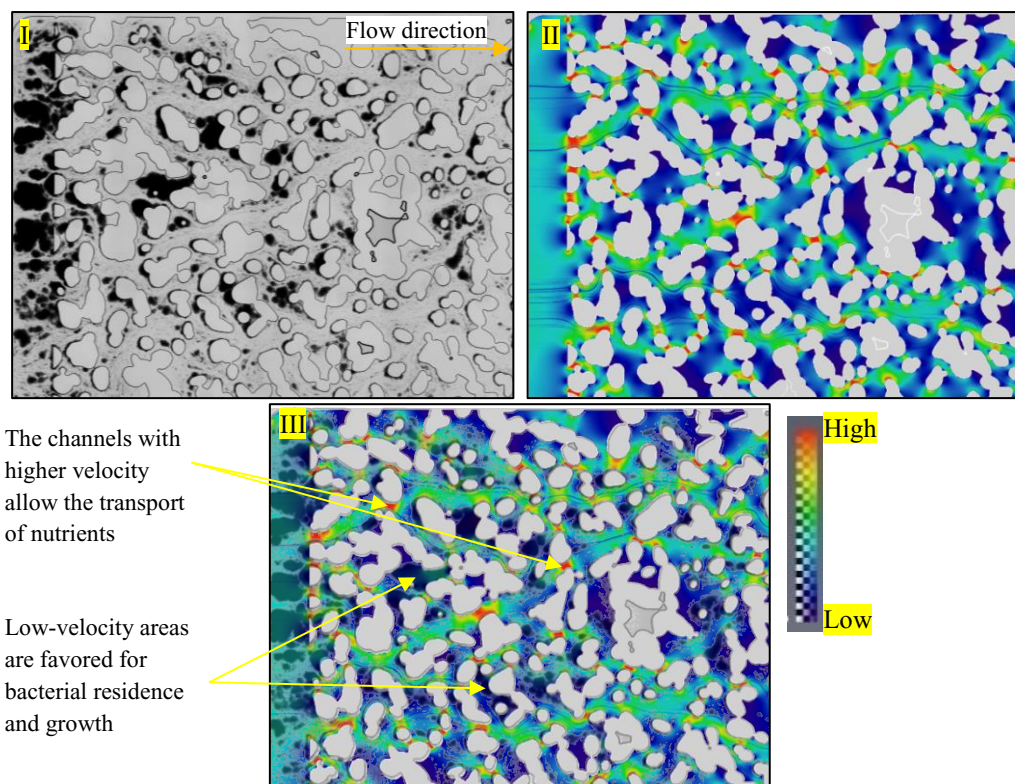


Figure 6-24 Microbial deposition correlated with the simulated velocity profile. (I): Bacterial deposition during NF deprived of filtration effects; (II): the simulated flow field in a water-saturated micromodel; (III): the overlaid images displaying a good agreement of the microbial deposition tendency in the lower velocity areas and the transport of nutrient in higher velocity channels.

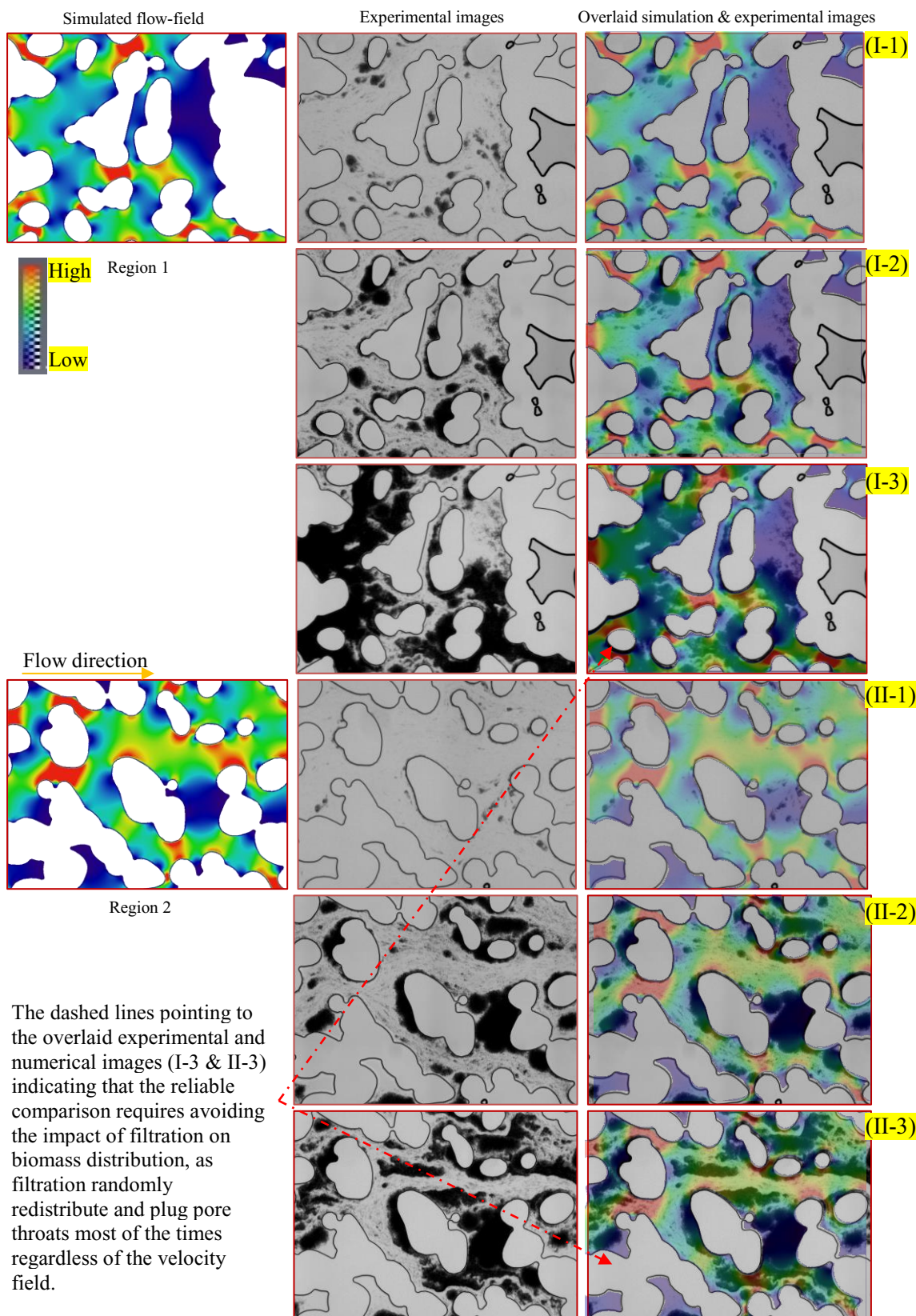
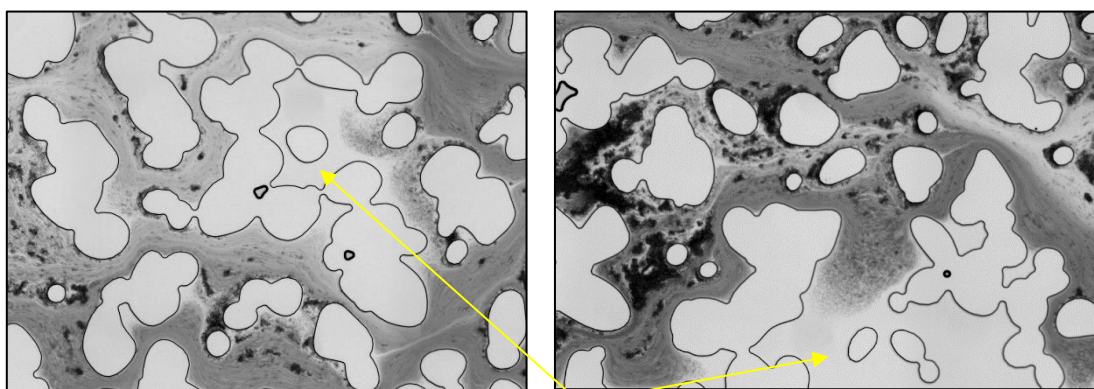


Figure 6-25 Correlation between initially deposited bacterial cells (state 1), accumulated biomass during NF without the influence of filtration (state 2), and after filtration (state 3) for two selected regions (I&II). In the first, second, and third columns, the simulated velocity field, experimental image, and overlaid images are shown. An excellent agreement among initial bacterial deposition and the growth with the simulated velocity field is detected. However, after filtration, biomasses are redistributed regardless of the velocity field.

In Figure 6-25, two areas within the micromodel are selected, and the initial bacterial deposition, added growth during NF, and the biomass redistribution led by filtration events are displayed. Each step is compared to the simulated velocity field by overlaying the images. The initial attachment of bacteria to the surface (state 1) always occurs in the low-velocity regions. Once bacteria have attached to the surface, their distribution is not only affected by velocity field, but also by their growth. Also, some bacterial cells may detach and move and reside in other locations. Under the NF growth condition, the bacterial cells' distribution and pore-scale hydrodynamics are coupled (state 2). Once the cloudy stream enters the pore-space, the bacterial cells irregularly redistribute, and many pore throats are plugged regardless of the velocity field (state 3). Therefore, a reliable comparison requires avoiding the impact of filtration on biomass distribution.

Even though the initial deposition of bacteria did not occur in the same pores in replicate experiments, a trend in the velocity distribution in pore-space where cells were initially deposited, was detected. The likelihood of initial bacterial deposition was always higher in low-velocity regions. However, we have observed that not all low-velocity parts were favored by bacterial cells. The particle tracing experiments, which will be discussed in section 6.4, revealed the existence of preferential paths, as well as areas, which were not affected by particles at all. The same observations have been detected during the passage of a cloudy stream. As can be seen in Figure 6-26, despite the flow of the concentrated fluid, some low-velocity regions were not affected. It is very likely that despite the low-velocity in these regions, the bacterial cells rarely diffuse to these areas to adhere to the surface; as well, nutrients follow the same rule.



Areas, which were not influenced by flow of bacteria (low velocity)

Figure 6-26 The passage of the cloudy stream through micromodel showing low-velocity regions in the micromodel, which are not prone to bacterial deposition.

Correlation between bacterial deposition and growth and hydrodynamics of pore space seems to be promising; however, further analysis and quantifications on this matter is required to complete our understanding. In natural systems, we deal with the microbial consortia, which

are composed of a variety of species. Within the microbial communities, each strain competes and performs chemically tough tasks to avoid its elimination from the consortium (Jawedac, et al., 2019). This may be one of the factors that complicate the prediction of a relationship between the hydrodynamics of a microenvironment and biofilm growth (Coyte, et al., 2017; Baveye & Darnault, 2017).

Our contribution develops a basic framework to understand how hydrodynamics affects bacterial evolution in porous environments. There are several encouraging extensions to our current study that will be discussed in chapter 7.

6.3.2 Microbial growth impact on hydraulic properties of pore-network

Diverse processes that are coupled to fluid flow and interacting with it can alter the pore surface network or pore morphology; examples are sedimentation, clay dispersion, formation drying and salt precipitation, and microbiological activities (Ott, et al., 2014; Ott & Oedai, 2015; Hommel, et al., 2018; Pavelic, et al., 2011). Hydraulic properties of the porous media can be described and measured to evaluate the morphology alteration impacts on the flow field (Hommel, et al., 2018). The permeability-porosity relationship for two models (TD and ROI) was estimated to investigate the effect of bacterial growth and filtration on pore space.

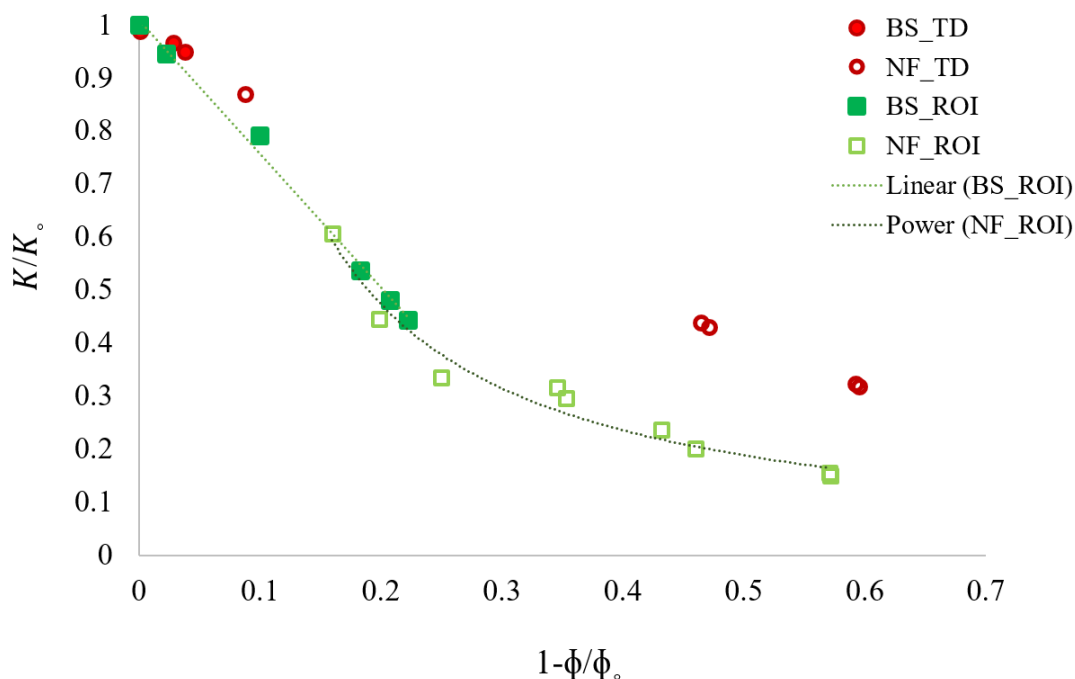


Figure 6-27 Relationship of permeability and porosity reduction for TD and ROI models. Trendlines for ROI models are plotted, showing a linear trend for the BS phase and a polynomial trend for the NF phase. An expressive trendline for TD simulations cannot be made due to insufficient data and heterogeneity that was led by filtration.

Via numerical modeling, permeability values were computed. The selection of images was made cautiously to capture the main alterations at different flooding times. The porosity then calculated from the segmented images. The normalized porosity-permeability (Φ/Φ_0 and K/K_0) reduction relationships for two phases of flooding are displayed in Figure 6-27.

The simulated models showed a different porosity-permeability relationship. As discussed earlier, the micromodel medium may not be considered an REV concerning biomass evolution in the experiments. Therefore, having an accurate statement for the porosity-permeability relationship is not possible. Yet, the trendlines for the ROI model appear to be more meaningful as the distribution of biomass in the ROI model was more homogenous. A linear and polynomial trendline for the BS and NF phases can be assumed, respectively. A distinct trendline for TD dataset may not be driven. Possible explanations for this are because of insufficient data points and due to a highly heterogeneous biomass distribution that was led by filtration events. Selected images corresponding to the porosity-permeability simulated points are presented in Appendix G: Porosity-permeability relationship.

Some aspects may be considered to improve the estimate on the hydraulic properties of the pore network. First, selecting a larger area of investigation to likely present an REV; secondly, repeating the tests until some resemblance in results (both quantitative and qualitative) is observed. Additionally, as found in the ink-injection test, the biomass structure indicates to have some internal porosity and permeability. In spite of this evidence, the biomasses were treated as non-porous materials in the numerical model. Although this way of biomass modeling is widely accepted, the extent of the physical penetrability of biomass can influence the predicted hydraulic conductivity. Therefore, additional numerical models are required to test the biomass permeability and its effect on the hydraulic properties of the pore network.

6.4 Particle tracing in an established medium of biomass

Particle transport in fluid flow, which commonly refers to particle-fluid and particle-particle interactions, has a broad range of applications. These include managing and engineering environmental contaminants and related issues, underground-water management, removal of microbial and fines plugging in injection wells, MEOR, and many more (Abu-Ashour, et al., 1994; Wilson, et al., 1986; Jack, 1993; Molnar, et al., 2015; Bradford, et al., 2002).

Particle tracing in microfluidics has been experimented by (Marouf, 2018) in association with this doctoral dissertation. A similar microfluidic system was employed to describe the trajectories (e.g., flow lines) of neutrally buoyant micro-polystyrene particles with a 10- μm diameter, in a water-saturated medium. In his work, an experimental procedure combined with an image processing workflow, and a matrix-based programming language (MATLAB®), were utilized to analyze and visualize the fluid flow in porous media. Additionally, the particles' instantaneous and average interstitial velocities at different flow rates were measured. The experimental work and analysis provided useful insights into complex processes, such as microorganisms' transport in porous media.

In this section, some of the experimental and numerical results from Marouf, (2018), are presented. With the completion of experimentation in a water-saturated micromodel, an outlook for the particle transport in a medium with established biomass was tested, and the discoveries are discussed. Finally, preliminary numerical tracing modeling findings are described, and the directions for future work are proposed.

Initially, the average particle residence-time at a flow rate of 0.05 ml/hour was compared with the estimated water velocity from Darcy's equation across the micromodel. The experimental injection flow rate was chosen in a way to both satisfy the laminar flow assumption and to maintain the visibility and traceability of the particles. The comparison revealed that experimental particles were transported with a higher average velocity than water (details on the calculations can be found in (Marouf, 2018)). The outcome was consistent with previous research approving that larger colloidal particles transport with a higher average velocity due to their preferential pathways (Ginn, et al., 2002; Chrysikopoulos & Sim, 1996; Sirivithayapakorn & Keller, 2003).

As the next step, the particles-trajectories analysis workflow was developed to track the motion of suspended particles at a rate of 0.005 ml/hour in a region of interest. For this, a sufficient number of image sequences were acquired, and the Particle Tracker 2D/3D plugin in ImageJ2/ Fiji® was utilized. This plugin implements the feature point detection and tracking

algorithm; it permits the visualization and analysis of the detected particles, as well as previewing their trajectories individually and collectively (Sbalzarini & Koumoutsakos, 2005). The exact x , y , and z coordinates were saved for each particle's centroid within each time frame in the output file. The trajectories were generated by linking each detected particle with what was thought to be the counterpart in the previous time frame. If a particle disappeared from some frames; the linking algorithm executed an interpolation function to correlate the last detected coordinates with the next detection and filled these detection gaps (Marouf, 2018). A sample visualized flow paths, and the output table by this plugin is displayed in Figure 6-28.

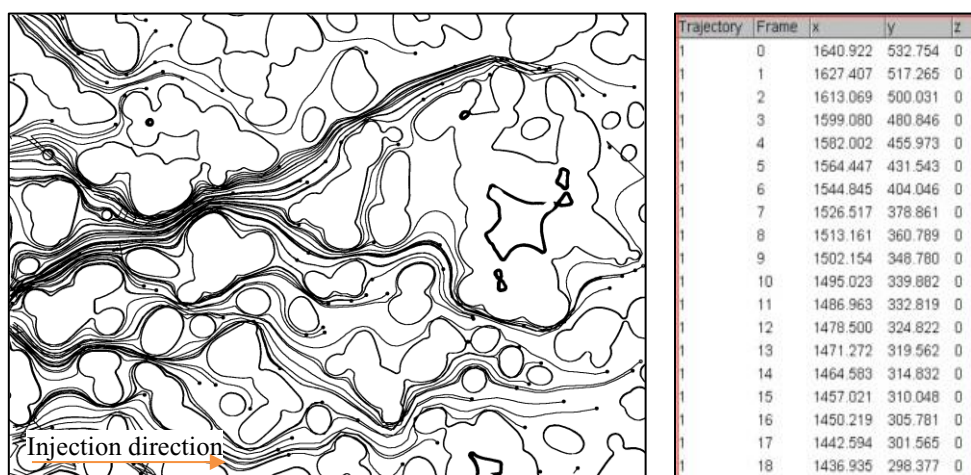


Figure 6-28 Left: visualized particle trajectories via developed workflow. Right: the Particle Tracker 2D/3D output table providing exact x , y , and z coordinates [source: (Marouf, 2018)].

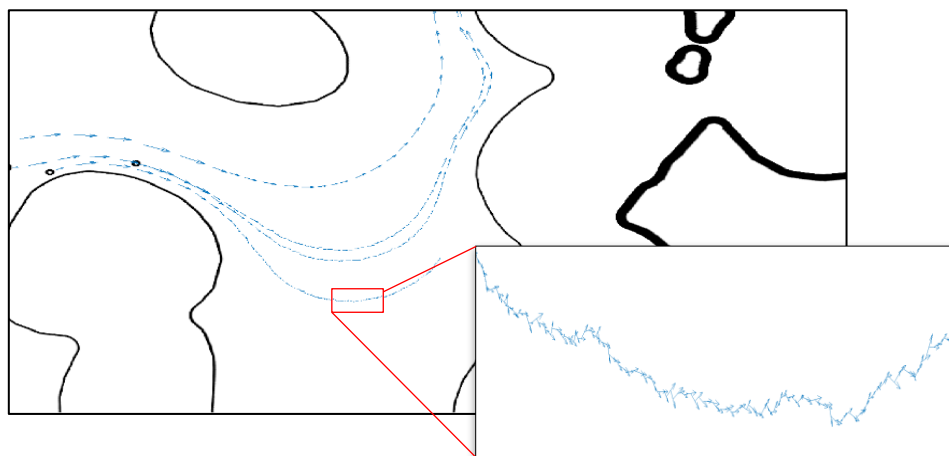


Figure 6-29 A sample of velocity computation for the traced particles, performed in MATLAB. Brownian motion effect is highlighted [source: (Marouf, 2018)].

Finally, by combining the Particle Tracker 2D/3D output table file with a code written in MATLAB®, the average and instantaneous interstitial velocity were computed and visualized. For this, the particles' coordinates' information was imported into MATLAB®, and the particle's velocity magnitude at each timeframe was computed. A sample result is displayed in Figure 6-29. Surprisingly, Brownian motion was observed in some low-velocity areas within

the pore network, which indicates the relatively high dissipation effect of Brownian motion due to the particle's collisions with water molecules (Marouf, 2018).

In summary, a workflow was developed, to quantitatively visualize the flow trajectories. The direct observation of particles' flow and average velocity measurements proved the early breakthrough behavior of particles in the saturated micromodel. The existence of particles' preferential flow pathways was demonstrated. Moreover, the diffusion effect on slow-motion particles was observed. Additionally, during these experiments, some inaccessible zones for particles to transport within the pore space were detected; these observations deliver noteworthy information for correlation of hydrodynamics and initial locations for bacterial deposition, which was discussed earlier (see section 6.3.1). The potential preferential pathways may highly contribute to nutrient dispersion in the pore space, while favored low-velocity regions for bacterial depositions must be differentiated from areas that are not influenced by particle transportation.

We extended the tracing experimentation by flooding the same micro-polystyrene particles into a medium, in which biomass had already developed, and the pore network contained bacterial suspension. Bacterial cells produced a sticky and sluggish solution that caused a completely different movement for particles compared to the water-saturated situation. In this case, not only particles transported but also bacterial conglomerates in different sizes moved along the fluid stream. Sometimes backward particle movements and often particle trapping have been observed (also see the time-lapse movies of tracing experiments in the supplementary multimedia material). An example experimental image is shown in Figure 6-30.

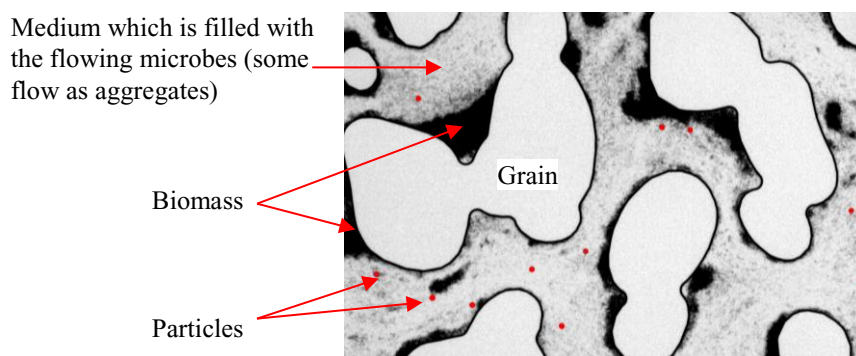


Figure 6-30 An experimental image of particle tracing in a medium with established biomass.

To visualize the particle trajectories, images corresponding to a series of particle flooding in a porous medium were imported into ImageJ2/ Fiji® as a stack. A stack of images is “multiple spatially or temporally related images that are displayed in a single window”. Analysis of a stack was done by the Z-projection method, in which different projection methods were applied to the pixels within the stack to track the particle movements (Ferreira & Rasband, 2012).

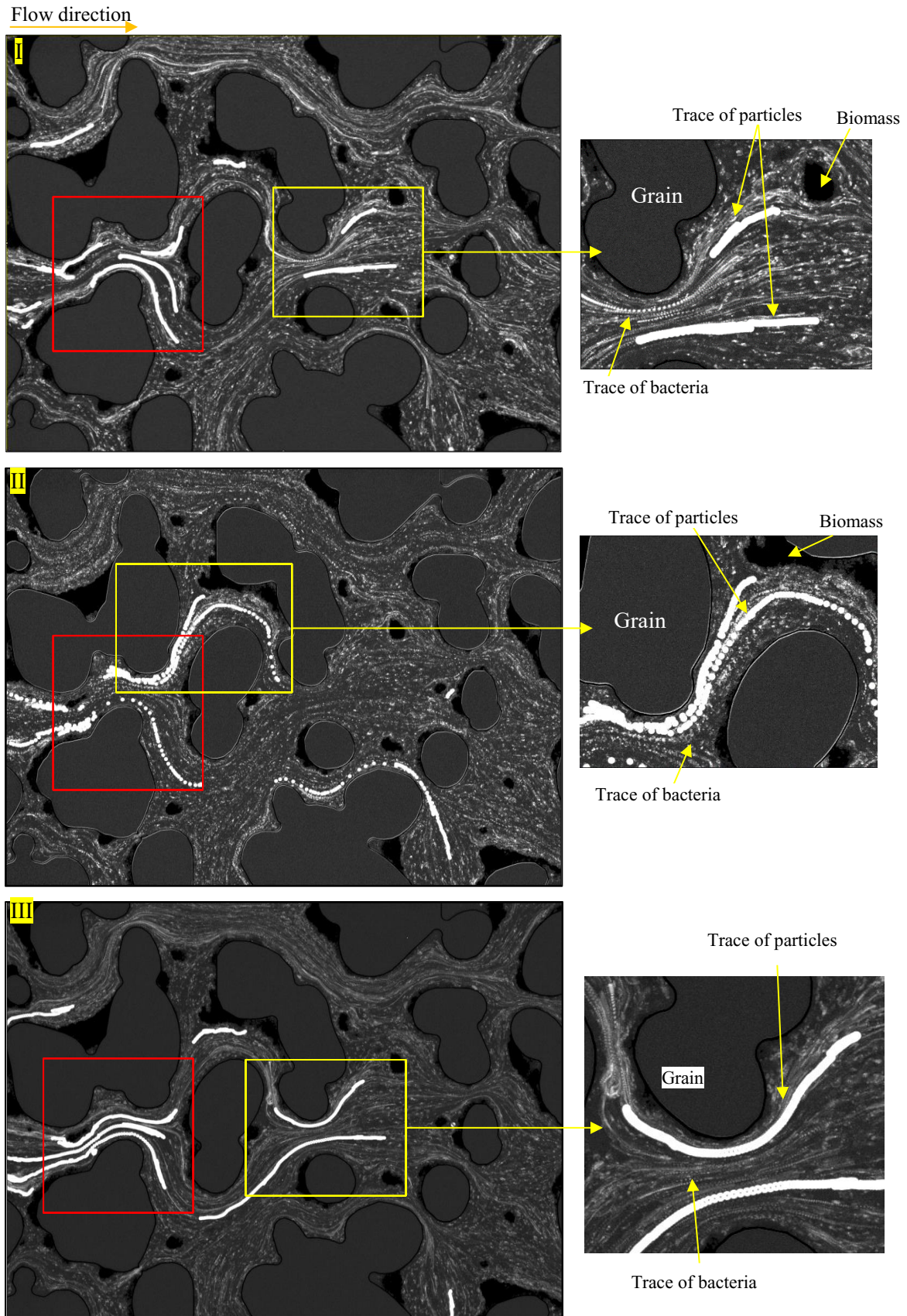


Figure 6-31 The resulting image analysis for particle tracking in porous media with established biomass at different times (I, II & III); here, both particles and bacterial conglomerates with different sizes could be traced. Similar preferential flow paths can be seen in the red square.

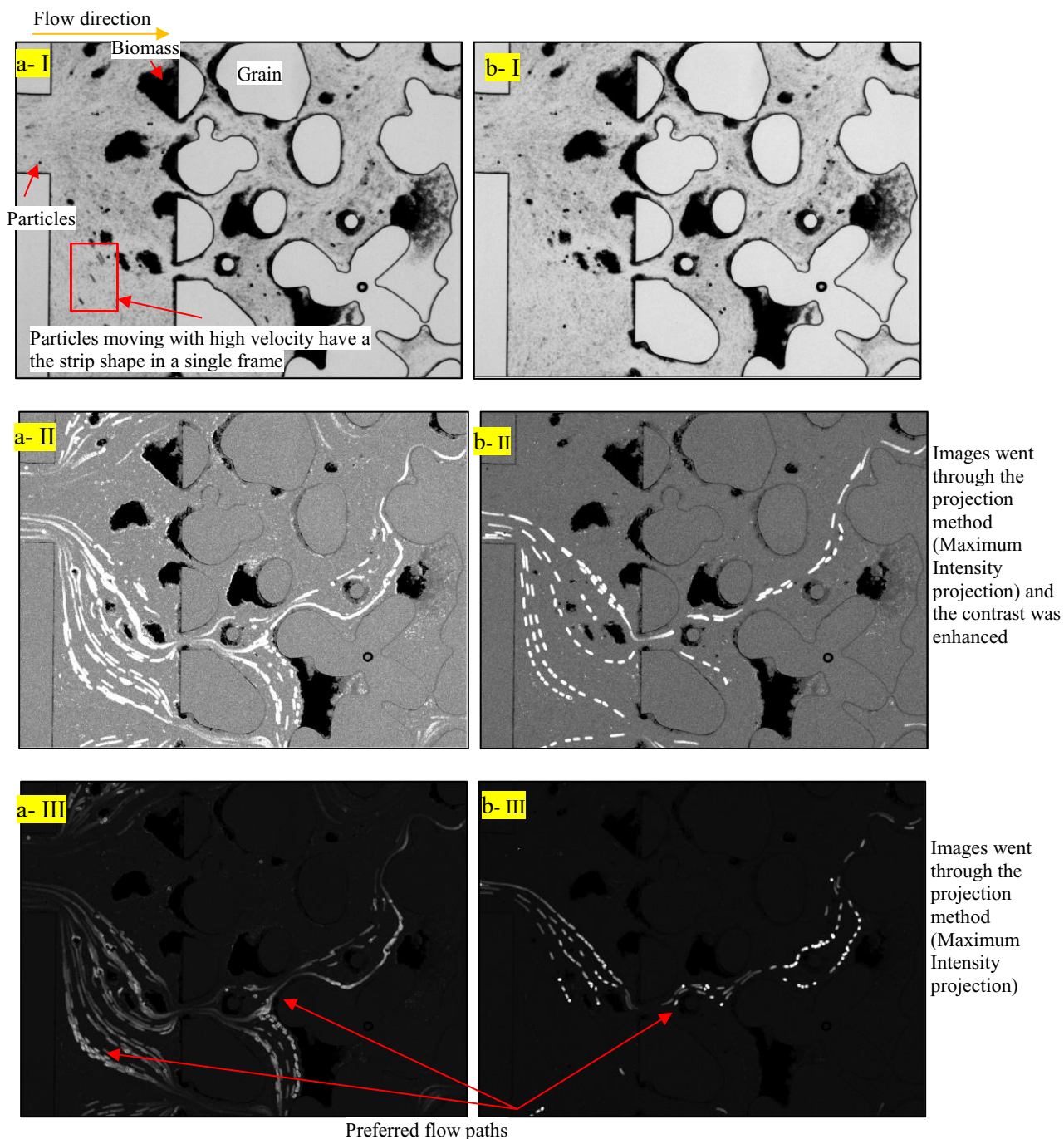


Figure 6-32 Particle tracking flooded with a high rate, was tested at different times (a & b). In (I), one experimental image is shown. Particles moving with a higher velocity are distinguishable with the strip shape. The images as a stack were analyzed by the projection method analysis and are shown in (II& III) by different visualization methods.

The resulting outputs for three experiments in an identical location are displayed in Figure 6-31. Apart from particles, suspended bacterial colonies were traced. As can be seen in the images, and especially in the zoomed-in regions, bacterial conglomerates with different sizes were traced along with the particles. The white traces sometimes appear as lines in various thicknesses, and occasionally as dots by different dimensions. Even though data points were

limited, some similar preferential pathways were detected, which are highlighted in the red squares. Time-lapse movies are available in the supplementary material.

In another test, particles were injected with higher velocity. This experiment repeated at the same location for different sequences (see Figure 6-32, a & b). State (I) presents a snapshot of the experimental image. Some particles moved with a higher velocity, which appeared as stripes. States (II) and (III) display the results of the stack images that were analyzed by the projection method with different contrast enhancement. In the first experiment, a larger number of particles passed through the medium, and consequently, more flow paths were detected. In the second experiment, fewer particles were flooded; however, they seemed to take the same routes.

Particle tracking in a medium with biomass and the bacterial suspension was a challenging task due to the lack of information about the complex fluid. Complex fluids have unusual properties and are referred to as gases or liquids containing suspended particles within them (Lappa, 2004). Even though the movement of particles and bacterial aggregates were assessed and visualized, it is difficult to describe such results and make conclusive statements. Thus, further investigations with this regard s required. Nonetheless, we benefited from the experimental observations and analysis in setting up the numerical tracing models (e.g., the adhesion model for particle-biomass).

Preliminary numerical results on particle transport

We have simulated the flow behavior of the suspended particles in water in a medium with established biomass. An experimental image during NF of an ROI test was selected, and the flow of particles was modeled. Models were run on GeoDict® via the FilterDict module. FilterDict was assigned to the calculation and visualization of particle motion and deposition in microstructures. Particle deposition simulation was based on local flow velocities or friction, and Brownian motion (Wiegmann, et al., 2014). Before displaying the numerical results, the main features in the FilterDict module are discussed as follows.

FilterDict modeling options

FilterDict supports simulations of different filter processes via three key steps (Wiegmann, et al., 2014):

- First, a proper flow solver computes the fundamental flow through the partially clogged filter. Here, the laminar flow is assumed, afterward, depending on the particle sizes, Stokes (when particles' size is one or several voxels) or Stokes-Brinkman (when

particles are much smaller than the voxel size) equations can be employed for fluid flow modeling.

- Secondly, particles are chased in the calculated flow field. An ordinary differential equation solves the tracking of particles; furthermore, effects such as friction with fluid, particles' electric attraction and filter surface, and diffuse motion are included in the equations.
- Finally, various adhesion models may be chosen for particles that touch the filter surface to decide whether the particle sticks to the surfaces or continues flowing.

Factors that influence the movement of particles are discussed in chapter 5.4. In the same way, FilterDict can simulate the three main transport mechanisms of a suspended particle in porous media; friction with fluid, electric attraction, and diffusive or Brownian motion. (Wiegmann, et al., 2014).

Mathematical equations describing the movement of particles are described as follows (Wiegmann, et al., 2014):

$$\begin{aligned}
 dx &= v dt \\
 [dv &= -\gamma \times (v(x) - v_0(x))dt + \frac{QE_0(x)}{m}dt + \sigma \times dW(t)]^* \\
 C_c &= 1 + K_n \left(1.17 + 0.525 e^{-\frac{0.78}{K_n}} \right) \\
 \gamma &= 6\pi\mu \frac{R}{C_c m} \\
 \sigma^2 &= \frac{2K_B T \gamma}{m} \\
 K_n &= \frac{\lambda}{R}
 \end{aligned}$$

In these equations, t is time, x is the particle position, v is particle velocity; γ is friction coefficient, v_0 is fluid velocity, Q is particle charge, E_0 is an electric field, m is particle mass, σ is flow resistivity, $dW(t)$ is 3rd probability (Wiener) measure; C_c is Cunningham correction, K_n is Knudsen number, μ is dynamic viscosity, R is particle radius, K_B is Boltzmann constant, T is ambient temperature, and λ is mean free path (Wiegmann, et al., 2014). The equation which is marked by the * term indicates three components of particle interactions; the red term corresponds to the particle friction with fluid- the dominant force in most cases, in which particle trajectories are close to streamlines of the original flow field-; the blue term corresponds to the electric attraction- where particles and pore surface are electrically loaded, leading to attraction or bouncing effects-; and the green term corresponds to the diffusive (Brownian) motion- when small random direction changes of particles caused by irregularities in the particle surface and particle collisions among particles-.

Adhesion models

FilterDict supports different adhesions models depending on whether a particle touches a filter structure and deposits on it, or it continues moving (Wiegmann, et al., 2014).

- **Hamaker model:** in this model, the particle's velocity is compared to the adhesive forces. When the particle's velocity is minimal while touching the structures' surface, the particle is caught by the filter. The velocity in this model must respect the following condition:

$$v^2 = \frac{H}{4\pi\rho a_0 R^2}$$

where, H is the adhesion (Hamaker constant), ρ is the particle density, a_0 is the adhesion distance, and R is the particle's radius.

The adhesion model requires two parameters to be fitted in it; adhesion (Hamaker constant) and a restitution parameter. The restitution parameter ranges from 0 to 1 and controls the amount of energy that is not absorbed by the collision. A restitution parameter of 1 implies no loss in energy; in this case, the particle moves with the same speed that it had before the collision. The restitution values smaller than one refers to energy absorption by the collision and, consequently, slowing down the particles. For instance, setting a restitution value of 0.5 in the model means that particle energy drops by half in the collision and becomes around 30% slower; particle energy is proportional to particle velocity squared.

- **Caught on first touch model:** assumes as soon as a particle touches a filter surface, it sticks in it. This is the simplest adhesion model embedded in FilterDict.
- **Sieving model:** never allows for a particle to stick to the filter, unless a particle that is caught by the filter does not move anymore and simply lies on the filter at two different points. Here a restitution parameter should be fitted in the model, and this parameter is utilized in the same way as explained in the Hamaker model.
- **Collision count model:** is the generalization version of the Caught on the first touch model. In this model, the maximal number of collisions value is set and indicates a certain amount of times that particles may touch the materials in the structure. Here, a probability for adhesion at each collision is specified. Moreover, after the collisions, the restitution parameter is defined in the same way as in the Hamaker model.

Model description and results

Although the presented test model doesn't represent the exact experimental setup, it provided useful insights for prospect models. Here, Stokes equations were used as the simulated particle sizes were bigger than a voxel size. In all directions "reflective" boundary condition was selected. As before, the biomass handled as a non-porous material. Adhesion model for particle-grain is set to "sieving" model, and particle-biomass is set to "caught on first touch" model with a 0.5 collision parameter. No charge was considered for particles, and Brownian motion was activated for particle diffusivity. 100000 number of particles with different sizes were flooded from a box-shaped area from the inlet area (see Figure 6-33, I) with the time step of 0.01 s. Particle size distribution included sizes of $3.5e^{-7}$, $5e^{-7}$, $2e^{-6}$, $3e^{-6}$, $4e^{-6}$ [m] with equal share of 20% of each. A series of snapshots for a particle transport test is displayed in Figure 6-33. Snapshots of the particle tracing numerical results show the particles' transport time. As the injection area is a rectangle area in the inlet, which covers the enclosed areas by biomasses, a lot of particles got trapped there. As well, at the end of the flood, some particles got filtered in other areas and through attaching to the surfaces and biomass. Additionally, the hydrodynamic boundary layer was seen (see Figure 6-34).

We have performed several other tests to explore optimum criteria and settings to improve the comparison with the experimental data. Different adhesion models, as well as a change in the injection zone, were tested. Our investigations imply a couple of necessary improvements that need to be adapted in our next models.

First, it was found out that the particles' paths were strongly dependent on the injection region. Not only tracing simulations must be performed on the total porous structure of the micromodel, but also the inlet channels needed to be comprised in the model. Moreover, the curvature in the depth profile in the particle tracking experiments expressively affected the particle trajectories and trapping that needs to be represented in the numerical models. We have already undertaken the exact 3D structure, including the flow channels, and considerable progress has been made towards optimizing the numerical models.

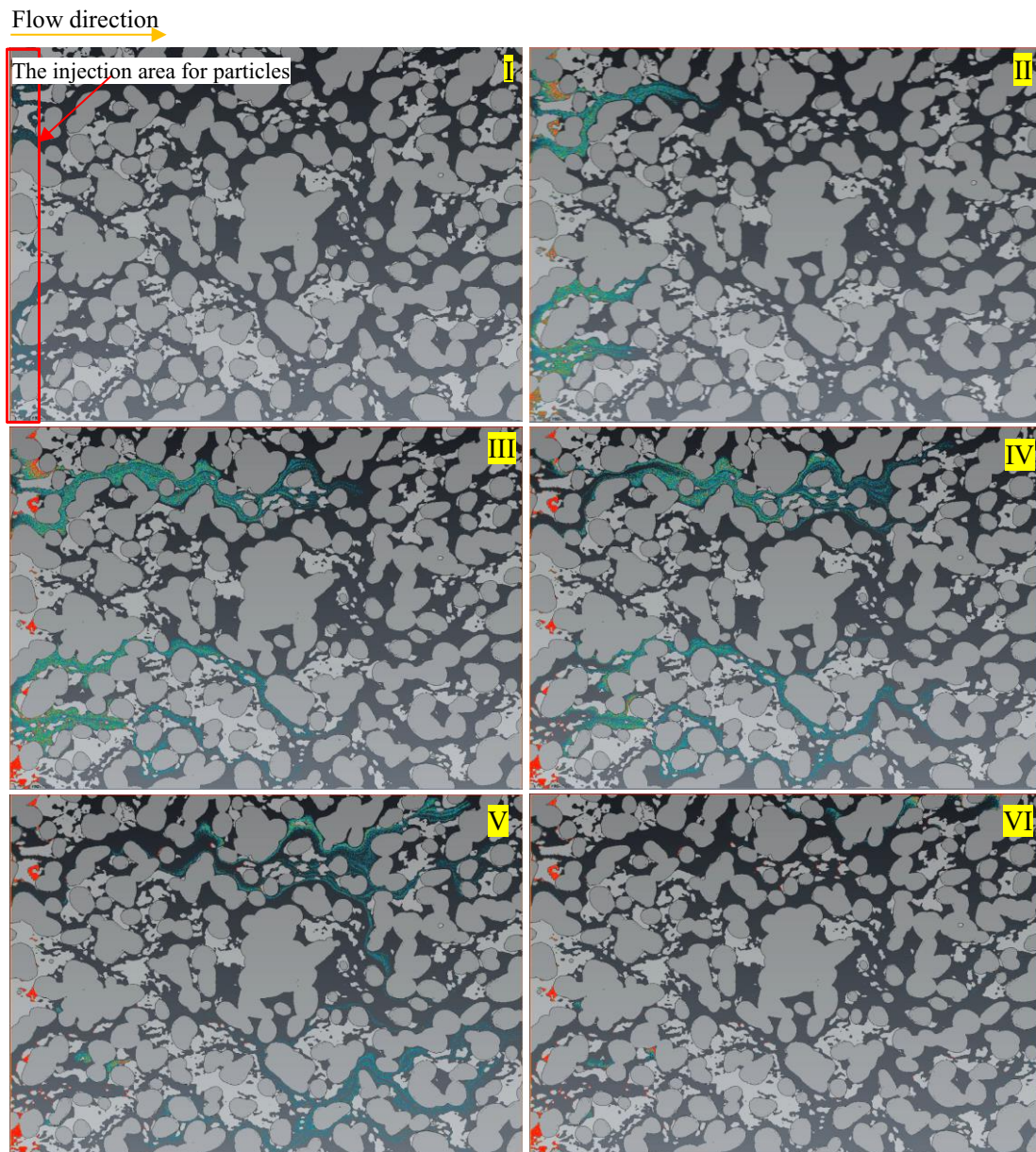


Figure 6-33 Snapshots of the particle tracing numerical results showing the particles' transport. In (I), the region at which particles are initially injected is shown; in (VI) trapped particles at the end of flood is shown. The 'caught on first touch' model with a 0.5 collision parameter has a high probability for particles to get trapped.

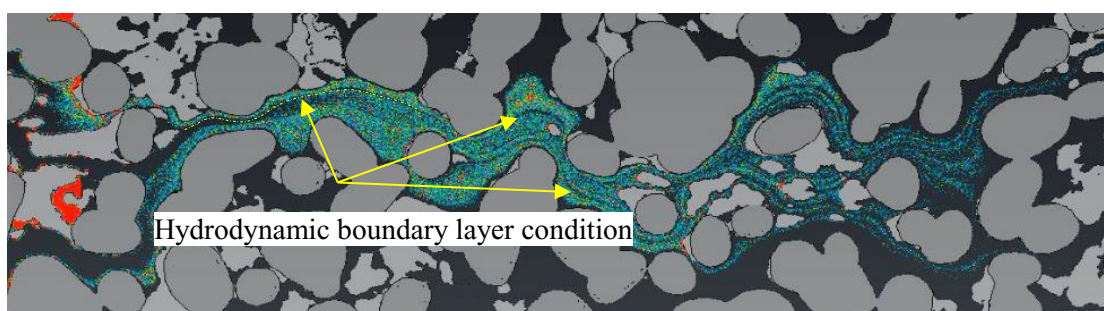


Figure 6-34 Hydrodynamic boundary layer was detected in the simulations.

Summary

The main conclusions of this chapter can be summarized as follows:

- The microbial transport and growth in two phases (BS & NF) through microfluidic experiments under the saturated condition have been investigated. The experimental outcomes elucidate some of the key mechanisms and physical phenomena, causing bacterial attachment, biomass growth, pore plugging, and flow path change.
- By segmenting experimental images, bacterial evolution was analyzed. Special consideration was given to capture and maintain the maximal information in the original images.
- During the BS flooding, initial attachment of bacterial cells and aggregates occurred. Biomass growth indicated a minor increasing trend during this phase; a similar trend was observed from pressure drop data across the micromodel.
- During the NF, additional growth and accumulation of biomass, remarkably in the initial precipitation sites, were detected. Both biomass growth and pressure drop data revealed a steeper increasing trend with stepwise spikes, which was led by filtration events due to the sudden release of accumulated biomass in the flow lines and valves.
- Through numerical modeling, the impact of bacterial colonization and filtration on the hydraulic properties of the porous network was explored. Bacterial activities, and filtration altered and lowered the physical properties of the medium (permeability and porosity).
- A general relationship for porosity-permeability requires repeating the experiments and considering a larger field of view that can be accounted as an REV concerning bacterial activities, and finally, adaptation of assumptions that better represent experimental conditions, such as handling the biomass as a semi-porous material.
- The simulated flow field data were compared with the initial sites where bacterial cells and aggregates initially deposited. The results point to the likelihood of precipitation of bacterial and aggregated cells in the low-velocity regions, while the high-velocity zones contribute to the flow of nutrients to other areas in the micromodel.
- Bacterial growth under starvation (nutrient-limited) condition was tested. The growth happens at much lower rates compared to experiments under saturated

conditions. As well, an outlook into bacterial growth and transport under unsaturated conditions was performed.

- The experimental and numerical particle tracking studies have been carried out. Preliminary findings provided fundamental understandings and suggestions for future tests and models.

Chapter 7 Summary, conclusions, and recommendations

In this dissertation, some aspects of underground hydrogen storage and conversion assessment were studied. The significance of this work was the broad range of problems that were addressed and investigated in a single study. Combining different facets of hydrogen storage offered an understanding of the critical mechanisms and parameters that can contribute to hydrogen loss due to diffusion and geochemical reactions. As well, the experimental and numerical investigation on bacterial growth and colonization is the groundwork for future efforts in understanding metabolic hydrogen conversion into methane.

This study began with an overview of a depleted gas field that was selected as a hydrogen storage site. Based on the geological and production-injection historical data, a static and a dynamic model was constructed. From the resulting hydrogen spatial distribution, the diffusive gas loss into the caprock and the reservoirs' boundaries was estimated.

Next, the potential reactions of hydrogen with brine and reservoir minerals were evaluated. An introduction to the geochemical modeling concepts was given. Followed by the concept presentation, a multi-step geochemical modeling approach was described. The modeling steps included: (1) the equilibrium batch model, which assumed instantaneous reactions (equilibrium) for hydrogen and minerals; (2) the primary kinetic batch model, which considered mineral reactions to be kinetically controlled, while hydrogen reactions were assumed to occur at local thermodynamic equilibrium. The last step (3) was the final kinetic batch model, in which both minerals and hydrogen reactions were considered to be kinetically controlled. A sensitivity analysis of the hydrogen reaction rate and the assumption of having equilibrium/disequilibrium for redox pairs were carried out to investigate their significance on the outcomes. Our models' findings suggested that the main reasons for potential hydrogen loss were due to the equilibrium assumption among redox pairs, and pyrite reduction to pyrrhotite. Lack of reliable kinetic data imposed consideration of the full range of uncertainty in our modeling workflow.

The biological activities of *in-situ* bacteria in the studied reservoir resulted in partial hydrogen consumption and methane production, which inspired the experimental examination of bacterial actions in the pore space. A literature study to the theoretical basis on bacterial attachment and growth was given, and transport formulations of microorganisms and colloidal particles were discussed. Next, the pore-scale microfluidic experiments were employed to elucidate bacterial cells' evolution, discover the favorability of porous media for bacterial growth, and compare different flooding conditions.

Experiments were carried out in two flooding phases. In phase I, a bacterial suspension solution at the stationary growth phase was injected, and biomass formation and growth were monitored. Phase II was proceeded by the injection of the nutrient solution into the micromodel. This study showed different modes of microbial accumulation through primary and secondary growth and filtration, from *in-situ* microbial growth to the intermittent release of biomass.

The resulting microscopic images were segmented and analyzed to quantify bacterial behavior. Direct flow simulations on the segmented images - the "Digital Twin" – were performed, and the influence of the bacterial colonization and filtration on the hydraulic properties of the pore space was assessed. The biomass was handled as an impermeable precipitate, and a relationship between porosity and permeability was derived.

Bacterial growth under starvation (nutrient-limited) condition was similarly tested. The growth happened at much lower rates compared to experiments under saturated conditions. As well, an outlook into bacterial growth and transport under unsaturated conditions was performed. These experiments are of much interest and value, specifically in the case of hydrogen storage and conversion.

Particle tracing experiment in a medium with established biomass was carried out, and preliminary numerical tracing modeling findings were described; finally, the directions for future work were proposed. The experimental and numerical tracing tests are strong tools that can complement the microbial growth experiments.

Moreover, the pore-scale numerical simulations were directly compared with micromodel experimental data. A good agreement between the simulated flow field data and the biomass precipitation sites was obtained. Microbial cells tended to precipitate in the low-velocity zones, while the high-velocity zones contributed to the flow of nutrients. This validated that numerical simulations based upon the Navier-Stokes equations can predict the areas where microbes tend to adhere and grow.

The microfluidic experiments deliver noteworthy quantitative and qualitative information to better understand and qualify the microbial processes in porous media. The experimentally and numerically derived insights so far have been very promising and encouraging, which are also relevant for a variety of applications from the main topic of this study, underground hydrogen gas storage and conversion, to other underground applications and processes, such as water management, soil remediation, and microbial enhanced oil recovery.

Finally, it is essential to note that natural systems deal with the microbial consortia, which are composed of a variety of species; also, bacterial growth has a reduced rate relative to bacteria growing in the perfect condition at micromodel. Similarly, in the microbial communities, each strain competes to avoid its elimination from the consortium (Jawedac, et al., 2019). When extending the findings of this study to practical applications in natural systems, these remarks must be carefully taken into account, and not to be directly transferred and generalized.

Recommendation and future work

Although findings and the implemented numerical and experimental methods were significant, there are still many unanswered questions regarding a proper understanding of underground hydrogen storage and conversion. Due to a variety of topics that have been studied and lack of time, many different experiments and numerical adaptations and scenarios have been left for the future. However, considerable insights have been gained, and many ideas derived from the outcomes, based on which recommendations for prospect work can be made:

- The geochemical parameters and reaction rates that were utilized in the models were not simple but lacked experimental data in the presence of hydrogen. The proposed geochemical workflow would be of much more value if the experimental kinetic rates in the presence of hydrogen for key reactions would be provided.
- We expect to observe the filtration and pluggings in actual reservoir pore space; however, the extent to which the filtration happens requires the field data. Nevertheless, we can separate the growth mode by considering/omitting the filtration events and estimate the porosity-permeability relationship for both cases.
- As observed in the experiments, biomass revealed to have some internal penetrability that allowed the penetration of ink. The prospect of being able to simulate the biomass as a semi-permeable material encourages future models. Consequently, this will possibly change the estimate for the overall permeability of the porous media and impact the simulated flow field in the pore space.

- Correlation between initial bacterial deposition and flow hydrodynamics across pore space is the first step towards understanding and predicting biomass accumulation on a more fundamental basis. Our study underlined a very well association of the initial deposition of bacterial cells with the simulated flow field. Another task to perform is the quantification of this association. Ideally, working towards building a model that can predict the locations that are favored by bacterial cells, and implementing the growth rate, biomass evolution, and pore blocking can be foreseen.
- It would be useful to look into different injection rates, and pore network patterns and investigate their effect on the pore blocking and filtration. Moreover, the nutrient-limited experiment can be suggested to be repeated on a micromodel with the established biomass (at the end of phase I or II). In this way, possible processes such as decreases in the growth, detachment, and biofilm sloughing can be studied.
- Two-phase (unsaturated) condition is a step closer to the UHS and energy conversion themes and are targets of our future research at this scale. Understanding the biomass accumulation mechanisms and evolution of flow pathways is essential to optimize the nutrient loading rates and bacterial transport in porous media. It can be recommended to include proper implementation of such tests to allow for observation of bacterial behavior under passive and active two-phase conditions. The passive state refers to a two-phase condition, in which inactive gas presents as an irreducible (residual) phase. The inactive gas phase, such as N_2 , allows investigating how bacterial cells behave in a gas-water interface and in what ways biomass develops. The injection rate should also be carefully adjusted not to change the initial gas distribution in the pore-network. The active two-phase system has the highest complexity and involves the injection of the active gas phase. The active gas phase, in the case of hydrogen storage and conversion, is a mixture of H_2 and CO_2 , which is the nutrient for Archaea. The product of microbial activities, in this case, is biomass and CH_4 . In this circumstance, we intend to find influencing controlling parameters that are involved in hydrogen consumption, biomass growth, and plugging in pore space.
- The numerical tracing experiments and simulations are reliable tools to mimic and complement the bacterial suspension tests. At this stage, we already made an exact 3D model of the micromodel and tested a few comparable particle tracing scenarios which we intend to finalize and publish in the near future.

References

1. “Abu-Ashour, J. et al., 1994. Transport of microorganisms through soil. *Water, Air, and Soil Pollution*, 75(1-2), p. 141–158.
2. Afrapoli, M. S., Alipour, S. & Torsa, O., 2012. Analysis of Microscopic Displacement Mechanisms of a MIOR Process in Porous Media with Different Wettability. *Transp Porous Med*, Volume 93, p. 705–719.
3. Alami, Y., Achouak, W. & Marol, C., 2000. Rhizosphere Soil Aggregation and Plant Growth Promotion of Sunflowers by an Exopolysaccharide-Producing Rhizobium sp. Strain Isolated from Sunflower Roots. *Appl Environ Microbiol*, Volume 66, p. 3393–3398.
4. Allison, L., 1947. Effect of microorganisms on permeability of soil under prolonged submergence. *Soil Science*, 63(6), pp. 439–450.
5. Amann-Hildenbranda, A., Bertier, P., Busch, A. & Krooss, B. M., 2013. Experimental investigation of the sealing capacity of generic clay-rich caprocks. *International Journal of Greenhouse Gas Control*, p. 620–641.
6. Armstrong, R. T. & Wildenschild, D., 2012. Microbial enhanced oil recovery in fractional-wet systems: a pore-scale investigation, Transport in Porous Media. *Transport in Porous Media*, 92(3), p. 819–835.
7. Arthur, R. C. et al., 2000. *Compilation of Kinetic Data for Geochemical Calculations*, Tokaimura: Japan Nuclear Cycle Development Institute.
8. Aufrecht, J. A. et al., 2019. Pore-scale hydrodynamics influence the spatial evolution of bacterial biofilms in a microfluidic porous network. *PLOS ONE*, pp. 1-17.
9. Bachmann, R. T., Johnson, A. C. & Edyvean, R. G. J., 2014. Biotechnology in the petroleum industry: An overview. *International Biodeterioration & Biodegradation*, Volume 86, p. 225–237.
10. Balch, W. et al., 1979. Methanogens: reevaluation of a unique biological group. *Microbiol Rev.*, 43(2), pp. 260-296.
11. Baveye, P. C. & Darnault, C., 2017. Microbial competition and evolution in natural porous environments: Not that simple. *Proceedings of the National Academy of Sciences*, 114(14), pp. E2802-E2803.
12. Baveye, P. et al., 1998. Environmental Impact and Mechanisms of the Biological Clogging of Saturated Soils and Aquifer Materials. *Critical Reviews in Environmental Science and Technology*, 28(2), pp. 123-191.
13. Bear, J., 1988. *Dynamics of Fluids in Porous Media*. Amsterdam : Elsevier.
14. Berndt, M. E., Allen, D. E. & Seyfried, J. W. E., 1996. Reduction of CO₂ during serpentinization of olivine at 300 °C and 500 bar. *Geology*, 24(4), pp. 351-354.
15. Berta, M. et al., 2018. Geochemical Effects of Millimolar Hydrogen Concentrations in Groundwater: An Experimental Study in the Context of Subsurface Hydrogen Storage. *Environ. Sci. Technol*, Volume 52, pp. 4937-4949.
16. Betelu, S. et al., 2012. *Mechanistic and kinetic study of pyrite (FeS₂)-hydrogen (H₂) interaction at 25°C using electrochemical techniques*. Montpellier, France, s.n.
17. Bethke, C., 1996. *Geochemical Reaction Modeling: Concepts and Applications*. New York: Oxford University Press.
18. Bethke, C., 2008. *Geochemical and Biogeochemical Reaction Modeling*. s.l.:Cambridge University Press.
19. Bethke, C. M., Farrell, B. & Yeakel, S., 2018. *GWB Essentials Guide*, Champaign, Illinois: Aqueous Solutions LLC.
20. Bethke, C. M., Farrell, B. & Yeakel, S., 2018. *GWB Reaction Modeling Guide*, Champaign, Illinois: Aqueous Solutions, LLC.
21. Bishop, P. L., Gibbs, J. T. & Cunningham, B. E., 1997. Relationship Between Concentration and Hydrodynamic Boundary Layers over Biofilms. *Environmental Technology*, 18(4), pp. 375-385.

22. Blackburn, N., Seech, A. & Trevors, J., 1994. Survival and Transport of lac-lux Marked *Pseudomonas fluorescens* Strain in Uncontaminated and Chemically Contaminated Soils. *System. Appl. Microbiol.*, 17(4), pp. 574-580.
23. Bolster, C. H., Mills, A. L., Hornberger, G. M. & Herman, J. S., 1999. Spatial distribution of deposited bacteria following miscible displacement experiments in intact cores. *Water Resources Research*, 35(6), pp. 1797-1807.
24. Bradford, S. A., Yates, S. R., Bettahar, M. & Simunek, J., 2002. Physical factors affecting the transport and fate of colloids in saturated porous media. *Water Resources Research*, 38(12), pp. 63-1-63-12.
25. Brown, L. R., 2010. Microbial enhanced oil recovery (MEOR). *Current Opinion in Microbiology*, Volume 13, p. 316–320.
26. Brunauer, S., Emmett, P. & Teller, E., 1938. Adsorption of Gases in Multimolecular Layers. *American Chemical Society*, Volume 60, pp. 309-319.
27. Bryant, R. S., Burchfield, T. E., Dennis, D. & Hitzman, D., 1990. Microbial Enhanced Waterflooding: Mink Unit Project. *SPE Reservoir Engineering*, pp. 9-13.
28. Bryant, R. S. & Douglas, J., 1988. Evaluation of Microbial Systems in Porous Media for EOR. *SPE Reservoir Engineering*, pp. 489-495.
29. Camesano, T. A. & Logan, B. E., 1998. Influence of Fluid Velocity and Cell Concentration on the Transport of Motile and Nonmotile Bacteria in Porous Media. *Environ. Sci. Technol.*, 32(11), p. 1699–1708.
30. Cantucci, B. et al., 2009. Geochemical modeling of CO₂ storage in deep reservoirs: The Weyburn Project (Canada) case study. *Chemical Geology*, Volume 265, pp. 181-197.
31. Carden, P. & Paterson, L., 1979. Physical, chemical and energy aspects of underground hydrogen storage. *International Journal of Hydrogen Energy*, 4(6), pp. 559-569.
32. Carrel, M. et al., 2018. The spatial distribution of the biofilm patches uncovered that the wall shear stresses controlled the biofilm development. *Water Research*, 134(1), pp. 280 - 291.
33. Chanou, A., Osinski, G. & Grieve, R., 2014. A methodology for the semi-automatic digital image analysis of fragmental impactites. *Meteoritics & Planetary Science*, 49(4), pp. 621-635.
34. Chatenever, A. & Calhoun Jr., J. C., 1952. Visual Examinations of Fluid Behavior in Porous Media - Part I. *Journal of Petroleum Technology*, Volume 195, pp. 149-156.
35. Christensen, T. H. K. P. et al., 1994. Attenuation of landfill leachate pollutants in aquifers. *Critical Reviews in Environmental Science and Technology*, 24(2), pp. 119-202.
36. Chrysikopoulos, C. V. & Sim, Y., 1996. One-dimensional virus transport in homogeneous porous media with time dependent distribution coefficient. *Journal of Hydrology*, 185(1-4), p. 199–219.
37. Conrad, R., 1999. Contribution of hydrogen to methane production and control of hydrogen concentrations in methanogenic soils and sediments. *FEMS Microbiology Ecology*, 28(3), pp. 193-202.
38. Corapcioglu, M. Y. & Panday, S., 1989. Fundamental Equations for Transport Processes in Storage Reservoirs. In: M. Tek, ed. *Underground Storage of Natural Gas: Theory and practice*. s.l.:Kluwer Academic Publishers , pp. 55-73.
39. Corapeioglu, M. Y. & Haridas, A., 1985. Microbial transport in soils and groundwater: A numerical model. *Adv. Water Resources*, 8(4), pp. 188-200.
40. Costerton, J. W., Stewart, P. S. & Green, E. P., 1999. Bacterial Biofilms: A Common Cause of Persistent Infections. *Science*, Volume 284, pp. 1318-1322.
41. Coyte, K. Z. et al., 2017. Microbial competition in porous environments can select against rapid biofilm growth. *Proceedings of the National Academy of Sciences*, 114(2), pp. E161-E170.
42. Crescente, C. et al., 2006. *An experimental study of driving mechanisms in MIOR processes by using Rhodococcus sp. 094..* Toronto, Society of Petroleum Engineers.
43. Cross, M. M., Manning, D. A., Bottrell, S. H. & Worden, R. H., 2004. Thermochemical sulphate reduction (TSR): experimental determination of reaction kinetics and implications of the observed reaction rates for petroleum reservoirs. *Organic Geochemistry*, Volume 35, p. 393–404.
44. Cunningham, A. et al., 1997. Biofilm Processes in Porous Media - Practical Applications. In: S. A. Penny & D. L. Haldeman, eds. *Microbiology of the Terrestrial Deep Subsurface*. Boca Raton: CRC Press, Inc., pp. 325-347.

45. Cunningham, A., Characklls, W., Abedeen, F. & Crawford, D., 1991. Influence of Biofilm Accumulation on Porous Media Hydrodynamics. *Environ Sci Technol*, Volume 25, p. 1305–1311.
46. Cusack, F. et al., 1987. Diagnosis and Removal of Microbial/Fines Plugging in Water Injection Wells. *Society of Petroleum Engineers*, pp. 303-306.
47. Cussler, E. L., 1984. *Diffusion Mass Transfer in Fluid Systems*. 3rd ed. s.l.:Cambridge University Press.
48. Davis, J. B. & Updegraff, D. M., 1954. Microbiology in the petroleum industry. *Bacteriol Rev.*, 18(4), pp. 215-238.
49. De Lucia, M. et al., 2012. Modelling CO₂-induced fluid–rock interactions in the Altensalzwedel gas reservoir. Part I: from experimental data to a reference geochemical model. *Environmental Earth Sciences*, pp. 563-572.
50. De Ruig, M. J. & Hubbard, S. M., 2006. Seismic facies and reservoir characteristics of a deep-marine channel belt in the Molasse foreland basin, Puchkirchen Formation, Austria. *AAPG Bulletin*, 90(5), pp. 735-752.
51. Dillon, P. J., Hickinbotham, M. R. & Pavelic, P., 1994. *Review of International Experience in Injecting Water into Aquifers for Storage and Reuse*. s.l., Water Down Under 94: Groundwater Papers; Preprints of Papers, 1994, p.13-14, 16-19.
52. Donlan, R. M., 2002. Biofilms: Microbial Life on Surfaces. *Emerging Infectious Diseases*, 8(9), pp. 881-890.
53. Dussaud, M., 1989. New Techniques in Underground Storage of Natural Gas in France. In: K. A. Publishers, ed. *Underground Storage of Natural Gas: Theory and Practice*. s.l.:Springer Netherlands, pp. 371-383.
54. Ehrlich, H. L., 1996. How microbes influence mineral growth and dissolution. *Chemical Geology*, Volume 132, pp. 5-9.
55. Elimelech, M. & O'Melia, C. R., 1990. Kinetics of deposition of colloidal particles in porous media. *Environ. Sci. Technol.*, 24(10), p. 1528–1536.
56. Emadi, S. H., Borhani, T. N. G. & Soudmand-asli, A., 2011. *Application of Microbial Profile Modification for in Situ Enhanced Oil Recovery*. Miri, Sarawak, Malaysia, s.n.
57. Enzmann, F., Mayer, F., Rother, M. & Holtmann, D., 2018. Methanogens: biochemical background and biotechnological applications. *AMB Express*, 8(1), pp. 1-22.
58. Eveloy, V. & Gebreegziabher, T., 2018. A Review of Projected Power-to-Gas Deployment Scenarios. *Energies*, 11(7), pp. 1-52.
59. Fanning, J. C., 2000. The chemical reduction of nitrate in aqueous solution. *Coordination Chemistry Reviews*, 199(1), pp. 159-179.
60. Farhat, N. M. et al., 2016. Spatial heterogeneity of biofouling under different cross-flow velocities in reverse osmosis membrane systems. *Journal of Membrane Science*, Volume 520, pp. 964-971.
61. Fasanino, G. & Meunier, G., 1989. Geostatistics applied to underground gas storage. In: M. Tek, ed. *Underground Storage of Natural Gas: Theory and Practice*. Dordrecht / Boston / London: Kluwer Academic Publishers , pp. 93-114.
62. Ferreira, T. & Rasband, W., 2012. *ImageJ User Guide, IJ 1.46r*, s.l.: s.n.
63. Fleury, M., Berne, P. & Bachaud, P., 2008. Diffusion of dissolved CO₂ in caprock. *Energy Procedia*, pp. 3461-3468.
64. Foh, S., Novil, M., Rockar, E. & Randolph, P., 1979. *Underground hydrogen storage Final report*, Chicago: Institute of Gas Technology.
65. Fontes, D. E., Mills, A. L., Hornberger, G. M. & Herman, J. S., 1991. Physical and Chemical Factors Influencing Transport of Microorganisms through Porous Media. *Appl Environ Microbiol.*, 57(9), p. 2473–2481.
66. Freeze, R. A. & Cherry, J. A., 1979. *Groundwater*. Englewood Cliffs, New Jersey: Prentice-Hall.
67. Gannon, J., Mingelgrin, U., Alexander, M. & Wagenet, R., 1991. Bacterial transport through homogeneous soil. *Soil Biology and Biochemistry*, 23(12), pp. 1155-1160.
68. Gannon, J. T., Manilal, V. B. & Alexander, M., 1991. Relationship between Cell Surface Properties and Transport of Bacteria through Soil. *Appl. Environ. Microbiol.*, 57(1), pp. 190-193.
69. Garcia, J.-L., Patel, B. K. C. & Ollivier, B., 2000. Taxonomic, Phylogenetic, and Ecological Diversity of Methanogenic Archaea. *Anaerobe*, Volume 6, pp. 205-226.

70. Gaus, I. et al., 2008. Geochemical and solute transport modelling for CO₂ storage, what to expect from it?. *International Journal of Greenhouse Gas Control*, 2(4), pp. 605-625.
71. Gerlach, R. & Cunningham, A. B., 2011. Influence of Biofilms on Porous Media Hydrodynamics. In: *Porous Media: Applications in Biological Systems and Biotechnology*. s.l.:Taylor and Francis Group, LLC, pp. 174-230.
72. Ghiorse, W. C. & Wilson, J. T., 1988. Microbial Ecology of the Terrestrial Subsurface. In: A. I. Laskin, ed. *Advances in Applied Microbiology*. s.l.:Academic Press, pp. 107-172.
73. Giffaut, E. et al., 2014. Andra thermodynamic database for performance assessment: ThermoChimie. *Applied Geochemistry*, Volume 49, pp. 225-236.
74. Ginn, T. R. et al., 2002. Processes in microbial transport in the natural subsurface. *Advances in Water Resources*, Volume 25, p. 1017-1042.
75. Ginn, T. et al., 2002. Processes in microbial transport in the natural subsurface. *Advances in Water Resources*, 25(8-12), pp. 1017-1042.
76. Gonçalves, M. A., 2005. GEOCHEMICAL MODELS. In: J. H. Lehr & J. Keeley, eds. *Water Encyclopedia*. s.l.:s.n., p. 138-140.
77. Götz, M. et al., 2016. Renewable Power-to-Gas: A technological and economic review. *Renewable Energy*, Volume 85, pp. 1371-1390.
78. Guangdi, L. et al., 2012. New insights into natural gas diffusion coefficient in rocks. *Petroleum Exploration and Development*, 39(5), p. 597-604.
79. Hagemann, B., 2018. *Numerical and Analytical Modeling of Gas Mixing and Bio-Reactive Transport during Underground Hydrogen Storage*, Göttingen: CUVILLIER VERLAG, Göttingen.
80. Halim, A. et al., 2015. Investigation of spore forming bacterial flooding for enhances oil recovery in a North Sea chalk reservoir. *Journal of Petroleum Science and Engineering*, Volume 133, pp. 444-454.
81. Halim, A. Y., Nielsen, S. M., Nielsen, K. F. & Lantz, A. E., 2017. CPC TESTING: Towards the understanding of microbial metabolism in relation to microbial enhanced oil recovery. *Journal of Petroleum Science and Engineering*, Volume 149, pp. 151-160.
82. Hall, A. J., 1986. Pyrite-pyrrhotine redox reactions in nature. *Mineralogical Magazine*, Volume 50, pp. 223-229.
83. Harvey, R. W. & Garabedian, S. P., 1991. Use of Colloid Filtration Theory in Modeling Movement of Bacteria through a Contaminated Sandy Aquifer. *Environmental Science & Technology*, 25(1), pp. 178-185.
84. Hassannayebi, N., Azizmohammadi, S., De Lucia, M. & Ott, H., 2019. Underground hydrogen storage: application of geochemical modelling in a case study in the Molasse Basin, Upper Austria. *Environmental Earth Sciences*, 78(177).
85. Helgeson, H. C., 1971. Kinetics of mass transfer among silicates and aqueous solutions. *Geochimica et Cosmochimica Acta*, 35(5), pp. 421-469.
86. Helgeson, H. C., Murphy, W. M. & Aagaard, P., 1984. Thermodynamic and kinetic constraints on reaction rates among minerals and aqueous solutions. II. Rate constants, effective surface area, and the hydrolysis of feldspar. *Geochimica et Cosmochimica Acta*, 48(12), pp. 2405-2432.
87. Hendry, M. J., Lawrence, J. R. & Maloszewski, P., 1997. The Role of Sorption in the Transport of *Klebsiella oxytoca* Through Saturated Silica Sand. *Groundwater*, 35(4), pp. 574-584.
88. Hoch, A. R. & James, M., 2012. Comparison of alternative approaches to modelling gas migration through a higher strength rock. *Mineralogical Magazine*, 76(8), p. 3319-3326.
89. Holland, T. J. B. & Powell, R., 1998. An internally consistent thermodynamic data set for phases of petrological interest. *Journal of Metamorphic Geology*, 16(3), pp. 309-343.
90. Holm, N. et al., 2015. Serpentinization and the Formation of H₂ and CH₄ on Celestial Bodies (Planets, Moons, Comets). *ASTROBIOLOGY*, 15(7), pp. 587-600.
91. Hommel, J., Coltman, E. & Class, H., 2018. Porosity-Permeability Relations for Evolving Pore Space: A Review with a Focus on (Bio-)geochemically Altered Porous Media. *Transport in Porous Media*, 124(2), p. 589-629.
92. Hou, Z., Rockhold, M. L. & Murray, C. J., 2012. Evaluating the impact of caprock and reservoir properties on potential risk of CO₂ leakage after injection. *Environ Earth Sci*, Volume 66, p. 2403-2415.

93. Hunt, R. J. & Johnson, W. P., 2017. Pathogen transport in groundwater systems: contrasts with traditional solute transport. *Hydrogeology Journal*, 25(4), p. 921–930.
94. Ingram, G., Urai, J. & Naylor, M., 1997. Sealing processes and top seal assessment. *Norwegian Petroleum Society Special Publications*, Volume 7, pp. 165-174.
95. Jack, T., 1993. M.O.R.E. to M.E.O.R.: An Overview of Microbially Enhanced Oil Recovery. *Developments in Petroleum Science*, Volume 39, pp. 7-16.
96. Jacobs, E. et al., 2013. Determination of gas diffusion coefficients in saturated porous media: He and CH₄ diffusion in Boom Clay. *Applied Clay Science*, Volume 83–84, p. 217–223.
97. Jang, L.-K., Sharma, M. & Yen, T., 1984. The Transport of Bacteria in Porous Media and Its Significance in Microbial Enhanced Oil Recovery. *SPE*, pp. 387-393.
98. Jawedac, K., Yazdani, S. S. & Koffas, M. A., 2019. Advances in the development and application of microbial consortia for metabolic engineering. *Metabolic Engineering Communications*, Volume 9, pp. 1-10.
99. Jeong, H. Y., Jun, S., Cheon, J.-Y. & Park, M., 2018. A review on clogging mechanisms and managements in aquifer storage and recovery (ASR) applications. *Geosciences Journal*, pp. 1-13.
100. Jing, Y., Armstrong, R. T., Ramandi, H. L. & Mostaghimi, P., 2017. Topological Characterization of Fractured Coal. *Journal of Geophysical Research: Solid Earth*, Volume 12, pp. 9849-9861.
101. Johnson, W. P., Martin, M. J., Gross, M. J. & Logan, B. E., 1996. Facilitation of bacterial transport through porous media by changes in solution and surface properties. *Colloids and Surfaces : Physicochemical and Engineering Aspect*, Volume 107, pp. 263-271 .
102. Jones, S. B., Or, D. & Bingham, G. E., 2003. Gas Diffusion Measurement and Modeling in Coarse-Textured Porous Media. *Vadose Zone Journal*, Volume 2, p. 602–610.
103. Jucker, B. A., Zehnder, A. J. B. & Harms, H., 1998. Quantification of Polymer Interactions in Bacterial Adhesion. *Environ. Sci. Technol.*, 32(19), pp. 2909-2915.
104. Karimaie, H. & Lindeberg, E., 2017. Experimental Verification of CO₂ Dissolution Rate Due to Diffusion Induced Convection. *Energy Procedia*, Volume 114, pp. 4917-4925.
105. Kiyosu, Y. & Krouse, H. R., 1993. Thermochemical reduction and sulfur isotopic behavior of sulfate by acetic acid in the presence of native sulfur. *Geochemical Journal*, 27(1), pp. 49-57.
106. Knapp, R. et al., 1993. *Microbial field pilot study*, United States: s.n.
107. Kohen, R. & Nyska, A., 2002. Invited Review: Oxidation of Biological Systems: Oxidative Stress Phenomena, Antioxidants, Redox Reactions, and Methods for Their Quantification. *Toxicologic Pathology*, 30(6), pp. 620-650.
108. Kolbel-Boelke, J., Anders, E.-M. & Nehr Korn, A., 1988. Microbial Communities in the Saturated Groundwater Environment II: Diversity of Bacterial Communities in a Pleistocene Sand Aquifer and their In Vitro Activities. *Microb Ecol*, Volume 16, pp. 31-48.
109. Konn, C., Charlou, J. L., Holm, N. G. & Mousis, O., 2015. The Production of Methane, Hydrogen, and Organic Compounds in Ultramafic-Hosted Hydrothermal Vents of the Mid-Atlantic Ridge. *Astrobiology*, 15(5), pp. 381-399.
110. Kostakioti, M., Hadjifrangiskou, M. & Hultgren, S. J., 2013. Bacterial Biofilms: Development, Dispersal, and Therapeutic Strategies in the Dawn of the Postantibiotic Era. *Cold Spring Harb Perspect Med*, 3(4), pp. a010306-a010306.
111. Krooss, B. & Leythaeuser, D., 1988. Experimental measurements of the diffusion parameters of Hght hydrocarbons in water-saturated sedimentary rocks-II. Results and geochemical significance. *Organic Geochemistry*, 12(2), pp. 91-108.
112. Krooss, B. M., Schloemer, S. & Ehrlich, R., 1998. Experimental investigation of molecular transport and fluid flow in unfaulted and faulted pelitic rocks. *Geological Society Special Publications*, Volume 147, pp. 135-146.
113. Kroupa, A., 2013. Modelling of phase diagrams and thermodynamic properties using Calphad method – Development of thermodynamic databases. *Computational Materials Science*, Volume 66, pp. 3-13.
114. Kryachko, Y., 2018. Novel approaches to microbial enhancement of oil recovery. *Journal of biotechnology*, Volume 266, pp. 118-123.
115. Kumara, A. et al., 2017. Biofilms: Survival and defense strategy for pathogens. *International Journal of Medical Microbiology*, 307(8), pp. 481-489.
116. Kuypers, M. M. M., Marchant, H. K. & Kartal, B., 2018. The microbial nitrogen-cycling network. *Nature Reviews Microbiology*, Volume 16, p. 263–276.

117. Lacasta, A. et al., 1999. Modeling of spatiotemporal patterns in bacterial colonies. *Physical Review E*, 59(6).
118. Langmuir, D., 1997. *Aqueous Environmental Geochemistry*. s.l.:Prentice-Hall.
119. Lappa, M., 2004. *Fluids, Materials and Microgravity-Numerical Techniques and Insights into Physics*. Oxford: Elsevier.
120. Lappin-Scott, H. M., Cusack, F. & Costerton, J. W., 1988. Nutrient Resuscitation and Growth of Starved Cells in Sandstone Cores: a Novel Approach to Enhanced Oil Recovery. *Appl Environ Microbiol.*, 54(6), p. 1373–1382.
121. Lefevre, E., Bossa, N., Wiesner, M. R. & Gunsch, C. K., 2016. A review of the environmental implications of in situ remediation by nanoscale zero valent iron (nZVI): Behavior, transport and impacts on microbial communities. *Science of The Total Environment*, Volume 565, pp. 889-901.
122. Libert, M. et al., 2011. Molecular hydrogen: An abundant energy source for bacterial activity in nuclear waste repositories. *Physics and Chemistry of the Earth*, Volume 36, p. 1616–1623.
123. Linden, S., Cheng, L. & Wiegmann, A., 2019. *FlowDict user guide*, Kaiserslautern: Fraunhofer Institut Techno- und Wirtschaftsmathematik ITWM-Math2Market GmbH.
124. Liu, H. H., Ranjith, P. G., Georgi, D. T. & Lai, B. T., 2016. Some key technical issues in modelling of gas transport process in shales: a review. *Geomechanics and Geophysics for Geo-Energy and Geo-Resources*, 2(4), p. 231–243.
125. Li, Z., Dong, M., Li, S. & Huang, S., 2006. CO₂ sequestration in depleted oil and gas reservoirs—caprock characterization and storage capacity. *Energy Conversion and Management*, Volume 47, p. 1372–1382.
126. Lovley, D. & Phillips, E., 1988. Novel mode of microbial energy metabolism: organic carbon oxidation coupled to dissimilatory reduction of iron or manganese. *Appl. Environ. Microbiol.*, 54(6), p. 1472–1480.
127. Lovley, D. R., 2003. Cleaning up with genomics: applying molecular biology to bioremediation. *Nature Reviews Microbiology*, Volume 1, pp. 35–44.
128. Ludwig, W., Schleifer, K.-H. & B. Whitman, W., 2009. Order II. Lactobacillales ord. nov.. In: P. Vos, et al. eds. *Bergey's Manual of Systematic Bacteriology, Volume 3: The Firmicutes*. Dordrecht Heidelberg London New York: Springer-Verlag New York, pp. 464-735.
129. Lund, P. D., Lindgren, J., Mikkola, J. & Salpakari, J., 2015. Review of energy system flexibility measures to enable high levels of variable renewable electricity. *Renewable and Sustainable Energy Reviews*, Volume 45, pp. 785-807.
130. Lüttge, A. & Arvidson, R. S., 2008. The Mineral–Water Interface. In: S. L. Brantley, J. D. Kubicki & A. F. White, eds. *Kinetics of Water-Rock Interaction*. New York: Springer, pp. 73-107.
131. Malkovsky, I. V. & Pek, A. A., 2009. Effect of Elevated Velocity of Particles in Groundwater Flow and Its Role in Colloid-facilitated Transport of Radionuclides in Underground Medium. *Transport in Porous Media*, 78(2), pp. 277-294.
132. Mand, T. D. & Metcalf, W. W., 2019. Energy Conservation and Hydrogenase Function in Methanogenic Archaea, in Particular the Genus Methanosarcina. *Microbiology and Molecular Biology Reviews*, 83(4).
133. Marouf, M., 2018. *Particle Tracing in Saturated Micromodel*. Leoben: montanuniversität leoben.
134. Marshall, K. C. & Cruickshank, R. H., 1973. Cell surface hydrophobicity and the orientation of certain bacteria at interfaces. *Arch. Mikrobiol.*, 91(1), p. 29–40.
135. Martin, M. J. et al., 1996. Scaling bacterial filtration rates in different sized porous media. *Journal of Environmental Engineering*, 122(5), pp. 407-415.
136. Martin, R., 2013. *Clogging issues associated with managed aquifer recharge methods*. s.l.:IAH Commission on Managing Aquifer Recharge, Australia .
137. Martin, R. E., Bouwer, E. J. & Hanna, L. M., 1992. Application of Clean-Bed Filtration Theory to Bacterial Deposition in Porous Media. *Environ. Sci. Technol.*, 26(5), pp. 1053-1058
138. Marty, N. C. M. et al., 2015. A database of dissolution and precipitation rates for clay-rocks minerals. *Applied Geochemistry*, Volume 55, pp. 108-118.
139. McCarthy, J. F. & Zachara, J. M., 1989. Subsurface transport contaminants. *Environ. Sci. Technol.*, 23(5), pp. 496-502.

-
140. McCollom, T. M. & Seewald, J. S., 2001. A reassessment of the potential for reduction of dissolved CO₂ to hydrocarbons during serpentinization of olivine, *Geochimica et Cosmochimica Acta*. *Geochimica et Cosmochimica Acta*, 65(21), p. 3769–3778.
 141. McDowell-Boyer, L. M., Hunt, J. R. & Sitar, N., 1986. Particle transport through porous media. *Water Resources Research*, 22(13), pp. 1901-1921.
 142. McKellar, M. & Wardlaw, N., 1982. A method of making two-dimensional glass micromodels of pore systems. *Journal of Canadian Petroleum Technology*, Volume 21, pp. 39-41.
 143. McNabb, J. F. & Dunlap, W. J., 1975. Subsurface Biological Activity in Relation to Ground-Water Pollution. *Ground Water*, 13(1), pp. 33-34.
 144. Meile, C. & Scheibe, T. D., 2019. Reactive Transport Modeling of Microbial Dynamics. *Elements*, 15(2), pp. 111-116.
 145. Milferstedt, E. & Morgenroth, K., 2009. Biofilm engineering: linking biofilm development at different length and time scales. *Reviews in Environmental Science and Bio/Technology*, 8(3), pp. 203-208.
 146. Molnar, I. L. et al., 2015. Predicting colloid transport through saturated porous media: A critical review. *Water Resources Research*, Volume 51, p. 6804–6845.
 147. Morales, V. L., Parlange, J.-Y. & Steenhuis, T. S., 2010. Are preferential flow paths perpetuated by microbial activity in the soil matrix? A review. *Journal of Hydrology*, 393(1-2), pp. 29-36.
 148. Murphy, E. et al., 1992. The influence of microbial activity and sedimentary organic carbon on the isotope geochemistry of the Middendorf Aquifer. *Water Resour. Res.*, 28(3), p. 723–740.
 149. Nambi, I. M., Werth, C. J., Sanford, R. A. & Valocchi, A. J., 2003. Pore-scale analysis of anaerobic haloferrous bacterial growth along the transverse mixing zone of an etched silicon pore network. *Environ. Sci. Technol.*, 37(24), p. 5617–5624.
 150. Nealson, K. H., Inagaki, F. & Takai, K., 2005. Hydrogen-driven subsurface lithoautotrophic microbial ecosystems (SLiMEs): do they exist and why should we care?. *TRENDS in Microbiology*, 13(9), pp. 405-410.
 151. Nordstrom, D. K., 2000. Aqueous Redox Chemistry and the Behavior of Iron in Acid Mine Waters. *Workshop on Monitoring Oxidation-Reduction Processes for Ground-water Restoration*, pp. 43-47.
 152. Oberdorfer, J. A. & Peterson, F. L., 1985. Waste-Water Injection: Geochemical and Biogeochemical Clogging Processes. *Ground Water*, 23(6), pp. 753-761.
 153. OECD/IEA, 2015. *Technology Roadmap Hydrogen and Fuel Cells*, Paris: International Energy Agency.
 154. Ogata, A. & Banks, R., 1961. *A Solution of the Differential Equation of Longitudinal Dispersion in Porous Media*, s.l.: U.S. geological survey professional paper 411-A.
 155. Ott, H., Andrew, M., Snippe, J. & Blunt, M. J., 2014. Microscale solute transport and precipitation in complex rock during drying. *Geophysical Research Letters*, Volume 41, p. 8369–8376.
 156. Ott, H. & Oedai, S., 2015. Wormhole formation and compact dissolution in single- and two-phase CO₂-brine injections. *Geophysical research Letters*, Volume 42, p. 2270–2276.
 157. Palandri, J. L. & Kharaka, Y. K., 2004. *A compilation of rate parameters of water-mineral interaction kinetics for application to geochemical modeling*, Menlo Park, California: U.S. GEOLOGICAL SURVEY.
 158. Park, S.-J. & Seo, M.-K., 2011. Chapter 1 - Intermolecular Force. In: S. Park & M. Seo, eds. *Interface Science and Composites*. s.l.: Elsevier BV, pp. 1-57.
 159. Patel, J. et al., 2015. Recent developments in microbial enhanced oil recovery. *Renewable and Sustainable Energy Reviews*, Volume 52, pp. 1539-1558.
 160. Paulsen, J., Ekran, S. & Oppen, E., 1999. Visualisation of bacterial degradation and mobilization of oil in a porous medium. *Environmental Geology*, 38(3), pp. 204-208.
 161. Pavelic, P. et al., 2011. Laboratory assessment of factors affecting soil clogging of soil aquifer treatment systems. *Water Research*, 45(10), pp. 3153-3163.
 162. Picioreanu, C., van Loosdrecht, M. C. M. & Heijnen, J. J., 2000. Modelling and predicting biofilm Structure. In: *Community Structure and Co-operation in Biofilms*. Cambridge: Cambridge University Press, pp. 129-166.

-
163. Pintelon, T. R., Picioreanu, C., van Loosdrecht, M. C. & Johns, M. L., 2012. The effect of biofilm permeability on bio-clogging of porous media. *Biotechnology and Bioengineering*, 109(4), pp. 1031-42.
164. Pitzer, K. & Brewer, L., 1961. *Revised edition of Thermodynamics*. 2nd ed. New York: MacGraw-Hill.
165. Powelson, D. K. & Mills, A. L., 1996. Bacterial Enrichment at the Gas-Water Interface of a Laboratory Apparatus. *Appl. Environ. Microbiol.*, 62(7), pp. 2593-2597.
166. Prescott, L. M., Harley, J. P. & Klein, D. A., 2002. *Microbiology*. 5th ed. s.l.:The McGraw-Hill Companies.
167. Raiders, R. A., Knapp, R. M. & McInerney, M. J., 1989. Microbial selective plugging and enhanced oil recovery. *Journal of Industrial Microbiology*, Volume 4, pp. 215-230.
168. Rajinder, P. G. & Swartzendruber, D., 1962. Flow-Associated Reduction in the Hydraulic Conductivity of Quartz Sand. *Soil Science Society of America*, 26(1), pp. 6-10.
169. Raleigh, J. T. & Flock, D. L., 1965. A Study of Formation Plugging With Bacteria. *Journal of Petroleum Technology*, Volume 17, pp. 201-206.
170. Redman, J. A., Grant, S. B., Olson, T. M. & Estes, M. K., 2001. Pathogen Filtration, Heterogeneity, and the Potable Reuse of Wastewater. *Environ. Sci. Technol.*, 35(9), p. 1798-1805.
171. Ren, X. et al., 2018. Sorption, transport and biodegradation – An insight into bioavailability of persistent organic pollutants in soil. *Science of The Total Environment*, Volume 610-611, pp. 1154-1163.
172. Rijnaarts, H. H. M. et al., 1996. Bacterial Deposition in Porous Media: Effects of Cell-Coating, Substratum Hydrophobicity, and Electrolyte Concentration. *Environ. Sci. Technol.*, 30(10), p. 2877-2883.
173. Rimstidt, J. D., 2014. *Geochemical Rate Models: An Introduction to Geochemical Kinetics*. Cambridge: Cambridge University Press.
174. Rinck-Pfeiffer, S., Ragusa, S., Sztajn bok, P. & Vandeveld, T., 2000. Interrelationships between biological, chemical, and physical processes as an analog to clogging in aquifer storage and recovery (ASR) wells. *Water Research*, 34(7), pp. 2110-2118.
175. Rittmann, B. E., 1993. The Significance of Biofilms in Porous Media. *Water Resources Research*, 29(7), pp. 2195-2202.
176. Rudyk, S. & Søgaard, E., 2011. Microbial-Enhanced Oil Recovery (MEOR). In: C. Whitby & T. L. Skovhus, eds. *Applied Microbiology and Molecular Biology in Oilfield Systems*. London: Springer, pp. 179-187.
177. Ryan, J. N. & Elimelech, M., 1996. Colloid mobilization and transport in groundwater. *Colloids and Surfaces A: Physicochemical and Engineering Aspects*, Volume 107, pp. 1-56.
178. Saaltink, M., Ayora, C. & Carrera, J., 1998. A mathematical formulation for reactive transport that eliminates mineral concentrations. *Subsurface Hydrology*, 34(7), p. 1649-1656.
179. Sbalzarini, I. & Koumoutsakos, P., 2005. Feature point tracking and trajectory analysis for video imaging in cell biology. *J Struct Biol.*, 151(2), pp. 182-195.
180. Schafer, A. et al., 1998. Transport of bacteria in unsaturated porous media. *Journal of Contaminant Hydrology*, 33(1-2), p. 149-169.
181. Schetz, J. & Bowersox, R. D. W., 2011. *Boundary Layer Analysis*. 2nd ed. Reston: American Institute of Aeronautics and Astronautics.
182. Schijven, J. F. & Hassanizadeh, S. M., 2000. Removal of Viruses by Soil Passage: Overview of Modeling, Processes, and Parameters. *Critical Reviews in Environmental Science and Technology*, 30(1), p. 49-127.
183. Schneider, C. A., Rasband, W. S. & Eliceiri, K. W., 2012. NIH Image to ImageJ: 25 years of image analysis. *Nature Methods*, 9(7), pp. 671-675.
184. Schott, J. & Oelkers, E. H., 1995. Dissolution and crystallization rates of silicate minerals as a function of chemical affinity. *Pure & Appl. Chem.*, 67(6), pp. 903-910.
185. Seewald, J. S., Zolotov, M. Y. & McCollom, T., 2006. Experimental investigation of single carbon compounds under hydrothermal conditions. *Geochimica et Cosmochimica Acta*, 70(2), pp. 446-460.
186. Seki, K., Miyazaki, T. & Nakano, M., 1996. Reduction of Hydraulic Conductivity Due to Microbial Effects. *Transactions of The Japanese Society of Irrigation, Drainage and Reclamation Engineering*, 1996(181), pp. 137-144.
187. Shelford, V. E., 1931. Some Concepts of Bioecology. *Ecology*, 12(3), pp. 455-467.

-
188. Sirivithayapakorn, S. & Keller, A., 2003. Transport of colloids in saturated porous media: A pore-scale observation of the size exclusion effect and colloid acceleration. *Water Resources Research*, 39(4), pp. 1-9.
189. Sivasankar, P. & Suresh Kumar, G., 2019. Influence of bio-clogging induced formation damage on performance of microbial enhanced oil recovery processes. *Fuel*, Volume 236, pp. 100-109.
190. Smuk, A., 2007. *LEHEN 2 (LEH-002) Gas-Erweiterungsbohrung*. Wien: Rohöl-Aufsuchungs Aktiengesellschaft.
191. Song, J. & Zhang, D., 2013. Comprehensive Review of Caprock-Sealing Mechanisms for Geologic Carbon Sequestration. *Environ. Sci. Technol.*, Volume 47, p. 9–22.
192. Steefel, C. & Lasaga, A., 1994. A coupled model for transport of multiple chemical species and kinetic precipitation/dissolution reactions with application to reactive flow in single phase hydrothermal systems. *American Journal of Science*, Volume 294, pp. 529-592.
193. Sternberg, S. R., 1983. Biomedical Image Processing. *Computer*, 16(1), pp. 22-34.
194. Stewart, P. S. & Franklin, M. J., 2008. Physiological heterogeneity in biofilms. *Nature Reviews Microbiology*, Volume 6, p. 199–210.
195. Stewart, T. & Fogler, H., 2001. Biomass plug development and propagation in porous media. *Biotechnol Bioeng*, 72(3), pp. 353-363.
196. Stoodley, P., Boyle, J., Dodds, I. & Lappin-Scott, H., 1997. Consensus model of biofilm structure. In: *Biofilms: community interactions and control*. Cardiff, UK: Bionline, pp. 1-9.
197. Stoodley, P., Dodds, I., Boyle, J. & Lappin-Scott, H., 1999a. Influence of hydrodynamics and nutrients on biofilm structure. *Journal of Applied Microbiology Symposium Supplement*, Volume 85, pp. 19s-28s.
198. Stoodley, P., Lewandowski, Z., Boyle, J. D. & Lappin-Scott, H. M., 1999b. The formation of migratory ripples in a mixed species bacterial biofilm growing in turbulent flow. *Environmental Microbiology*, 1(5), pp. 447-455.
199. Strapoć, D. et al., 2011. How Specific Microbial Communities Benefit the Oil Industry. In: C. Whitby & T. L. Skovhus, eds. *Applied Microbiology and Molecular Biology in Oilfield Systems*. London: Springer, pp. 211-216.
200. Sugai, Y. et al., 2013. Considerations on the possibility of microbial clogging of re-injection wells of the wastewater generated in a water-dissolved natural gas field. *International Biodeterioration & Biodegradation*, Volume 81, pp. 35-43.
201. Taylor, J. et al., 1986. Technical and economic assessment of methods for the storage of large quantities of hydrogen. *International Journal of Hydrogen Energy*, 11(1), pp. 5-22.
202. Thomas, D. et al., 2016. *Power-to-Gas Roadmap for Flanders*, Belgium: WaterstofNet vzw.
203. Thullner, M., 2010. Comparison of bioclogging effects in saturated porous media within one- and two-dimensional flow systems. *Ecological Engineering*, 36(2), pp. 176-196.
204. Thullner, M. & Baveye, P., 2008. Computational Pore Network Modeling of the Influence of Biofilm Permeability on Bioclogging in Porous Media. *Biotechnology and Bioengineering*, 99(6), pp. 1337-1351.
205. Truche, L., 2009. *Transformations minéralogiques et géochimiques induites par la présence d'hydrogène dans un site de stockage de déchets radioactifs*, Toulouse III: s.n.
206. Truche, L., Berger, G., Albrecht, A. & Domerg, L., 2013. Engineered materials as potential geocatalysts in deep geological nuclear waste repositories: A case study of the stainless steel catalytic effect on nitrate reduction by hydrogen. *Applied Geochemistry*, Volume 35, pp. 279-288.
207. Truche, L. et al., 2010. Kinetics of pyrite to pyrrhotite reduction by hydrogen in calcite buffered solutions between 90 and 180 °C: implications for nuclear waste disposal. *Geochimica et Cosmochimica Acta*, 74(10), pp. 2894-2914.
208. Truche, L. et al., 2013. Sulphide mineral reactions in clay-rich rock induced by high hydrogen pressure. Application to disturbed or natural settings up to 250 degrees C and 30 bar. *Chemical Geology*, Volume 351, pp. 217-228.
209. Tufenkji, N., 2007. Modeling microbial transport in porous media: Traditional approaches and recent developments. *Advances in Water Resources*, 30(6-7), p. 1455–1469.
210. Tufenkji, N. & Elimelech, M., 2005. Spatial Distributions of Cryptosporidium Oocysts in Porous Media: Evidence for Dual Mode Deposition. *Environ. Sci. Technol.*, 39(10), p. 3620–3629.

211. Updegraff, D. M., 1983. The effect of microorganisms on the permeability and porosity of petroleum reservoir rock. In: *Microbial Enhanced Oil Recovery*. Tulsa, OK.: PennWell Publishing Co, pp. 37-44.
212. Updegraff, D. M. & Wren, G. B., 1954. The Release of Oil from Petroleum-Bearing Materials by Sulfate-Reducing Bacteria. *Appl Microbiol.*, 2(6), pp. 309-322.
213. Vandevivere, P., 1995. Bacterial clogging of porous media: A new modelling approach. *Biofouling*, 8(4), pp. 281-291.
214. Vandevivere, P. & Baveye, P., 1992. Saturated Hydraulic Conductivity Reduction Caused by Aerobic Bacteria in Sand. *Soil Science Society of America Journal*, Volume 56.
215. Voigt, M. et al., 2018. Evaluation and refinement of thermodynamic databases for mineral carbonation. *Energy Procedia*, Volume 146, pp. 81-91.
216. Vo, K., 2015. *libretexts*. [Online]
Available at:
https://chem.libretexts.org/Core/Physical_and_Theoretical_Chemistry/Kinetics/Reaction_Rates/Experimental_Determination_of_Kinetics/Spectrophotometry
[Accessed 8 May 2018].
217. Wang, J., Ju, Y., Gao, F. & Liu, J., 2015. A simple approach for the estimation of CO₂ penetration depth into a caprock layer. *Journal of Rock Mechanics and Geotechnical Engineering*, pp. 1-12.
218. Wang, J. & Peng, Y., 2014. Numerical modeling for the combined effects of two-phase flow, deformation, gas diffusion and CO₂ sorption on caprock sealing efficiency. *Journal of Geochemical Exploration*, 144(Part A), pp. 154-167.
219. Wan, J., Wilson, J. & Kieft, T., 1994. Influence of the gas-water interface on transport of microorganisms through unsaturated porous media. *Appl Environ Microbiol*, 60(2), pp. 509-516.
220. Warsi, O. M. & Dykhuizen, D. E., 2017. Evolutionary implications of Liebig's law of the minimum: Selection under low concentrations of two nonsubstitutable nutrients. *Ecology and Evolution*, 7(14), p. 5296–5309.
221. Watnick, P. & Kolter, R., 2000. Biofilm, City of Microbes. *Journal of Bacteriology*, 182(10), p. 2675–2679.
222. Watts, N. L., 1987. Theoretical aspects of cap-rock and fault seals for single- and two-phase hydrocarbon columns. *Marine and Petroleum Geology*, 4(4), pp. 274-307.
223. White, A., 2008. Quantitative Approaches to Characterizing Natural Chemical Weathering Rates. In: B. S., K. J. & W. A., eds. *Kinetics of Water-Rock Interaction*. New York, NY: Springer, pp. 469-543.
224. White, A. F. & Peterson, M. L., 1990. Role of Reactive-Surface-Area Characterization in Geochemical Kinetic Models. In: R. D. Basset & R. L. Melchior, eds. *Chemical Modeling of Aqueous Systems II*. s.l.: American Chemical Society, p. 461–475.
225. Wiegmann, A. et al., 2014. *GeoDict 2012 user guide*. s.l.: Math2Market.
226. Wiegmann, A., Rief, S., Latz, A. & Iliev, O., 2018. *Toward Predicting Filtration and Separation: Progress & Challenges*. Kaiserslautern, Germany: Fraunhofer Institut für Techno- und Wirtschaftsmathematik.
227. Wilson, J. T., Leach, L. E., Henson, M. & Jones, J. N., 1986. In Situ Bioremediation as a Ground Water Remediation Technique. *Groundwater Monitoring and Remediation*, 6(4), pp. 56-64.
228. Wimpenny, J., Manz, W. & Szewzyk, U., 2000. Heterogeneity in biofilms. *FEMS Microbiology Reviews*, 24(5), p. 661–671.
229. Wolterbeek, T. K. T. & Raoof, A., 2018. Meter-Scale Reactive Transport Modeling of CO₂-Rich Fluid Flow along Debonded Wellbore Casing-Cement Interfaces. *Environmental Science & Technology*, 52(6), pp. 3786-3795.
230. Yao, K.-M., Habibian, M. T. & O'Melia, C. R., 1971. Water and Waste Water Filtration: Concepts and Applications. *Environ. Sci. Technol.*, 5(11), pp. 1105-1112.
231. Youssef, N., Elshahed, M. S. & McInerney, M. J., 2009. Microbial Processes in Oil Fields: Culprits, Problems, and Opportunities. In: A. I. Laskin, S. Sariaslani & G. M. Gadd, eds. *Advances in Applied Microbiology*. Burlington: Academic Press, pp. 141-251.
232. Yun, W., Ross, C. M., Roman, S. & Kovscek, A. R., 2017. Creation of a dual-porosity and dual-depth micromodel for the study of multiphase flow in complex porous media†. *Lab on a Chip*, 17(8), p. 1462–1474.

-
233. Zarihos, I. M., Hassanizadeh, S. M., van Oosterhout, L. M. & van Oordt, W., 2018. Manufacturing a Micro-model with Integrated Fibre Optic Pressure Sensors. *Transport in Porous Media*, 122(1), p. 221–234.
234. Zhang, P. et al., 2001. Extended tailing of bacteria following breakthrough at the Narrow Channel focus area, Oyster, Virginia. *Water Resources Research*, 37(11), pp. 2687-2698.
235. Zheng, L. & Spycher, N., 2017. Modeling the potential impacts of CO₂ sequestration on shallow ground water: The fate of trace metal and organic compounds before and after leakage stops. *Greenhouse Gas Sci Technol*, p. 161–184.
236. Zhong, H. et al., 2017. Transport of bacteria in porous media and its enhancement by surfactants for bioaugmentation: A review. *Biotechnology Advances*, 35(4), pp. 490-504.
237. Zhu, C. & Anderson, G., 2002. *Environmental Applications of Geochemical Modeling*. s.l.:Cambridge University Press.
238. Zhu, W. et al., 2015. High-Pressure Microscopic Investigation on the Oil Recovery Mechanism by in Situ Biogases in Petroleum Reservoirs. *Energy Fuels*, 29(12), p. 7866–7874.
239. Zobell, C. E., 1946. Action of Microorganisms on Hydrocarbons. *Bacteriol Rev.*, 10(1-2), pp. 1-49."

Chapter 8 Appendixes

Appendix A: Material balance analysis

We have used material balance analysis to determine the original gas-in-place (OGIP) based on production and static pressure data, and to confirm there was no active aquifer connected to the reservoir formation. For this work MBAL software (<http://www.petex.com>) was used. The reservoir was assumed as a tank (the identical pressure and fluid properties at any location in the reservoir). This study confirms that there is no active aquifer connected to the field.

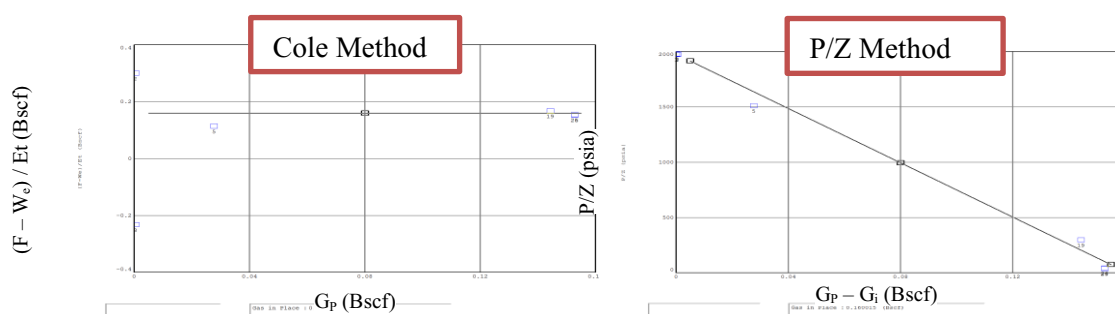


Figure 8-1 Diagnostics plots indicate the absence of any active aquifer in the reservoir.

To estimate the OGIP, three scenarios were considered. Low, medium and high case studies were simulated to get the OGIP, and the values are reported in Table 8-1. This estimation was utilized in the construction of the dynamic model.

Table 8-1 Reported original gas in place values obtained from three scenarios considering low, medium, and high estimates.

Case study	Low case	Medium case	High case
Gas initially in place (Bscf)	0.15	0.16	0.17
Gas initially in place ($\times 10^6$ m ³)	4.247	4.531	4.814

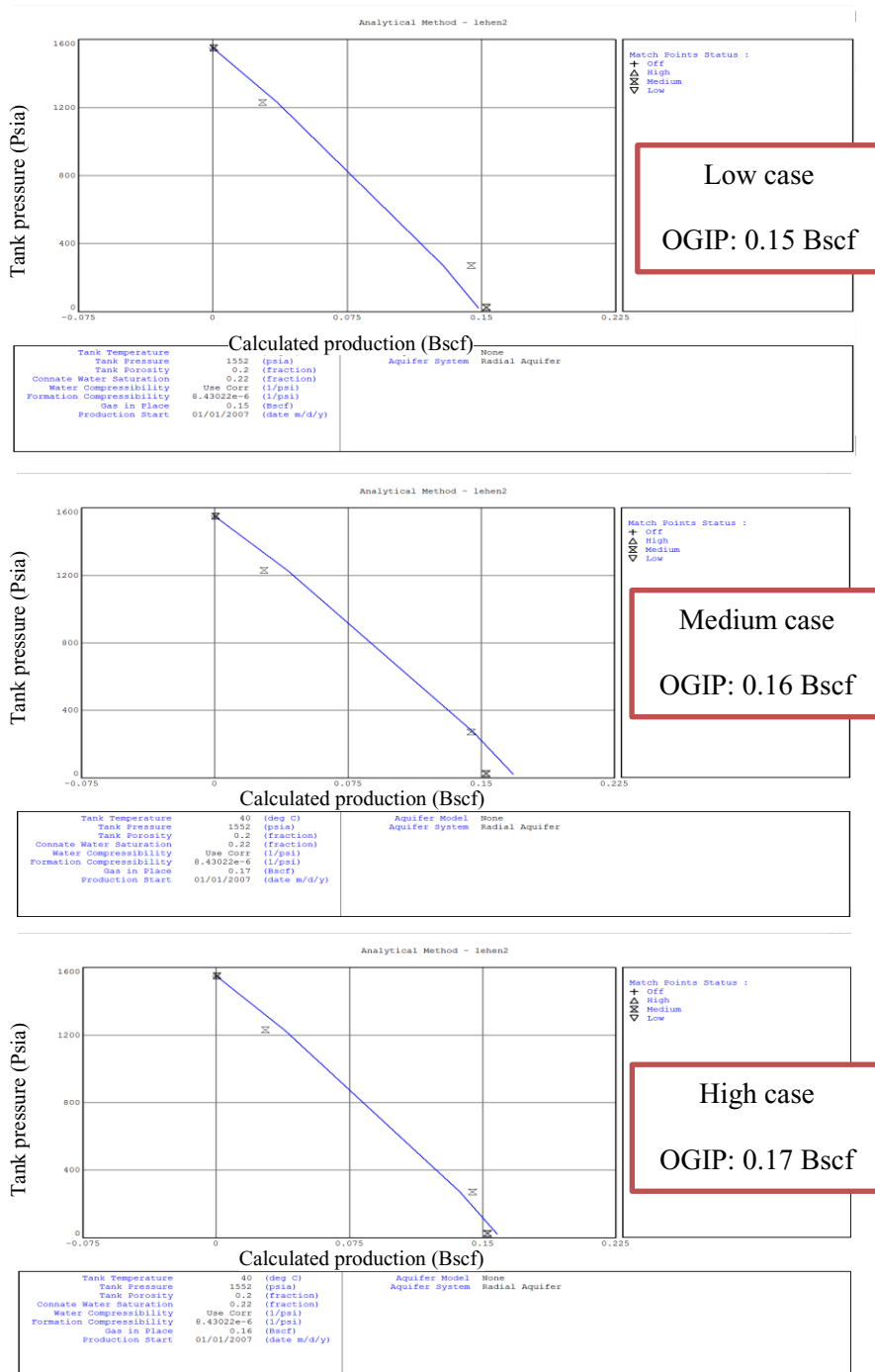


Figure 8-2 Calculated OGIP values obtained from three scenarios for Lehen-2.

Appendix B: Structure and Stratigraphy modeling steps

In the following, detailed steps, which were completed within the SKUA Structure & Stratigraphy module, is described. The requirements of the workflow include input data such as horizon interpretations, well data (i.e., horizon markers), a stratigraphic column, and fault interpretations. The workflow creates a model made of the fault network and horizon grids by the enclosed volume of interest.

Initially, different data sources for horizon- modeling were selected, including the digitized curves corresponding the structural maps, well markers, the eroded unconformity layer and the fault data in forms of digitized curves (Figure 8-3). Using the in-built workflow, horizons and the fault network were created (Figure 8-4). To adjust the horizons at the exact locations of the well markers, well data were checked and honored (Figure 8-5). By doing this step, the horizons were adjusted to the reported values of markers, which enhanced the accuracy of a geological model. At this stage, the geological model was finalized, and the geological grid was ready to be used in the dynamic model. For this sub-domain matching to the reservoir was selected, and imported into the dynamic modeling tool (Figure 8-6).

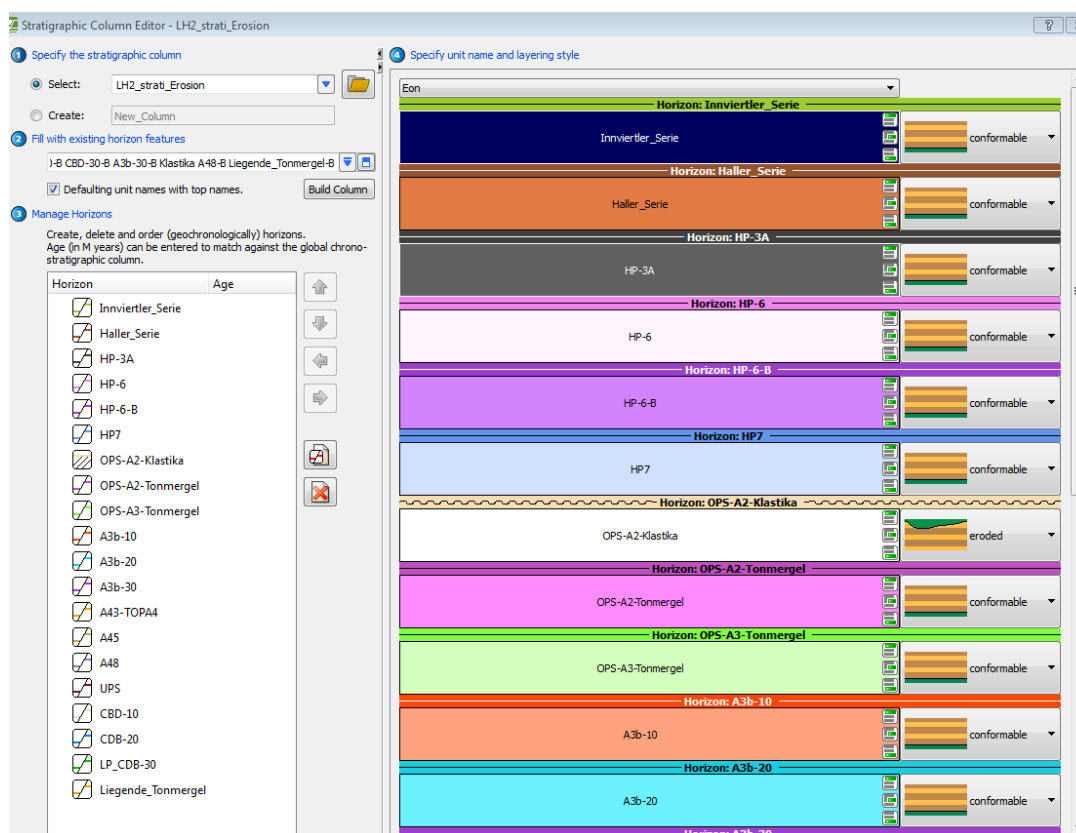


Figure 8-3 Stratigraphic column used in the structural model, the well markers, horizons, fault network, and unconformity were imported.

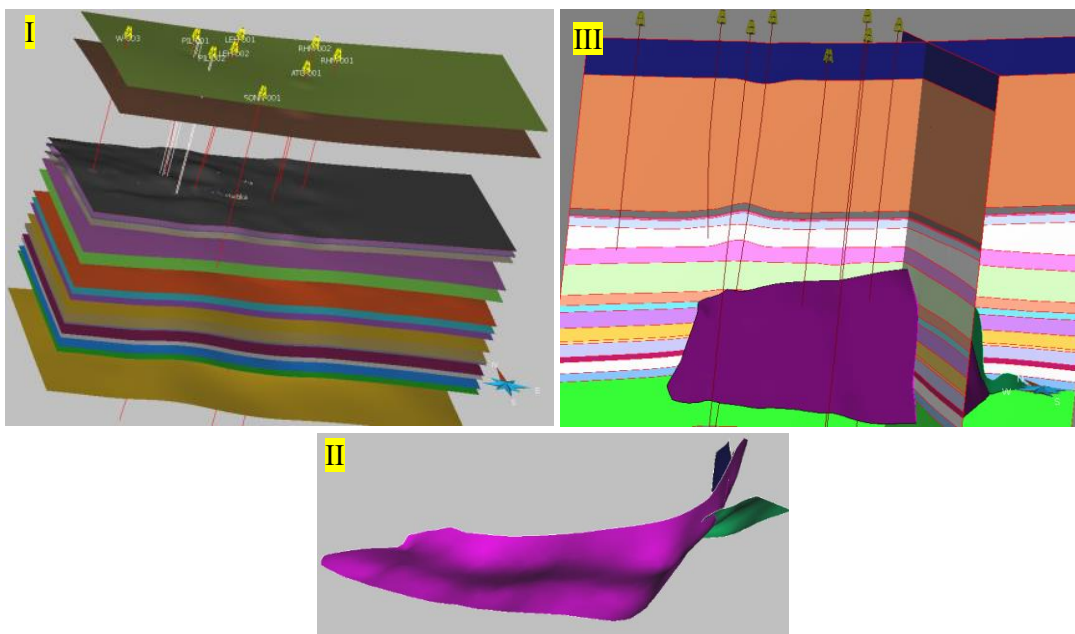


Figure 8-4 (I) Model horizons; (II) the fault network; (III) the integrated model.

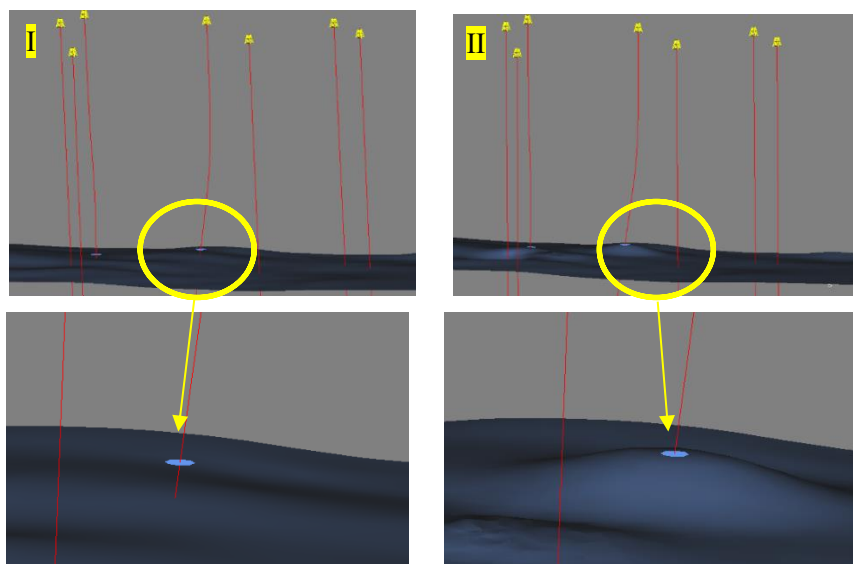


Figure 8-5 Honoring the well markers with the “flex only” option to enhance the accuracy of the geological model (I and II respectively show one of the interpreted horizons before and after honoring markers).

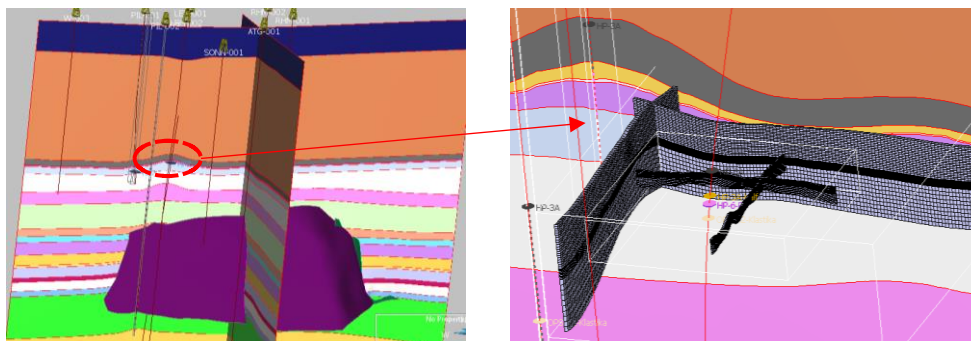


Figure 8-6 (I) Final 3D geological model, and (II) selected reservoir sub-domain model that was imported to the dynamic model.

Appendix C: Bacterial growth curve and cell counting at the stationary phase

The bacterial growth pattern is directly linked to the bacteria's environment. Often for microorganisms to grow and reproduce, some minerals, sources of energy, elements such as carbon, nitrogen, phosphorus, and sulfur should be present and supplied (Prescott, et al., 2002). Colonies exhibit a variety of forms depending on the bacterial species and the culture environment. Growth conditions can easily be controlled in the lab; thus, one can identify the particular properties of the bacteria and their growth media that affect growth patterns. Generally, having less favorable environmental conditions leads to more complex colonial growth pattern (Lacasta, et al., 1999). Microorganisms' growth is described as an increase in cellular constituents and, thus, a rise in cell number. To estimate the bacterial growth, the changes in the total population number should be measured. During the growth, cells copy their DNA continuously and divide up constantly by the binary fission process (Prescott, et al., 2002).

Microorganisms are cultivated in a liquid medium, called a batch culture or closed system. Bacteria in a favorable growth medium, follow a distinctive pattern of increasing in number of cells followed by a decrease. Different bacteria reproduce at distinct rates. The generation time is the time that it takes for the population to double. The microorganisms' growth is normally plotted as the logarithm of the number of viable cells vs. the incubation time. The subsequent curve shows four distinct phases (Prescott, et al., 2002) (Figure 8-7).

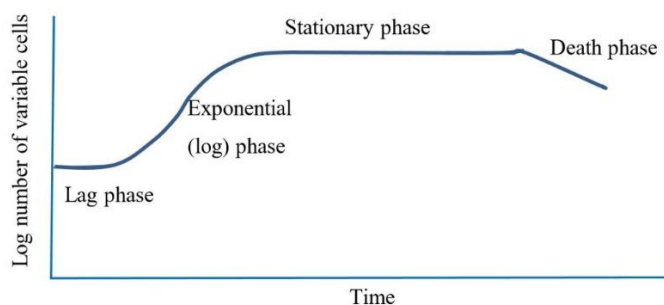


Figure 8-7 A typical microbial growth curve in batch culture including four phases of the growth.

The lag phase corresponds to the period when microorganisms are introduced into the culture medium, and the cells are adjusting to their new environment; consequently, cells are preparing for cell division. There is no immediate increase in cell numbers in this period. The lag phase duration is a function of the microorganisms' condition and the nature of the medium. When the inoculum is from an old culture or has been refrigerated, this phase could be relatively long. Likewise, the inoculation of a culture into a medium with a different chemical constituents results in a more prolonged lag phase (Prescott, et al., 2002).

During the exponential (log) growth phase, microorganisms are growing and dividing at the maximal rate possible. The exponential phase lasts up until conditions of growth become less favorable. In this phase, generation time can be calculated. The microorganisms that grow faster will have a steep slope. The exponential growth is a balanced growth; the cellular components are produced at constant rates compared to each other. When a change in the nutrient levels or environmental settings happens, unbalanced growth may occur. In this condition, the rates of cell constituents are changed relative to each other up until another balanced state is reached (Prescott, et al., 2002).

The exponential phase eventually leads to the stationary phase, in which the curve flattens. During this phase, population growth stops, and the growth curve becomes horizontal. In other words, “there is a balance between cell division and cell death”; therefore, there is no net increase in the number of cells (Prescott, et al., 2002). A population-level of around 10^9 cells per ml is frequently accomplished by bacteria at the stationary phase. There are several explanations for the microorganisms to enter the stationary phase. One is associated with the lack of nutrients in the system; this slows down the population growth. For the aerobic organisms, the lack of oxygen availability is another reason. The third reason for the growth cease may be due to the accumulation of toxic waste products. The final argument may be due to reaching a critical population level for the microorganisms that can stop the growth (Prescott, et al., 2002).

A closed system doesn't allow to add nutrients or remove the waste products that begin to build up; consequently, a decrease in the number of living cells in the population happens. This phase is called the Decline or Death Phase (Prescott, et al., 2002).

A Spectrophotometer was utilized to measure the optical density (OD) within numerous intervals for the cell mass growth measurement. In a spectrophotometry technique, the absorbance of the light for a chemical substance is determined by measuring the light intensity as a light beam goes through a sample solution. The measurement is used to determine the amount of a known chemical substance (Vo, 2015). For the measurement, the culture was placed in a cuvette, while a light beam passed through it. Depending on the cell density, the light is scattered by the cells, which is known as turbidity. The scattering intensity or turbidity is frequently called optical density, and it is proportional to the cell density. By measuring OD at 600 nm for *Lactobacillus Casei* and plotting it versus time, the growth curve was obtained. The primary purpose of this measurement was to identify the starting point of the stationary phase (at around 22 hours after incubation), which was employed as the starting point of the tests (Figure 8-8).

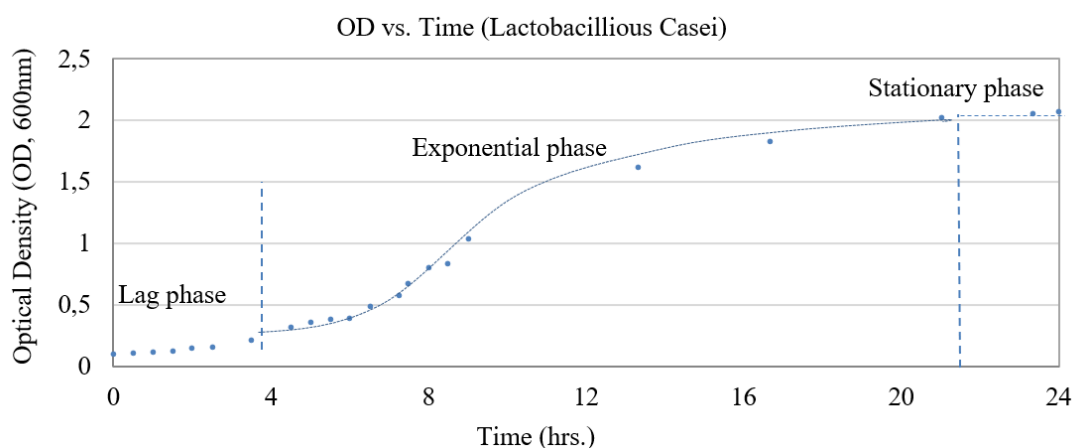


Figure 8-8 *Lactobacillus Casei* growth curve; the start of the stationary phase was estimated at approximately 22 hrs after incubation.

Cell counting at the stationary growth phase

There are different methods for microbial growth measurement to define growth rates and generation times. The approaches used for estimating bacterial growth are either direct or indirect counts of cells or microbial biomass. An obvious, inexpensive, and relatively rapid way to determine microbial numbers is done by direct counting. Using a counting chamber, one can obtain information about the size and morphology of microorganisms. A counting chamber is a precision slide measuring equipment that is made of special optical glass and is used to count cells and particles in suspensions under a microscope.

For this study, a Hemocytometer cell counting device is used (Figure 8-9). The cell counting includes 25 squares, which cover an area of 1 mm², with a depth of 0.01 mm. To estimate the cell concentration at the start of the stationary phase, the sample was diluted with the ration of 1 to 5, then it was located under the coverslip. Cell counts were done in five different squares (Figure 8-9, III): square 1:118, square 2:120, square 3:136, square 4:126, and square 5:98, with the average cell count value of 119.6. The volume of each square in the inside chamber can be calculated from the width and height of the square (0.25mm x 0.25mm) multiplied by the sample height:

$$v = 0.25\text{mm} * 0.25\text{mm} * 0.1\text{mm} = 0.00625\text{mm}^3 = 0.00000625\text{ ml}$$

Knowing the volume of the square and the average cell count, the number of cells in 1 ml of solution was estimated as:

$$\text{number of cells in 1 ml} = 19136000\text{ cells}$$

As the dilution ratio was 1 to 5, the total number of cells in the original solution at the start of the stationary phase was 95680000 cells per 1 ml. The number of cells is in agreement with the reported values in the literature; a frequent population level of around 10⁹ cells per ml is

accomplished by bacteria at the stationary phase (Prescott, et al., 2002). The disadvantage of the direct counting measurements, despite the ease and rapidness of these procedures, is that they do not discriminate between living and dead cells.

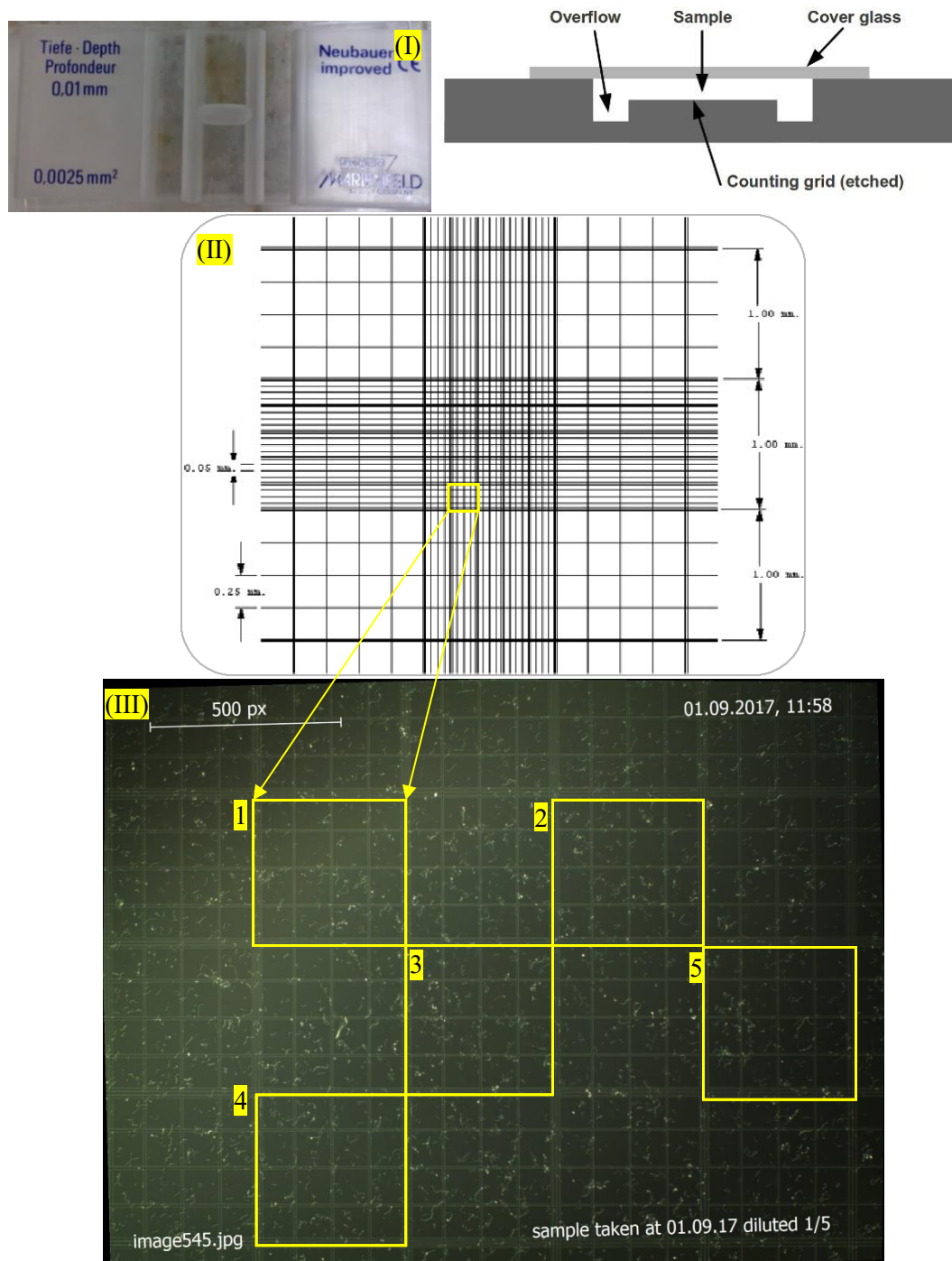


Figure 8-9 Cell counting at the start of the stationary phase of the bacterial growth. (I): Hemocytometer cell counting chamber and the side view of the chamber; the cover glass and the space below it holding the bacterial suspension. (II): Top view of the chamber showing gridding that is in the center of the slide. (III): Microscopic image of an enlarged view of the grid holding the bacterial sample. The bacteria were counted in five different squares, and the average number of bacteria in these squares was then used to compute the concentration of cells in the original sample.

Appendix D: Image processing procedure

Montaged images of micromodels were analyzed to evaluate biomass growth over time using ImageJ software. ImageJ is a freeware, Java-based image processing program established at the National Institutes of Health with its own GUI. The significant advantages of this tool are the vast and knowledgeable user community, as well as the available extensive plugins and macros for specific purposes (Schneider, et al., 2012).

The optical images converted to binary images to distinguish the biomass (i.e., number of black pixels). A challenge in the image analysis was to correct for the uneven illuminated background effect from the microscope used in the first setup and to represent the biomass in a binary image without losing the real features in the original images. Therefore, an algorithm was written to remove the background, enhance images, and keep as much as possible information of the original images to track the biomass growth over time (see Figure 8-11). Images that were taken in ROI experiments suffer from this consequence. The binary image from the original image without any correction and effect of the uneven illumination background is displayed in (Figure 8-10; (a) to (c)); the binary image went through all correction is shown in (Figure 8-10; (d)).

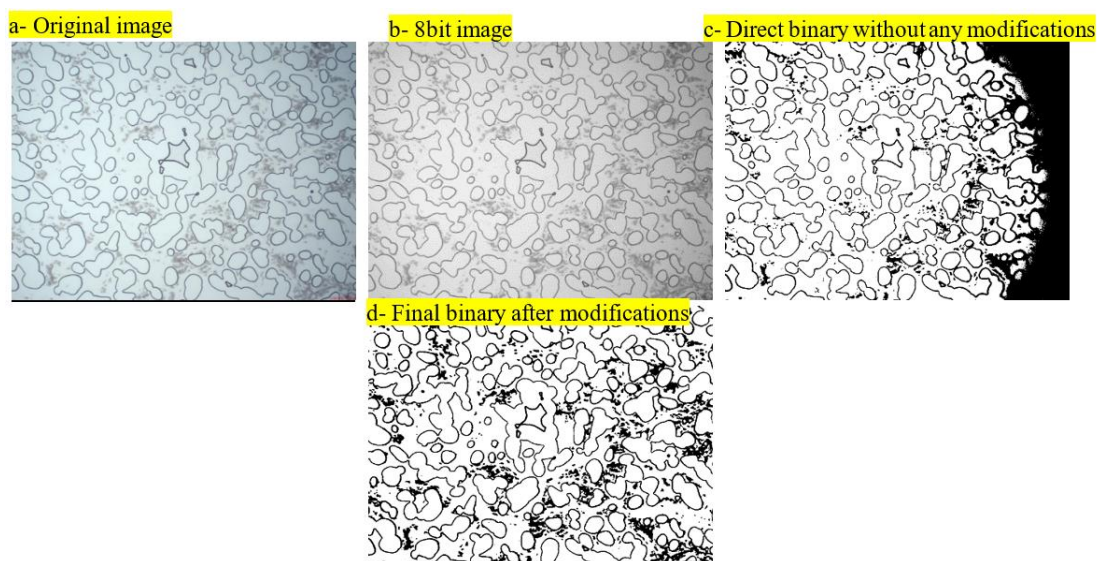


Figure 8-10 Uneven illumination background effect on the binary image. (a): Original image; (b): 8-bit image; (c): binary image from the 8-bit binary image without any corrections; (d) final binary image after all the corrections were applied.

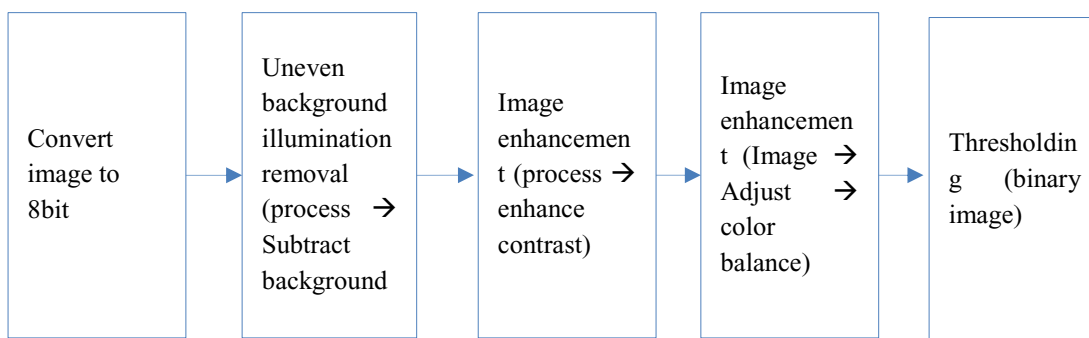


Figure 8-11 Image analysis sequence.

At first, all images corrected for the background uneven illumination effect. To subtract the image background (Process → Subtract Background; “Rolling ball radius” set to “80.0 pixels”– “Light background”) was used. This command removes smooth continuous backgrounds from images. The background normalization was done by an algorithm called “rolling ball” that is described in (Sternberg, 1983). The “rolling ball” algorithm, in which the user defines the radius, is rolled over the pixel-intensity “topography” of the entire surface of an image (Figure 8-12; (a-I, b-I & c-I)). The surface plot shows this topography. Here all topography which touches the “rolling ball” surface, in other words, it is tangent to it, was calculated as the background of the image; consequently, converted to white (Figure 8-12). By applying the “rolling ball,” all of the peaks that have a radius larger than the “ball”, which can enter into the peak, were subtracted (Chanou, et al., 2014).

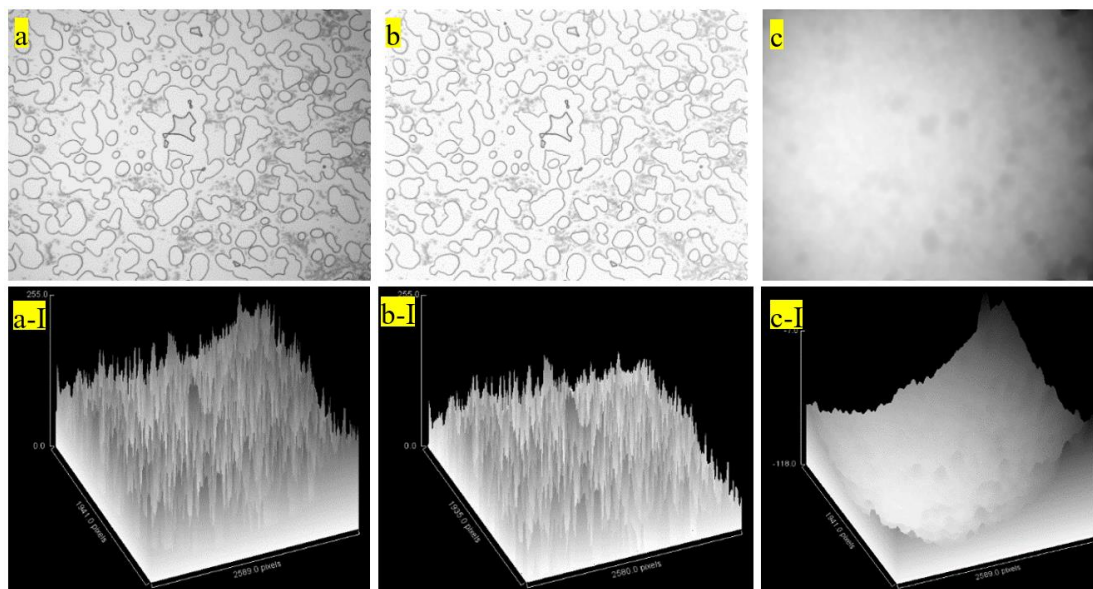


Figure 8-12 Images and corresponding surface plots showing the difference in illumination; (a): the original image, (b): the image corrected by “subtract background,” and (c): the subtracted image. The surface plots of the images are shown below each image, correspondingly. The rolling ball algorithm was applied in b-I.

Figure 8-13 shows more details on the background subtraction correction. Two sections in the original and the processed images are chosen, and the profile plots for them are drawn. To quality control the subtract background option, the two grey plots for the region (a) in Figure 8-13 are plotted in the same graph alongside the difference plot in Figure 8-14. This plot indicates that all the features (sharp values) in both images are preserved.

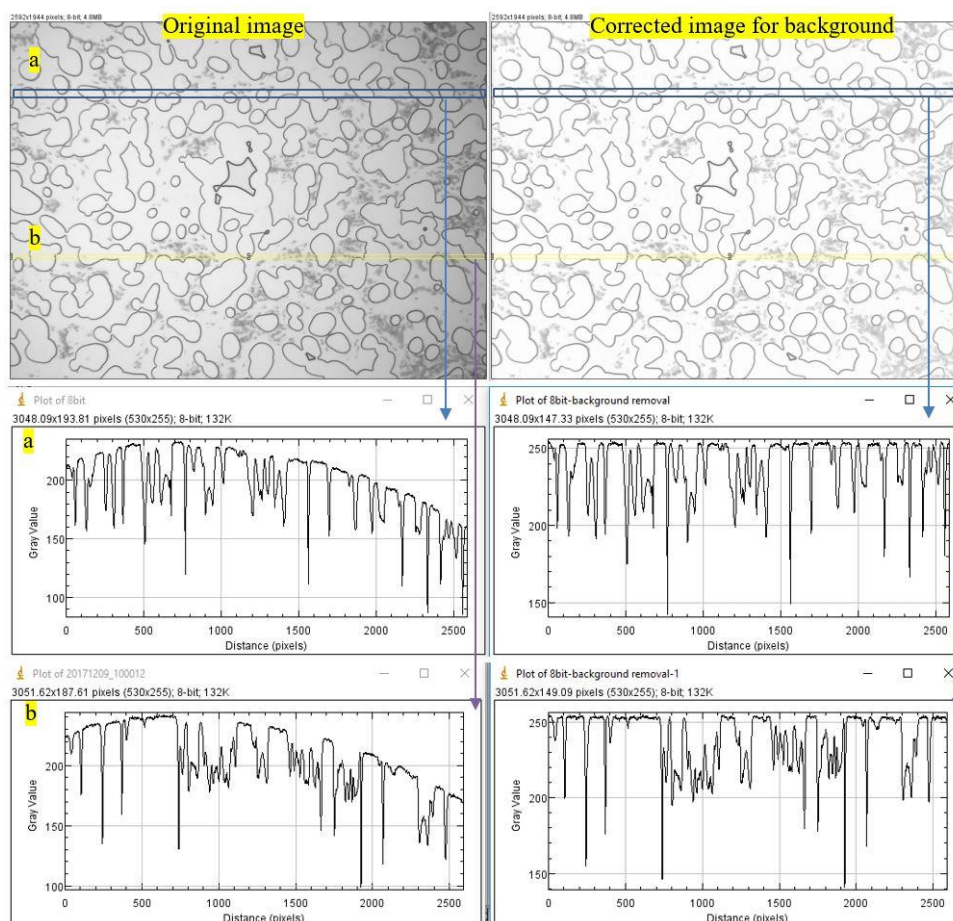


Figure 8-13 Illustration of the process of “Subtract Background” in ImageJ. This command corrects an unevenly illuminated background, as shown in the left profiles using ‘sliding paraboloid’ or a legacy ‘rolling ball’ algorithm. The grey value profiles for two regions (a & b) are shown below each image, via “Analyze->Plot Profile” command. The sharp features after the image correction are preserved.

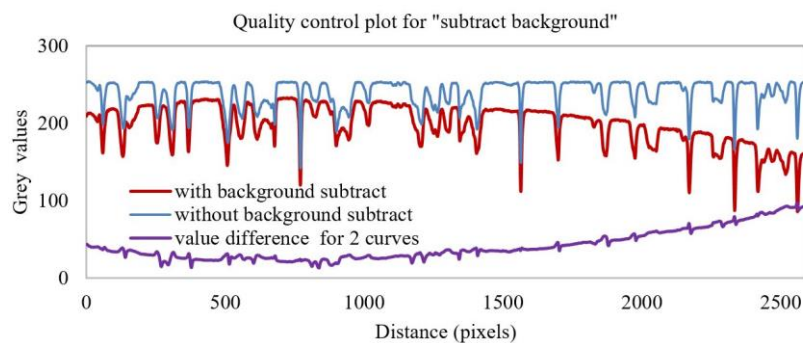


Figure 8-14 Quality control plot for the background subtract, applied in ImageJ. All the features are preserved and shifted to correct the unevenness in illumination.

The next step of modifying images was “image enhancement” (Figure 8-15). This was done by (process → enhance contrast; saturated pixels set to 8% and set to normalize). This command applies image contrast enhancement by using either histogram stretching or histogram equalization. The selected Saturated Pixels value decides on the number of image pixels that are allowed to become saturated. The bigger this value, the higher the contrast will be (Ferreira & Rasband, 2012).

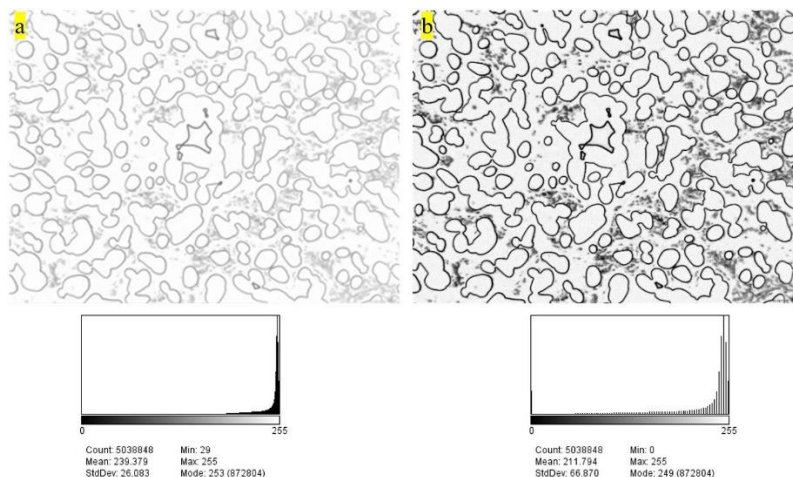


Figure 8-15 Image enhancement (initial image (a) → image after contrast enhancement (b)) using (process → enhance contrast) command. Pixel intensity versus a number of pixels shown in histograms below the images.

Next, the localized enhancement applied to the images (Figure 8-16). For this purpose (Image → Adjust → color balance) command was used.

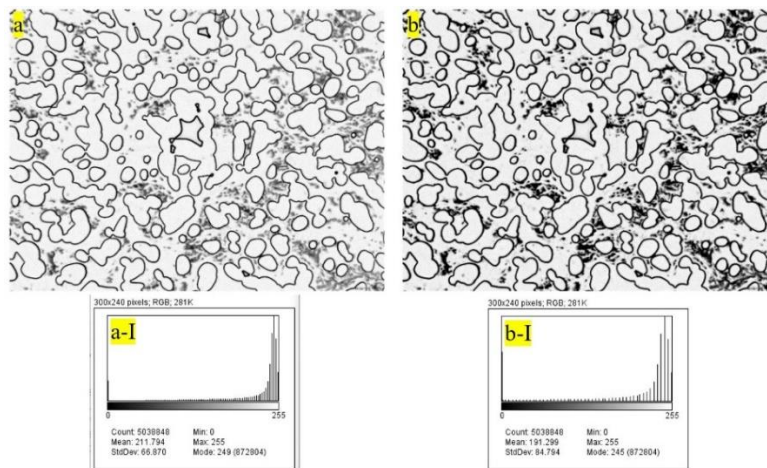


Figure 8-16 Image enhancement step. (a): Initial image from the previous step; (b): after contrast adjustment.

The final step in image analysis was thresholding (image → adjust → threshold). Thresholding splits the image into the foreground and background. The lower and upper threshold values were set, and the grayscale image was segmented into features of interest and background. A comparison of all steps and final processed images are shown in Figure 8-17 and Figure 8-18.

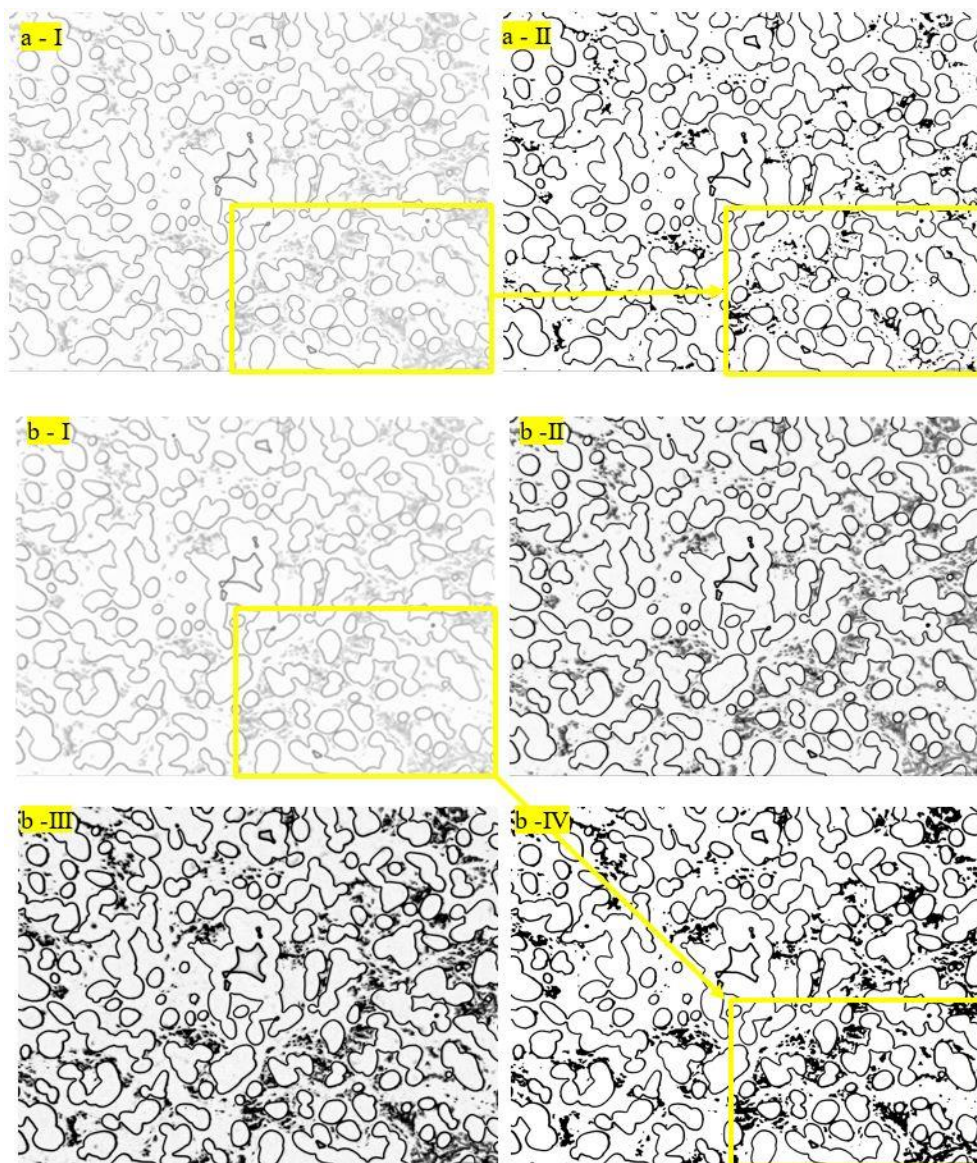


Figure 8-17 Comparison of binarizing processes after removing the uneven background illumination with and without applying other correction. (a-I& a-II): Images of the initial image and the binary image without extra processing option; in this way, some biomass was disappeared. In (b-I, b-II, b-III& b-IV) sequence of image analysis by ImageJ are shown; (b-I): image after “enhancement” processing– (b-II): image after correction by “adjust color”– (b-III): image converted into the binary by “thresholding” – (b-IV): finalized binarized image. Comparing images of (a-II& b-IV) displays the features, and biomass was kept in the final binary image after all processing steps are completed.

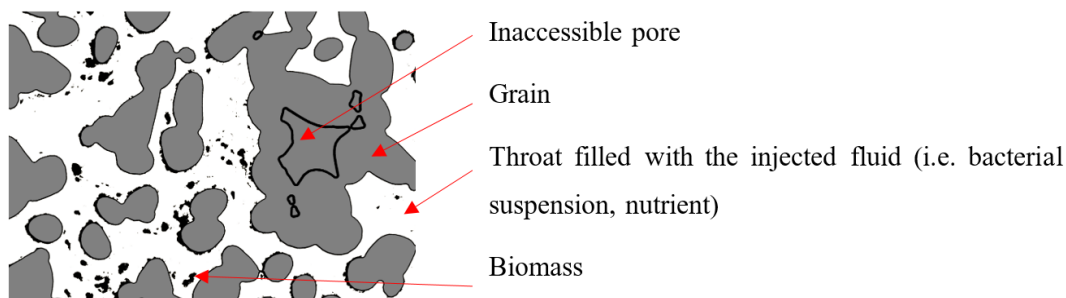


Figure 8-18 A sample of a final processed image.

Appendix E: Clogging and unclogging of biomass

Figure 8-19 illustrates the high-resolution images showing both clogging and unclogging of biomass in the pore throat due to the flow of the cloudy stream. The time-lapse video is available in the supplementary multimedia material.

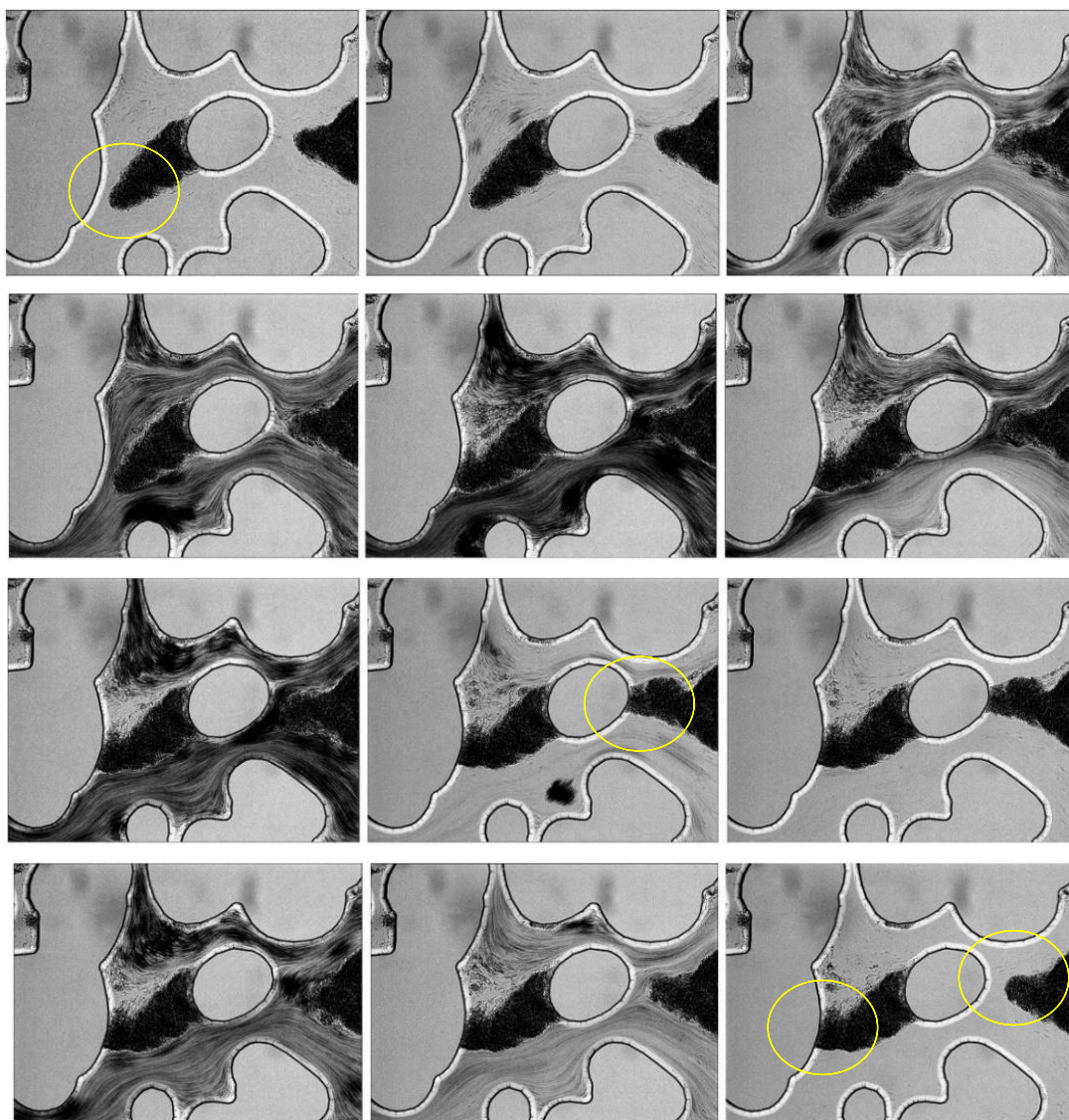


Figure 8-19 Frames from a movie depicting clogging and unclogging (circled areas) of biomass caused by the cloudy stream.

Appendix F: Biomass growth and pressure response during NF

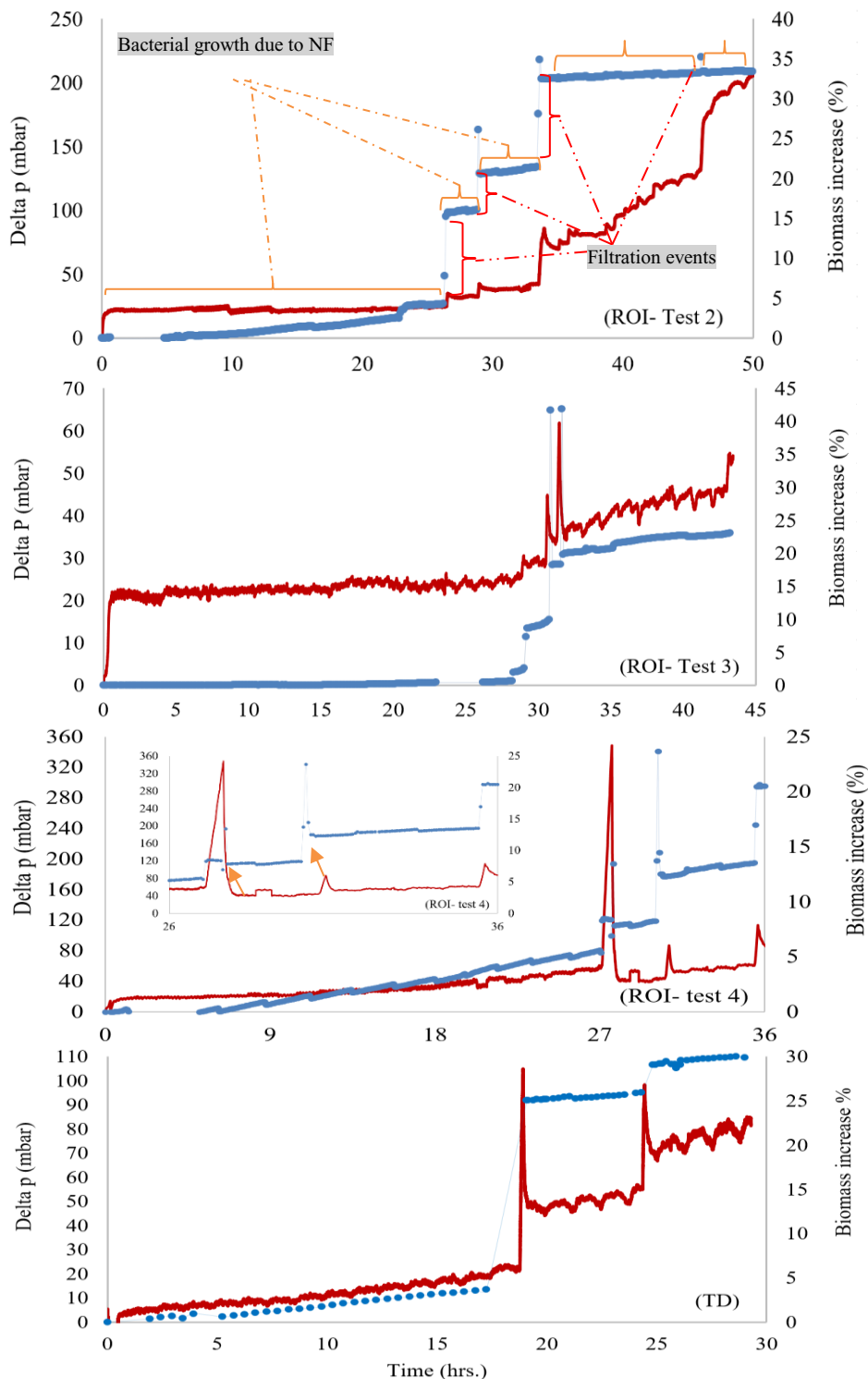
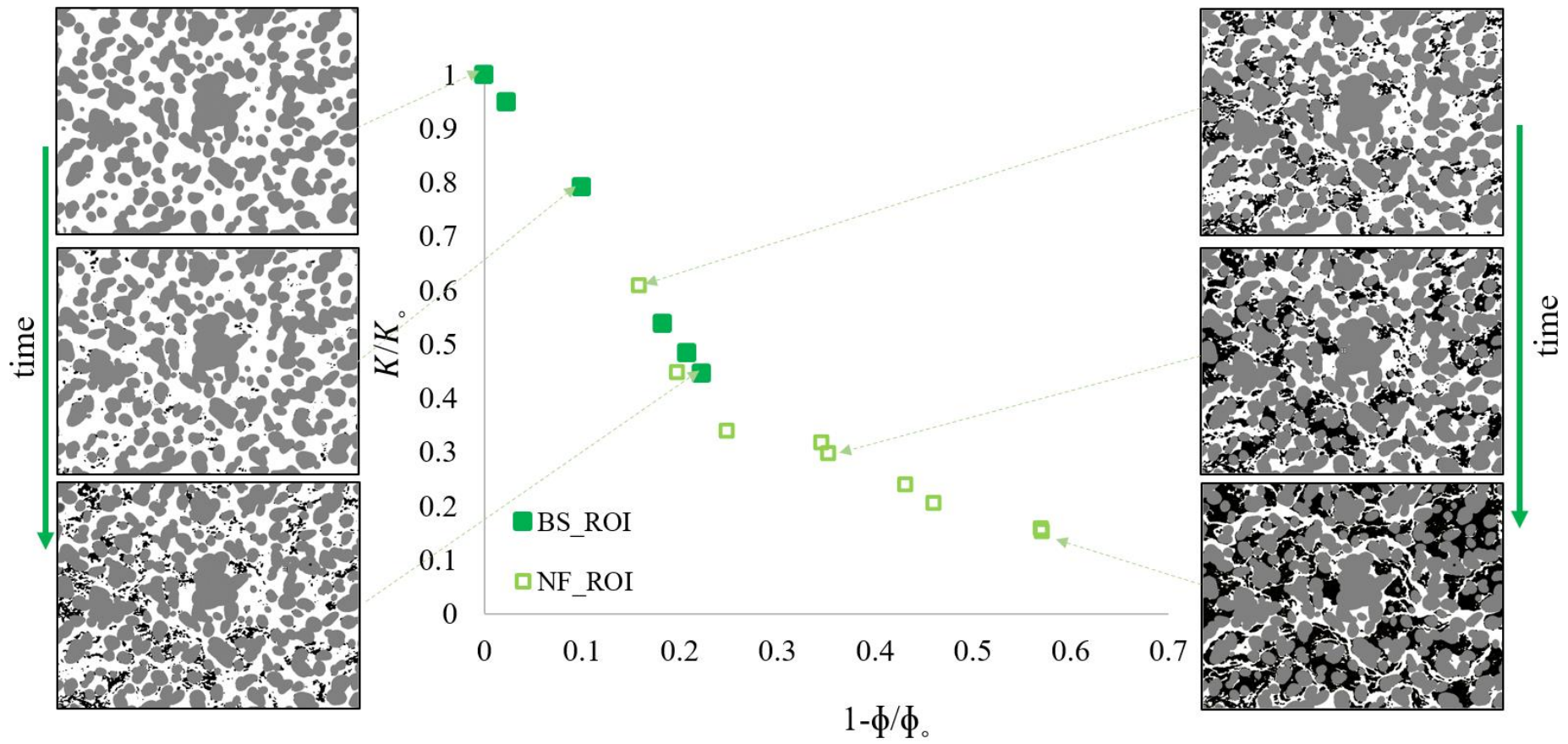


Figure 8-20 Comparison of pressure drop data and biomass increase during NF. Here, two factors contribute to biomass growth; nutrient supply and filtration events. Pressure drop slope increases steadily when the bacterial growth is merely due to nutrient supply, and it jumps abruptly at the filtration times. Most of the points at which the cloudy stream was acquired (spikes of the blue curves) exactly match the pressure curve spikes. The exception occurs in ROI-Test 4, in which the first spikes don't exactly happen at the same time; however, the next spike in the growth curve matches the pressure spike. There is no accountable reason for this mismatch.

Appendix G: Porosity-permeability relationship



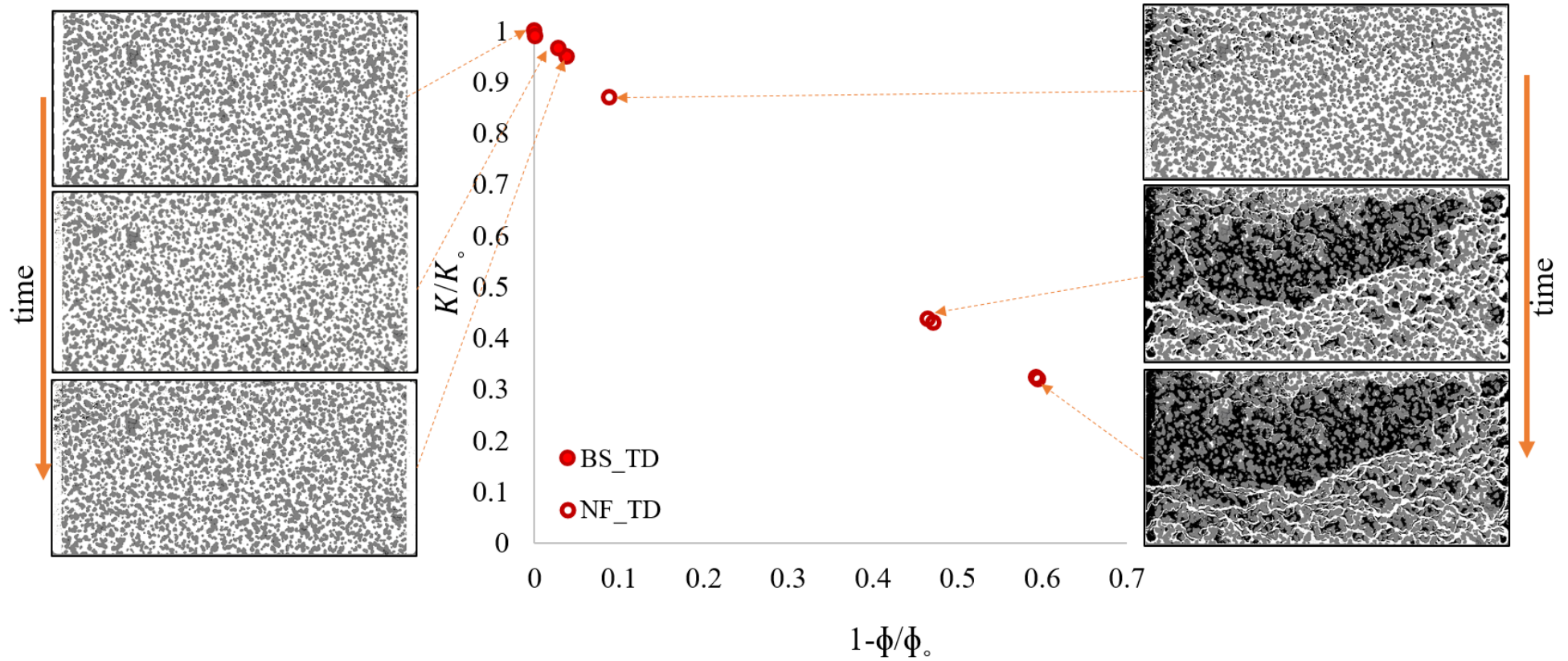


Figure 8-21 Porosity-permeability relationship for TD and ROI simulations associated with the simulated images showing homogeneous and heterogeneous biomass distribution for ROI and TD models. As the experiments show, preferential paths associated with the filtration triggers the transport. Accumulation of biomass due to filtration alters permeability and procedure a microporous material and produces an anti-correlated porosity-permeability relationship.

Appendix H: Bacterial growth under the starvation condition

An experiment was performed to investigate bacterial growth under the limited nutrient condition, e.g., bacterial starvation condition. The limited nutrient condition can represent conditions in the reservoir during well shut-in in which no extra nutrient can reach microorganisms. For the experiment, a clean micromodel was flooded by ethanol and then saturated by autoclaved water. Then it was saturated by the bacterial solution at the stationary growth condition. Afterward, the inlet and outlet lines were closed, and the micromodel was kept at 37°C for 38 days. The micromodel was imaged during various intervals to observe the bacterial growth (see Figure 8-22). Observations show the slow growth of bacteria. The growth made a trapped gas bubble in the micromodel to be dissolved. However, until the very end, the bacteria never accumulated as biomass and no biofilm formed at all.

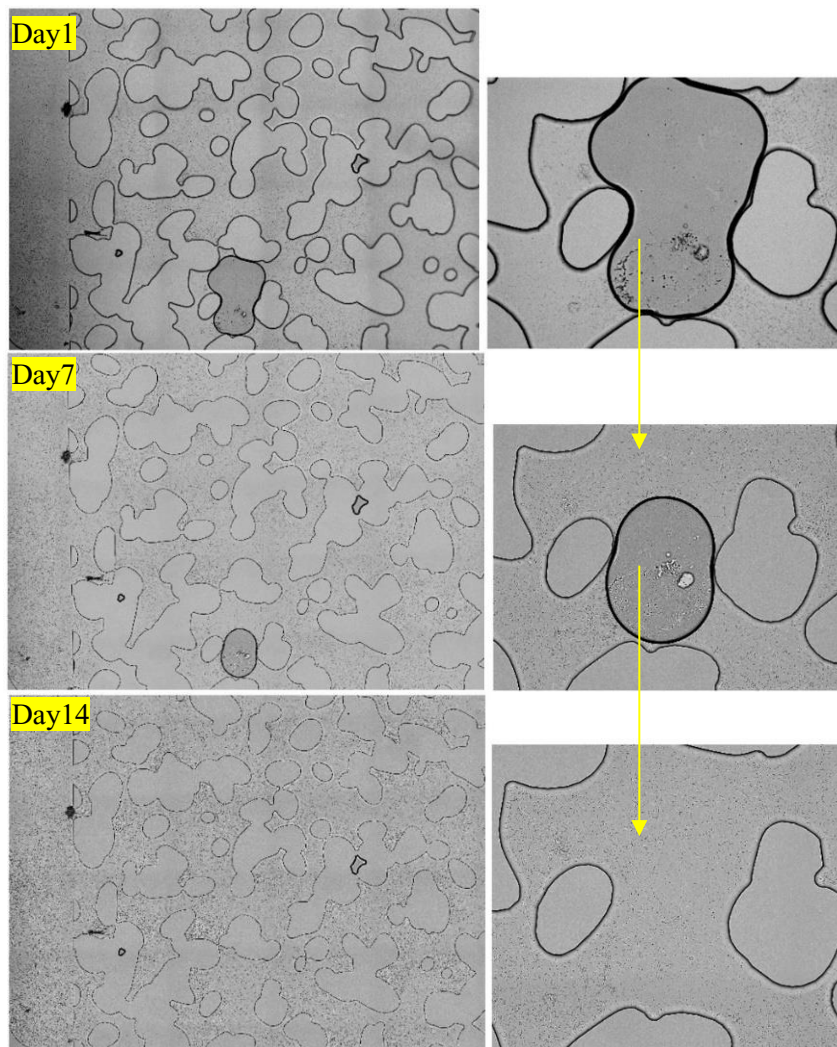


Figure 8-22 Bacterial growth during starvation condition at the beginning, after 7 days, and after 17 days of incubation; the bacteria inside the medium seemingly grew and made the bubble disappears, however, there was no indication of biomass accumulations until the end of the experiment.

Figure 8-23 illustrates the formation of local aggregates of bacteria close to the outlet area after 38 days of incubation.

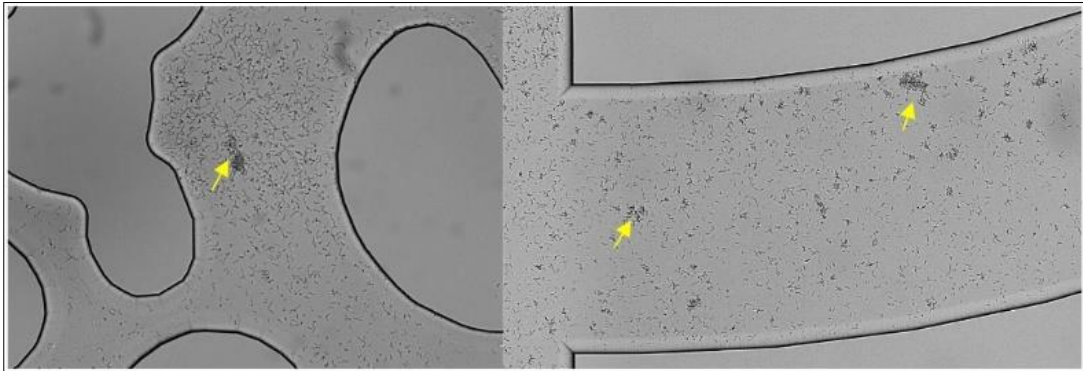


Figure 8-23 Formation of biomass after 38days of incubation.

From the observations, it is recommended to repeat this nutrient-limited experiment on a micromodel in which the biomass has already formed. In this way, possible processes such as decreases in the growth, detachment, and biofilm sloughing can be studied.

Appendix D: Bacterial growth and transport under unsaturated condition

One of the challenges throughout all experiments was preventing the appearance of gas bubbles in the medium, which led to an unwanted unsaturated medium. One of the experiments with this issue was considered as an outlook for the unsaturated condition and completed for both phases of flooding. The first stage of the experiment started by the BS flooding the same way that described for saturated tests. At two times, after almost 4 and 15 hrs of flooding, gas bubbles trapped in the injection syringe entered the pore space, which resulted in the jump in the pressure signal (see Figure 8-24).

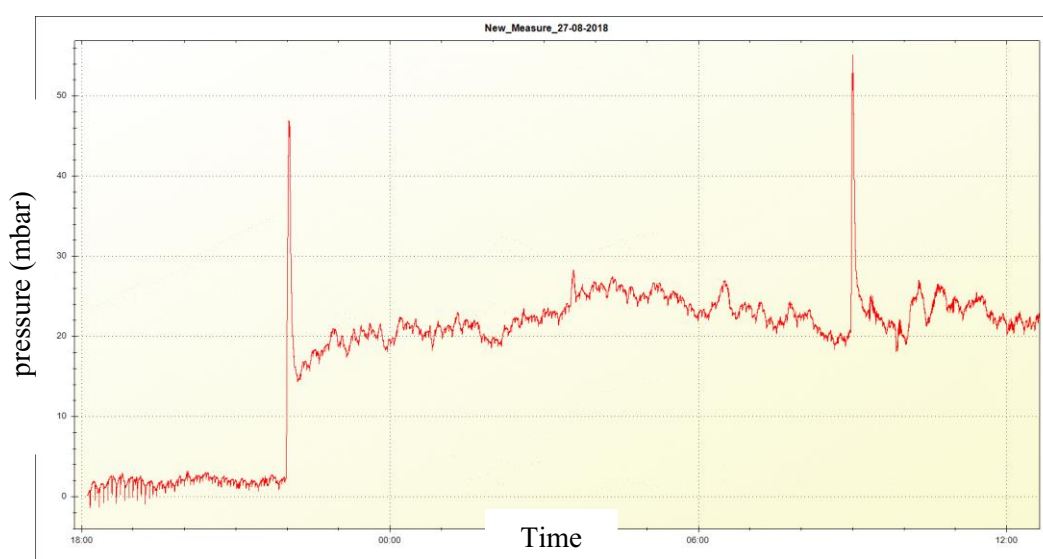


Figure 8-24 Pressure signal during nutrient flooding under unsaturated condition - the pressure jumps here correspond to the air entering into the system.

Micromodel was imaged during phase I. Description of a typical image under unsaturated condition is displayed in Figure 8-25. Selected images during bacterial suspension flooding are shown in Figure 8-26. Similarly, as saturated tests, the bacterial growth in this phase is seen. However, the invasion of air in the system removes some biomass and disrupts the distribution (Figure 8-26; III& IV). In this case, a much smaller injection rate should be applied to avoid such substantial disruption.

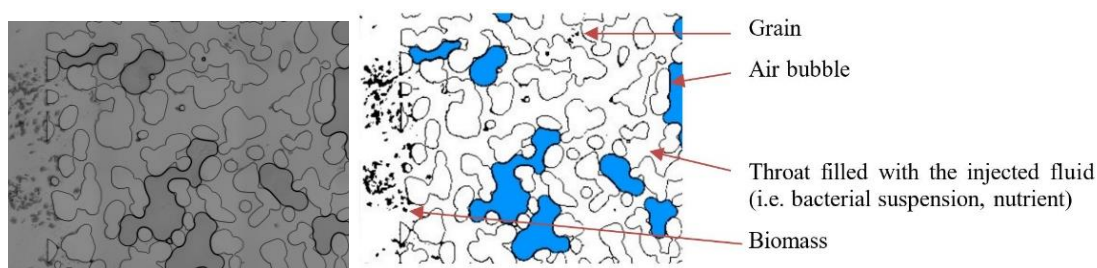


Figure 8-25 A sample microscopic (left) and processed (right) image under unsaturated condition.

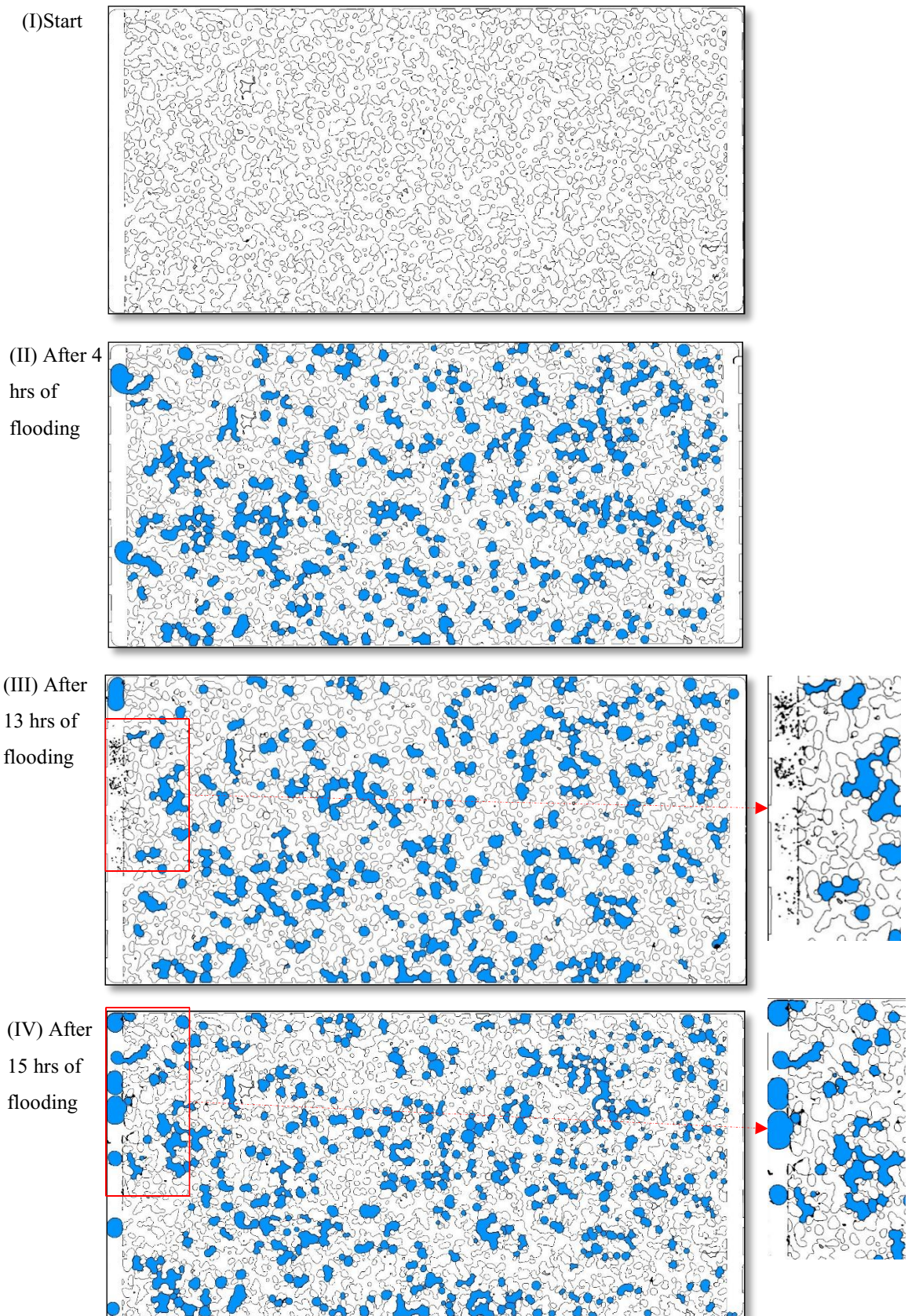


Figure 8-26 Distribution of biomass and air in the micromodel during bacterial suspension flooding under unsaturated condition.

The NF phase was followed; biomass colonization during this phase is presented in Figure 8-29. Similar to the saturated experiments, nutrient enhances the bacterial growth, which once more was disrupted as gas bubbles entered the pore space.

The pressure response in this phase of flooding is displayed in Figure 8-27. After almost 9 hrs of flooding, another source of gas entered the system, which resulted in the jump in the pressure signal. In general, biomass growth increased with a slight trend. Some local observations display this growth in Figure 8-30. The zoomed-in areas show the biomass evolves, and the color becomes darker; however, the release of the gas intrudes the biomass.

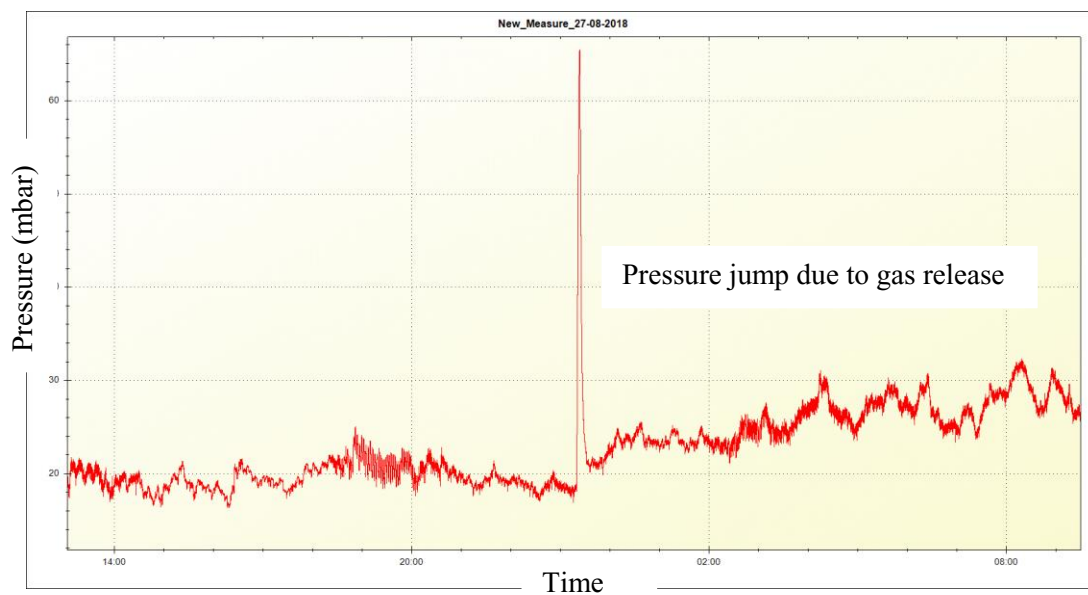


Figure 8-27 Pressure signal during nutrient flooding under unsaturated condition - the pressure jump here corresponds to the air entering into the system.

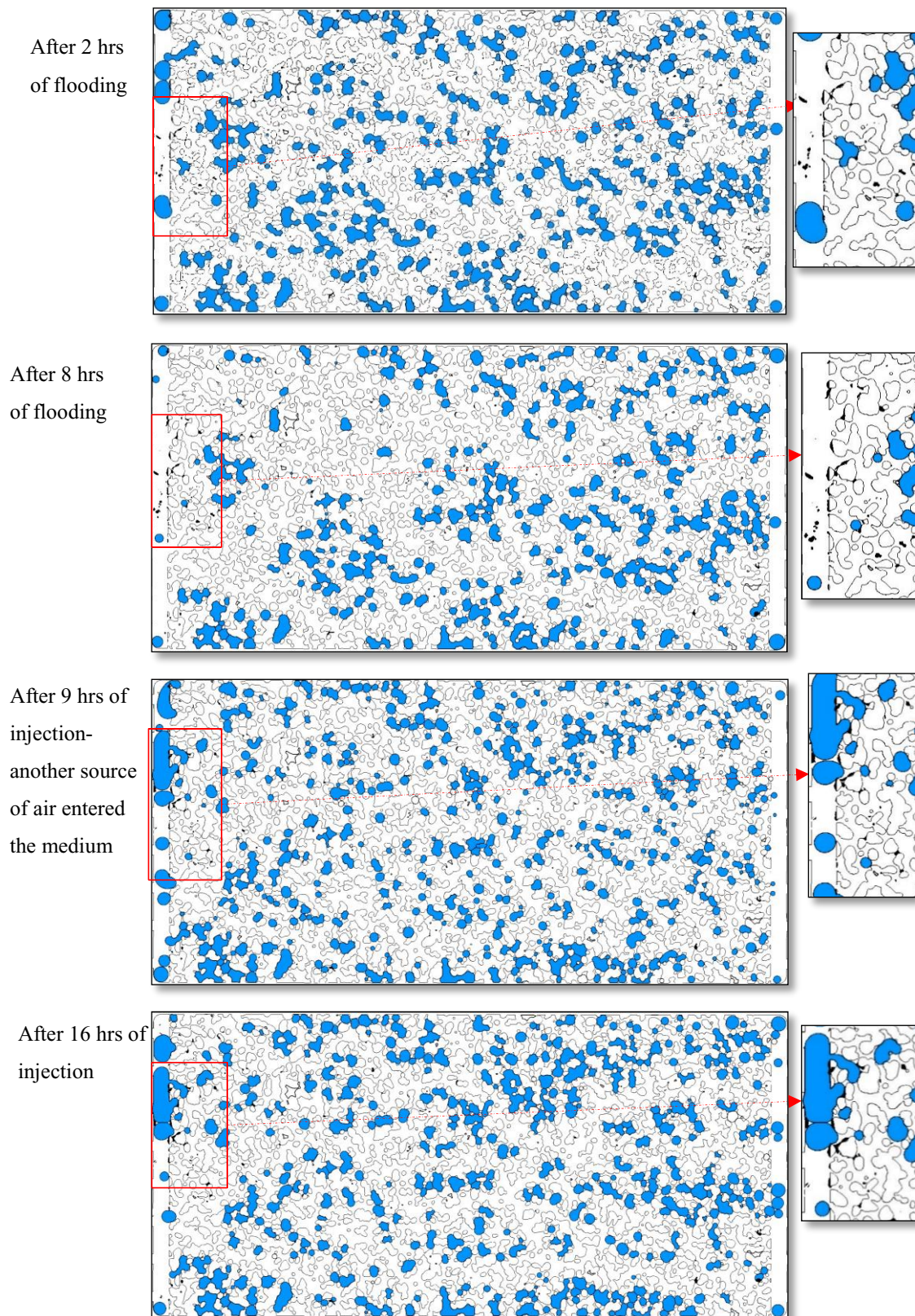


Figure 8-28 Distribution of biomass and air in the micromodel during NF under unsaturated condition.

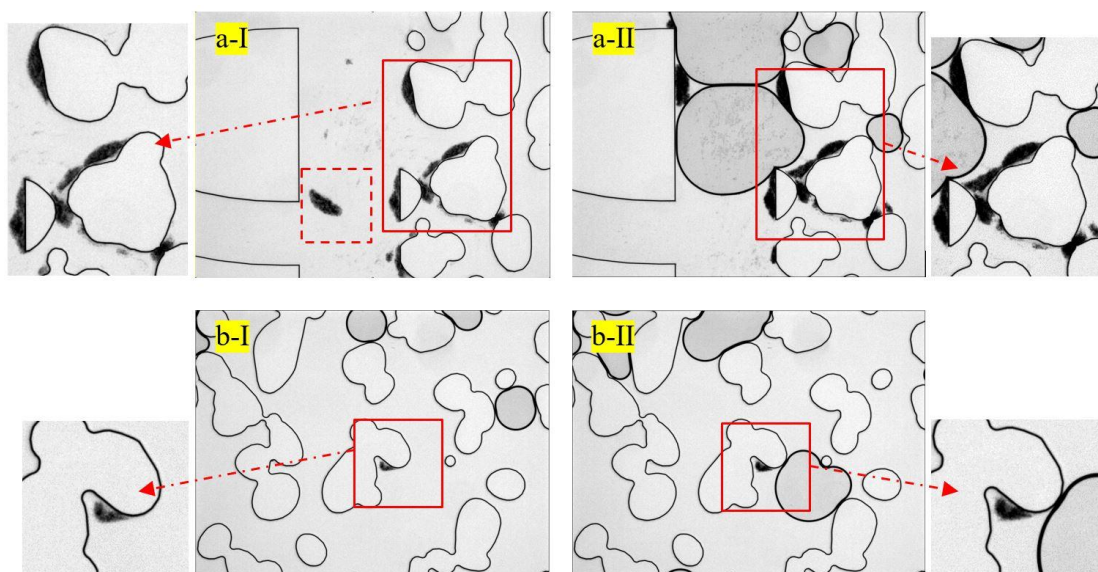


Figure 8-29 Biomass growth during nutrient flooding at different locations under unsaturated condition (a & b); time difference between state I and II is 9 hrs. The entrance of the gas bubble partially removes some biomass (marked in a-I); however, the nutrient flooding enhances the bacterial growth (biomass density gets higher and darker as shown in the zoomed-in areas in both images).

At the end of the experiment, a couple of more tests were carried out. By applying a higher injection rate, the combination of cloudy stream and gas removal under unsaturated condition were observed (see Figure 8-30).

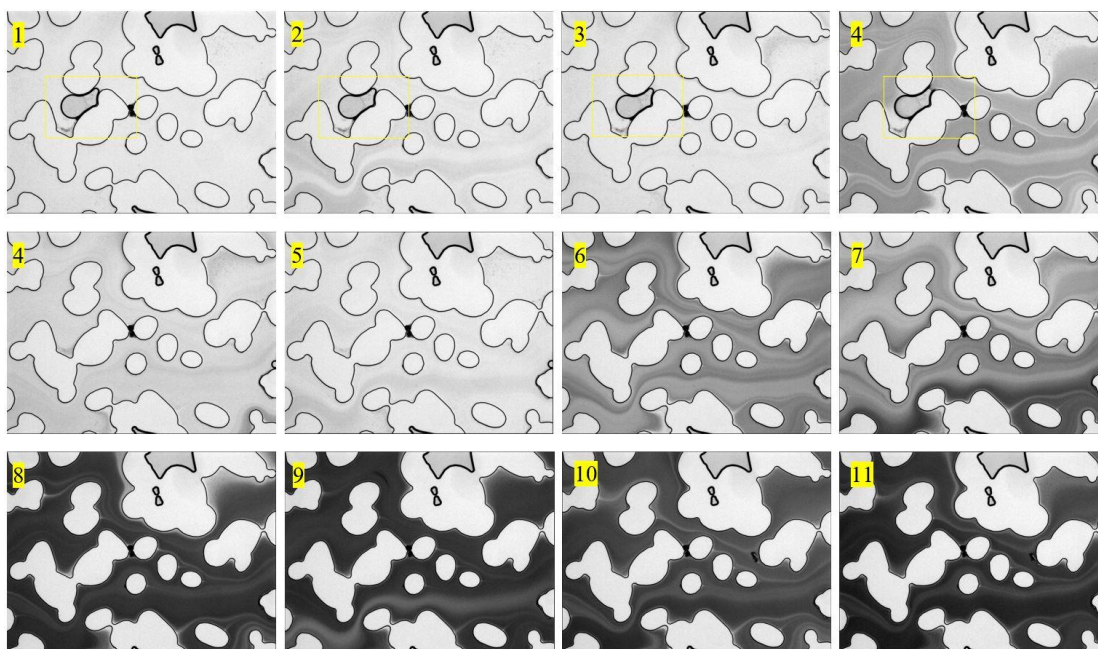


Figure 8-30 Combination of a cloudy stream with the air bubble removal; pictures are taken in intervals of one second.

Nomenclature

ζ	reaction progress
G°	Gibbs energy per mole
γ_i	activity coefficient
a_i	Activity
I	ionic strength
m_i	molal concentration
R	gas constant
T	Temperature
K_{eq}	equilibrium constants
ΔG°	standard Gibbs free energy
ΔH°	standard enthalpy of reaction
ΔS°	standard entropy of reaction
R	gas constant (8.3143 J K ⁻¹ mol ⁻¹)
K	equilibrium constant
A_{geo}	specific geometric surface area
A_{BET}	total surface area
V_m	molar volume of a substance
W_m	molecular weight of the substance
K	molecular weight of the substance
Φ	permeability
S_g	porosity
S_w	gas saturation
p_c	water saturation
p_n	capillary pressure
p_w	pressure of non-wetting phase
\rightarrow	pressure of wetting phase
v_w	wetting phase flow velocity
\rightarrow	wetting phase flow velocity
v_n	non-wetting phase flow velocity
ρ_w	wetting phase density
ρ_n	non-wetting phase density
μ_w	wetting phase viscosity
μ_n	non-wetting phase viscosity
K_{rw}	wetting phase relative permeability
K_{rn}	non-wetting phase relative permeability
q_w	mass injection rate of wetting phase
q_n	mass injection rate of non-wetting phase
N	number of chemical species
C_{ig}	mass fraction of the <i>i</i> th component in the gas phase
C_{iw}	mass fraction of the <i>i</i> th component in the water
D_{eff}	phase effective gas diffusion
D_{aqu}	gas diffusion in the aqueous phase
τ	tortuosity

Abbreviations

UHS	Underground Hydrogen Storage
T&D	Transmission and distribution
PtX	Power to energy
PtG	Power to Gas
FCEV	fuel cell electric vehicles
TVD	True Vertical Depth
OGIP	Original gas in place
BHP	Bottom-hole pressure
MEOR	Microbial Enhanced Oil Recovery
EPS	Extracellular Polymeric Substances
SSA	Specific surface area
BET	Brunauer–Emmett–Teller
EPS	extracellular polymeric substances
CFT	Colloidal filtration theory
BS	Bacterial suspension
NF	Nutrient flooding
VRE	variable renewable energy
OD	optical density
ROI	Region of interest
TD	Total domain
REV	representative elementary volume
TST	Transition state theory